

**Understanding Dalitz Decays of the K_L , in
particular the decays of $K_L \rightarrow e^+e^-\gamma$ and
 $K_L \rightarrow e^+e^-e^+e^-$.**

by

Jason R. LaDue

B.A., University of Illinois - Urbana-Champaign, 1996

M.S., University of Colorado - Boulder, 1999

A thesis submitted to the
Faculty of the Graduate School of the
University of Colorado in partial fulfillment
of the requirements for the degree of
Doctor of Philosophy
Department of Physics

2003

This thesis entitled:
Understanding Dalitz Decays of the K_L , in particular the decays of $K_L \rightarrow e^+e^-\gamma$ and
 $K_L \rightarrow e^+e^-e^+e^-$.
written by Jason R. LaDue
has been approved for the Department of Physics

Prof. Anthony Barker

Prof. Webster Cash

Prof. John Cumalat

Prof. Uriel Nauenberg

Prof. Eric Zimmerman

Date _____

The final copy of this thesis has been examined by the signatories, and we find that
both the content and the form meet acceptable presentation standards of scholarly
work in the above mentioned discipline.

LaDue, Jason R. (Ph.D., Physics)

Understanding Dalitz Decays of the K_L , in particular the decays of $K_L \rightarrow e^+e^-\gamma$ and $K_L \rightarrow e^+e^-e^+e^-$.

Thesis directed by Prof. Prof. Anthony Barker

This analysis studies Dalitz decays of the K_L meson, including $K_L \rightarrow e^+e^-\gamma$ and $K_L \rightarrow e^+e^-e^+e^-$ modes. These modes provide information on the $K_L\gamma\gamma$ vertex. This is needed in order to extract the V_{td} dependence from the decay of $K_L \rightarrow \mu^+\mu^-$.

A search of the 1997 KTeV data set reveals 92269 $K_L \rightarrow e^+e^-\gamma$ events. A corresponding study of the $K_L \rightarrow \pi^0\pi^0\pi_D^0 \rightarrow (\gamma\gamma)(\gamma\gamma)(e^+e^-\gamma)$ decay reveals a number of kaons equal to $(2.62 \pm 0.08) \times 10^{11}$. A measurement of the branching ratio from these studies gives $BR(K_L \rightarrow e^+e^-\gamma) = (10.192 \pm 0.036_{\text{stat}} \pm 0.073_{\text{sys}} \pm 0.285_{\text{ext sys}}) \times 10^{-6}$. Using the combined 1997 and 1999 KTeV data sets, 1,056 $K_L \rightarrow e^+e^-e^+e^-$ events are found with a background of 6.5 ± 0.3 . Studying the $K_L \rightarrow \pi^0\pi^0\pi^0 \rightarrow (\gamma\gamma)(e^+e^-\gamma)(e^+e^-\gamma)$ decay, a number of kaons for the combined period is found to be $(5.83 \pm 0.23) \times 10^{11}$. The branching ratio is $BR(K_L \rightarrow e^+e^-e^+e^-) = (4.16 \pm 0.13_{\text{stat}} \pm 0.13_{\text{sys}} \pm 0.17_{\text{extsys}}) \times 10^{-8}$.

A form factor study, probing $K_L\gamma\gamma$ vertex, is done with two different models. The Bergström, Massó, and Singer model has a single free parameter called α_{K^*} . The best fit to the data for this model occurs at $\alpha_{K^*}(K_L \rightarrow e^+e^-\gamma) = -0.186 \pm 0.011_{\text{stat}} \pm 0.009_{\text{sys}}$ for $K_L \rightarrow e^+e^-\gamma$ events and $\alpha_{K^*}(K_L \rightarrow e^+e^-e^+e^-) = -0.03 \pm 0.13_{\text{stat}} \pm 0.04_{\text{sys}}$ for $K_L \rightarrow e^+e^-e^+e^-$. The D'Ambrosio, Isidori, and Portolés model has two free parameters, α_{DIP} and β_{DIP} . The best fit to the data gives a value of $\alpha_{DIP}(K_L \rightarrow e^+e^-\gamma) = -1.630 \pm 0.038_{\text{stat}} \pm 0.028_{\text{sys}}$ from $K_L \rightarrow e^+e^-\gamma$ and $\alpha_{DIP}(K_L \rightarrow e^+e^-e^+e^-) = -1.08 \pm 0.41_{\text{stat}} \pm 0.13_{\text{sys}}$ and $\beta_{DIP}(K_L \rightarrow e^+e^-e^+e^-) = 13 \pm 54_{\text{stat}} \pm 43_{\text{sys}}$ from $K_L \rightarrow e^+e^-e^+e^-$. Only the $K_L \rightarrow e^+e^-e^+e^-$ mode is sensitive to β_{DIP} .

Dedication

To my Mother and the KTeV group.

Acknowledgements

I would like to thank Tony Barker for his efforts to teach and motivate me to do the best I could.

I would like to give special thanks to the Colorado group for their assistance and understanding, Patrick Toale, Peter Mikelsons, Mike Wilking, Hanwen Huang, Jim Hirschauer, Polly Fordyce, Jin-Yuan Wu, and Joe Ramas.

I would also like to thank Jason Hamm and Elizabeth Turner for allowing me to give them a ton of shifts during the 1999 run. I would like to thank Bob Tschirhart for being an understanding run manager.

Finally, I would like to give a big thanks to the entire KTeV collaboration, because without them I would not have been able to write this thesis: A. Alavi-Harati, T. Alexopoulos, M. Arenton, K. Arisaka, S. Averitte, R.F. Barbosa, A.R. Barker, M. Barrio, L. Bellantoni, A. Bellavance, J. Belz, D.R. Bergman, E. Blucher, G.J. Bock, C. Bown, S. Bright, E. Cheu, S. Childress, R. Coleman, M.D. Corcoran, G. Corti, B. Cox, A.R. Erwin, R. Ford, A. Glazov, A. Golossanov, G. Graham, J. Graham, E. Halkiadakis, J. Hamm, K. Hanagaki, S. Hidaka, Y.B. Hsiung, V. Jejer, D.A. Jensen, R. Kessler, H.G.E. Kobrak, A. Lath, A. Ledovskoy, P.L. McBride, P. Mikelsons, E. Monnier, T. Nakaya, K.S. Nelson, H. Nguyen, V. O'Dell, R. Pordes, V. Prasad, X.R. Qi, B. Quinn, E.J. Ramberg, R.E. Ray, A. Roodman, S. Schnetzer, K. Senyo, P. Shanahan, P.S. Shawhan, J. Shields, W. Slater, N. Solomey, S.V. Somalwar, R.L. Stone, E.C. Swallow, S.A. Taegar, R.J. Tesarek, G.B. Thomson, P.A. Toale, A. Tripathi, R. Tschirhart, S.E. Turner, Y.W. Wah, J. Wang, H.B. White, J. Whitmore, B. Winstein, R. Winston, T. Yamanaka, E.D. Zimmerman

The KTeV Collaboration

Contents

Chapter

1	Introduction	1
1.1	Symmetries	1
1.2	The Neutral Kaon	1
1.3	The “Golden Mode”	3
1.4	Two Photon Decays of the Neutral Kaon	5
1.5	Form Factor	12
1.5.1	Vector Meson Dominance	14
1.5.2	BMS Model	15
1.5.3	DIP Model	17
1.6	Previous Measurements	18
1.6.1	$K_L \rightarrow e^+e^-\gamma$	18
1.6.2	$K_L \rightarrow e^+e^-e^+e^-$	18
1.6.3	Form Factor	19
2	The KTeV Detector	21
2.1	Beam	22
2.1.1	Proton Beam	22
2.1.2	Kaon Beam	23
2.2	Vacuum	24
2.2.1	Photon Vetoes	27
2.3	Charged Spectrometer	27
2.3.1	Analysis Magnet	28
2.3.2	Drift Chamber	30

2.3.3	Drift Chamber Calibration	31
2.3.4	Photon Vetoes	34
2.4	Transition Radiation Detector	35
2.5	Trigger Hodoscope	37
2.6	Calorimeter	37
2.6.1	Crystals	38
2.6.2	Calorimeter Instrumentation	39
2.6.3	Calibration	40
2.6.4	Photon Vetoes	41
2.7	Muon System	44
3	The KTeV Trigger and Event Selection	46
3.1	Organization of Data Collection	46
3.2	Level 1 Trigger	47
3.2.1	Photon Vetoes	48
3.2.2	Trigger Hodoscope	48
3.2.3	E-Total	48
3.2.4	DC ORs	49
3.2.5	Muon System	49
3.2.6	Beam Trigger	50
3.3	Level 2 Trigger	51
3.3.1	Hardware Cluster Counter	51
3.3.2	DC Hit Counting	52
3.3.3	Track Finding	61
3.3.4	Stiff Track Trigger	61
3.3.5	TRD Trigger	62
3.4	Data Acquisition	62
3.5	Level 3 Trigger	65
3.6	Data Reduction	66
3.6.1	E799 Split	66
3.6.2	Crunch	67

4	Event Reconstruction	69
4.1	Tracking	69
4.1.1	Good DC Hits	69
4.1.2	Tracks	70
4.2	Clusters	72
4.2.1	Energy	73
4.2.2	Position	74
4.2.3	Corrections	74
4.3	TRD Identification	77
4.4	Vertexing	79
4.4.1	Track-Cluster Matching	80
4.4.2	Vertex Selection	80
5	Event Simulation	84
5.1	Kaon Production	84
5.2	Kaon Decay	86
5.2.1	$K_L \rightarrow \gamma\gamma$ Generator	86
5.2.2	$K_L \rightarrow e^+e^-\gamma$ Generator	87
5.2.3	$K_L \rightarrow e^+e^-e^+e^-$ Generator	88
5.2.4	$K_L \rightarrow \pi^0\pi^0\pi^0$, $K_L \rightarrow \pi^0\pi^0\pi_D^0$ and $K_L \rightarrow \pi^0\pi_D^0\pi_D^0$ Generator . .	91
5.3	Particle Tracing	93
5.3.1	Decay Product Interaction with Material	94
5.3.2	Detector Simulation	102
5.4	Accidental Overlays	108
5.5	Trigger	110
6	General Event Selection	111
6.1	Bad Spills	111
6.2	Fiducial Region	114
6.3	Trigger Verification	116
6.4	Calorimeter	118
6.5	Spectrometer	122

6.6	E/P	130
6.7	Transition Radiation Detector	132
6.8	Transverse Momentum	134
7	$K_L \rightarrow e^+e^-\gamma$ Branching Ratio	137
7.1	Data Selection	138
7.1.1	Backgrounds	139
7.1.2	Normalization Cuts	145
7.1.3	Data Numbers	146
7.2	Monte Carlo Sample	148
7.3	Flux	149
7.4	Branching Ratio	152
7.5	Systematics	152
7.5.1	Varying Sets Of Cuts	152
7.5.2	Upstream Detector Material	153
7.5.3	Track Hit Inefficiency	154
7.5.4	Hit resolution	155
7.5.5	Energy Slope	157
7.5.6	Energy resolution	157
7.5.7	γ Inefficiency	159
7.5.8	Radiative Corrections	163
7.5.9	Varying BMS Form Factor α_K^*	163
7.6	Result	165
8	$K_L \rightarrow e^+e^-e^+e^-$ Branching Ratio	168
8.1	Data Selection	169
8.1.1	Backgrounds	172
8.1.2	Normalization Cuts	175
8.1.3	Data Numbers	179
8.2	Monte Carlo Sample	179
8.3	Flux	181
8.4	Branching Ratio	182

8.5	Systematic Uncertainty	182
8.5.1	Varying Sets Of Cuts	182
8.5.2	Upstream Detector Material	183
8.5.3	Track Hit Inefficiency	183
8.5.4	Hit resolution	184
8.5.5	Energy Slope	184
8.5.6	Energy resolution	184
8.5.7	γ Inefficiency	185
8.5.8	Radiative Corrections	185
8.5.9	Varying the Form Factor	185
8.6	Result	186
9	Form Factor Measurements	188
9.1	Shape χ^2 Fit	188
9.1.1	Systematics	189
9.2	Log Likelihood	192
9.2.1	Systematics	199
9.3	Results	200
	Bibliography	204
	Appendix	
A	TRD Trigger Studies	208
A.1	Trigger Definition	208
A.2	TRD Trigger Efficiency	208
A.3	Efficiency Curves	209
A.4	Simulating Curves	212
B	Material Studies	215

Tables

Table

1.1	Theoretical Rates with and without radiative corrections. The cutoff is $E_\gamma^* > 5\text{MeV}$ for single Dalitz and $x_{4e} > 0.95$ for double Dalitz.	12
1.2	Theoretical Rates for $K_L \rightarrow e^+e^-e^+e^-$	12
1.3	Previously Measured Branching Ratios for $K_L \rightarrow e^+e^-\gamma$	19
1.4	Previously Measured Branching Ratios for $K_L \rightarrow e^+e^-e^+e^-$	19
1.5	Previously Measured α_{K^*}	20
1.6	Previously Measured α_{DIP}	20
2.1	Position and Dimensions of the Ring Counter Vetoes.	27
2.2	The Size and Dimensions of each part of the Spectrometer.	30
2.3	Wires and cables per DC plane. Listed as a function of increasing z . 'Primed' planes refer to the downstream plane of a plane-pair.	31
2.4	Position and Dimensions of the Spectrometer Vetoes.	35
2.5	Position and Dimensions of the TRD.	36
2.6	Position and Dimensions of CA and CIA.	42
3.1	Trigger Rates at various levels. The beam intensity for the 97 numbers is 4×10^{12} protons per spill, while 99 numbers are for 8×10^{12} protons per spill.	66
3.2	The number and size of events of interest.	68
5.1	Independently Measured Branching Ratios for π^0 and K_L Decays of Interest.	93

5.2	Material in the Upstream segment of the detector. X is the path length of the material and X_0 is the characteristic radiation length of the material.	98
5.3	Probability of bremsstrahlung for upstream detector elements.	102
6.1	Bad Spill Summary. † refers to the cutting only on certain CPUs for this bit.	112
6.2	Additional Bad Spills and Reasons.	113
7.1	$K_L \rightarrow e^+e^-\gamma$ Cuts.	139
7.2	The Number of Events in the Data for Signal and Normalization modes. † indicates that the estimated background of 476 events has been subtracted.	148
7.3	The Monte Carlo Numbers and Acceptance for $K_L \rightarrow e^+e^-\gamma$ events. The errors are statistical.	148
7.4	The Monte Carlo Numbers and Acceptance for $K_L \rightarrow \pi^0\pi_D^0\pi_D^0$ events. The errors are statistical.	148
7.5	The number of kaons produced from the Target in the specific region of energy and vertex z as discussed in section 5.1, for the two run periods. The errors are statistical.	152
7.6	The Branching Ratio for $K_L \rightarrow e^+e^-\gamma$ as a function of run period. The errors are statistical.	152
7.7	Definition of Loose and Tight Cut for $K_L \rightarrow e^+e^-\gamma$	153
7.8	List of Sources of Uncertainty for the Branching Ratio measurement of $K_L \rightarrow e^+e^-\gamma$	166
8.1	$K_L \rightarrow e^+e^-e^+e^-$ Cuts.	169
8.2	The Monte Carlo prediction of Background to $K_L \rightarrow e^+e^-e^+e^-$	175
8.3	The Monte Carlo prediction of Backgrounds to $K_L \rightarrow \pi^0\pi_D^0\pi_D^0$	178
8.4	The number of events in the data for signal and normalization modes.	179
8.5	The Monte Carlo simulation numbers and acceptance for $K_L \rightarrow e^+e^-e^+e^-$ events. The errors are statistical only.	180
8.6	The Monte Carlo simulation numbers and acceptance for $K_L \rightarrow \pi^0\pi_D^0\pi_D^0$ events.	180

8.7	The Background Subtracted Number of $K_L \rightarrow \pi^0 \pi_D^0 \pi_D^0$ Events and The Number of Kaons produced from the Target for the two run periods. The errors are statistical. The 1997 flux agrees within errors with the flux found from $K_L \rightarrow \pi^0 \pi^0 \pi_D^0$	181
8.8	The number of $K_L \rightarrow e^+ e^- e^+ e^-$ events after background subtraction and the Branching Ratio as a function of run period. The errors are statistical.	182
8.9	Definition of Loose and Tight Cuts for $K_L \rightarrow e^+ e^- e^+ e^-$	183
8.10	List of Sources of Uncertainty for the Branching Ratio measurement. . .	187
9.1	List of sources of uncertainty for the $K_L \rightarrow e^+ e^- \gamma$ form factor measurement.	191
9.2	Measurements of the α_{K^*} and α_{DIP} from the $K_L \rightarrow e^+ e^- \gamma$ mode with all uncertainties.	192
9.3	List of Sources of Uncertainty for the $K_L \rightarrow e^+ e^- e^+ e^-$ Form Factor Measurement.	201
9.4	Measurements of α_{K^*} , α_{DIP} , and β_{DIP}	202
A.1	Changes in the Branching Ratio and α_{K^*} measurement for $K_L \rightarrow e^+ e^- \gamma$ due to the TRD Trigger element.	214
B.1	Uncertainties in Measuring the amount of Material.	216
B.2	Amounts of Material.	216

Figures

Figure

1.1	Example of possible $\Delta S = 2$ oscillations of K^0 to \bar{K}^0	2
1.2	QED Feynman Graphs to $K_L \rightarrow \mu^+ \mu^-$	4
1.3	Short-Distance Feynman Graphs to $K_L \rightarrow \mu^+ \mu^-$	5
1.4	Long-distance Feynman Graphs to $K_L \rightarrow \mu^+ \mu^-$	6
1.5	Feynman Graph for Two Photon decay, $K_L \rightarrow \gamma \gamma$	6
1.6	Feynman Graph Single Dalitz decay, $K_L \rightarrow e^+ e^- \gamma$	8
1.7	Feynman Graph for Radiative Single Dalitz decay, $K_L \rightarrow e^+ e^- \gamma \gamma$	8
1.8	Feynman Graph for One Loop Corrections to Single Dalitz decay, $K_L \rightarrow e^+ e^- \gamma \gamma$	9
1.9	Diagram of ϕ the phase space variable.	10
1.10	Feynman Graph for Double Dalitz decay, $K_L \rightarrow e^+ e^- e^+ e^-$	11
1.11	Exchange Feynman Graphs for Double Dalitz decay, $K_L \rightarrow e^+ e^- e^+ e^-$. .	11
1.12	Feynman Graphs for Radiative Double Dalitz.	13
1.13	Feynman Graphs for Radiative Double Dalitz.	13
1.14	Vector Meson Dominance model for $K_L \gamma^* \gamma^*$ vertex.	15
1.15	Standard Kaon Vector-Vector Transition.	17
1.16	Kaon Vector-Vector Transition.	17
2.1	The Secondary Beam region, NM2	25
2.2	3-dimensional view of Detector.	26
2.3	Top Down view of Detector. x and z scales are different.	28
2.4	Cross-sectional View of a Ring Counter Veto.	29
2.5	Spectrometer Elements. x and z scales are different.	29

2.6	y view schematic of the field and sense wire arrangement within a drift chamber.	32
2.7	Distribution of E/P for run 14934. Top plot has only Online Calibration, bottom plot has complete DC calibration.	34
2.8	Cross-sectional View of a Spectrometer Veto.	35
2.9	Cross-sectional View of TRD.	37
2.10	Trigger Hodoscope plan view.	38
2.11	3-dimensional view of CsI Calorimeter.	39
2.12	Distribution of E/P . Both CsI and offline DC calibrations have been performed.	41
2.13	Collar Anti plan view.	42
2.14	Hadron Anti plan view.	43
2.15	Muon Trigger plane. Dashed lines indicate the 1 cm counter overlap in MU2.	44
2.16	Muon Trigger plane.	45
3.1	Possible HCC bit patterns and corresponding weights for 2×2 groups of blocks. Filled blocks represent those with the HCC bit on.	52
3.2	Example of Clustering in the Calorimeter. The Bold Boxes indicate that HCC bit is on. Assume that the 25 crystals are an entire array, each dot is the center of a 2×2 array considered by the HCC. The numbers represent the weight of that 2×2 array. The total weight is +8, so there are two Clusters.	53
3.3	Example of Clustering in the real Calorimeter. Shading indicates energy in logarithmic steps from 0.01GeV-0.1GeV, 0.1-1.0GeV, 1.0-10.0GeV and more then 10.0GeV. The bold boxes indicate that the HCC bit is on. The circles are where the HCC algorithm found a cluster.	54
3.4	Path of DC Signals to DCHC.	55
3.5	Diagram of a Kumquat Module.	56
3.6	An example of Hit Counting.	57
3.7	Photograph of a Banana Module.	58
3.8	Diagram of a Banana Module.	59

3.9	t_1 vs. t_2 and in-time pair region boundary for hits on tracks, with two good track.	60
3.10	t_1 vs. t_2 and in-time pair region boundary for isolated pairs rejected. . .	61
3.11	TRD trigger requirements	63
4.1	Sum of Distance. x view hits on tracks in $Ke3$ from the 1999 run period.	70
4.2	Sum of Distance scenarios.	71
4.3	Hits in the Drift Chambers showing the Best Fit Track, the Matching Clusters, Hits in Trigger Hodoscope, and Hits in the TRDs. Top is downward looking view shown the x plane, the other showing y plane of the same event.	72
4.4	Energy of Individual Clusters. Shading indicates energy in logarithmic steps from 0.01GeV-0.1GeV, 0.1-1.0GeV, 1.0-10.0GeV and more then 10.0GeV. The bold boxes indicate that the HCC bit is on. The circles are where the reconstruction algorithm found a seed.	73
4.5	Picture of the Energy for Clusters in the CsI. These clusters overlap. Shading indicates energy in logarithmic steps from 0.01GeV-0.1GeV, 0.1-1.0GeV, 1.0-10.0GeV and more then 10.0GeV. The bold boxes indicate that the HCC bit is on. The circles are where the reconstruction algorithm found a cluster.	75
4.6	TRD ADC Values for Pions and Electrons from runs 8384, 8387, and 8397 for a Single Chamber [1].	78
4.7	Π_{TRD} Values for Pions and Electrons from runs 8384, 8387, and 8397 [1].	79
4.8	Hits in the CsI, lines show the path of the tracks in x and y projected onto the face of the CsI. The Diamond is the best fit vertex.	81
4.9	View of Hits in the Drift Chambers showing the Best Fit Track, the Matching Clusters, Hits in Trigger Hodoscope, Hits in the TRDs and the Common Vertex. Top plot is a downward looking view showing the x plane, the other plot shows y plane.	83
5.1	Plot A is the Decay Vertex at Generation of the Kaon. Plot B is the Generated Kaon Momentum.	85

5.2	Generated Phase Space for $K_L \rightarrow e^+e^-\gamma$. X ranges from 0.0 to 1.0 and Y ranges from -1.0 to 1.0. The Z-axis is the number of events at generation.	88
5.3	BMS form factor squared as a function of phase space variable x and the parameter α_{K^*} .	89
5.4	Generated Phase Space. Comparing x for Tree Level graphs to Tree Level plus One Loop and Radiative Graphs.	90
5.5	$X_{4e} = m_{eee}^2/M_K^2$ for $K_L \rightarrow e^+e^-e^+e^-$.	91
5.6	X_{11} versus X_{22} Phase Space Variables for $K_L \rightarrow e^+e^-e^+e^-$ at Generation.	92
5.7	$\cos(\theta_{11})$ versus $\cos(\theta_{22})$ Phase Space Variables for $K_L \rightarrow e^+e^-e^+e^-$ at Generation.	93
5.8	ϕ/π Phase Space Variable for $K_L \rightarrow e^+e^-e^+e^-$ at Generation.	94
5.9	$x_{11} + x_{22}$ comparing Two Values of α_{DIP} at Generation. β_{DIP} is set to +1.0 for both sets.	95
5.10	x_{11} and x_{22} comparing Two Values of β_{DIP} during Generation. α_{DIP} is set to -1.0 for both sets.	96
5.11	$x_{11} + x_{22}$ Comparing Tree Level graphs to Tree Level plus One Loop and Radiative Graphs.	97
5.12	$\cos(\theta_{11}) + \cos(\theta_{22})$ Comparing Tree Level graphs to Tree Level plus One Loop and Radiative Graphs.	98
5.13	Feynman Diagrams for Three π^0 Single Dalitz decay, $K_L \rightarrow \pi^0\pi^0\pi_D^0 \rightarrow (\gamma\gamma)(\gamma\gamma)(e^+e^-\gamma)$.	99
5.14	Feynman Diagrams for Three π^0 Double Single Dalitz decay, $K_L \rightarrow \pi_D^0\pi^0\pi_D^0 \rightarrow (e^+e^-\gamma)(\gamma\gamma)(e^+e^-\gamma)$.	99
5.15	Picture of the Upstream Detector Elements showing the Vacuum Window, Helium Bags, and DC 1.	100
5.16	Comparison of Data (Dots) to MC (Histogram) DC 2Y Hit Positions in the DC for $K_L \rightarrow \pi^0\pi^0\pi_D^0$ Charged Tracks. The plots on the left use a MC without a DC Map, the right with the DC Map. The top plot of the pair is Data, MC overlay, the bottom is a ratio.	105

5.17	Map of the Single Hit and High SOD Inefficiency for DC 1X from the 1997 data set. Vertical axis is a position along the wire, horizontal axis is the wire number.	106
5.18	Map of the isolated single and high SOD Inefficiency for DC 1X from the 1999 data set. Vertical axis is a position along the wire, horizontal axis is the wire number.	107
6.1	Bad Spill Bits for $K_L \rightarrow \pi^0 \pi^0 \pi_D^0$ Events. The cross hatched bins are ones in which that bit is cut on most of the time, open boxes are bits not used.	114
6.2	Energy of the $K_L \rightarrow \pi^0 \pi^0 \pi_D^0$ data (Dots) compared to MC (Histogram) requiring only two good tracks and 7 hard ware clusters.	115
6.3	Vertex Z of the $K_L \rightarrow \pi^0 \pi_D^0 \pi_D^0$ data (Dots) compared to MC (Histogram) after all cuts. Lower plot is the ratio.	115
6.4	Vertex Z of the $K_L \rightarrow \pi^0 \pi^0 \pi_D^0$ MC, Generated versus Neutral Reconstruction.	117
6.5	Vertex Z of the $K_L \rightarrow \pi^0 \pi^0 \pi_D^0$ MC, Generated versus Charge Reconstruction.	118
6.6	Vertex X of the $K_L \rightarrow \pi^0 \pi^0 \pi_D^0$ data (Dots) compared to MC (Histogram) after all cuts.	119
6.7	Vertex Y of the $K_L \rightarrow \pi^0 \pi^0 \pi_D^0$ data (Dots) compared to MC (Histogram) after all cuts. Lower plot is the ratio.	119
6.8	Vertex Y of the $K_L \rightarrow \pi^0 \pi^0 \pi_D^0$ data, Winter (Dots) compared to Summer (Histogram).	120
6.9	Vertex Y of the $K_L \rightarrow \pi^0 \pi^0 \pi_D^0$ data, Early Summer Runs (Dots) compared to Late Summer Runs (Histogram). Lower plot is the ratio. . . .	120
6.10	Distance between Clusters in the CsI measured in meters. Comparing $K_L \rightarrow \pi^0 \pi^0 \pi_D^0$ Data (Dots) and MC (Histogram) after all other cuts. . .	121
6.11	Distance between Clusters in the CsI measured in meters. Comparing $K_L \rightarrow \pi^0 \pi_D^0 \pi_D^0$ Data (Dots) and MC (Histogram) after all other cuts. .	121
6.12	Two Dimensional View of the Face of the Calorimeter showing the Position of Clusters for $K_L \rightarrow \pi^0 \pi^0 \pi_D^0$ Data. Each event will have 7 clusters in this plot.	122

6.13	Minimum Cluster Energy for $K_L \rightarrow e^+e^-\gamma$ Data (Dots) compared to MC (Histogram) after all other cuts.	123
6.14	Minimum Cluster Energy for $K_L \rightarrow \pi^0\pi^0\pi_D^0$ Data (Dots) compared to MC (Histogram) after all other cuts.	123
6.15	Vertex χ^2 for $K_L \rightarrow \pi^0\pi_D^0\pi_D^0$ Data (Dots) compared to MC (Histogram) after all other cuts.	124
6.16	Vertex χ^2 for $K_L \rightarrow e^+e^-\gamma$ Data (Dots) compared to MC (Histogram) after all other cuts.	125
6.17	Off-Magnet χ^2 for $K_L \rightarrow \pi^0\pi_D^0\pi_D^0$ Data (Dots) compared to MC (Histogram) after all other cuts.	125
6.18	Off-Magnet χ^2 for $K_L \rightarrow \pi^0\pi^0\pi_D^0$ Data (Dots) compared to MC (Histogram) after all other cuts.	126
6.19	Distance between tracks in DC 1X measured in meters. Dots are $K_L \rightarrow e^+e^-e^+e^-$ data and histogram is signal and conversion background MC after a complete reconstruction.	127
6.20	Distance between Tracks in DC 1X measured in meters. Dots are $K_L \rightarrow e^+e^-e^+e^-$ data and histogram is signal MC after a complete reconstruction. Lower plot is the ratio of the two.	128
6.21	Distance between Tracks in DC 1X measured in meters. Dots are $K_L \rightarrow e^+e^-\gamma$ data and histogram is signal MC after a complete reconstruction. Lower plot is the ratio of the two.	128
6.22	The Min-Maximum Track Separation in DC 1X measured in meters. Dots are $K_L \rightarrow e^+e^-e^+e^-$ Data and Histogram is Signal MC.	129
6.23	Total Mass measured in GeV after all cuts including a cut on Min-Maximum Separation. Dots are $K_L \rightarrow e^+e^-e^+e^-$ Data and Histogram is Conversion MC. The Conversion MC is approximately 100 times the data flux.	129
6.24	Kaon Energy measured in GeV after all cuts including a cut on Min-Maximum Separation. Dots are $K_L \rightarrow e^+e^-e^+e^-$ Data and Histogram is Conversion MC. The Conversion MC is approximately 100 fluxes worth of data.	130

6.25	m_{ee}^{11} for $K_L \rightarrow e^+e^-e^+e^-$ signal MC (Dots) compared to Conversion background MC (Histogram). Also shown is a hypothetical cut at 5MeV, which is not made in the actually analysis.	131
6.26	E/P for Data (dots) and MC (histogram) of electrons, using $Ke3$ decays. Electrons selected using Π_{TRD} (<i>i.e.</i> the TRD) [2].	132
6.27	E/P for Data during the Crunch. Trigger 1, 4 Tracks. The drop off at 0.75 is due to the requirement that two of the tracks must have an $E/P > 0.75$ from the L3 Trigger.	133
6.28	E/P for Data(dots) $K_L \rightarrow e^+e^-\gamma$ compared to MC(histogram after all cuts have been made. Top plot is an overlay, bottom is a ratio.	133
6.29	Π_{TRD} for both charged tracks for $K_L \rightarrow \pi^0\pi^0\pi_D^0$ events. The top plot is the 1997 data set, the bottom is 1999 data set.	134
6.30	Defining the Quantity of Transverse Momentum \vec{P}_T	135
6.31	\vec{P}_T^2 for fully reconstructed $K_L \rightarrow \pi^0\pi^0\pi_D^0$ events where Data (dots) is compared to the MC (histogram). Lower plot is the ratio of Data over MC.	136
7.1	A Detector picture showing a $K_L \rightarrow e^+e^-\gamma$ event.	140
7.2	A Detector picture showing a $K_L \rightarrow \pi^0\pi^0\pi_D^0$ event.	141
7.3	Total Invariant Mass versus \vec{P}_T^2 for $K_L \rightarrow e^+e^-\gamma$ Data events. Box defines the signal region.	142
7.4	Total Invariant Mass for $K_L \rightarrow e^+e^-\gamma$ Candidate events for Data events. The hatched plot overlayed is the same mass after a \vec{P}_T^2 cut is made. . .	143
7.5	Total Invariant Mass for $K_L \rightarrow e^+e^-\gamma$ Candidate events for Data events. The hatched plot overlayed is the same mass after a Π_{TRD} cut is made. . .	143
7.6	Total Invariant Mass for 1997 $K_L \rightarrow e^+e^-\gamma$ Candidate events for Data events. A fit is performed for the exponentially falling edge between 0.4425 and 0.4575 MeV, then extrapolated into the signal region denoted by the vertical lines. The number of events from this fit is 79.	144
7.7	Total Invariant Mass for 1999 $K_L \rightarrow e^+e^-\gamma$ Candidate events for Data events. A fit is performed for the exponentially falling edge between 0.4425 and 0.4575 MeV, then extrapolated into the signal region denoted by the vertical lines. The number of events from this fit is 476.	145

7.8	The Dalitz χ^2 for $K_L \rightarrow \pi^0\pi^0\pi_D^0$ events where Data (Dots) is overlaid with MC (Histogram).	146
7.9	The π^0 Mass for $K_L \rightarrow \pi^0\pi^0\pi_D^0$ events where the Data (Dots) is overlaid on MC (Histogram). The plots on the left show the mass for $\pi^0 \rightarrow e^+e^-\gamma$, Plots on the Right show mass for $\pi^0 \rightarrow \gamma\gamma$	147
7.10	Total Invariant Mass versus \vec{P}_T^2 for $K_L \rightarrow \pi^0\pi^0\pi_D^0$ events, Plot (A). Plot (B) is the projection on the x-axis and (C) is the projection on y-axis. .	147
7.11	Track Separation at DC 1 x view, comparing Data (Dots) to MC (Histogram) for $K_L \rightarrow \pi^0\pi^0\pi_D^0$ events.	149
7.12	Track Separation at DC 1 x view, comparing Data (Dots) to MC (Histogram) for $K_L \rightarrow e^+e^-\gamma$ events.	150
7.13	Kaon Energy for $K_L \rightarrow e^+e^-\gamma$ events, Comparing Data (Dots) to MC (Histogram) with the ratio shown below. The arrows show the region selected by the cut.	150
7.14	z Position of the Kaon Decay Vertex for $K_L \rightarrow e^+e^-\gamma$ events, Comparing Data (Dots) to MC (Histogram) with the ratio shown below. The arrows show the region selected by the cut.	151
7.15	The Total Invariant Mass for $K_L \rightarrow \pi^0\pi^0\pi_D^0$ events where Data (Dots) is overlaid with MC (Histogram).	151
7.16	The Change in the Branching Ratio as a Function of Varying the Amount of Material in the Upstream part of the Detector.	154
7.17	Drift Chamber 1 Y Illumination Plot (in meters) with DC Map \times Factor 1.4	155
7.18	Drift Chamber 1Y Illumination Ratio of Monte Carlo with Map Weight of 1.0 compared to Map Weight of 1.4 using reweighting (left) and generated (right)	156
7.19	Drift Chamber 1Y Sum-of-Distance (SOD) minus 6.35mm comparing $K_L \rightarrow \pi^0\pi^0\pi_D^0$ Data (Dots) and MC (Histogram). Top plot is an overlay, bottom plot is a ratio of Data to MC.	156

7.20	Drift Chamber 1Y Sum-of-Distance (SOD) minus 6.35mm comparing $K_L \rightarrow \pi^0 \pi^0 \pi_D^0$ Data MC with (Dots) and without (Histogram) an Additional Amount of Hit Smearing. Top plot is an overlay and the Bottom plot is a ratio of MC with additional smearing over MC without.	157
7.21	Total Kaon Energy after all cuts for $K_L \rightarrow \pi^0 \pi^0 \pi_D^0$ Data (Dots) compared to MC (Histogram). Top plot is overlay and the Bottom is the ratio of Data over MC.	158
7.22	Total Kaon Energy after all cuts for $K_L \rightarrow \pi^0 \pi^0 \pi_D^0$ Data (Dots) compared to MC (Histogram) with reweighting applied. Top plot is overlay and the Bottom is the ratio of Data over MC.	158
7.23	The E/P after all selection cuts for $K_L \rightarrow \pi^0 \pi^0 \pi_D^0$ events. Plot (A) is the data, plot (B) is the Default MC, and plot (C) has had the energy resolution smeared.	159
7.24	The Dalitz χ^2 for $K_L \rightarrow \pi^0 \pi^0 \pi_D^0$ events comparing the Data (Dots) to Default MC (Left Histogram) and the Smeared MC (Right Histogram). Plots on the Top are overlays while those on the bottom are ratios of Data over MC.	160
7.25	The Branching Ratio as a function of the Energy Smearing Parameter δ	160
7.26	Top plot is the Position of the γ that is closest to a CsI Calorimeter Edge for the Data, the Bottom is the same for the MC. The first vertical line is the value of the nominal cut, the second is the value of the cut +5mm.	161
7.27	Top plot is the Energy of the γ with the Smallest Energy for the Data, the Bottom is the same for the MC. The first vertical line is the value of the nominal cut, the second is the value of the cut +10MeV.	162
7.28	The functional dependence of the far E/P used in the MC generation for $K_L \rightarrow \pi^0 \pi^0 \pi_D^0$ events. The Test Tail was the best fit shape from a study of $K_L \rightarrow \pi^0 \pi^0 \pi^0$ events [3], the Default Tail is what was assumed, and the No Tail was from turning off all tails.	163
7.29	The ratio of MC with the Default E/P Tail (Dots) to MC (Histogram) with the New E/P Tail measured from $K_L \rightarrow \pi^0 \pi^0 \pi^0$ events [3]. Top plot is the overlay and the bottom is the ratio.	164

7.30	Total Invariant Mass for $K_L \rightarrow e^+e^-\gamma$ MC events. The dots include one loop correction and radiative graphs and the histogram does not.	164
7.31	m_{ee} Ratio of Monte Carlo with $+1\sigma$ of best fit α_{K^*} over -1σ	165
7.32	Previously measured values of the Branching Ratio of $K_L \rightarrow e^+e^-\gamma$ with the current measurement also shown.	167
8.1	A Detector picture showing a $K_L \rightarrow e^+e^-e^+e^-$ event.	170
8.2	A Detector picture showing a $K_L \rightarrow \pi^0\pi_D^0\pi_D^0$ event.	171
8.3	Total Invariant Mass for $4e^\pm$ Data events coming from a common vertex. The plot on the right is for 4 cluster events and the right is 8 cluster events.	172
8.4	Total Invariant Mass versus \vec{P}_T^2 for $e^+e^-e^+e^-$ Data events. Box defines the signal region.	173
8.5	Total Invariant Mass for $e^+e^-e^+e^-$ events and the effect of a \vec{P}_T^2 cut on the data.	174
8.6	Min-Maximum Separation at DC 1 x view, comparing Data (Dots) to MC (Histogram) for $K_L \rightarrow e^+e^-e^+e^-$ events.	175
8.7	X_{4e} for Monte Carlo generated with $K_L \rightarrow e^+e^-e^+e^-$ and $K_L \rightarrow e^+e^-e^+e^-\gamma$ events. All events below 0.95 are considered to be $K_L \rightarrow e^+e^-e^+e^-\gamma$ events.	176
8.8	Total Invariant Mass versus \vec{P}_T^2 for $K_L \rightarrow \pi^0\pi_D^0\pi_D^0$ Data events. Box defines the signal region.	177
8.9	Total Invariant Mass for $K_L \rightarrow \pi^0\pi_D^0\pi_D^0$ Data events showing the effect of a \vec{P}_T^2 cut on the data.	178
8.10	2-Dalitz χ^2 comparing Data (Dots) with MC (Histogram) for $K_L \rightarrow \pi^0\pi_D^0\pi_D^0$ events. The arrow shows the location of the cut.	179
8.11	$\pi^0 \rightarrow e^+e^-\gamma$ Mass comparing Data (Dots) to MC (Histogram) for $K_L \rightarrow \pi^0\pi_D^0\pi_D^0$ events. The arrows show the location of the cut.	180
8.12	$\pi^0 \rightarrow \gamma\gamma$ Mass comparing Data (Dots) to MC (Histogram) for $K_L \rightarrow \pi^0\pi_D^0\pi_D^0$ events.	181
8.13	Change in the Measured Branching Ratio for $K_L \rightarrow e^+e^-e^+e^-$ between using the Tight and Loose Cut Values (Table 8.9) while keeping the rest of the Cuts at Nominal (Table 8.1). The error bars take into account the fact that most of the events are the same.	184

8.14	The change in the branching ratio as a function of varying the amount of material in the upstream part of the detector.	185
8.15	Total Invariant Mass for $K_L \rightarrow e^+e^-e^+e^-$ MC where the Dots have One Loop Corrections and Radiative Diagrams and the Histogram is Tree Level.	186
8.16	Previously measured values of the Branching Ratio of $K_L \rightarrow e^+e^-e^+e^-$ with the current measurement also shown.	187
9.1	Shape χ^2 fit for the BMS parameter α_{K^*} with $K_L \rightarrow e^+e^-\gamma$ events from the 97 MC with a Generated Value of $\alpha_{K^*} = -0.10$	190
9.2	Shape χ^2 fit for the BMS parameter α_{K^*} with $K_L \rightarrow e^+e^-\gamma$ events from the 97 MC with a generated value of $\alpha_{K^*} = -0.10$	191
9.3	Shape χ^2 fit for the BMS parameter α_{K^*} with $K_L \rightarrow e^+e^-\gamma$ events from the 97 run period.	192
9.4	Shape χ^2 fit for the DIP parameter α_{DIP} with $K_L \rightarrow e^+e^-\gamma$ events from the 97 run period.	193
9.5	Comparison of Data (Dots) and MC (Histogram) m_{ee} distribution for 97 $K_L \rightarrow e^+e^-\gamma$ events, where the best fit value of α_{K^*} (on the right) and the best fit α_{DIP} on the left is used in the MC. Top plot is the overlay, while the bottom is the ratio.	194
9.6	The change in the α_{K^*} parameter as a function of varying the amount of material in the upstream part of the detector.	195
9.7	Log-Likelihood as a Function of the Fit Parameters α_{DIP} and β_{DIP} near the region of the minimum for $K_L \rightarrow e^+e^-e^+e^-$ data.	198
9.8	1-dimensional Log-Likelihood as a Function of the Fit Parameter $\alpha_{DIP}(\beta_{DIP})$ at the minimum $\beta_{DIP}(\alpha_{DIP})$ for the Plot on the Left(Right) found for $K_L \rightarrow e^+e^-e^+e^-$ MC with an input of value of $\alpha_{DIP} = -1.0$ and $\beta_{DIP} = +1.0$	199
9.9	1-dimensional Log-Likelihood as a Function of the Fit Parameter $\alpha_{DIP}(\beta_{DIP})$ at the Minimum $\beta_{DIP}(\alpha_{DIP})$ for the plot on the Left(Right) found for $K_L \rightarrow e^+e^-e^+e^-$ Data.	200

9.10	Left hand side, first plot is a comparison $m_{ee}^{11} + m_{ee}^{22}$ for Tree Level Monte Carlo with $\mathcal{O}(\alpha_{EM}^3)$ Monte Carlo. The second plot on the left hand side is R_{10} the ratio of the $\mathcal{O}(\alpha_{EM}^3)$ MC over the Tree Level MC. The third plot represents an estimate of the possible size of $\mathcal{O}(\alpha_{EM}^4)$ corrections. The quantity R_{21} plotted there is defined as $R_{21} = 1 - (R_{10} - 1)^2$. That is, we estimate the fractional effect of the second order correction to be the square of the fractional effect of the first order corrections.	201
9.11	Previously measured values of the BMS parameter α_{K^*} with the newly measured result.	202
9.12	Previously measured values of the DIP parameter α_{DIP} with the newly measured result.	203
A.1	Black is ADC spectrum, Red is Spectrum with the Low Threshold Kumquat bit set.	209
A.2	Black is ADC spectrum, Red is Spectrum with the High Threshold Kumquat bit set.	210
A.3	Ratio of A.1. Efficiency curve for the Low Threshold.	210
A.4	Ratio of A.2. Efficiency curve for the High Threshold.	211
A.5	Theoretical pulse shape, in time, for a TRD wire.	211
A.6	Fit to the High Threshold efficiency curve.	212
A.7	Number of events verses the Probability that a Track has 4 out of 8 TRD hits that satisfy the High Threshold requirement.	213
A.8	4 out of 8 probability ratio, total tracks over tracks with KQ latches on.	213
B.1	$M_{e^+e^-}$ Data over Monte Carlo for $K_L \rightarrow e^+e^-\gamma$: Default Material. . . .	217
B.2	$M_{e^+e^-}$ Subset of the Data over Monte Carlo for $K_L \rightarrow e^+e^-\gamma$: Modified Material.	217
B.3	Scaled Z versus $1/P^2$	218
B.4	RMS of Scaled Z in bins of $1/P^2$ for the normalization data.	219
B.5	RMS of Scaled Z in bins of $1/P^2$ for the normalization data and Monte Carlo with default material.	220

B.6	RMS of Scaled Z in bins of $1/P^2$ for the normalization data and Monte Carlo with 20% material.	221
B.7	The slope of RMS of Scaled Z from 3 different Monte Carlos versus the material they were generated at. The horizontal line is the equivalent slope from the data. The vertical line is the intersection of the data with a fit to the 3 Monte Carlos.	222
B.8	The amount of material from 50 different methods of fitting the RMS of Scaled Z to a line.	222
B.9	The amount of material for Summer 97(red), Winter 97(green), and 1999(blue).	223

Chapter 1

Introduction

1.1 Symmetries

Symmetries exist in physics when a change can be imposed on a system and the properties of that system remain the same. Of particular interest are the three discrete symmetries of C (Charge Conjugation), P (Parity), and T (Time Reversal). C is the exchange of particles with antiparticles, such as the change of electron, e^- with positrons, e^+ . P is the mirror reflection of the position vector, *e.g.* $\vec{j} = (x, y, z)$ and $P\vec{j} = (-x, -y, -z)$. T is the reversal of time, *e.g.* $\pi^+ \rightarrow \mu^+ \nu_\mu \longleftrightarrow \mu^+ \nu_\mu \rightarrow \pi^+$.

Up until 1957 when Co^{60} β decay was discovered [4], it was believed that each of C , P , and T were individually symmetries of nature. However, that experiment showed the violation of P in weak decays. In 1964, Christenson, Cronin, Fitch and Turlay [5] observed the CP violating decay of the long-lived kaon into a two pion final state. The rate for this was found to be very small ~ 1 in 500 decays, but it occurred.

CP violation is a fascinating topic. It provided a clue for the existence of a third family of quarks and leptons. It implies that there is T violation, provided that the combination of CPT is conserved, a requirement for local field theory with Lorentz invariance. Finally, it is necessary to explain the dominance of matter over antimatter in the universe. It is also one of the reasons for the extensive study of the neutral kaon.

1.2 The Neutral Kaon

The neutral kaon is strange meson, meaning that it is composed of two quarks one of which is a strange quark. The strong eigenstates are

$$K^0 = d\bar{s}, S = +1 \tag{1.1}$$

$$\bar{K}^0 = \bar{d}s, S = -1 \quad (1.2)$$

where S is the strangeness quantum number.

Strangeness is not conserved under second-order ($\Delta S = 2$) weak transitions, of which diagram 1.1 is an example. Therefore, it is useful to construct eigenstates of C , as was done by Gell-Mann and Pais [6].

$$K_1 = \frac{1}{\sqrt{2}}(|K^0\rangle + |\bar{K}^0\rangle) \quad (1.3)$$

$$K_2 = \frac{1}{\sqrt{2}}(|K^0\rangle - |\bar{K}^0\rangle). \quad (1.4)$$

Since $C|K^0\rangle = -|\bar{K}^0\rangle$ and $C|\bar{K}^0\rangle = -|K^0\rangle$, it is easy to prove that $C|K_1\rangle = -|K_1\rangle$ and $C|K_2\rangle = +|K_2\rangle$. Furthermore it can be shown that K_1 and K_2 are eigenstates of CP ,

$$\begin{aligned} CP|K_1\rangle &= +|K_1\rangle \\ CP|K_2\rangle &= -|K_2\rangle. \end{aligned} \quad (1.5)$$

Thus, K_1 is the CP even state and K_2 is the CP odd state. If CP were a perfect symmetry then K_1 and K_2 would be the mass eigenstates of the neutral kaon. Further, the decays of $K_1 \rightarrow 2\pi$ and $K_2 \rightarrow 3\pi$ would be allowed while $K_1 \rightarrow 3\pi$ would be suppressed and $K_2 \rightarrow 2\pi$ would be forbidden. Because there is more allowed phase space for the K_1 it would have a significantly shorter lifetime than the K_2 . It was found in 1956 [7] that there are indeed a long-lived and a short-lived kaon. However, the 1964 experiment showed the long-lived kaon also decayed into the 2π channel.

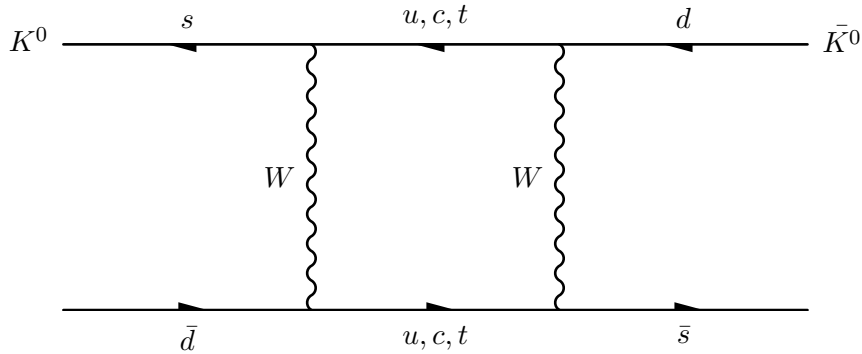


Figure 1.1: Example of possible $\Delta S = 2$ oscillations of K^0 to \bar{K}^0 .

The K_1 and K_2 states do not describe the mass eigenstates. A state that includes a mixture of both K_1 and K_2 is needed. Given that there is a long-lived state, K_L , and a short-lived state, K_S , and that the K_L state only decays via the 2π channel infrequently, ~ 1 in 500 decays, the mixing parameter must be small. The states can be written as,

$$\begin{aligned} |K_L\rangle &= \frac{1}{\sqrt{1+|\epsilon|^2}}(|K_2\rangle + \epsilon |K_1\rangle) \\ &= \frac{1}{\sqrt{2(1+|\epsilon|^2)}}[(1+\epsilon)|K^0\rangle - (1-\epsilon)|\bar{K}^0\rangle] \\ |K_S\rangle &= \frac{1}{\sqrt{1+|\epsilon|^2}}(|K_1\rangle + \epsilon |K_2\rangle) \\ &= \frac{1}{\sqrt{2(1+|\epsilon|^2)}}[(1+\epsilon)|K^0\rangle + (1-\epsilon)|\bar{K}^0\rangle], \end{aligned} \quad (1.6)$$

where the parameter ϵ represents the amount of indirect CP violation.

1.3 The “Golden Mode”

The K_L is also interesting for another reason. The decay $K_L \rightarrow \mu^+\mu^-$ allows one to measure the $|V_{td}|$ component of the Cabibbo, Kobayashi, and Maskawa (CKM) mixing matrix [8, 9, 10, 11, 12, 13]. The CKM matrix describes the weak mixing of quarks. If d , s and b are the strong, flavor eigenstates of the quarks, then the corresponding weak eigenstates are d' , s' and b' and the two are related by

$$\begin{pmatrix} d' \\ s' \\ b' \end{pmatrix} = V \begin{pmatrix} d \\ s \\ b \end{pmatrix}, V = \begin{pmatrix} V_{ud} & V_{us} & V_{ub} \\ V_{cd} & V_{cs} & V_{cb} \\ V_{td} & V_{ts} & V_{tb} \end{pmatrix}. \quad (1.7)$$

Therefore V_{td} connects the top quark to the down quark through the W boson.

Extracting $|V_{td}|$ from $K_L \rightarrow \mu^+\mu^-$ is somewhat complicated. The branching ratio for this mode can be written as

$$B(K_L \rightarrow \mu^+\mu^-) = |ReA|^2 + |ImA|^2, \quad (1.8)$$

where A is the decay amplitude normalized to $\Gamma(K_L \rightarrow \text{All})$. The second term, $|ImA|^2$, corresponds to the case when the K_L couples to the final state via two real photons, see figure 1.2. This contribution can be calculated in closed form using Quantum Electrodynamics (QED), as was done by Sehgal [14], and gives

$$|ImA|^2 = \frac{\alpha_{EM}^2 m_\mu^2}{2M_K^2 \beta_\mu} \left[\ln \frac{1-\beta_\mu}{1+\beta_\mu} \right]^2 B(K_L \rightarrow \gamma\gamma), \quad (1.9)$$

where m_μ is the muon mass, M_K is the kaon mass and

$$\beta_\mu = \sqrt{1 - \frac{4m_\mu^2}{M_K^2}}.$$

The most recent measurements of $B(K_L \rightarrow \gamma\gamma)$ [15] give a value of $|ImA|^2 = (7.07 \pm 0.18) \times 10^{-9}$, from [14]. This is very close to $B(K_L \rightarrow \mu^+\mu^-) = (7.18 \pm 0.17) \times 10^{-9}$, from [16]. This also yields an upper limit on $|ReA|^2$ of 0.37×10^{-9} .

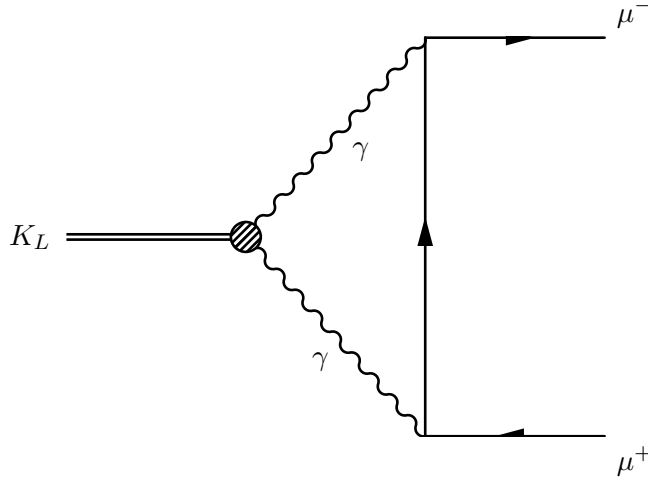


Figure 1.2: QED Feynman Graphs to $K_L \rightarrow \mu^+\mu^-$.

The result for $|ReA|^2$ is not the whole story either. It must be split into two more components

$$ReA = ReA_{long} + ReA_{short}. \quad (1.10)$$

The second term is the dispersive “short-distance” piece and depends on diagrams shown in figure 1.3 with W and Z bosons. This is the piece with the interesting $|V_{td}|$ contributions. The loop integrals which involve the u, c, t have terms which go as the mass of the quark squared. The dominant term comes from the top quark. The “long-distance” dispersive contribution comes from $K_L \rightarrow \mu^+\mu^-$ decays with intermediate states involving off-shell photons. An example of this is shown in figure 1.4. This contribution can be calculated using chiral perturbation theory and a detailed understanding of the $K_L \rightarrow \gamma^*\gamma^*$ form factor. The long-distance component must be subtracted from the total amplitude to obtain the short-distance component.

The “long-distance” and “short-distance” components are so named for the range of the interaction, which is the Compton wavelength of the force carrier ($\hbar c/mc^2$). The photon is massless, leading to an infinite range. The W and Z bosons are very heavy, on the order of 80 GeV for the W boson and 91 GeV for the Z boson, so the range of the “short-distance” component is very short, on the order of a few thousandths of a fermi.

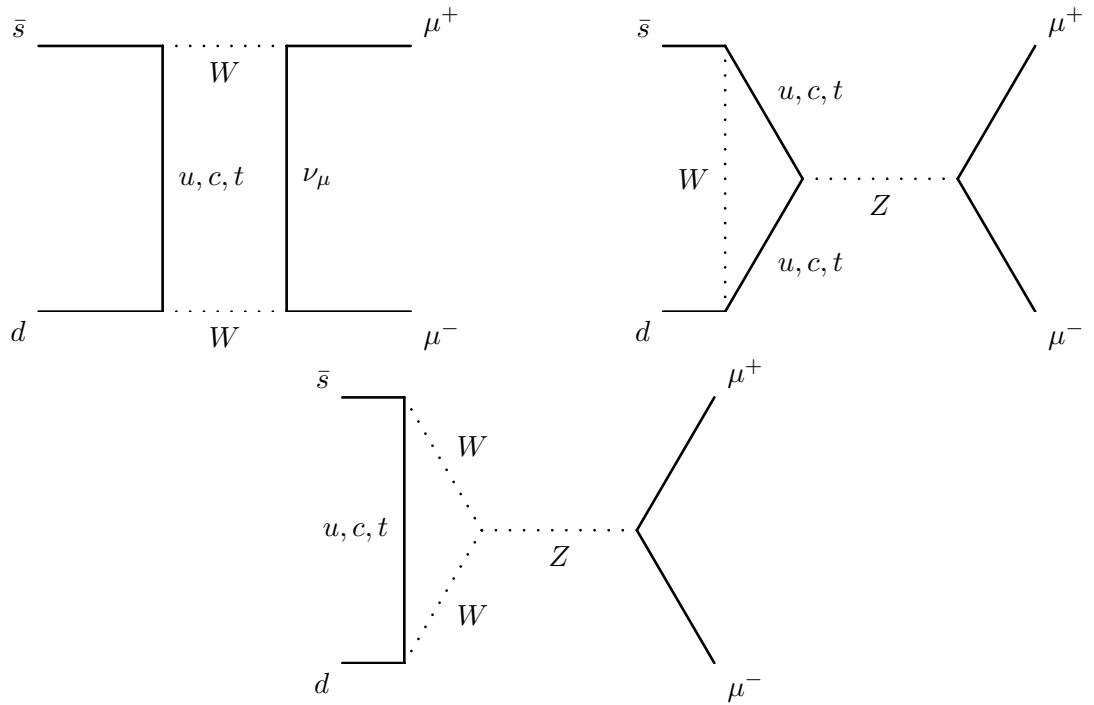


Figure 1.3: Short-Distance Feynman Graphs to $K_L \rightarrow \mu^+ \mu^-$.

1.4 Two Photon Decays of the Neutral Kaon

The K_L can undergo many types of decays, but one is the decay $K_L \rightarrow \gamma\gamma$, $BR = (5.86 \pm 0.15) \times 10^{-4}$ [15]. Figure 1.5 shows the Feynman diagram for this decay. If one of these photons is far enough off-shell, then it can create an electron-positron pair. This is typically called a Dalitz decay, first studied by R. H. Dalitz [17] in the π^0 system. Thus, $K_L \rightarrow e^+ e^- \gamma$ is called the kaon single Dalitz decay and $K_L \rightarrow e^+ e^- e^+ e^-$ is called the kaon double Dalitz decay as both photons are virtual and produce electron-positron pairs.

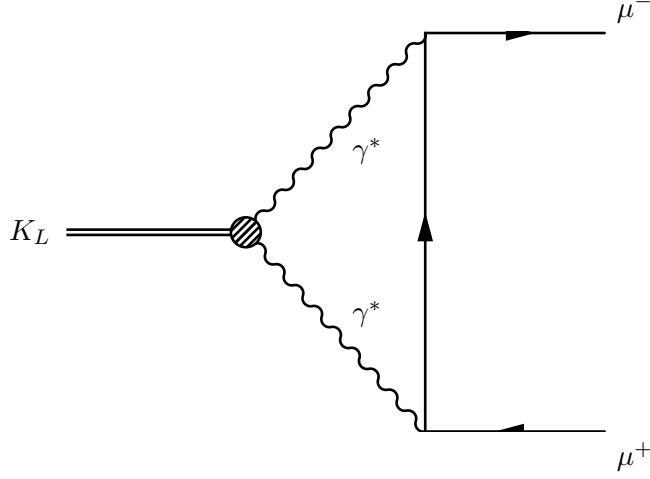


Figure 1.4: Long-distance Feynman Graphs to $K_L \rightarrow \mu^+ \mu^-$.

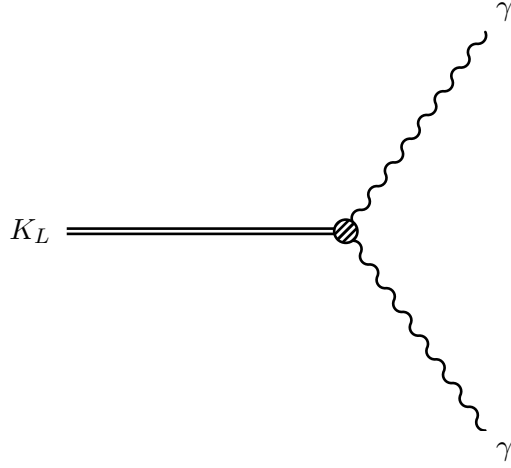


Figure 1.5: Feynman Graph for Two Photon decay, $K_L \rightarrow \gamma \gamma$.

The Lagrangian for $K_L \rightarrow \gamma \gamma$ is

$$\mathcal{L}_I(x) = -i\tilde{g} \frac{f(q_1^2, q_2^2)}{4M_K} \epsilon_{\mu\nu\rho\sigma} F^{\mu\nu}(x) F^{\rho\sigma}(x) \phi(x), \quad (1.11)$$

where $f(0,0)$ is the form factor and $\phi(x)$ is the field of the kaon. Using equation 1.11, the total rate for $K_L \rightarrow \gamma \gamma$ can be calculated:

$$\Gamma_{\gamma\gamma} = \frac{|\tilde{g}|^2 |f(0,0)|^2 M_K}{16\pi}. \quad (1.12)$$

Usually $f^2(0,0)$ is defined to be one.

The rates for the tree-level single and double Dalitz decays of the kaon can be figured in a similar way [18]. The Lagrangian is essentially the same as equation 1.11

with the exception of the form factor term which can be a function of the momentum (*i.e.* q^2) of one or two virtual photons for the single and double decays respectively. In other words, $K_L \rightarrow e^+e^-\gamma$ probes $f(q^2, 0)$ and $K_L \rightarrow e^+e^-e^+e^-$ probes $f(q_1^2, q_2^2)$. The tree-level Feynman diagram for $K_L \rightarrow e^+e^-\gamma$ is shown in figure 1.6 and for $K_L \rightarrow e^+e^-e^+e^-$ in figure 1.10.

The single Dalitz final state consists of three particles whose kinematics can be described by two variables

$$x = \frac{(p_1 + p_2) \cdot (p_1 + p_2)}{M_K^2} = \frac{m_{ee}^2}{M_K^2} \quad (1.13)$$

$$y = \frac{2q \cdot (p_1 - p_2)}{M_K^2(1 - x)} \quad (1.14)$$

The variable y is the angle between the positron and the photon in the e^+e^- center of mass. The rate, normalized to the $K_L \rightarrow \gamma\gamma$ rate, for $K_L \rightarrow e^+e^-\gamma$ as a function of q^2 can be written [19, 20] as

$$\frac{1}{\Gamma_{\gamma\gamma}} \frac{d\Gamma_{e^+e^-\gamma}}{dx} = \frac{2\alpha_{EM}}{3\pi} |f(x, 0)|^2 \lambda^3(1, x, 0) \mathcal{G}(x), \quad (1.15)$$

where

$$\lambda(a, b, c) = \sqrt{a^2 + b^2 + c^2 - 2(ab + bc + ac)}, \quad (1.16)$$

and

$$\mathcal{G} = \left(1 + \frac{2m_e^2}{xM_K^2}\right) \left(1 - \frac{4m_e^2}{xM_K^2}\right)^{1/2}. \quad (1.17)$$

The theoretical tree level rate of $\Gamma_{e^+e^-\gamma}/\Gamma_{\gamma\gamma} = 1.59\%$ [19], where a flat form factor is assumed (*i.e.* $f(x, 0) = 1$). Radiative graph contributions to the single Dalitz decay come from four diagrams like the one in figure 1.7 [20]. The other three diagrams have the photon radiating off the electron instead of the positron and the exchange of the two photons for both previous graphs. Infinities arise in the calculations of these graphs, but they can be removed by the inclusion of one loop corrections, some of which are illustrated in figure 1.8. These corrections have been calculated and included in all the work that follows, except where noted. The total rate for $K_L \rightarrow e^+e^-\gamma\gamma$ events with both tree level and radiative events normalized to the $K_L \rightarrow \gamma\gamma$ rate is $\Gamma_{e^+e^-\gamma(\gamma)}/\Gamma_{\gamma\gamma} = 1.61\%$. The radiative corrections add a particle to the final state, but experimental precision limits

the ability to detect the extra photon. That means that for sufficiently soft photons, the $K_L \rightarrow e^+e^-\gamma\gamma$ decay is indistinguishable from $K_L \rightarrow e^+e^-\gamma$. Historically a center of mass energy (E_γ^*) of 5 MeV for the radiated photon is assumed to distinguish what is called $K_L \rightarrow e^+e^-\gamma\gamma$ from the $K_L \rightarrow e^+e^-\gamma$ events. If this cutoff is used the rate ratio becomes $\Gamma_{e^+e^-\gamma(\gamma)}/\Gamma_{\gamma\gamma} = 1.51\%$. The rates are summarized in table 1.1.

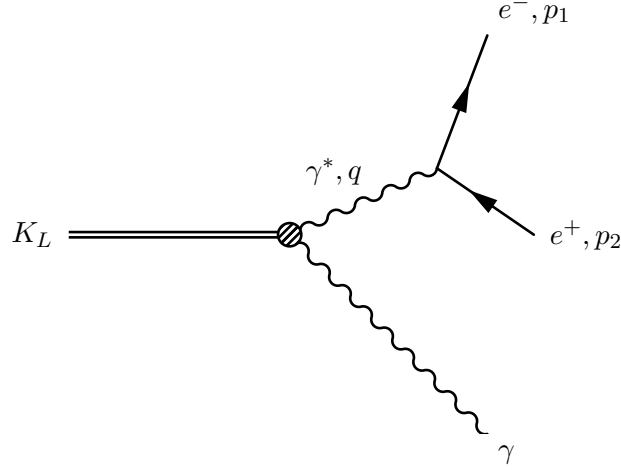


Figure 1.6: Feynman Graph Single Dalitz decay, $K_L \rightarrow e^+e^-\gamma$.

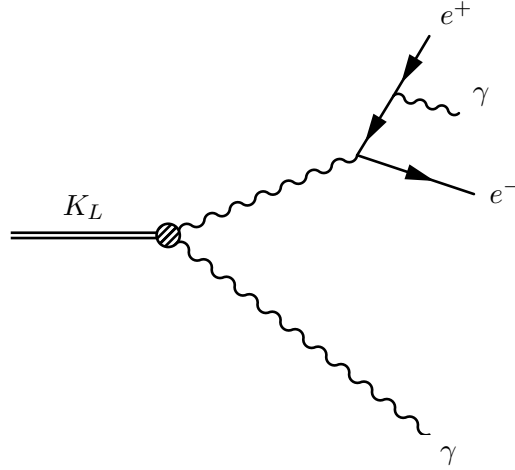


Figure 1.7: Feynman Graph for Radiative Single Dalitz decay, $K_L \rightarrow e^+e^-\gamma\gamma$.

The double Dalitz decay has a four particle final state with two sets of identical particles. A four particle final state can be kinematically described by a set of five

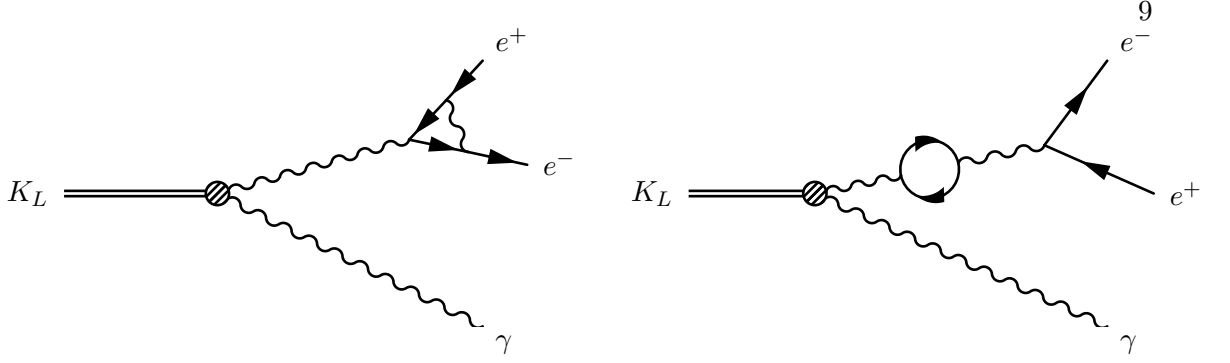


Figure 1.8: Feynman Graph for One Loop Corrections to Single Dalitz decay, $K_L \rightarrow e^+e^-\gamma\gamma$.

independent variables. The variables are

$$x_{12} = \frac{(p_1 + p_2) \cdot (p_1 + p_2)}{M_K^2}, \quad (1.18)$$

$$x_{34} = \frac{(p_3 + p_4) \cdot (p_3 + p_4)}{M_K^2}, \quad (1.19)$$

$$y_{12} = \frac{2(p_3 + p_4) \cdot (p_1 - p_2)}{M_K^2 \lambda(1, x_{12}, x_{34})}, \quad (1.20)$$

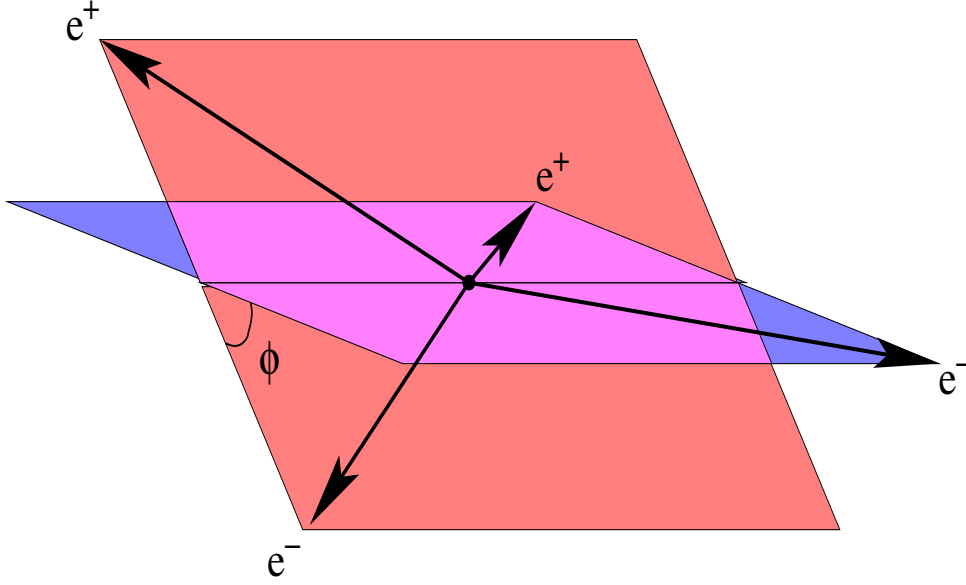
$$y_{34} = \frac{2(p_1 + p_2) \cdot (p_3 - p_4)}{M_K^2 \lambda(1, x_{12}, x_{34})}, \quad (1.21)$$

$$\phi = \tan^{-1} \left(\frac{16\epsilon_{\mu\nu\rho\sigma} p_1^\mu p_2^\nu p_3^\rho p_4^\sigma}{M_K^2 \lambda(1, x_{12}, x_{34}) [M_K^2 y_{12} y_{34} (1 - x_{12} - x_{34}) - 2(p_1 - p_2) \cdot (p_3 - p_4)]} \right), \quad (1.22)$$

where p_i is the momentum of particular particle. The variable ϕ is the angle between the normals of the two planes defined by each pair of leptons in the center of mass as illustrated in figure 1.9. Thus, at $\phi = 0$ the two lepton pairs lie in a plane with like sign leptons adjacent. Another way to write ϕ , following the Miyazaki and Takasugi paper [19] is

$$\phi = \cos^{-1} \left(\frac{(\vec{p}_1 \times \vec{p}_2) \cdot (\vec{p}_3 \times \vec{p}_4)}{|\vec{p}_1 \times \vec{p}_2| \cdot |\vec{p}_3 \times \vec{p}_4|} \right). \quad (1.23)$$

One of the tree level Feynman diagrams is shown in figure 1.10. Because of the identical particles in the final state additional exchange diagrams are necessary, an example is shown in 1.11. The matrix element for decay is the sum of the contributions from each of the diagrams, $\mathcal{M} = \mathcal{M}_1 + \mathcal{M}_2$. The total rate contains $|\mathcal{M}|^2$ there are

Figure 1.9: Diagram of ϕ the phase space variable.

three terms, $\Gamma = \Gamma_1 + \Gamma_2 + \Gamma_{12}$. The first term is from the first diagram (figure 1.10) the second from the exchange (figure 1.11) and the last is the interference between the two. The differential rate for the first diagram as a function of the x 's can be written as

$$\begin{aligned} \frac{1}{\Gamma_{\gamma\gamma}} \frac{d\Gamma_{e^+e^-e^+e^-}^1}{dx_{12}dx_{34}} &= \frac{\alpha_{EM}^2}{2\pi^2} |f(x_{12}, x_{34})|^2 \frac{\lambda^3(1, x_{12}, x_{34}) \lambda(1, p_1^2/m_{12}^2, p_2^2/m_{12}^2)}{4x_{12}x_{34}} \\ &\quad \lambda(1, p_3^2/m_{34}^2, p_4^2/m_{34}^2) \left(3 - \lambda^2(1, p_1^2/m_{12}^2, p_2^2/m_{12}^2) \right) \\ &\quad \left(3 - \lambda^2(1, p_3^2/m_{34}^2, p_4^2/m_{34}^2) \right) \end{aligned} \quad (1.24)$$

where $m_{12}^2 = (p_1 + p_2)^2$. It is also interesting to see it as a function of the angle ϕ

$$\frac{1}{\Gamma_{\gamma\gamma}} \frac{d\Gamma_{e^+e^-e^+e^-}^1}{d\phi} = \frac{\alpha_{EM}^2}{12\pi^3} \left(\frac{I_1}{2} (1 - \cos 2\phi) + I_4 \right) \quad (1.25)$$

where

$$I_1 = \frac{2}{3} \int \int dx_{12} dx_{34} f^2(x_{12}, x_{34}) \frac{\lambda^3(1, p_1^2/m_{12}^2, p_2^2/m_{12}^2)}{4x_{12}x_{34}}, \quad (1.26)$$

$$I_4 = \int \int dx_{12} dx_{34} f^2(x_{12}, x_{34}) \frac{\lambda(1, p_1^2/m_{12}^2, p_2^2/m_{12}^2) \lambda(1, p_3^2/m_{34}^2, p_4^2/m_{34}^2)}{4x_{12}x_{34}} \lambda^3(1, x_{12}, x_{34}) (3 - \lambda^2(1, p_1^2/m_{12}^2, p_2^2/m_{12}^2) - \lambda^2(1, p_3^2/m_{34}^2, p_4^2/m_{34}^2)). \quad (1.27)$$

By assuming that $f(x_{12}, x_{34}) = 1$, one can obtain values for I_1 and I_4 by performing a numerical calculation, as is done in [18], $I_1 = 14.146$ and $I_4 = 27.725$. The theoretical tree level ratio of rates for $K_L \rightarrow e^+e^-e^+e^-$ is $\Gamma_{e^+e^-e^+e^-}/\Gamma_{\gamma\gamma} = 6.222(5) \times 10^{-5}$.

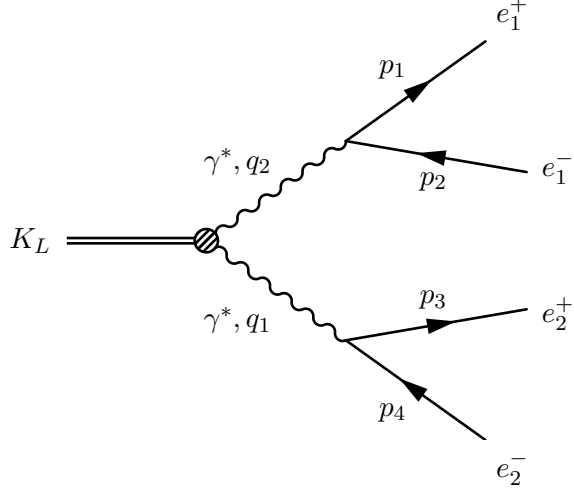


Figure 1.10: Feynman Graph for Double Dalitz decay, $K_L \rightarrow e^+e^-e^+e^-$.

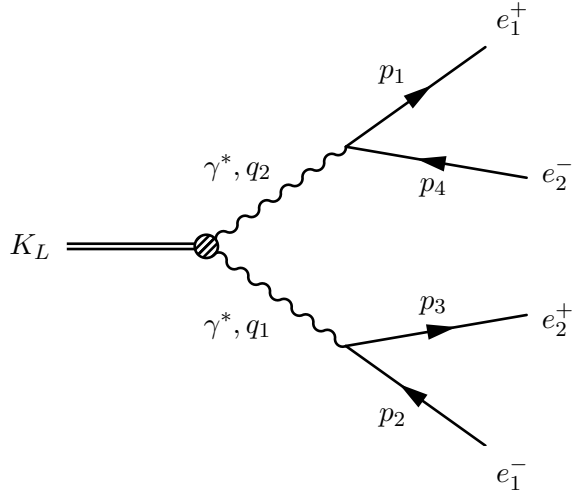


Figure 1.11: Exchange Feynman Graphs for Double Dalitz decay, $K_L \rightarrow e^+e^-e^+e^-$.

As in the single Dalitz case there are a number of graphs that contribute to the radiative corrections. In this case, there are five basic graphs that contribute. Figure 1.12 shows the graphs that contribute at the $\mathcal{O}(\alpha_{EM}^4)$ level, the vacuum polarization, vertex correction and the 5-point diagram. There are also the radiative graphs, shown

in figure 1.13, that are necessary to cancel the infra-red divergences that occur in the previous diagrams. There are a total of 16 different graphs. Extensive work has gone into calculating the contribution of these graphs and can be explored more fully in [18]. The rate for $K_L \rightarrow e^+e^-e^+e^-(\gamma)$ normalized to $K_L \rightarrow \gamma\gamma$ is $\Gamma_{e^+e^-e^+e^-(\gamma)}/\Gamma_{\gamma\gamma} = 6.406(4) \times 10^{-5}$. However, as in the single Dalitz case the ability to detect the photon is limited by the precision of the experiment. Therefore a cutoff in the quantity $X_{4e} = m_{eee}^2/M_K^2$ can be made. For this analysis, the cutoff is set at $X_{4e} > 0.95$ to define $K_L \rightarrow e^+e^-e^+e^-$ events. With this cutoff the ratio of rates becomes $\Gamma_{e^+e^-e^+e^-(\gamma)}/\Gamma_{\gamma\gamma} = 5.903(4) \times 10^{-5}$. The rates are summarized in table 1.1. Other values for the rate include a Vector-Meson Dominance (VMD) calculation with the ω mass resonance [21] of $\Gamma_{e^+e^-e^+e^-}/\Gamma_{\gamma\gamma} = 6.3 \times 10^{-5}$. A chiral perturbation calculation to $\mathcal{O}(p^6)$ of the rate was conducted by Zhang and Goity [22]. They predict several rates, with two modified by form factors based on VMD models these results are summarized in table 1.2.

Mode	$\Gamma_{\text{mode}}^{\text{tree}}/\Gamma_{\gamma\gamma}$	$\Gamma_{\text{mode}(\gamma)}/\Gamma_{\gamma\gamma}$	
		no cutoff	cutoff
$K_L \rightarrow e^+e^-\gamma$	0.0159	0.0161	0.0151
$K_L \rightarrow e^+e^-e^+e^-$	6.222×10^{-5}	6.406×10^{-5}	5.903×10^{-5}

Table 1.1: Theoretical Rates with and without radiative corrections. The cutoff is $E_\gamma^* > 5\text{MeV}$ for single Dalitz and $x_{4e} > 0.95$ for double Dalitz.

QED [19]	QED with Corrections [18]	VMD [21]	χPT [22]
6.22×10^{-5}	5.903×10^{-5}	6.3×10^{-5}	6.26×10^{-5} no FF
			6.50×10^{-5} with FF 1
			6.48×10^{-5} with FF 2

Table 1.2: Theoretical Rates for $K_L \rightarrow e^+e^-e^+e^-$

1.5 Form Factor

The form factor for the decay $K_L \rightarrow \gamma\gamma$ is a function of two variables: the invariant mass squared of each of the two photons (q_1^2 and q_2^2). If the mass squared of the virtual photon is greater than four times the mass squared of an electron ($M_{\gamma^*}^2 > 4m_e^2$), then the virtual photon may convert into an e^+e^- pair through internal conversion. In this

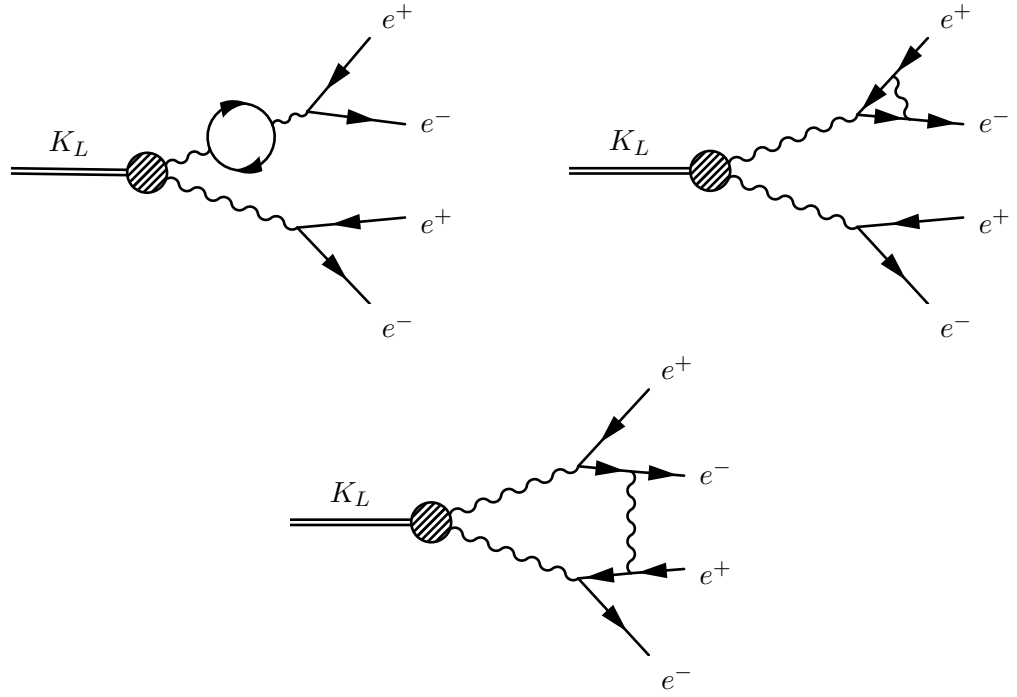


Figure 1.12: Feynman Graphs for Radiative Double Dalitz.

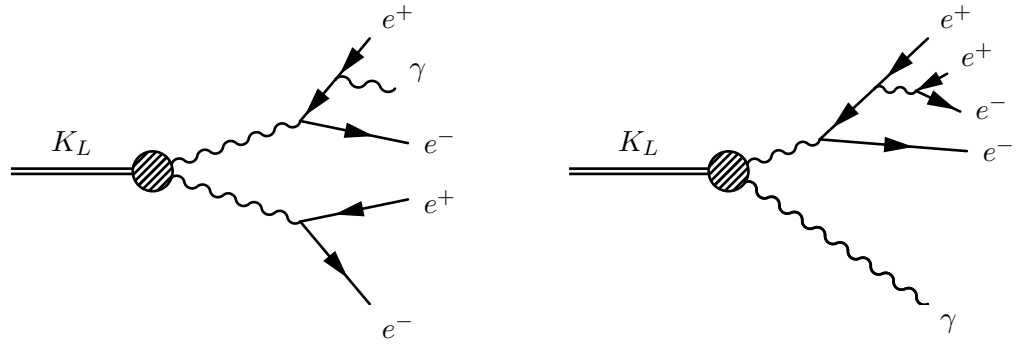


Figure 1.13: Feynman Graphs for Radiative Double Dalitz.

case, the invariant mass squared of the photon is equal to the invariant mass squared of the resultant e^+e^- pair ($q^2 = m_{ee}^2$).

Studies of different K_L decays provide information about different regions of the form factor function $f(q_1^2, q_2^2)$. The decay $K_L \rightarrow \gamma\gamma$ provides information about the form factor at a single point, $f(0, 0)$. A Feynman diagram for this decay is shown in

figure 1.5.

A $K_L \rightarrow \gamma^* \gamma$ decay with one virtual photon probes the region $f(q_1^2, 0)$. Since the photons are identical, the function is symmetric and the same decay also probes the region $f(0, q_2^2)$. In the decay $K_L \rightarrow e^+ e^- \gamma$, the virtual photon decays into an $e^+ e^-$ pair. The Feynman diagram for this decay is shown in figure 1.6.

Studies of this decay probe the region $4M_e^2 < q^2 < M_K^2$, as the invariant mass squared of the photon must be large enough to permit the formation of the $e^+ e^-$ pair but cannot be larger than the invariant mass squared of the parent particle.

Similarly the study of $K_L \rightarrow e^+ e^- e^+ e^-$ allows one to probe the $K_L \rightarrow \gamma^* \gamma^*$ vertex. The invariant mass of the two photons can be related to the masses of each $e^+ e^-$ pair. This is a two dimensional space that is probed. The Feynman diagram for this decay is shown in figure 1.10.

The actual form factor function depends on photon mass in a complex way, but models exist to approximate the behavior of the function for relevant values of photon mass. The simplest model involves a simple linear approximation,

$$f(x) = 1 + \alpha x.$$

More complicated models for the form factor exist and depend to varying degrees on vector meson dominance.

1.5.1 Vector Meson Dominance

Vector Meson Dominance (VMD) is a model of electromagnetic couplings discussed by Quigg and Jackson [21]. In this model there is no direct coupling of pseudoscalar meson with virtual photons. Instead, there is an intermediate interaction with vector mesons, *i.e.* the ρ , ω and ϕ . These vector mesons are allowed to fluctuate into photons since they share identical quantum numbers.

In VMD the $K_L \rightarrow \gamma^* \gamma$ coupling is modeled by including a q^2 -dependent factor representing the vector meson propagator and a number A_V representing the strength of the $V \gamma^*$ transition. Thus, the form factor for one virtual photon becomes

$$f(q^2, 0) = \sum_V \frac{A_V}{1 - q^2/M_V^2}. \quad (1.28)$$

When both photons are virtual, we can imagine the kaon coupling to a pair of virtual vector mesons, V and W , as shown in figure 1.14. The form factor for two virtual photons would then be given by

$$f(q_1^2, q_2^2) = \sum_{V,W} \frac{B_{VW}}{(1 - q_1^2/M_V^2)(1 - q_2^2/M_W^2)}, \quad (1.29)$$

where the numbers B_{VW} represent the strengths of the various possible $K_L VW$ couplings.

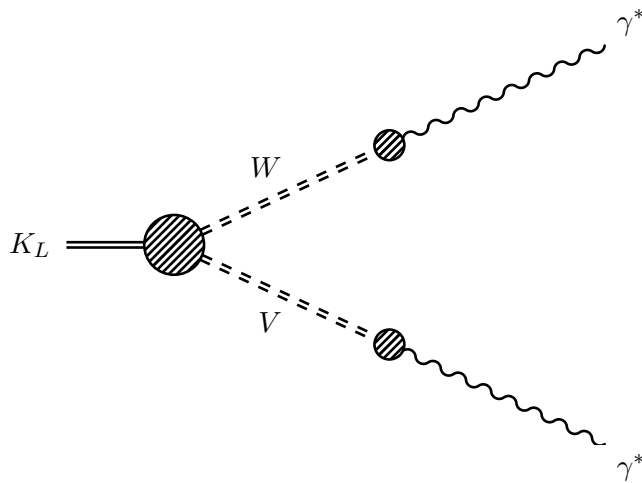


Figure 1.14: Vector Meson Dominance model for $K_L \gamma^* \gamma^*$ vertex.

1.5.2 BMS Model

Another model proposed by Bergström, Massó, and Singer uses vector-meson dominance theory to express the form factor as a function of a parameter α_{K^*} [23]. It differs from standard VMD, see figure 1.15, by including a strangeness changing vector-vector transition [23, 24]. A $K_L \rightarrow K^* \gamma$ vertex is included, as shown in figure 1.16.

The form factor therefore has the form

$$f_{BMS}(x) = \frac{1}{1 - x \cdot \frac{M_K^2}{M_\rho^2}} + \frac{2.3\alpha_K^*}{1 - x \cdot \frac{M_K^2}{M_{K^*}^2}} \cdot \left(\frac{4}{3} - \frac{1}{1 - x \cdot \frac{M_K^2}{M_\rho^2}} - \frac{1}{9} \frac{1}{1 - x \cdot \frac{M_K^2}{M_\omega^2}} - \frac{2}{9} \frac{1}{1 - x \cdot \frac{M_K^2}{M_\phi^2}} \right), \quad (1.30)$$

where $x = \frac{M_{\pi e}^2}{M_{K_L}^2}$, M_{K^*} , M_ρ , M_ω and M_ϕ are the masses of various mesons, α_{K^*} is the parameter describing the relative strength of the an intermediate pseudoscalar decay amplitude and a vector meson decay amplitude, and C is constant. The first term represents pseudoscalar-pseudoscalar transitions, while the second term represents vector-vector transitions involving K^*V vertices's. The constant C is composed of various coupling constants, see [15, 25, 26]:

$$\begin{aligned} C &= \sqrt{8\pi\alpha_{EM}} G_{NL} f_{K^*K\gamma} \frac{M_\rho^2}{f_{K^*} f_\rho^2 f_{K\gamma\gamma}} = 2.3 \\ G_{NL} &= \frac{1.1 \times 10^{-5}}{M_\rho^2} \\ f_{K^*K\gamma}^2 &= \frac{96\pi\Gamma(K^* \rightarrow K^0\gamma) M_{K^*}^3}{M_{K^*}^2 - M_K^2} \\ f_\rho^2 &= \frac{4\pi\alpha_{EM}^2 M_\rho}{3\Gamma(\rho \rightarrow e^+e^-)} \\ f_{K^*} &= f_\rho \frac{M_{K^*}}{M_\rho} \\ f_{K\gamma\gamma}^2 &= \frac{64\pi\Gamma(K_L \rightarrow \gamma\gamma)}{M_K^3}. \end{aligned}$$

Here G_{NL} is the coupling strength of the $K^* \rightarrow \rho, \omega, \phi$ transition, $f_{K^*K\gamma}$ is the coupling of the $K^* \rightarrow K^0\gamma$ transition, $f_{K\gamma\gamma}$ is the coupling of the $K_L \rightarrow \gamma\gamma$ transition, f_ρ is the coupling to the ρ meson, f_{K^*} is the coupling to the K^* and α_{EM} is the fine structure constant. Using all the relevant numbers from a world average [15], one can rewrite equation 1.30 as

$$f_{BMS}(x) = \frac{1}{1 - 0.418x} + \frac{2.3\alpha_K^*}{1 - 0.311x} \cdot \left[\frac{4}{3} - \frac{1}{1 - 0.418x} - \frac{1}{9(1 - 0.405x)} - \frac{2}{9(1 - 0.238x)} \right]. \quad (1.31)$$

Predictions for the value of $|\alpha_{K^*}|$ include a range of $0.2 - 0.3$ [27].

It is worthwhile to note that an $\alpha_{K^*} = 0.0$ reduces the BMS model to the VMD model as is illustrated in figure 1.15. A flat form factor(*i.e.* $f(x) = 1$) is $\alpha_{K^*} \approx 0.3$.

This model is one-dimensional in q^2 , so for the analysis of $K_L \rightarrow e^+e^-e^+e^-$ the total form factor is assumed to factor (i.e. $f(q_1^2, q_2^2) = f_{BMS}(q_1^2) \cdot f_{BMS}(q_2^2)$).

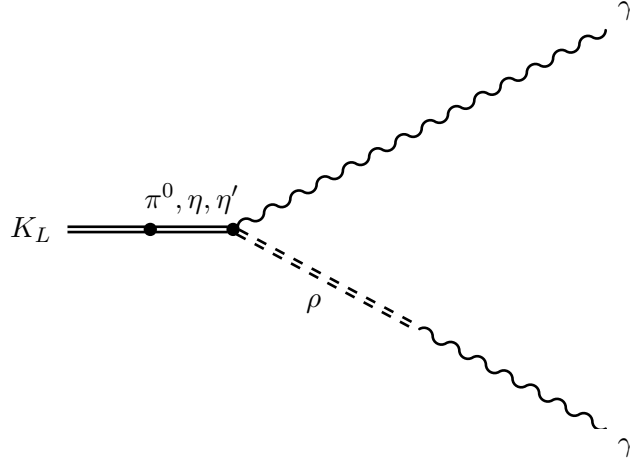


Figure 1.15: Standard Kaon Vector-Vector Transition.

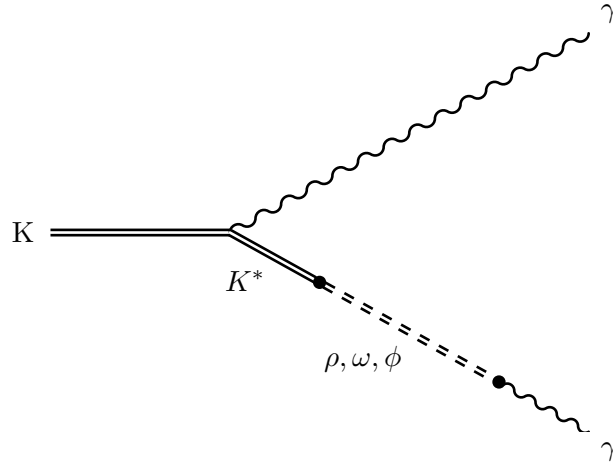


Figure 1.16: Kaon Vector-Vector Transition.

1.5.3 DIP Model

D'Ambrosio, Isidori and Portolés[11] have proposed a form factor model which is compatible with $\mathcal{O}(p^6)$ chiral perturbation theory. This model also contains the meson

poles of the VMD model. The form can be fit to any pole and has the form

$$f_{DIP}(x_1, x_2) = 1 + \alpha_{DIP} \left(\frac{x_1}{x_1 - \frac{M_V^2}{M_K^2}} + \frac{x_2}{x_2 - \frac{M_V^2}{M_K^2}} \right) + \beta_{DIP} \frac{x_1 x_2}{\left(x_1 - \frac{M_V^2}{M_K^2}\right) \left(x_2 - \frac{M_V^2}{M_K^2}\right)} \quad (1.32)$$

where M_V is the mass of a vector meson. Due to the relatively small mass of the ρ , it is usually evaluated at the ρ mass.

This formulation is particularly interesting due to the fact that it is sensitive to both q^2 values of the photons. In the case of the $K_L \rightarrow e^+ e^- \gamma$ analysis one of the q_i^2 is equal to zero. In the case where one of the q^2 is set to zero, α_{DIP} can be related to α_{K^*} :

$$\alpha_{DIP} = -1 + (3.1 \pm 0.5) \alpha_{K^*}. \quad (1.33)$$

It should be noted that due to the dominance of low m_{ee} events in $K_L \rightarrow e^+ e^- e^+ e^-$, that the sensitivity to β_{DIP} is not very good. The decay $K_L \rightarrow e^+ e^- \mu^+ \mu^-$ has better sensitivity; however, it also has a much smaller branching ratio.

1.6 Previous Measurements

1.6.1 $K_L \rightarrow e^+ e^- \gamma$

The decay $K_L \rightarrow e^+ e^- \gamma$ was first reported in 1980 by Carroll *et al.* in an experiment at Brookhaven [28] that found 4 events. They measured a branching ratio of $(17.4 \pm 8.7) \times 10^{-6}$. A decade would pass before more measurements were made.

Brookhaven experiment E845 observed 919 events in 1990 and measured a branching ratio of $(9.1 \pm 0.4_{-0.5}^{+0.6}) \times 10^{-6}$ [25]. They also measured a form factor. That same year a CERN experiment NA31 found 1053 events, measured a branching ratio of $(9.2 \pm 0.5_{stat} \pm 0.5_{sys}) \times 10^{-6}$ and a form factor [29]. The most recent result came from CERN experiment NA48 which had 6864 events and measured a branching ratio of $(10.6 \pm 0.02_{stat} \pm 0.02_{sys} \pm 0.04_{calc}) \times 10^{-6}$ and a form factor [30]. These numbers are summarized in the table 1.3.

1.6.2 $K_L \rightarrow e^+ e^- e^+ e^-$

The decay $K_L \rightarrow e^+ e^- e^+ e^-$ was first observed in 1991 by Barr *et al.* at the CERN NA31 experiment, [31] with only 2 events. This observation was superseded

Author	Year	Value
Carroll [28]	1980	$(17.4 \pm 8.7) \times 10^{-6}$
Barr [29]	1990	$(9.2 \pm 0.5_{stat} \pm 0.5_{sys}) \times 10^{-6}$
KE Ohl [25]	1990	$(9.1 \pm 0.4^{+0.6}_{-0.5}) \times 10^{-6}$
V. Fanti [30]	1999	$(10.6 \pm 0.2_{stat} \pm 0.2_{sys} \pm 0.4_{calc}) \times 10^{-6}$

Table 1.3: Previously Measured Branching Ratios for $K_L \rightarrow e^+e^-\gamma$

by a paper in 1995 by Barr *et al.* [32] which found a total of 8 events including the previous two and measured a branching ratio of $(10.4 \pm 3.7_{stat} \pm 1.1_{sys}) \times 10^{-8}$.

The Brookhaven experiment E845 observed 6 events and measured a branching ratio of $(3.07 \pm 1.25_{stat} \pm 0.26_{sys}) \times 10^{-8}$ [33]. The KEK experiment E137 observed 18 events with a cut on $m_{ee} > 470\text{MeV}/c^2$ and measured a branching ratio of $(6 \pm 2_{stat} \pm 1_{sys}) \times 10^{-8}$ [34]. The Fermilab experiment E799-I (the predecessor of the KTeV experiment) found 27 events and a branching ratio of $(3.96 \pm 0.78 \pm 0.32) \times 10^{-8}$ [35]. Also a result based on a subset of the KTeV data set was published finding 441 events with a branching ratio of $(3.72 \pm 0.18_{stat} \pm 0.23_{sys}) \times 10^{-8}$ [36, 37]. These results are summarized in table 1.4.

Author	Year	Value
Barr [31, 32]	1991	$(10.4 \pm 3.7_{stat} \pm 1.1_{sys}) \times 10^{-8}$
Vagin [33]	1993	$(3.07 \pm 1.25_{stat} \pm 0.26_{sys}) \times 10^{-8}$
Akagi [34]	1993	$(6 \pm 2_{stat} \pm 1_{sys}) \times 10^{-8}$
Gu [35]	1994	$(3.96 \pm 0.78 \pm 0.32) \times 10^{-8}$
Halkiadakis [36]	2001	$(3.72 \pm 0.18_{stat} \pm 0.23_{sys}) \times 10^{-8}$

Table 1.4: Previously Measured Branching Ratios for $K_L \rightarrow e^+e^-e^+e^-$

1.6.3 Form Factor

Most measurements of the form factor involve measuring the BMS parameter α_{K^*} . The first measurement of this parameter was done by the CERN experiment NA31 with Barr *et al.* in 1990 and found a value of $\alpha_{K^*} = -0.280 \pm 0.13$ [29]. Other $K_L \rightarrow e^+e^-\gamma$ experiments measured this parameter including Ohl [25] $\alpha_{K^*} = -0.280^{+0.099}_{-0.090}$ and NA48 [30] with $\alpha_{K^*} = -0.36 \pm 0.06_{stat} \pm 0.02_{sys}$. More recently, the KTeV experiment has measured a value of $\alpha_{K^*} = -0.163^{+0.026}_{-0.027}$ from the decay $K_L \rightarrow \mu^+\mu^-\gamma$ [38] and $\alpha_{K^*} =$

-0.19 ± 0.11 from the decay $K_L \rightarrow e^+e^-\mu^+\mu^-$ [39]. Two other modes measured an effective α , being different by not including next order corrections in their measurements. The measurement from $K_L \rightarrow e^+e^-\gamma\gamma$ [40] was $\alpha_{eff} = +0.016 \pm 0.083_{stat} \pm 0.042_{sys}$ and from $K_L \rightarrow e^+e^-e^+e^-$ [36] was $\alpha_{eff} = -0.14 \pm 0.16_{stat} \pm 0.15_{sys}$. Similarly, the parameter α_{DIP} has only been measured recently by KTeV. From the decay $K_L \rightarrow \mu^+\mu^-\gamma$ a value of $\alpha_{DIP} = -1.55 \pm 0.09$ was extracted. The study of the decay $K_L \rightarrow e^+e^-\mu^+\mu^-$ gave $\alpha_{DIP} = -1.57 \pm 0.37$. The statistics have been too small so far to extract a value for the parameter β_{DIP} . The sensitivity to β is just not that large. These results are summarized in the tables 1.5 and 1.6.

Author	Mode	Value
Barr [29]	$K_L \rightarrow e^+e^-\gamma$	$\alpha_{K^*} = -0.280 \pm 0.13$
Ohl [25]	$K_L \rightarrow e^+e^-\gamma$	$\alpha_{K^*} = -0.280^{+0.099}_{-0.090}$
Fanti [30]	$K_L \rightarrow e^+e^-\gamma$	$\alpha_{K^*} = -0.36 \pm 0.06_{stat} \pm 0.02_{sys}$
Alavi-Harati [38]	$K_L \rightarrow \mu^+\mu^-\gamma$	$\alpha_{K^*} = -0.163^{+0.026}_{-0.027}$
Alavi-Harati [39]	$K_L \rightarrow e^+e^-\mu^+\mu^-$	$\alpha_{K^*} = -0.19 \pm 0.11$

Table 1.5: Previously Measured α_{K^*}

Author	Mode	Value
Alavi-Harati [38]	$K_L \rightarrow \mu^+\mu^-\gamma$	$\alpha_{DIP} = -1.55 \pm 0.09$
Alavi-Harati [39]	$K_L \rightarrow e^+e^-\mu^+\mu^-$	$\alpha_{DIP} = -1.57 \pm 0.37$

Table 1.6: Previously Measured α_{DIP}

Chapter 2

The KTeV Detector

The experiment which provided the data for this thesis is generally known as KTeV. KTeV stands for “Kaons at the Tevatron”, and is an experiment that ran at Fermi National Accelerator Laboratory (Fermilab) in Batavia, Illinois. KTeV is a combination of two experiments that shared the same beamline and mostly the same detector. E832 is one experiment, which is primarily concerned with measuring the value of $\text{Re}(\epsilon'/\epsilon)$. The quantity ϵ' is a parameter describing direct CP violation and ϵ is the parameter describing indirect CP violation. The second experiment is E799-II, which is primarily concerned with the decay $K_L \rightarrow \pi^0 e^+ e^-$, but allowed for the study of a wide variety of rare kaon, pion and hyperon decays. The data for this thesis comes primarily from this second experiment.

The differences between the two experiments are fairly minor. The E832 experiment used a regenerator to produce parallel K_L and K_S beams in order to form the double ratio of $\frac{\Gamma(K_L \rightarrow \pi^+ \pi^-)/\Gamma(K_S \rightarrow \pi^+ \pi^-)}{\Gamma(K_L \rightarrow \pi^0 \pi^0)/\Gamma(K_S \rightarrow \pi^0 \pi^0)}$. E799-II removed the regenerator, changed some of the absorber and collimator settings, and put in a series of transition radiation detectors for additional particle identification.

The E799-II experiment was broken into three distinct run periods, sharing time with E832. KTeV began running in E832 mode late in 1996, switching over to E799 running in January of 1997 and continuing to March of 1997. This period is known as the *Winter* period. KTeV again switched to E832 mode and switched back in July of 1997. It ran in E799 mode until September, which constitutes the *Summer* period. The *Summer* and *Winter* periods together are referred to as the *1997* run. After this there was a two year shutdown in which several improvements were made to the detector, discussed later in this chapter. Running began again in June of 1999 with E832 and

switched to E799 in September. This period lasted until mid January of 2000 and is called the *1999* run.

2.1 Beam

The KTeV experiment was located on the Neutrino-Muon (NM) fixed-target beam-line. The Tevatron accelerates protons to energies of 800 GeV. The beam of protons is split out to the various fixed-target lines, *e.g.* NM. It all started with these protons.

2.1.1 Proton Beam

The protons were sent with a specific time structure. The protons arrived in $1 - 2ns$ pulses spaced by $19ns$. Each $19ns$ period was called an *RF Bucket*. These buckets arrived at 53MHz for a time period called *on-spill*. This was followed by an *off-spill* period during which more protons were accelerated. The amount of time *off-spill* was 40 seconds for the entire running of the experiment, while the time *on-spill* changed. During the 1997 run period the *on-spill* period was 20 seconds, changing to 40 seconds in the 1999 period. Between 2×10^{12} and 5×10^{12} protons arrived at the target during the 1997 period at any instance. The intensity was increased to $6 \times 10^{12} - 10 \times 10^{12}$ during the 1999 run, but due to the increased time *on-spill* the instantaneous intensity remained approximately the same.

The proton beam was focused to a transverse width of less than $250\mu m$ when it struck a Beryllium Oxide target. The target was located in the NM2 enclosure. The target was a block $3mm \times 3mm \times 30cm$, being ~ 1.1 interaction lengths long. The center of the target formed the origin of the KTeV coordinate system. The $+z$ direction, or *downstream*, extends from the target to the detector. $-z$ is the *upstream* direction and is approximately South. The $+y$ direction is up and the $+x$ completes the standard right hand rule, *i.e.* $\hat{x} = \hat{y} \times \hat{z}$. The beam of protons impacted at an angle of approximately 4.8mrad from the normal in the $+y$ direction. When the proton beam struck the target, a plethora of particles of all types are produced. A series of magnets, collimators, and absorbers followed the target to change this beam of mixed particles into a beam of neutral kaons.

A target monitor was located 1.8m in the $+x$ direction. This monitor consisted of three sequential scintillator counters. A small hole in the shielding that surrounded the target allowed for a particle to occasionally trigger all three counters. This formed an accidental trigger which was used to collect events off-spill. These events were used in the Monte Carlo simulation later as *accidental overlays*, which will be discussed in Chapter 5.

2.1.2 Kaon Beam

The “cleaning” up of the beam began with the 4.8mrad angle of the proton beam. The angle was chosen to maximize the number of neutral kaons with respect to neutrons. The first attempt to remove charged particles occurred with the Target Sweeper magnet. This magnet started at 0.6m and continued to 4.4m in the z axis. It gave a 475 MeV/c kick in the $-y$ direction to protons. Downstream of the Target Sweeper was the Primary Proton Dump, a water-cooled, 4.5m block of copper, which received these protons. The Primary Proton Dump was offset in the $-y$ direction to allow neutral particles to pass. Next came μ Sweeper 1, which started at 12.3m and continued to 17.8m. It was a magnet that gave a kick of 3625 MeV/c in the $+x$ direction. This swept muons out of the beam.

The Lead Absorber came next at 19m. This 3 inch lead wall absorbed photons produced at then target. It was 14 radiation lengths worth of material. It was immediately followed by the Primary Collimator. The Primary Collimator was a block of brass with two holes in it. Each of these holes pointed back to the target, making a 0.8mrad angle with z axis. The size of the holes at the downstream face of the collimator was 1.18×1.29 cm during the Winter run period and 1.62×1.73 cm for the Summer and 1999 runs. There was no real need for two holes in the Primary Collimator for the E799-II running, they were needed for the two separate beams required in the E832 running.

The beam entered a vacuum region next, which started at 21.8m. The vacuum region was contained by a 0.005 inch thick titanium window. Just after the window was another magnet, μ Sweeper 2, which started at 21.9m and went to 27.7m. This magnet provided a 3135 MeV/c kick in the Winter run and 1854 MeV/c kick in the Summer and 1999 periods. The kick swept out any charged particles which may have

been created by interaction with the Lead Absorber. The next element was the Spin Rotator magnet which begins at a z of 30.5m and continues to 36.5m. This magnet was responsible for polarizing the neutral hyperons (*i.e.* Ξ^0 and Λ^0), it had no effect on the spinless kaons. During the winter period only, a Slab Collimator was used to ensure that no event crossed beams, but it was removed for the summer and 1999 periods in order to use the larger beam sizes. The Slab Collimator was a wedge of stainless steel that started at 38.8m and continued to 40.8m.

The Beam Stops were downstream of the Slab Collimator, starting at 46.6m. They consisted of a pair of iron blocks with a total thickness of 5.95m. The Beam Stops were only in place when the beam was to be blocked. For example, the Beam Stops were in place whenever an access was made into the detector hall. They were also moved in when a beam of muons was desired.

At a z of 85-88m was the Defining Collimator. Much like the Primary Collimator it shaped the beam and had two holes. It differed in that the holes were $4.4 \times 4.4\text{cm}$ ($5.2 \times 5.2\text{cm}$) for the Winter (Summer and 1999) period, and that it was made of tungsten. The beams then entered the Final Sweeper magnet at 90-93m. This magnet provided a 1180 MeV/c kick to charged particles, removing any that may have remained or been generated by decays of neutral particles in the beam. Finally, the beam passed through a pair of $8.9 \times 8.9\text{cm}$ steel pipes before entering the detector.

The composition of the beam at this point was mostly neutrons and long-lived kaons. The ratio of neutrons to kaons was about 3:1 by the time the beam reached the decay region. However, the neutrons' long lifetime meant that their interaction with the detector was confined to accidental neutral activity. The beam had a small component of other neutral hadrons and photons. They included K_S , Λ^0 , and Ξ^0 . The total rate from these hadrons was 25 to 50 MHz. The two beams had a width of 0.50mrad (Winter) or 0.59mrad (Summer and 1999) and were separated by 1.6mrad in x .

2.2 Vacuum

Only kaons that decayed in a 65m long region of the vacuum chamber are considered for this analysis. The region began at a z of 94m and ended at a vacuum window at $z = 158.89\text{m}$. The vacuum region was kept at a pressure of 1.0×10^{-6} Torr in order

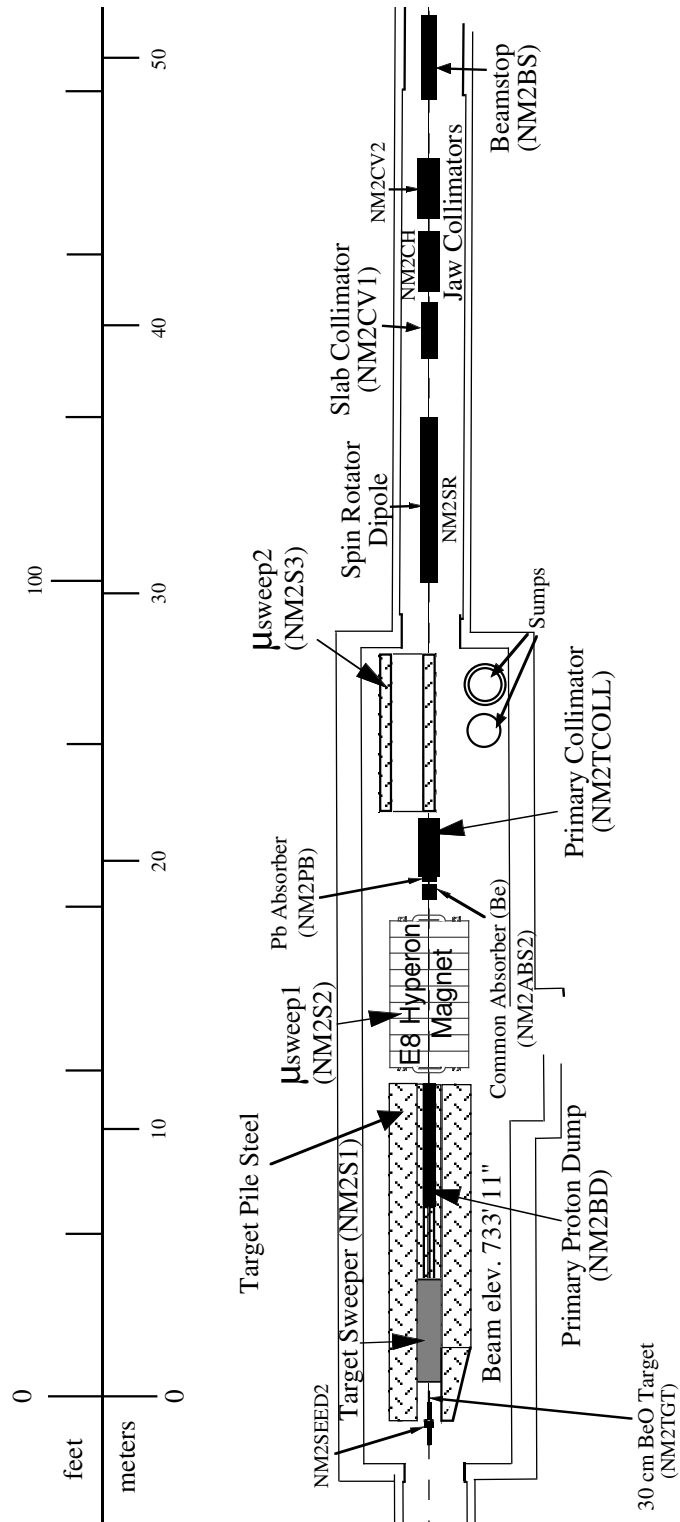


Figure 2.1: The Secondary Beam region, NM2

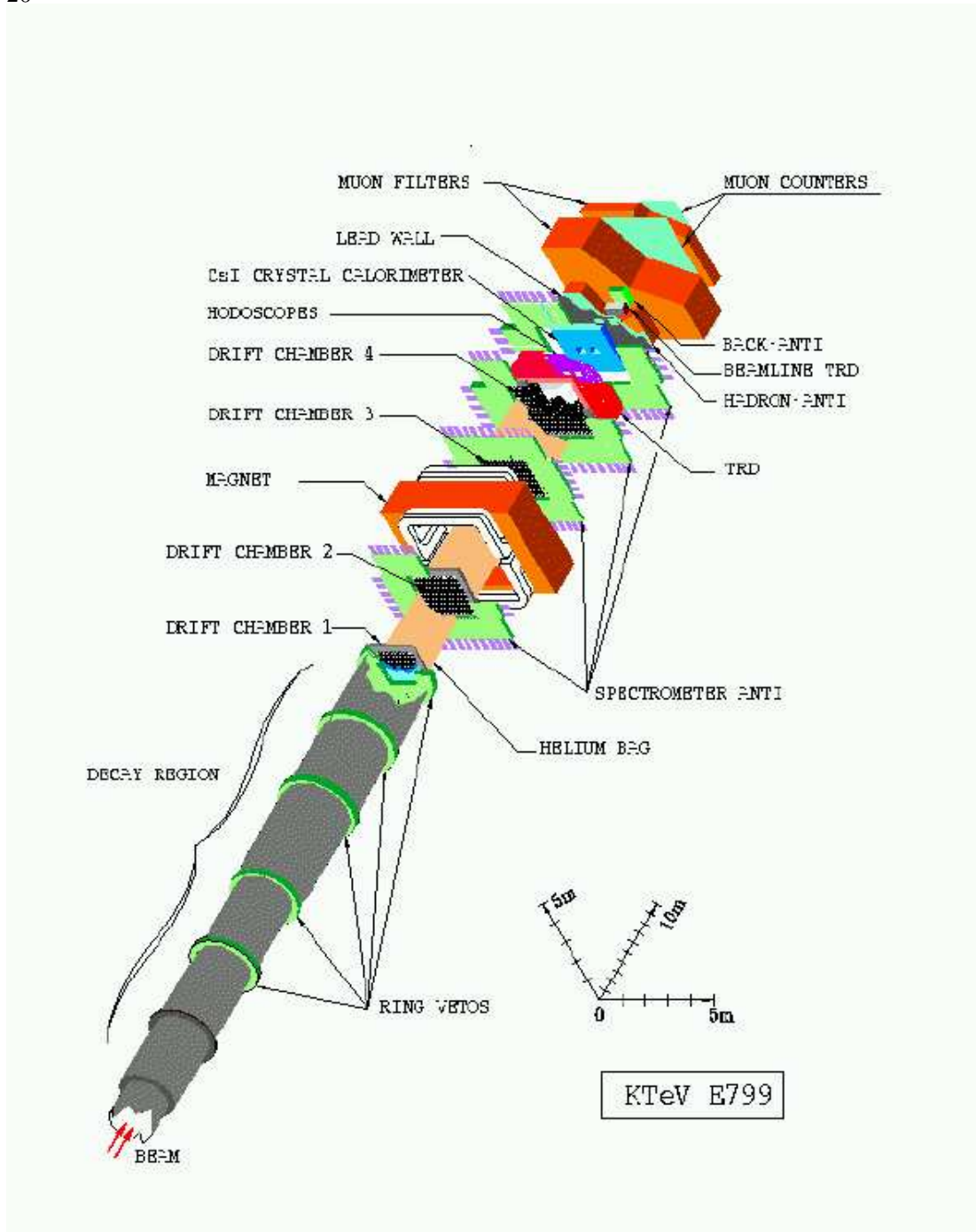


Figure 2.2: 3-dimensional view of Detector.

to minimize interactions of the decaying kaons with other particles. The window that capped the vacuum is a circle of radius 0.90m made of Kevlar laminated with Mylar.

The window consisted of about 0.0156% of a radiation length in z .

2.2.1 Photon Vetoes

The vacuum decay region was covered by a set of five photon veto detectors called Ring Counters (RC). These RCs were positioned to detect high angle particles leaving the detector before reaching the spectrometer and the calorimeter. Each RC consists of 24 lead-scintillator layers totaling 16 radiation lengths. The first 8 layers were 0.5 radiation lengths in z while the remaining 8 were 1.0 each. The RCs were circular in shape on the outer edge and square for the inner aperture. They were segmented into 16 overlapping paddles, see figure 2.4. Each paddle was connected to a light guide, whose light was fed into photomultiplier tubes (PMT). These signals were then discriminated and sent to trigger electronics to be discussed in Chapter 3. The positions and dimensions of the RCs is listed in table 2.1.

Ring Counter	z position(m)	Outer radius(m)	Inner aperture, $x \times y$ (m)
RC6	132.6	1.00	0.84×0.84
RC7	138.6	1.00	0.84×0.84
RC8	146.6	1.44	1.18×1.18
RC9	152.6	1.44	1.18×1.18
RC10	158.6	1.44	1.18×1.18

Table 2.1: Position and Dimensions of the Ring Counter Vetoes.

2.3 Charged Spectrometer

The charged spectrometer consisted of series of 4 Drift Chambers and an Analysis Magnet, as pictured in figure 2.5. Each element was separated by a plastic bag filled with Helium to minimize scattering of particles. The bags leaked quite a bit and one bag in particular was contaminated by air, more discussion is available in appendix B. Thus, for the 1999 run, these bags were replaced entirely and no evidence of substantial leaking could be found. The spectrometer was used to measure the momentum and position of charged particles. It measured the momentum by observing the bend of the particle as it passed through a known magnetic field. Measuring the positions of a track in the first two chambers gives the initial direction, the position of a track in the second

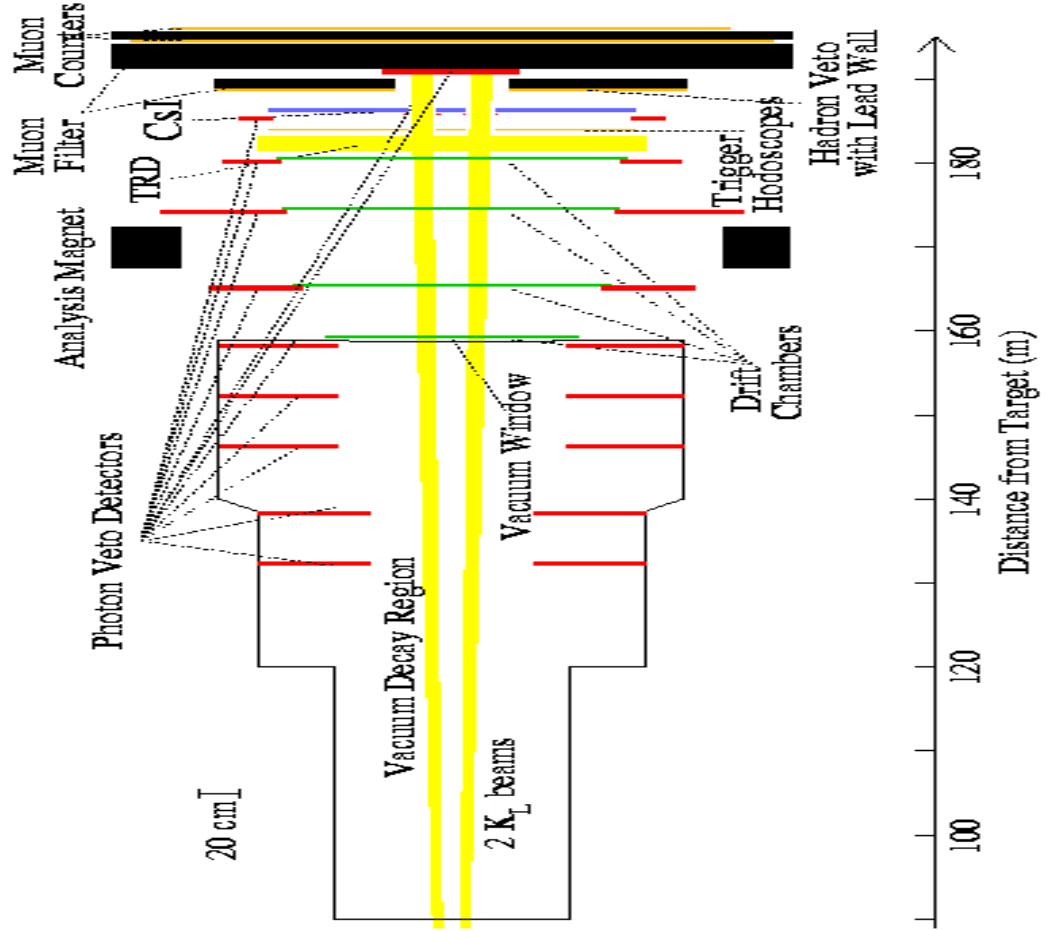


Figure 2.3: Top Down view of Detector. x and z scales are different.

two chambers gives the new direction, thus the momentum of the track is given by the kick given by the field divided by the change in the track direction. The position and size of each element is given in table 2.2.

2.3.1 Analysis Magnet

The Analysis Magnet was an electromagnetic dipole that creates a vertical field (*i.e.* in the y direction). The field strength was mapped initially with a Hall effect probe

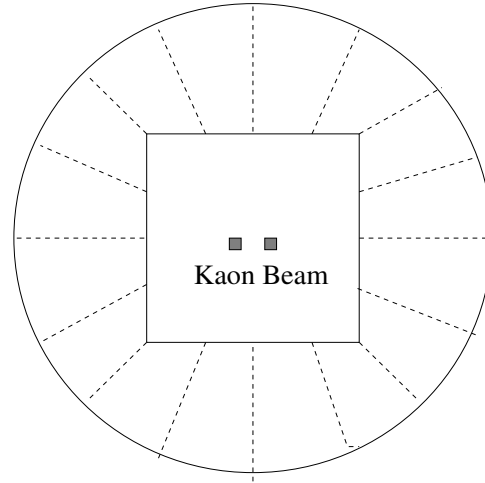


Figure 2.4: Cross-sectional View of a Ring Counter Veto.

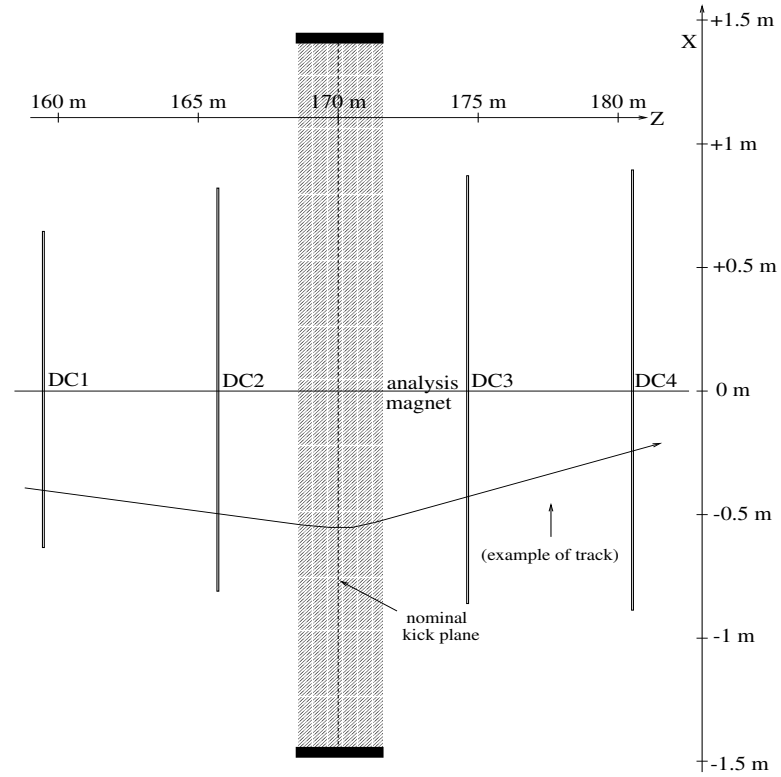


Figure 2.5: Spectrometer Elements. x and z scales are different.

to obtain an accuracy of $\pm 1\%$. Section 2.3.3 describes methods used later. Charged particles passing through this field received a momentum kick in the x direction. During

Element	z Position(m)	Size, $x \times y$ (m)
DC1	159.4	1.30×1.30
DC2	165.6	1.64×1.44
Analysis Magnet	170.0	2.90×2.00
DC3	174.6	1.74×1.64
DC4	180.5	1.90×1.90

Table 2.2: The Size and Dimensions of each part of the Spectrometer.

the 1997 period the kick was set at 205 MeV/c. However, for the 1999 period the kick was reduced to 150 MeV/c in order to increase acceptance for modes with a number of “soft” particles. The $K_L \rightarrow e^+e^-e^+e^-$ decay enjoyed an increase in acceptance of $\sim 15\%$ with the smaller field. The polarity of the field was changed every day or two. This was done in order to minimize any geometrical biases in the detector.

The exact value of the momentum kick was measured by looking at the invariant mass distribution of the $K_L \rightarrow \pi^+\pi^-$ events. The kick was fixed by the requirement that $M_{\pi\pi} = M_K$. These values were stored as a function of time in a database.

2.3.2 Drift Chamber

The drift chambers contained three essential elements, field wires, sense wires, and a gas. Charged particles passing through the chamber ionized the gas, releasing electrons. These electrons were accelerated toward the nearest anode wire (sense wire) by the electrical potential created by the voltage difference between the anode and cathode (field) wires. These electrons freed more electrons creating an avalanche of electrons that produce a measurable current on the sense wire. From the position of the wires and the time that the current arrived, the position of the particle could be determined.

The field wires were made of $25\mu\text{m}$ diameter gold-plated tungsten. The sense wires were made of $100\mu\text{m}$ gold-plated aluminum. The wires were arranged parallel to one another, separated by 12.7mm (which defines a “cell size”) and arranged into four views per chamber. First, two planes of sense wires strung in the y direction offset by 6.35mm, followed by two planes of sense wires strung in the x direction as illustrated in figure 2.6. The offset on these “plane-pairs” prevented left-right ambiguity. The number of

wires for each view is enumerated in table 2.3. The sense wires were surrounded by a hexagon of field wires. A pair of Mylar windows contain the gas which dwelt in the chamber. The gas was equal parts Argon and Ethane with 0.5% to 1.0% of Isopropyl Alcohol. The voltage difference between the field and sense wires was set between 2450 and 2600V during the 1997 run. This produces an electron drift speed of $50\mu\text{m}/\text{ns}$ and total drift time of less than 200ns. In 1999, the sense wires were cleaned and some electronics were upgraded which allowed the chambers to operate at a voltage difference of 2350 – 2450 V, with a higher gain. The lower voltage reduced the level of noise.

The sense wires were connected to amplifiers located on the drift chamber frames. The signals were discriminated and then sent on a number of cables to Time-to-Digital converters (TDCs) where the time was measured to a common stop provided by the Trigger Logic described in Chapter 3.

DC View	Wires	Cables
1Y	101	7
1Y'	101	7
1X	101	7
1X'	101	7
2Y	112	7
2Y'	112	7
2X	128	8
2X'	128	8
3Y	128	8
3Y'	128	8
3X	136	9
3X'	136	9
4Y	140	9
4Y'	140	9
4X	140	9
4X'	140	9

Table 2.3: Wires and cables per DC plane. Listed as a function of increasing z . 'Primed' planes refer to the downstream plane of a plane-pair.

2.3.3 Drift Chamber Calibration

A necessary component to reconstructing track positions in the drift chambers was creation of accurate position-to-time($X(t)$) maps. The document [41] provides the

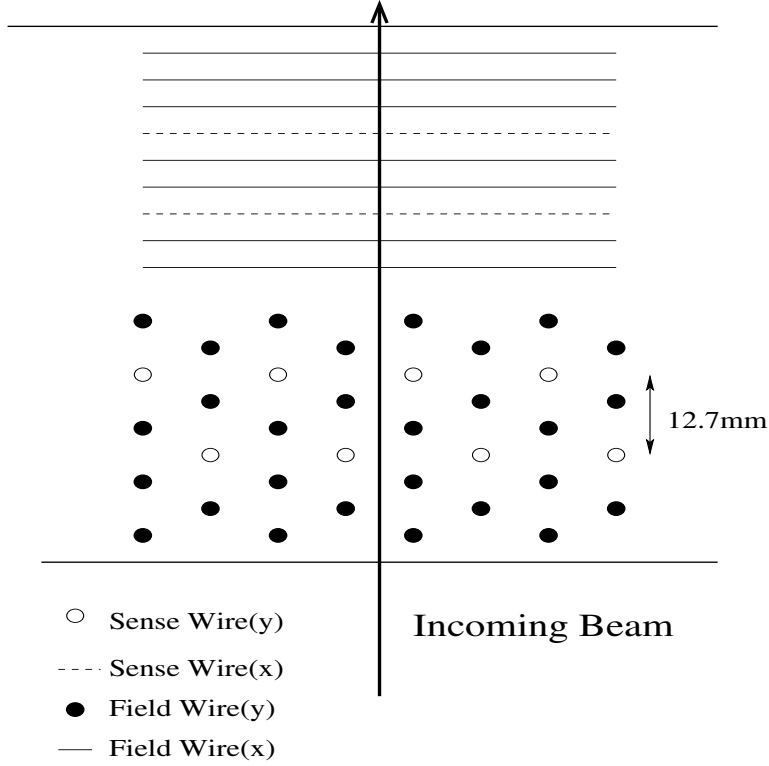


Figure 2.6: y view schematic of the field and sense wire arrangement within a drift chamber.

details of all calibration procedures for the charged spectrometer, but it is summarized below. The first step to finding the maps was finding the $T0$ offsets. Each wire followed a slightly different path to get to the TDC modules, which create slightly different offsets or time delays. The $T0$ was a measure of this offset, which was a function of wire length and the electronics in a module. The $T0$ was found using $K_L \rightarrow \pi e \nu$ (also called $Ke3$) events looking for sharp edges in the TDC distributions.

The $X(t)$ maps could be constructed once these $T0$'s were in place. These maps were created for each wire in cells along the length of the wire. They are created by producing a beam of straight through muons. As was mentioned in section 2.1.2, putting in the Beam Stops and turning off certain magnets in NM2 created this beam. These “muon runs” were performed every couple of days. The calculation of the maps assumed that the illumination of tracks was uniform across a cell. The conversion from

a TDC count t to a drift distances $X(t)$ is

$$X(t) = d_{cell} \cdot \frac{\sum_{t'=t_0}^t N(t')}{\sum_{t'=t_0}^{t_m} N(t')}, \quad (2.1)$$

where $d_{cell} = 6.35\text{mm}$ is the cell size, $N(t')$ is the number of hits at TDC count t' , t_0 is the earliest TDC hit (*i.e.* largest number of TDC counts) and t_m is the latest TDC hit (*i.e.* smallest number of TDC counts). In this case the TDC counts were equal to 0.5ns. After the data collection was completed, an offline calibration using $K_L \rightarrow \pi e \nu (Ke3)$ was done.

Using the calorimeter to measure energy, described in section 2.6, one could perform another important calibration. Electrons deposit all their energy in the calorimeter, so the ratio of their energy as measured by the calorimeter to the momentum measured by the spectrometer (E/P) should be close to 1. This measurement was sensitive to assumed magnetic kick of the analysis magnet, so the kick could be fine-tuned by taking a known sample of electrons and fixing the E/P to one. This was necessary because the analysis magnet polarity was changed as often as once a day. Further offline calibration of the kicks was done using a sample of $K_L \rightarrow \pi^+ \pi^-$.

Finally, there was a necessary alignment of the Drift Chambers with respect to one another and with respect to the rest of the detector. This alignment was a three stage process. The first stage involved the special muon runs, internally aligning the Drift Chambers with regard to one another. This was done by fixing DC 1 and DC 4, reconstructing a track and comparing the hits in DC 2 and 3 to the interpolated position from the track. This eliminated offsets and rotation of the two non-fixed Drift Chambers. An overall rotation of the spectrometer remained and was removed in step 2. Using $K_L \rightarrow \pi e \nu (Ke3)$ events and the fact that both charge particles come from a common vertex (see section 4.4 for more information on vertex finding), one could observe rotations of DC 2, 3 or 4 relative to DC 1. Lastly, the spectrometer as a whole was aligned with the rest of the detector using $K_L \rightarrow \pi^+ \pi^-$ and $K_L \rightarrow \pi e \nu (Ke3)$ events. The $K_L \rightarrow \pi^+ \pi^-$ events were used to align the spectrometer with the target by reconstructing the total momentum of the K_L and projecting it back to $z = 0.0m$. The $K_L \rightarrow \pi e \nu (Ke3)$ events were used to align with calorimeter by looking at the separation of extrapolated track position at the CsI with cluster position (see Chapter 4 for more information on reconstruction).

The overall momentum resolution of the spectrometer is found to be

$$\sigma(P) = 0.38\% \oplus 0.016\% \cdot P, \quad (2.2)$$

with P measure in GeV [42]. The constant term is due to multiple scattering and the linear term is due the finite position resolution for higher track momentum. The position resolution is about $100\mu\text{m}$ within the chamber. Figure 2.7 shows the effect on the E/P distribution these calibrations have. Online calibration is a quick and dirty form of the complete calibration. The mean is now closer to one, the width increase due to a lack of corresponding calibration with the CsI calorimeter.

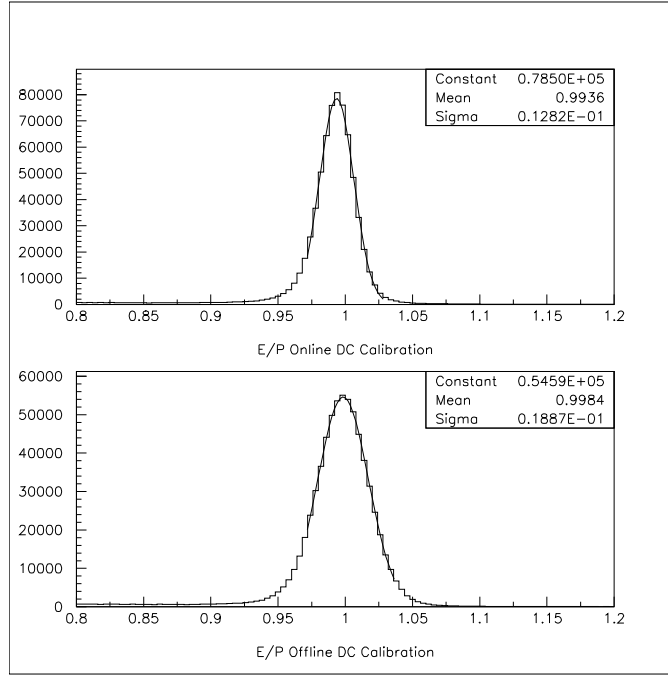


Figure 2.7: Distribution of E/P for run 14934. Top plot has only Online Calibration, bottom plot has complete DC calibration.

2.3.4 Photon Vetoes

Lead-scintillator arrays, much like those in 2.2.1 surrounded the outer edges of Drift Chambers 2, 3 and 4 as is seen in figure 2.3. These Spectrometer Anti's (SA) were used to detect particles that left the detector at high angles. Each SA was positioned just before a drift chamber and sized accordingly, see table 2.4. They were constructed

of 32 layers of lead-scintillator, each of 0.5 radiation lengths in depth, for a total of 16 radiation lengths. Several modules, see figure 2.8, made up each SA. Each module was cut at an angle so that particles could not escape down a crack.

Spectrometer	z position(m)	Outer Edge, $x \times y$	Inner Edge, $x \times y$	Modules
SA2	165.1	2.50×2.50	1.54×1.37	32
SA3	174.0	3.00×2.40	1.69×1.60	36
SA4	180.0	2.37×2.37	1.75×1.75	28

Table 2.4: Position and Dimensions of the Spectrometer Vetoes.

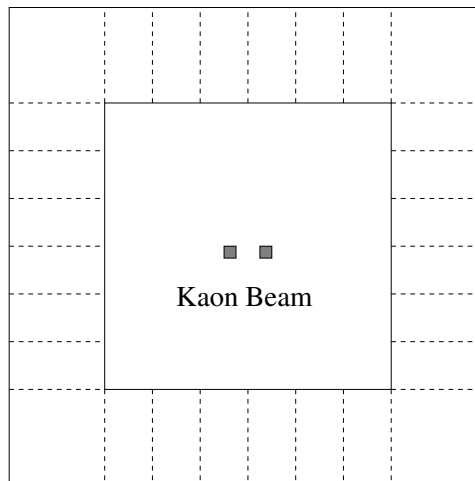


Figure 2.8: Cross-sectional View of a Spectrometer Veto.

2.4 Transition Radiation Detector

The Transition Radiation Detector (TRD) is an important tool in providing discriminating power between electrons and pions. It operated on the principle that charged particles passing over a boundary between material of different indexes of refraction produce transition radiation. The transition radiation energy is inversely proportional to the mass of the charged particle. The transition radiation for the typical energy of charged particles in KTeV (tens of GeV) was an x-ray (tens of keV). These x-rays were detected when they ionized gas in a Multi-Wire Proportional Chamber (MWPC). The KTeV TRD is extensively discussed in [43].

The probability of producing useful transition radiation for GeV particles was only $\sim 1\%$ for each crossing. Therefore, the radiation material for the KTeV TRD was a mat of polypropylene fiber. The x-rays were detected when they ionized the gas (mixture of 80% Xenon and 20% CO₂) and the freed electrons avalanched to the sense wires in the MWPC. The amount of ionization was a measure of the energy of the x-ray. Because xenon is a very dense gas, the MWPC produced bulges in the window that could significantly effect the performance. Even worse, these bulges could vary as a function of barometric pressure. To reduce this effect, volumes of buffer gas (mixture of 80% C₂F₆ and 20% CO₂ were placed outside of the MWPC's. Figure 2.9 shows the general layout of the TRD.

The field wires ran at a voltage of about 250V and the sense wires were at 2400V. The charge collection time was $\sim 225\text{ns}$. Signals from the wires were sent to amplifiers and then to ADCs. The TRDs are $2.1 \times 2.1\text{m}$ in size, but only the central 1.8m of wires were read out. Two 15cm square holes were cut in the fiber mats to allow the neutral beam to pass through. Also the wires in those regions were deadened by thickening them with electroplating. The wires were ganged together to reduce electronics as well. In the central 64cm two wires from the same plane were ganged, while four wires were ganged for the rest of the chamber. There were eight TRD chambers, one every 31cm. The positions are given in table 2.5.

TRD chamber	z position(m)	Size, $x \times y$
TRD1	181.1	2.1×2.1
TRD2	181.4	2.1×2.1
TRD3	181.7	2.1×2.1
TRD4	182.0	2.1×2.1
TRD5	182.3	2.1×2.1
TRD6	182.7	2.1×2.1
TRD7	183.0	2.1×2.1
TRD8	183.3	2.1×2.1

Table 2.5: Position and Dimensions of the TRD.

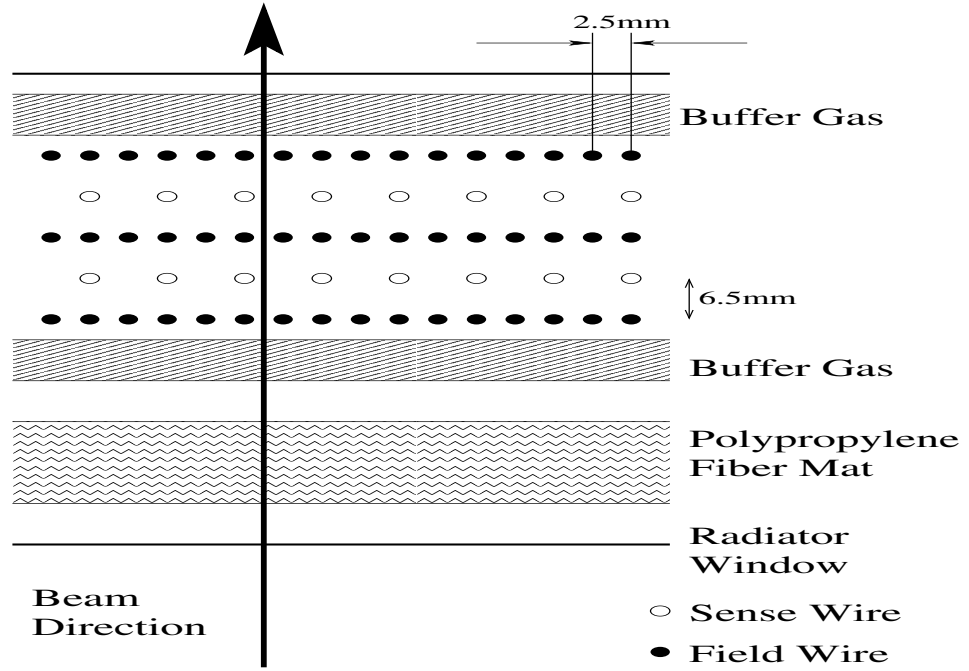


Figure 2.9: Cross-sectional View of TRD.

2.5 Trigger Hodoscope

The L1 Trigger, described in Chapter 3, required a prompt signal indicating the presence of charged particles in the detector. The Drift Chambers detected the passage of charged particles but the drift time could be upwards of 200ns. Therefore, two planes (upstream plane is V and downstream plane is V') of scintillators were placed at 183.9m in z . Each of the two planes consists of 32 paddles arranged along the y axis with five different widths, *i.e.* 9.92cm, 11.82cm, 13.74cm, 15.63cm and 17.76cm. The paddles were 1cm thick and had 14cm holes cut in the center to allow for the passage of the neutral beam. The different sizes of the paddles and arrangement of V' relative to V minimized the inefficiency due to cracks. Figure 2.10 shows a schematic of the Trigger Hodoscope.

2.6 Calorimeter

The electromagnetic calorimeter measured the energy and position of kaon decay products. It was the only instrument that measured photons in the detector, and was

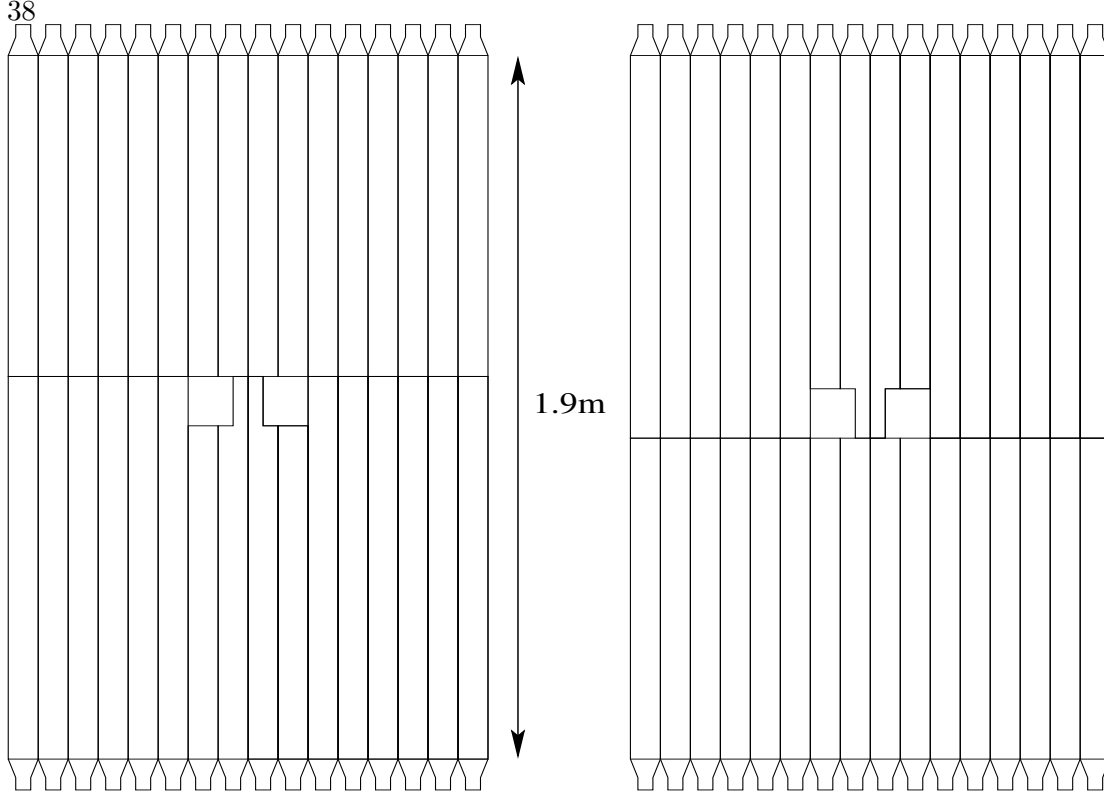


Figure 2.10: Trigger Hodoscope plan view.

very important to completing the measurement of charged particles. The calorimeter was constructed of pure CsI crystals and its front face was located at $z = 186.0\text{m}$. Figure 2.11 shows the layout of the Calorimeter. The crystals were kept in a special room (the Blockhouse) where the temperature and humidity were controlled. The humidity was kept to less the 4% at all times.

2.6.1 Crystals

There were 3100, 0.5m long pure CsI crystal stacked in a $1.9 \times 1.9\text{m}$ array. 868 large blocks (each with a face of $5 \times 5\text{cm}$) surrounded 2232 small blocks (each with a face of $2.5 \times 2.5\text{cm}$). Small blocks were used in the inner region to give greater position resolution there. Two $15 \times 15\text{cm}$ square holes allowed the neutral beam to pass through without harming the crystals. The scintillation light produced by the crystals was measured to be about 20 photoelectrons per MeV deposited [44]. The light had two components, a 8-10ns long pulse with a wavelength of 305nm and a long part with

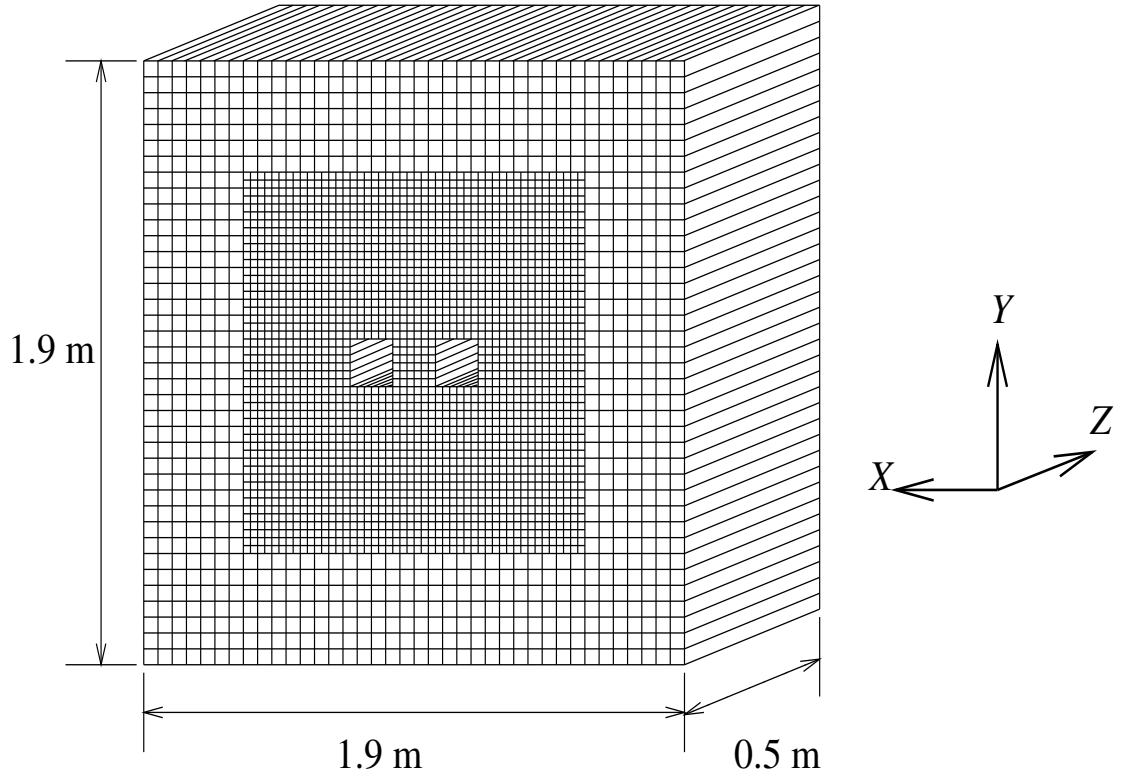


Figure 2.11: 3-dimensional view of CsI Calorimeter.

μs long pulses and a wavelength of 480nm.

The 50cm length of each crystal corresponds to 27 radiation lengths. This implied that virtually all electromagnetically interacting particles (*i.e.* photons and electrons) would deposit all their energy. The same length corresponded to 1.4 nuclear interaction, which gave a probability of about 70% for pions to hadronically shower in the CsI. The rest of the pions and muons deposit only minimum ionization energy (MIP) of about 0.3GeV in the calorimeter. The light response of each crystal was not necessarily uniform along the length. To compensate, each was wrapped in $13\mu\text{m}$ thick black or reflective mylar. The wrappings were individually determined for each crystal. This procedure enabled the responses to be uniform within 5% [45].

2.6.2 Calorimeter Instrumentation

Each crystal was connected to a PMT via a RTV rubber cookie. There was also a filter in the optical coupling to remove the slow component of the light. The tubes

ran at 900 to 1500V with a typical gain of 5000. The voltages were set to tune the thresholds for the Hardwire Cluster Counter discussed in section 3.3.1. The dynode signal from each PMT was used in the E-Total system of the L1 Trigger discussed further in section 3.2.3. The anode signal was sent to the Digital PMT base (DPMT).

The DPMT was a circuit board designed to digitize and buffer the signal from the PMT. The current from the PMT was sent first to the custom Charge Integrating and Encoding (QIE) chip, which integrated it. The current was divided into smaller chunks by powers of two ($I/2$, $I/4$, $I/8$, ..., $I/256$). Each current chunk charged a different capacitor. A comparator selected the capacitor with the highest, non-overflow voltage. This voltage was digitized by the flash ADC and stored as a mantissa. A number corresponding to the capacitor was also outputted as the range. Four such circuits were present in each QIE. They were activated in a round-robin fashion for each RF bucket. A word constructed from the mantissa, range and an ID was then sent to the Driver-Buffer-Clock (DBC), a FIFO (first-in, first-out) buffer. The buffer was 32 words deep and was only read out in response to certain signals from the trigger logic.

2.6.3 Calibration

The calorimeter was calibrated, in part, with light from a dye laser. This laser light was distributed via optical fiber to each crystal. The light was also distributed to several highly linear PIN diodes as a reference. The light intensity was varied by a slowly turning filter wheel during special Laser Scan runs. Laser Scans were taken every couple of days. The response to capacitance of each capacitor in the QIE was compared to the response of the PIN diode. The relationship between the PIN diode and the QIE was seen to be linear, so the slope and offset for each DPMT range was extracted as a calibration constant.

The conversion factor from charge to energy (Q/E) for each channel was also necessary for the Calorimeter calibration. Electrons from the $K_L \rightarrow \pi e \nu(K e 3)$ are required to form an E/P near 1. The calibration was an iterative process, with an initial guess given for each channel. After a calibration pass, a new constant was formed and the process was repeated, up to five times.

The energy resolution of the calorimeter is

$$\frac{\sigma(E)}{E} = 0.45\% \oplus 2\%/\sqrt{E} \quad (2.3)$$

where E is measured in GeV [45]. The constant term is due to many different factors such as light leakage, noise and non-uniformities. The second term is from the photo-statistics of the light. The position resolution for small blocks is $\sim 1\text{mm}$ and for large blocks it is $\sim 1.8\text{mm}$. Discussion of how the position is determined can be found in chapter 4.

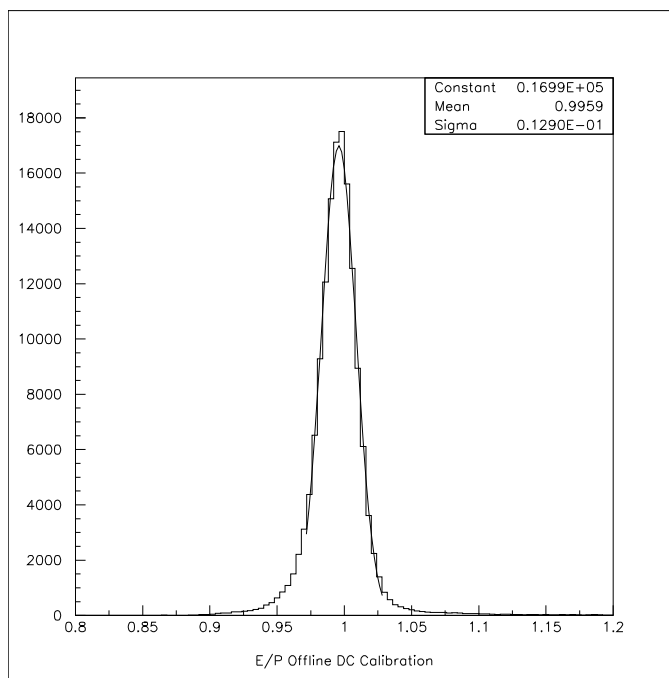


Figure 2.12: Distribution of E/P . Both CsI and offline DC calibrations have been performed.

2.6.4 Photon Vetoes

Surrounding the CsI Calorimeter was a rectangular series of lead-scintillator modules. They performed the same function as the SAs for the CsI, detecting photons exiting the detector. The CsI Anti (CIA) is illustrated in figure 2.8 and its position and dimensions are given in table 2.6.

A set of eight (four for each hole) veto counters surrounded the beam holes on

the upstream edge of the CsI. They formed a collar around the beam holes and were thus referred to as the Collar Anti (CA). Each module was constructed of three layer tungsten-scintillator sandwich, which corresponds to 9.7 radiation lengths. The purpose of this detector element is to prevent particles from hitting the edge of the beam hole and having a poorly measured energy. Figure 2.13 is a schematic of the CA and the position and dimensions are in table 2.6.

CsI Photon Veto	z position(m)	Inner Edge, $x \times y$ (m)	Outer Edge, $x \times y$ (m)
CIA	185.2	2.20×2.20	1.84×1.84
CA	185.9	0.18×0.18	0.15×0.15

Table 2.6: Position and Dimensions of CA and CIA.

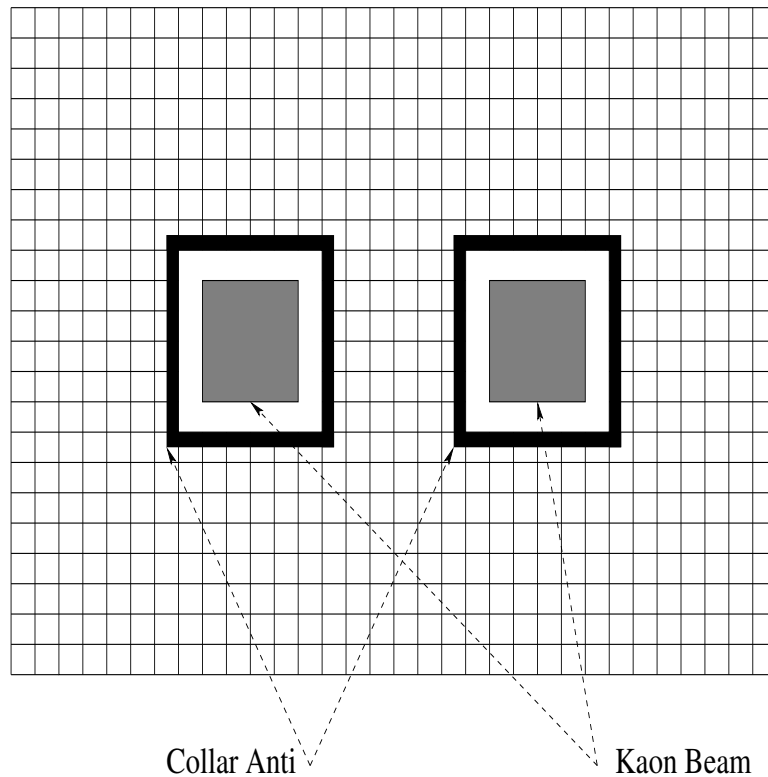


Figure 2.13: Collar Anti plan view.

Located just behind the calorimeter was a 15cm thick lead wall. The wall absorbed electromagnetic showers that leaked past the end of the CsI. The 0.9 nuclear interaction lengths also produced hadronic showers of some hadrons that didn't shower in the CsI.

The wall had a hole of $60 \times 30\text{cm}$ size in the center to allow the beam to pass. At a $z = 189.0\text{m}$ was Hadron Anti (HA). This set of 28 scintillator paddles triggers on hadron shower activity. The HA had a $64 \times 34\text{cm}$ hole in the center for the neutral beam. Figure 2.14 displays the HA layout.

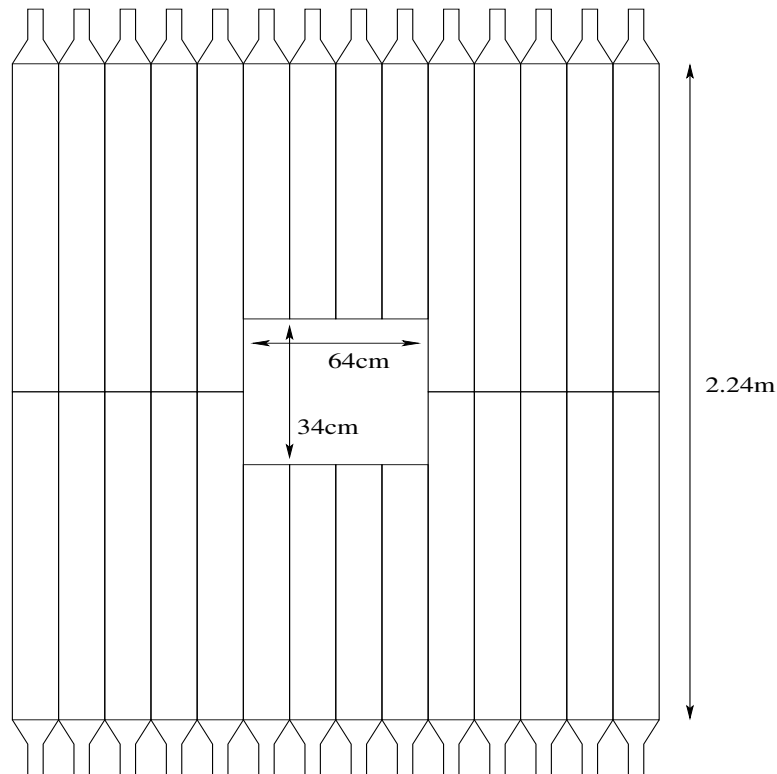


Figure 2.14: Hadron Anti plan view.

After the HA was a 1m thick steel wall called MUF1 (muon filter 1). The wall protected the HA from back splash of the downstream neutral beam dump *i.e.* MUF2, see section 2.7. A $60 \times 30\text{cm}$ hole cut in the steel allowed the neutral beam to reach the Back Anti (BA). The BA was intended to veto particles that escaped detection by going down the beam holes. However, in practice the neutrons in the beam made the BA useless for this analysis. The BA was constructed with 30 layers of lead-scintillator layers, totaling to 30 radiation lengths worth of material. The readout was divided into three sections in order to distinguish between hadronic and electromagnetic particles based on shower shape. The BA was $60 \times 30\text{cm}$ in cross section.

2.7 Muon System

At the far end of the detector was a 3m long steel wall, MUF2, which served as a the neutral beam dump. Behind this is a large set of 56 scintillator paddles, MU2. The paddles in MU2 overlapped by 1 cm in order prevent muons from escaping down a crack. This system was used in most triggers (discussed more in 3) as a veto to remove decays with muons. Figure 2.15 shows a diagram of this system.

Downstream of MU2 was another 1m long steel wall, MUF3. Finally there were two sets of 15cm wide scintillator paddles which formed MU3X and MU3Y. MU3Y had the paddles aligned parallel to the x axis and MU3X with the y axis, see figure 2.16. MU3 was important for those modes with muons in the final state such as $K_L \rightarrow e^+e^-\mu^+\mu^-$. Together, the lead wall and the three muon filters provided a total of 31 nuclear interaction lengths, meaning that there is only a 0.5% probability that hadronic shower from a pion could leak to MU3.

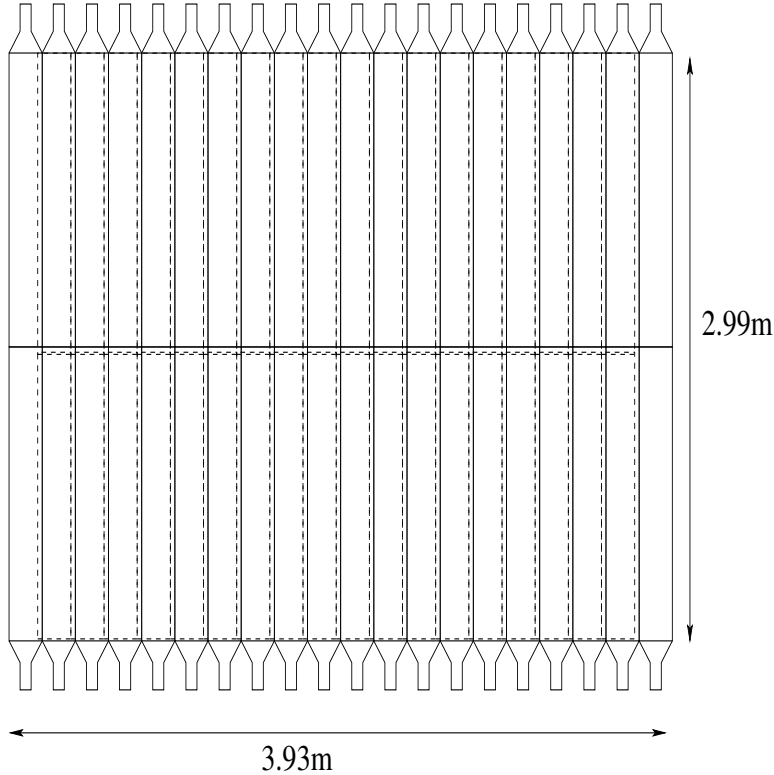


Figure 2.15: Muon Trigger plane. Dashed lines indicate the 1 cm counter overlap in MU2.

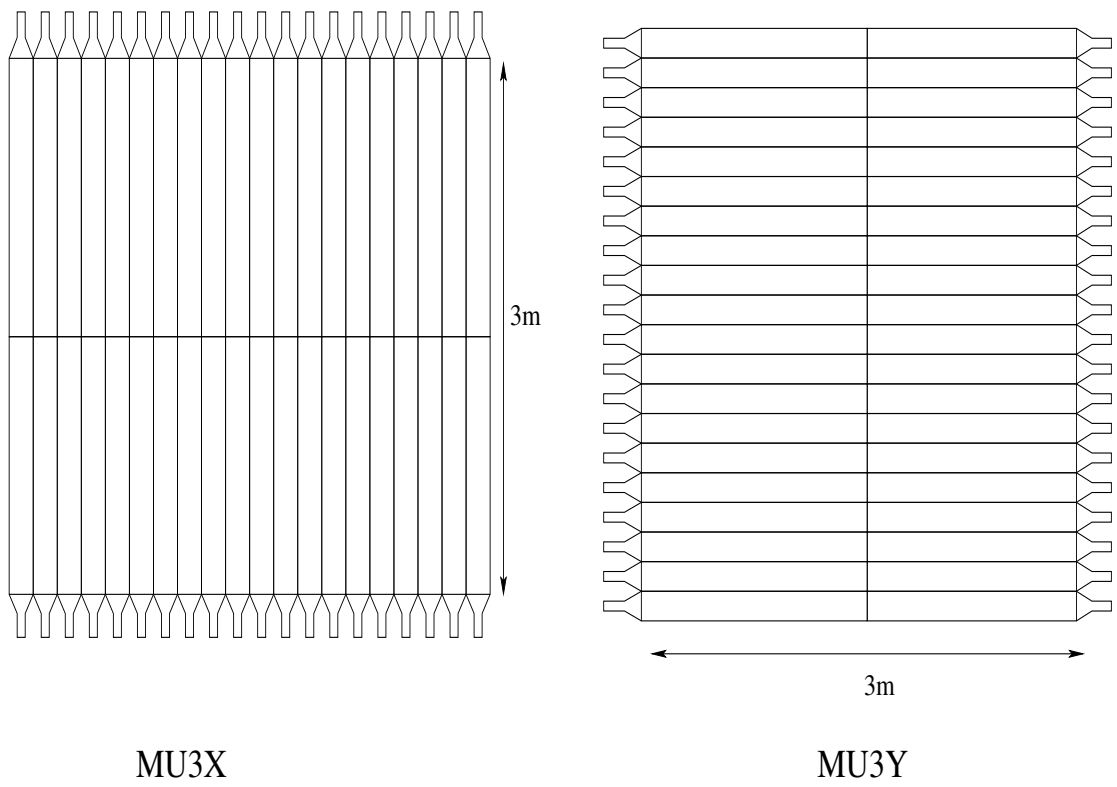


Figure 2.16: Muon Trigger plane.

Chapter 3

The KTeV Trigger and Event Selection

The process of selecting and storing data for later analysis is described in this chapter. The rate of kaons that decay in the accepted volume (as defined in section 2.2) is around 1MHz. This rate is too high for the data acquisition system to record events. Therefore a series of “online”, using hardware (Level 1 and Level 2 triggers), and “offline” (Level 3) requirements were made to reduce the incoming data to a manageable rate, approximately 1kHz.

3.1 Organization of Data Collection

As mentioned before in Chapter 2, the data used in this analysis were collected in periods of time (*i.e.* Winter, Summer, and 1999). These were gross divisions, the actual data taking was further subdivided. At the smallest level data was collected event by event while the beam was “on-spill”, see section 2.1.1. One period of the beam being “on” (*i.e.* protons on target) and then “off” (the protons are being accelerated) was called a “spill”. A spill could be 60 or 80 seconds long. A collection of spills was grouped into a “run”.

Ideally, a run was about an eight hour period in which detector performance and settings were uniform. Eight hours was the time that it took to fill up output tapes (discussed later in section 3.6) when the beam was at nominal intensity. In practice, runs varied in length anywhere from a few minutes to 14 hours. Short runs could be the result of electronics not initializing properly, poor beam quality, hardware problems, tests, or even incorrect settings. Long runs were almost always due to a lack of beam. If there were accelerator problems, then many spills could go by without any data being collected. Each run was numbered consecutively, starting at 1. The Winter period

consisted of runs numbered between 8088 and 8913, Summer included runs from 10463 to 10970, and 1999 had runs from 14625 to 15548.

A run was a period of time when settings and detector performance were the same. There were several basic types of runs, data collection runs (the vast majority of runs), laser scans (mentioned in 2.6.3), muon runs (mentioned in 2.3.3), and pedestal runs. There were also special runs in which the standard data taking configuration was changed in order to perform a study, *e.g.* a run in which the analysis magnet was turned off in order to study the amount of material in the detector (chapter 5 will discuss this further). Runs were sometimes terminated before tapes filled up do to problems with the detector. During the Summer period there were frequent problems with the CsI readout electronics that caused many runs to be ended early. Runs could also be ended in order to make changes to a detector, in order to improve performance.

Spills were numbered consecutively starting at 1 for each run. Thus all runs have a spill 1, while only very long runs would have spills about 600. A set of spills could be used to denote a period of time during a run.

3.2 Level 1 Trigger

This element of the trigger used the Tevatron RF signal as a clock, so it made decisions every 19ns. For this reason it was a deadtime-less Trigger. Each detector sent its decision signals (or sources) to an array of programmable logic modules. Delays, using lengths of cables, were employed to ensure that all the sources arrived simultaneously at the modules. A CAMAC interface loaded a memory lookup table that was referenced to determine if the event passed Level 1 (L1). It should be noted that not every single source will be discussed in this thesis, there are many that are not relevant, so only some of the trigger sources will be discussed here.

Two signals did not come from the detector described in Chapter 2, but instead from an outside source. The first was the GATE, which was sent when the beam was on-spill. The second was the NC_PING *i.e.* neutrino ping, which was turned on when the beam was being delivered to an adjacent beamline. It was used as a veto to prevent beam leakage in the adjacent beamline producing activity in the KTeV detector.

3.2.1 Photon Vetoes

Each counter for the veto systems, *i.e.* RC6, RC7, RC8, RC9, RC10, SA2, SA3, SA4, and the CIA, was set to fire when more than a certain amount of energy was deposited in a module. The source for each veto was a logical OR of all the modules in each system. The threshold for the RCs was set at 500MeV, while the SAs and the CIA was set at 400MeV. Thus, any energy over threshold in any module made the L1 source bit a logical true. The L1 sources were called, not surprisingly RC6, RC7, RC8, RC9, RC10, SA2, SA3, SA4, and CIA.

The CA ORed together the four modules around each hole to form two sources. These sources were called CA_LEFT and CA_RIGHT. The energy threshold was set to 13GeV.

The L1 sources for the HA were formed by summing the output of the various modules' PMTs. If this sum was above the energy deposited by 2.5 minimum-ionizing (MIP) particles, then the source HA_HI was turned on. A second source turned on if DC-coupled sum went above the threshold of about 7(2.5) MIP particles for the Winter(Summer) periods.

3.2.2 Trigger Hodoscope

The hodoscope was meant to provide information on charged particles passing through the detector, discussed in section 2.5. Thus, the L1 sources were set up to provide a count on the number of hits in each plane of the system. Thus, when a module had enough energy to go above threshold it counted as a hit, the number of hits were then summed for each in discriminator modules. The sources were V0_GE1S, V0_GE2S, V0_GE3S, V1_GE1S, V1_GE2S and V1_GE3S, which referred to 1 or more, 2 or more, and 3 or more hits in V and the same for V'. Recall that V was the upstream plane and V' was the downstream plane.

3.2.3 E-Total

In section 2.6.2, it was mentioned that the DPMT dynode signals were sent to the E-Total system. The sum of all crystals' dynode signals were summed. If that sum went above one of 4 thresholds, then a bit was set on one or more of the L1 sources,

ET_THR1, ET_THR2, ET_THR3, ET_THR4. The threshold corresponded nominally to 10(11), 18(16), 25, and 38 GeV for the 1997 (1999) run periods for each of threshold respectively. These thresholds drifted some during the course of the run period, and were periodically brought back to the nominal levels by tuning discriminator levels or by increasing the high voltage on calorimeter PMTs (*i.e.* gain matching).

The E-Total system also generated an HCC bit if a channel went above a preset threshold. These bits are important for the the Level 2 processor known as the Hardware Cluster Counter (HCC), explained in section 3.3.1.

3.2.4 DC ORs

At L1 there was a need to check that there was sufficient activity in the Drift Chambers to warrant keeping the event. While it was true that the maximum drift time to one wire was 200ns, a track traveling down the center of a cell had an average drift time of 60ns. This was due to the “plane-pair” system of sense wires. Therefore, by taking a logical OR of 16 wires (8 in the upstream view, 8 in the downstream view) at a time it was possible to count the activity in Drift Chambers. Each gang of wires formed a “paddle” of the DC-OR systems. The L1 sources for this system counted the number of paddles with hits in each chamber. The sources were 1DC1X, 2DC1X, 1DC1Y, 2DC1Y, 1DC2X, 2DC2X, 1DC2Y and 2DC2Y, which correspond to one or more hits or two or more hits in Chamber 1 X-view, 1+ or 2+ hits in Chamber 1 Y-view, 1+ or 2+ in Chamber 2 X-view, and 1+ or 2+ in Chamber 2 Y-view.

3.2.5 Muon System

The Muon System produced many sources dealing with the counting of the number of paddles with energy above a certain threshold. For the modes of interest in this thesis, there are no muons. Thus, the system was used as a veto. In particular, two L1 sources 1MU2 and 2MU2 are of interest. The first source was set to true if there was one hit in any of the modules composing MU2 (see section 2.7), the second if there was 2 or more hits. These sources were not used after run 8577, because this source had a high level of accidental loss.

3.2.6 Beam Trigger

The various L1 sources were combined to form 16 different “Beam Triggers”. These triggers classified whether or not the event might be an interesting physics event. There were also 16 different calibration triggers. The calibration triggers defined non-physics data, such as the laser data for the calibration of the CsI calorimeter discussed in section 2.6.3. In fact, no beam triggers were allowed when the calibration triggers were on.

An example of a beam trigger is Trigger 1, the 2E-NCLUS set. This trigger was used quite extensively for this analysis.

$$2E - NCLUS_{L1} = GATE \cdot \overline{NC_PING} \cdot \overline{RC6} \cdot \overline{RC7} \cdot \overline{RC9} \cdot \overline{RC10} \cdot \overline{SA2} \cdot \overline{SA3} \cdot (3.1)$$

$$\overline{SA4} \cdot \overline{CIA} \cdot \overline{(CA_LEFT + CA_RIGHT)} \cdot \overline{HA_HI}. \quad (3.2)$$

$$[(V0_GE1S \cdot V1_GE2S) + (V0_GE2S \cdot V1_GE1S)]. \quad (3.3)$$

$$(1DC1X \cdot 1DC1Y \cdot 1DC2X \cdot 1DC2Y) \cdot ET_THR3, \quad (3.4)$$

where all of the above are L1 sources and the operations were logical (*i.e.* \cdot is a logical AND, $+$ is a logical OR, and the bar operator changes true to false and vice-versa). Thus, Trigger 1 required that no particles were escaping the detector and that there were no hadrons exiting the CsI. Further, it required that there were two hits in one of the two Trigger Hodoscope banks and one hit in the other, that there were at least one hit in both x and y planes of Drift Chambers 1 and 2 and that there was at least 28GeV of energy in the CsI. Remember that this was not the total trigger, just the first component. More requirements were made at Level 2 and Level 3.

Each of the 16 beam triggers required different combinations of sources, *e.g.* Trigger 3, the DALITZ set, was identical except that it used ET_THR2 instead of ET_THR3. Trigger 3 is also used in this analysis. Also, the beam triggers varied some over the course of taking data. For example, the requirement that there was at least one hit in drift chambers 1 and 2 was loosened to allow for one chamber to have a missing hit in one view,

$$(1DC1X \cdot 1DC1Y \cdot 1DC2X \cdot 1DC2Y) \rightarrow \{[(1DC1X \cdot 1DC1Y) \cdot (1DC2X + 1DC2Y)] + [(1DC1X + 1DC1Y) \cdot (1DC2X \cdot 1DC2Y)]\}.$$

If the rate was very high for a particular trigger, then a prescale was added. This was done at the hardware level with CAMAC prescaler module. For example, Trigger 2, the 2TRK set, had a prescale so that only 1 out of 500 events was processed.

3.3 Level 2 Trigger

The output rate from the L1 Trigger was about 75kHz. Level 2 (L2) took this output and using hardware processors reduced it even more, to about 10 kHz. The L2 Trigger was considerably slower than the L1 Trigger, taking up to several μ s to complete. While the L2 was processing an event, it was BUSY and could not accept any more L1 events. When the L2 finished, then it could make a decision to accept or reject an event. This led to a dead time of about 35% for both 1997 and 1999 for both L2 processing and readout. Dead time was a period when the trigger was processing an event, and could not accept any more data. Each of the L2 Processors is discussed below.

3.3.1 Hardware Cluster Counter

An innovative method of determining the number of clusters in a CsI calorimeter was used at the L2 stage. Specific decay modes should have a characteristic number of clusters in the calorimeter. For example, the decay $K_L \rightarrow e^+e^-\gamma$ has three electromagnetic particles in the final state, so should form 3 cluster in the calorimeter. The Hardware Cluster Counter (HCC) counted these clusters by using bits from the Level 1 E-Total system, explained in section 3.2.3. This is discussed in greater detail elsewhere [46].

The HCC algorithm was based on counting the number of corners in a cluster. As one moved around the outside edge of a cluster in a clockwise direction, making a sum where every time a right turn was made add 1 and every time a left turn was made subtract 1. At the end, the sum should have a total value of +4 for a cluster. The HCC took the entire 3100 crystals of the CsI and combined them into every possible 2×2 array and compared it to a lookup table. The table gave a weight, the sum of all these weights divided by four gave the number of clusters. The table is shown in figure 3.1, and an example is in figure 3.2. Figure 3.3 shows the results from the actual experiment.

The output of the HCC is a count of 1 to 8 clusters plus an overflow bit for events with more than 8 clusters. The total time for the HCC to finish was about $2.5\mu\text{s}$.


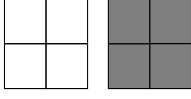


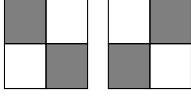
Hit Block Pattern	Pattern Weight
	0: No Turns
	0: No Turns
	+1: One Right Turn
	-1: One Left Turn
	+2: Two Right Turns

Figure 3.1: Possible HCC bit patterns and corresponding weights for 2×2 groups of blocks. Filled blocks represent those with the HCC bit on.

3.3.2 DC Hit Counting

The Drift Chamber Hit Counting (DCHC) system rejected events with insufficient activity in the spectrometer. There were two types of hardware processors used, the “Kumquats” and the “Bananas”. These modules counted DC Hits that occurred on different plane-pairs to determine if they were in time, *i.e.* they came from the same track. The Kumquats did this by requiring that both hits occurred within a fixed 205ns gate. The Bananas did this by requiring that both hits form a good SOD (sum-of-distance), which is described later. The output of these modules were used for other L2 processors (see sections 3.3.3 and 3.3.4 below) and consisted of a count of hit-pairs from 1-8 with an overflow bit, a mask of DC hits, and ORs of DC hits in wire paddles.

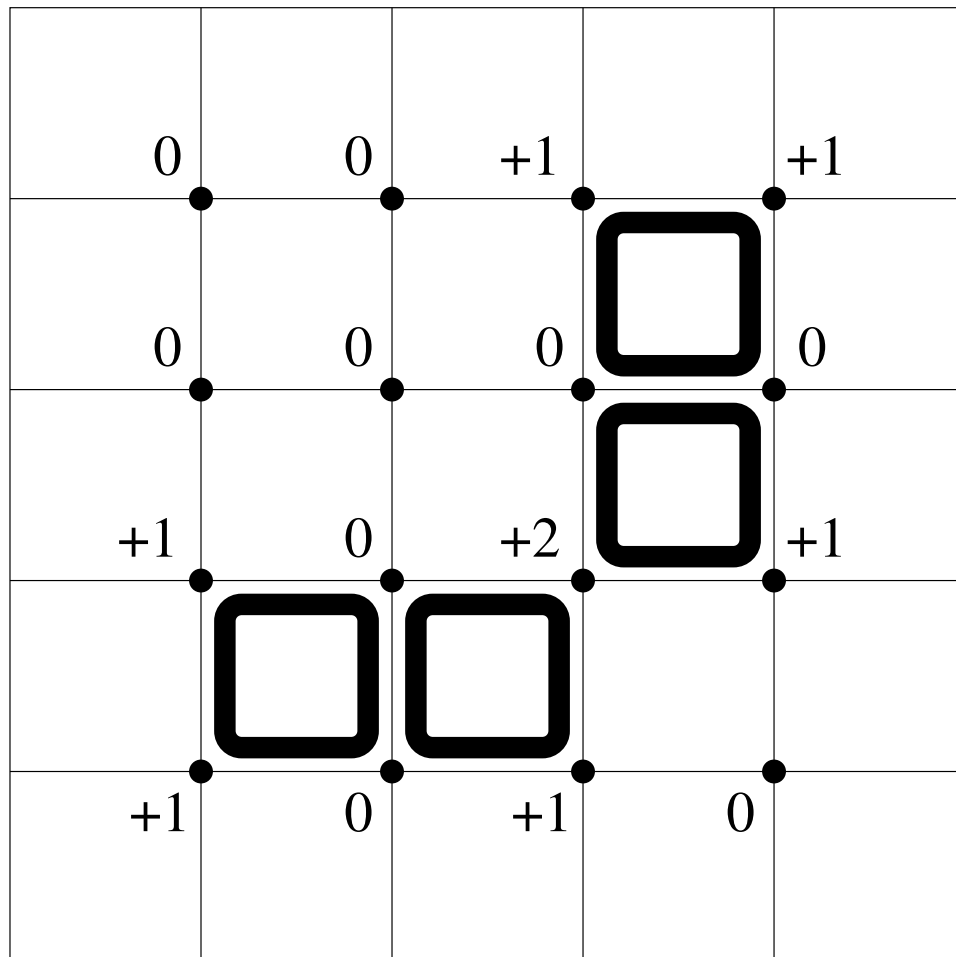


Figure 3.2: Example of Clustering in the Calorimeter. The Bold Boxes indicate that HCC bit is on. Assume that the 25 crystals are an entire array, each dot is the center of a 2×2 array considered by the HCC. The numbers represent the weight of that 2×2 array. The total weight is +8, so there are two Clusters.

The total time for this processor was about 900ns. A summary of the system follows, but more information is included in [1].

DC Signals

The signals from the Drift Chamber Wires followed a long path before reaching the DCHC system. The signals from each wire were amplified, discriminated, repeated, and received before being processed by the DCHC. A simple diagram is show in figure 3.4. After being amplified and discriminated the signals were repeated and sent to

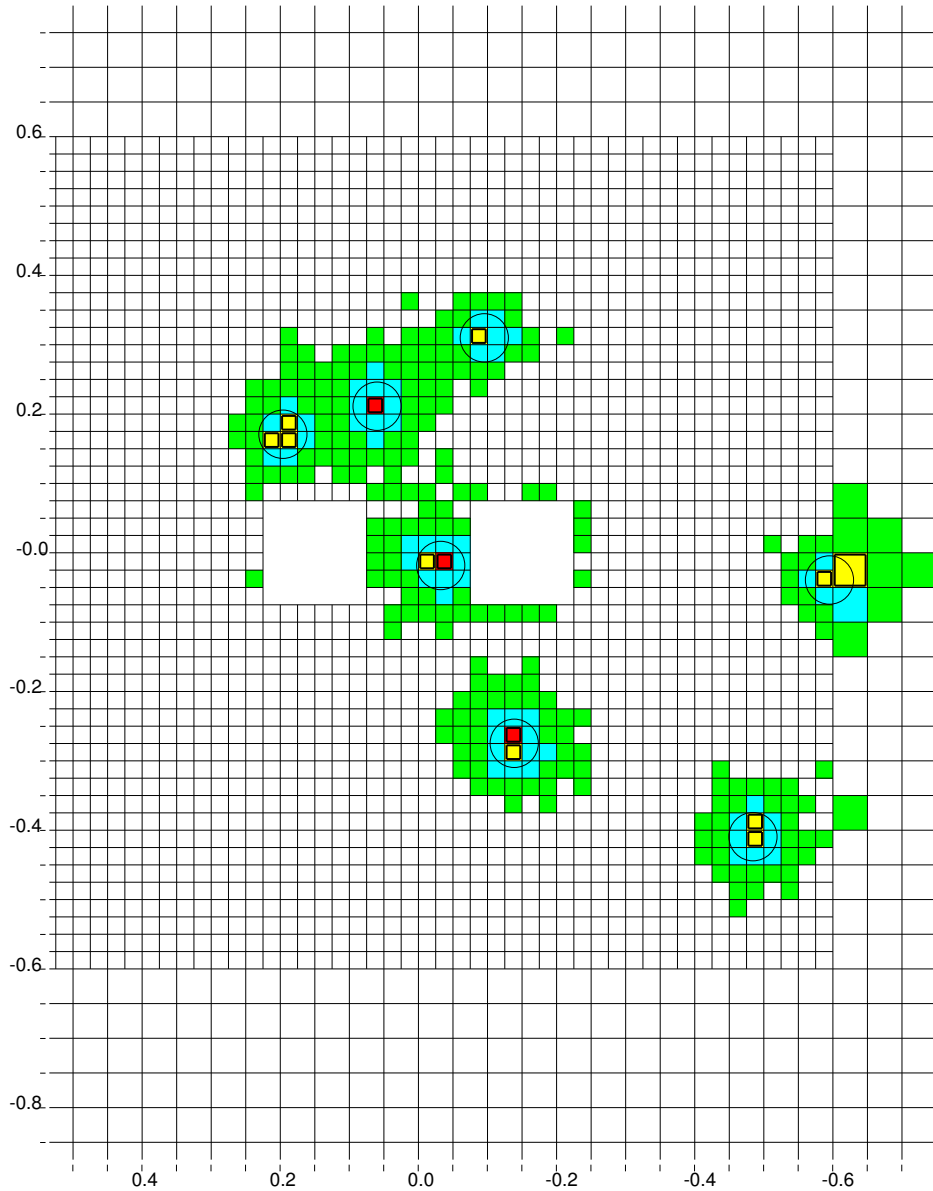


Figure 3.3: Example of Clustering in the real Calorimeter. Shading indicates energy in logarithmic steps from 0.01GeV-0.1GeV, 0.1-1.0GeV, 1.0-10.0GeV and more then 10.0GeV. The bold boxes indicate that the HCC bit is on. The circles are where the HCC algorithm found a cluster.

three different subsystems. The signals went to off-the-shelf Lecroy TDCs, the DC-ORs described in section 3.2.4, and to Receivers. The length of cables involved in taking signals from the DC to the DCHC was very large, 600 - 700 ns of delay. Thus, the signals were attenuated, so the Receivers took those signals and restored them. As indicated

in table 2.3, there were 64 flat-ribbon cable, with 17 pairs of wires each, for all of the Drift Chamber signal wires.

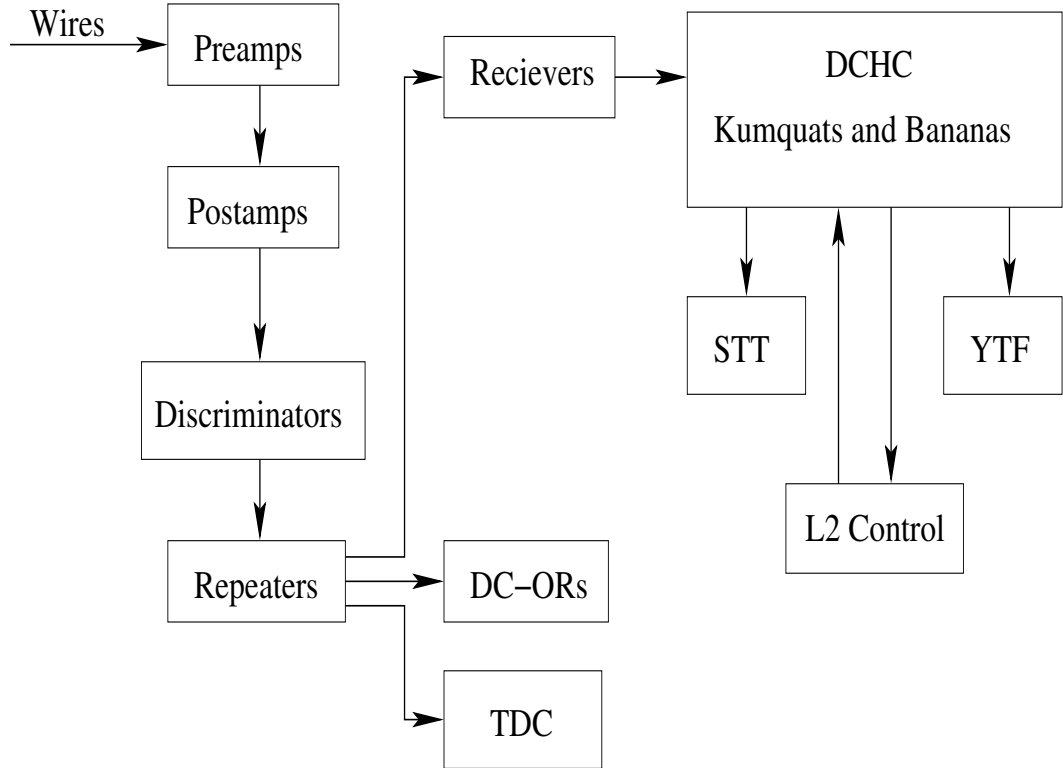
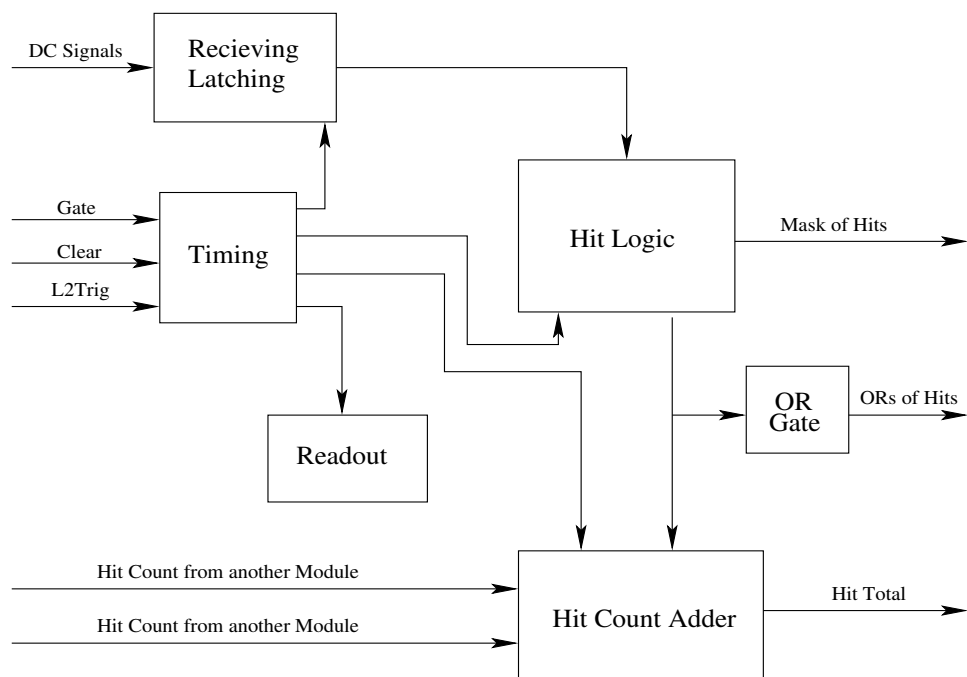


Figure 3.4: Path of DC Signals to DCHC.

From the Receivers, the signals interfaced with the DCHC modules. There was one module for each cable. The Kumquats and Bananas lived inside of Fastbus crates and received the signals via auxiliary cards on the back of the crate called Blossoms. There was one Blossom per module. The Blossoms also handled the inter-module hit counting cables and readout cables. There was one Fastbus crate for each DC View (*i.e.* DC1X, DC1Y, DC2X, ..., DC4Y). Each crate consumed on average 5 kilowatts of power, so they were specially cooled with forced air and chilled water. The high power draw also required that each crate was heavily monitored for fires, leaks or excess temperature.

Kumquat

The Drift Chambers downstream of the analysis magnet (DC 3X, DC 3Y, DC 4X



The hit counting circuit counted N continuous hits in the latched mask of hits as $N-1$ tracks. Single isolated hits also counted as one track. It was required for this algorithm to work, that a module used a copy of the signal from the neighboring wire in another module. That is, if module 2 spanned wires 33 - 64, then it would need information from wire 32 and 65 as well. This signal was transmitted via the Blossom board. Figure 3.6 shows an example of the hit counting process for various scenarios. The total hit counts from all modules for each chamber view was summed together through an adder tree. The total hit counts of each module could be sent to another module, or to the trigger system.

Bananas

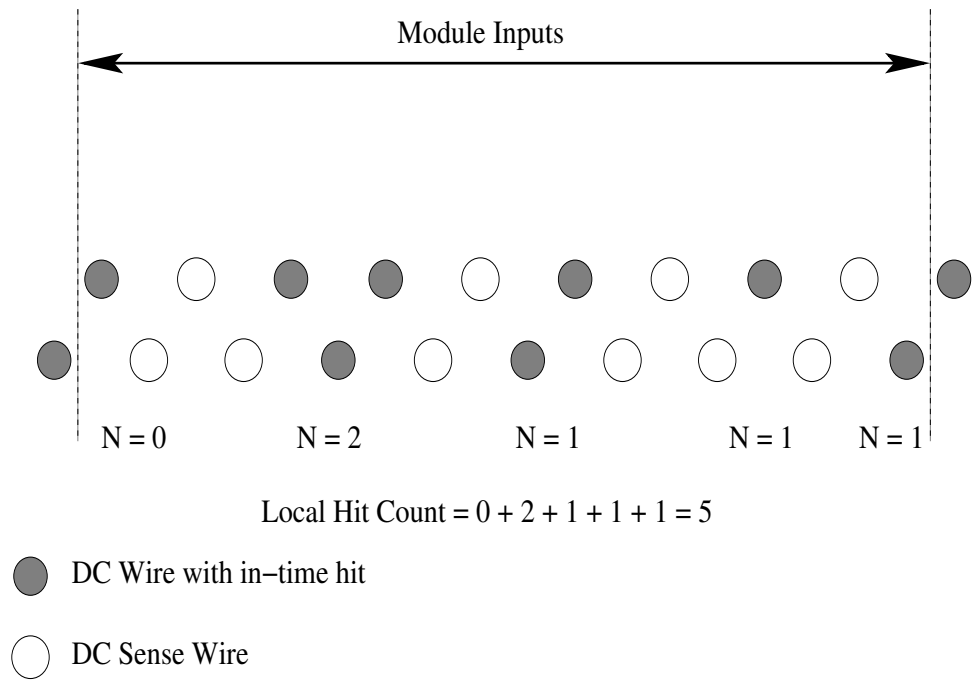


Figure 3.6: An example of Hit Counting.

The Bananas functioned almost identically to the Kumquats. However, instead of using a fixed width gate, the Bananas used a TDC to more accurately determine in-time versus out of time hits. A total of 29 Bananas instrumented the upstream chambers (*i.e.* DC 1X, DC 1Y, DC 2X and DC 2Y). Figure 3.7 is a picture of the Bananas showing the two different boards that made up each module. Figure 3.8 is a basic diagram of the functioning of the Banana.

The TDCs measured the time from the beginning of a latched hit until the end of the GATE signal. The GATE was longer than the one used for the Kumquats, being 464ns in length. The length was extended to allow very-early or very-late hits to determine if an isolated single belonged to an in-time or out-of-time pair. The TDCs, driven by a 625MHz on-board clock, measured the time in counts equal to 1.6ns using a total of 9 bits. The output of these TDC's were essentially the same as the other DC TDC's which had better time resolution. The TDC values for two adjacent wires were sent to a RAM lookup table. These tables represented all possible combinations of TDC values. The table could then be used to define in-time and out-of-time regions. These

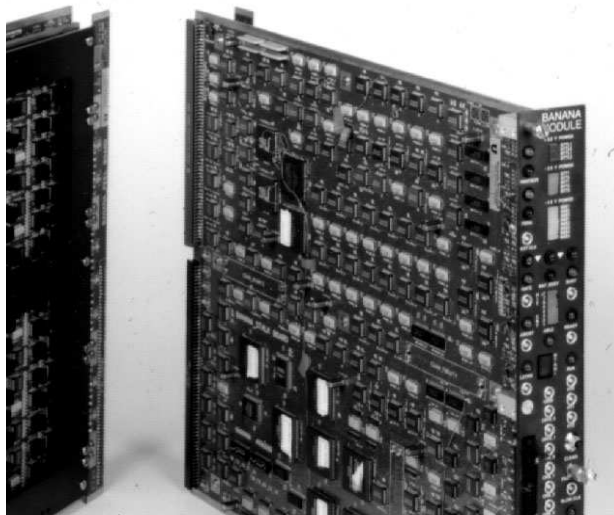


Figure 3.7: Photograph of a Banana Module.

lookup tables were malleable and could be changed during the course of the run. E832 used square maps, while E799 used a map reminiscent of the B2 bomber. Other maps, such as banana shapes and triangles were considered, but never used during actual data taking.

Figure 3.9 shows the region used to define in-time hits for the E799 experiment, the B2 bomber shape. The dots in this plot represent a pair of hits on complementary planes of a Drift Chamber (DC) view. The axes are the drift time for one plane versus the other plane. In figure 3.9 larger counts correspond to earlier hits. The banana shape with the high density of dots comes from the acceleration of the electrons as they approach the wire. Under ideal condition the t_1 and t_2 correlation would be a straight line. The in-time region includes a triangular bit for earlier activity in the chamber. This region is populated by delta rays and events with two track in the same cell. As a charged particle moves through the gas, sometimes electrons are knocked off and move through the chamber at large angles, ionizing the gas as they go, this kind of secondary

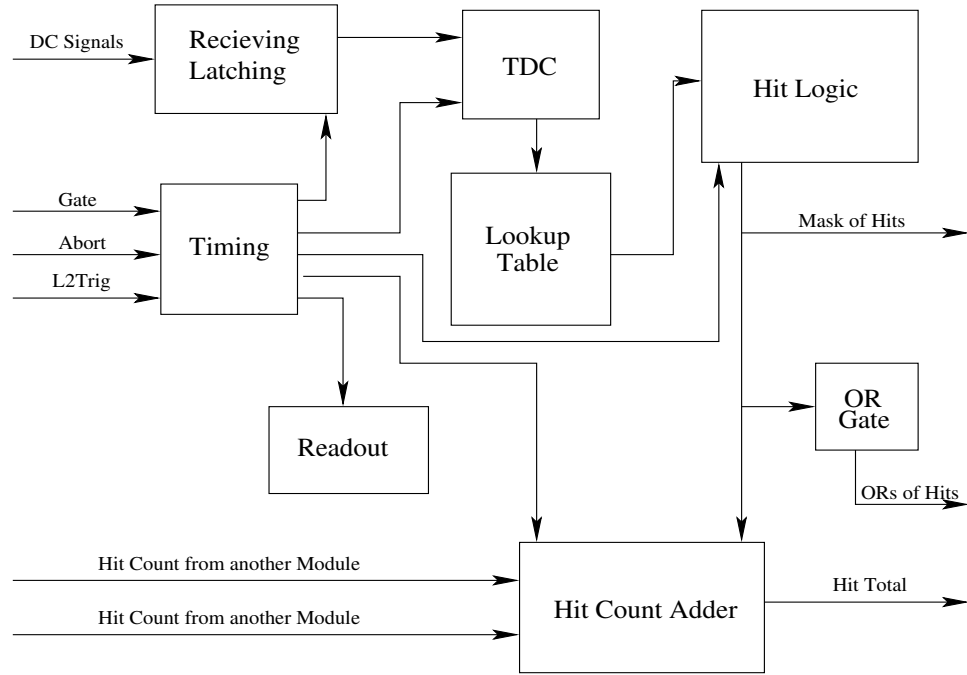


Figure 3.8: Diagram of a Banana Module.

ionizing track is a delta ray. Tracks with delta rays can still be reconstructed, so the region is kept.

Figure 3.10 shows a plot of events rejected by Bananas from a large sample of events with an isolated pair of hits, like the third set from figure 3.6. The diagonal strip comes from the out-of-time tracks. The upper-right (early hits) and lower-left (late hits) rectangular regions are from uncorrelated hits. The unpopulated regions come from events where t_1 and t_2 would have been good pairs, thus accepted. The hit counting was the same as for the Kumquats, except that the mask of in-time hits comes from the output of the look-up tables.

The output of each Banana and Kumquat included 4 words worth of data. A module identification number, a mask of hits, the hit count, and a mask of the ORs. The Bananas also outputted a word for each hit with TDC information. Thus, each Banana could output from 4 to 36 words depending on the activity in the chamber. The readout occurred through a FERA interface, same as all of the Data Acquisition (DAQ), except the CsI calorimeter. Because the size of the words coming from the Bananas

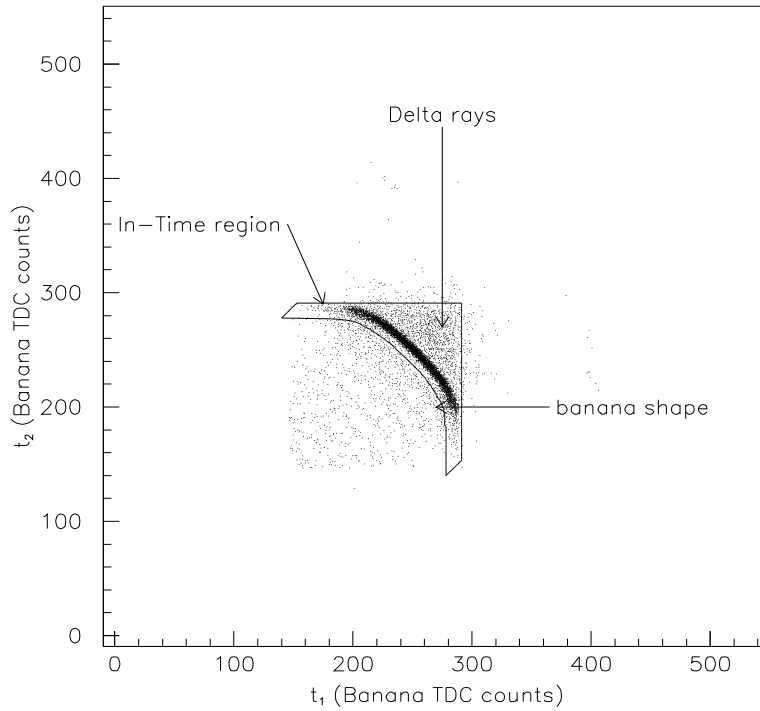


Figure 3.9: t_1 vs. t_2 and in-time pair region boundary for hits on tracks, with two good track.

could be quite large, the output was buffered using FIFOs. This way, the Bananas could process an event even if the DAQ had not finished collecting the previous information. In 1997 running, this feature was not implemented. In 1999, new FERA Latches were installed allowing for the buffering to function. These latches carried information about the event being processed. In practice, the rate was never high enough for the buffering to be evident, though it was thoroughly tested and functional. Each Fastbus crate also had its own local controller, a BiRa FSCC (Fastbus Smart Crate Controller) which could be used to interface with the modules. The FSCC had on board CPUs and could be logged into individually. This was necessary to load the lookup tables that define the in-time regions for each banana (a process that took up to a minute per module). This was also useful in debugging problems with the modules that arose during the course of the running.

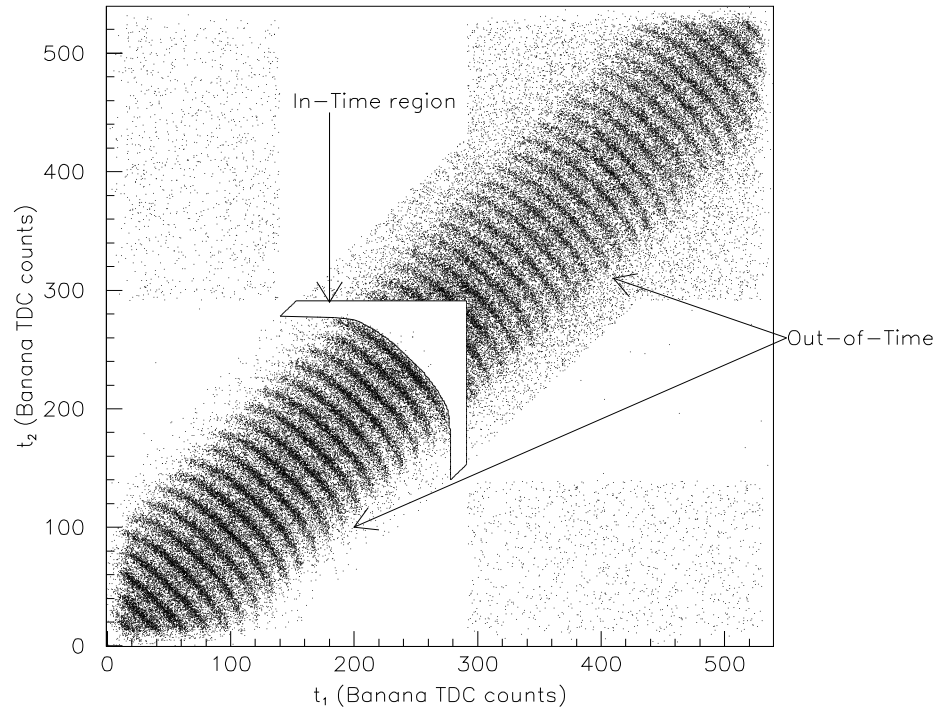


Figure 3.10: t_1 vs. t_2 and in-time pair region boundary for isolated pairs rejected.

3.3.3 Track Finding

The Y-Track Finder (YTF) looked for a pattern of hits in the y view of the Drift Chambers. It separated the Chambers into upper and lower segments and gangs of 4, 8, 16, or 32 wires (depending on how close to the edge of the chamber) to decide how many consistent hits there were. It uses outputs from the DCHC modules to do this. This L2 element was not used in this analysis.

3.3.4 Stiff Track Trigger

The Stiff Track Trigger (STT) L2 Processor looked for patterns of DC hits consistent with a very high momentum track. The high momentum translated to a very small bend at the analysis magnet. The processor used the hits from the beam region of x views of the Drift Chambers, processed by the DCHC modules, and looked for straight tracks. The STT was used primarily for the Hyperon modes which frequently

have protons going down the beam holes of the CsI calorimeter as one of the decay products. The STT was not used in this analysis.

3.3.5 TRD Trigger

This L2 Processor looked for good K_L Dalitz events while reducing the backgrounds from K_L decays with pions. It did this by using the TRD to look for a good electron track. Kumquat modules were used to provide latched hit information for groups of ganged wires from the MWPC as described in section 2.4. This information was also sent to FERA Analog-to-Digital Converters(ADCs). The hit information was a measure of the energy of the x-rays produced, which was inversely proportional to the mass of the parent particle. Thus, hits with large pulse signals were from electrons and small signals were from pions. Two thresholds were used to identify electrons. A low threshold with higher pion contamination and a high threshold with low contamination.

The first part of the trigger required that there is a low threshold hit in TRD chamber 1 or 2. This formed the front seed. Similarly there was a back seed formed from the OR of low threshold hits in either TRD chamber 7 and 8. A line was drawn from the back seed to the front seed, as long as both existed. At least four out of eight TRD chambers were required to have high threshold hits along this line. The number tracks that satisfied those criterion was counted to be used by the trigger. Below is a diagram showing the various elements of the trigger requirement in somewhat idealized form. Only one of the two electrons available from $K_L \rightarrow e^+e^-\gamma$ was required to satisfy the trigger.

The trigger was used during part of the 1997 run, but turned off for the 1999 run. Instead, a prescale was placed on Trigger 3 which accepted only 1 out of 5 events. The efficiency of this trigger is discussed in Appendix A.

3.4 Data Acquisition

The different elements could be combined to form L2 Triggers. For example, Trigger 1 required at Level 2

$$2E - NCLUS_{L2} = HCC_GE4 \cdot 2HCY_LOOSE \cdot 1HC2X, \quad (3.5)$$

$$(3.6)$$

1HCY: Required that there be at least one good track found by the DCHC in all the Drift Chambers.

1HC2X: Required that there be at least one good track found in DC 2X.

TRD_1E: Required that there be at least one track in the TRD consistent with an electron.

If an event passed the L1 and L2 requirements for a specific trigger, then it was read out and the information sent to the next stage. The reading out of an event began with the digitization of information. For many L2 elements, the output was in the form of a number of hits or clusters or whatever. The Drift Chambers produced information on which wires were hit, the TDC information on the hit, *etc.* The output of each Photon Veto was sent to a CAMAC ADC where the energy deposited was digitized. Copies of the L1 sources, the outputs of the L2 Processors, and masks of L1 and L2 Triggers were also sent to latches to be read out. 16 bit scaler modules also provided a spill and event number. In 1997, the ADCs used were 12 bit ADCs, this was reduced to 9 bit ADCs for the 1999 period to reduce data size.

All this information was gathered at an individual module level and then sent to a DYC3 module in a camac crate. The DYC (Damn Yankee Controller) gathered all the information for its crate of modules, and when that was completed sent it out on a RS485 bus. It did this only when it received a permit signal. When it finished sending the information, the DYC sent a ‘ ‘permit out” signal, which told the next DYC in the chain to begin adding its information. In this way a token-ring system was formed. Each crate of the ring sent its data one at a time. These token-rings were referred to as “streams”.

There were a total of six streams in the KTeV experiment. Four of these streams were dedicated to reading out the CsI information. The other two streams (Streams 5 and 6) read out the rest of the detectors. The CsI information was sparsified before it was read out, cutting out channels with little energy. The information was sent to VME buffers. The buffers were called DDD for the three components of each, a DM115 input controller, a DC2 FIFO, and DPM (Dual Port Memory). 24 DDD’s were arranged in grids of 6 streams and 4 planes. Each of the four planes got information for different

events. The information of each plane was sent to a different computer for processing. The 24 DDDs consisted of enough memory for an entire spills worth of data, about 4.6 Gb in 1997, increased to 4.9 Gb in 1999.

3.5 Level 3 Trigger

Four Silicon Graphics Challenge L computers were used to process the events for the Level 3 Trigger. Each Challenge consisted of several, 200MHz MIPS R10000 CPUs. Each of the Challenges received input from an individual plane of buffers. Software was run on each of the computers that performed a streamlined reconstruction of each event. The algorithms involved will be discussed in Chapter 4. One of the Challenges was dedicated to calibration events, events from the calibration triggers. This Challenge also ran monitoring software that filled online histograms which could be monitored during the data taking to ensure that the detector was working correctly.

The software would send events that passed the L3 requirements to one of several Digital Linear Tapes (DLT). Each DLT was capable of holding 10 Gb of information during the 1997 run. A change to DLT-IIIXT from DLT-III during the 1999 run allowed for each tape to hold 15 Gb. The Challenge dedicated to Calibration used only one tape drive, while the others used 3 or 4 drives writing out in parallel.

The L3 requirements for Trigger 1 were as follows:

- The event needed to have two good tracks from oppositely charged particles.
- The tracks must be consistent with having come from a single decay vertex.
- There must be 4 or more clusters in the calorimeter, using a software algorithm similar to the HCC.
- Each of the two tracks needed to point to a cluster in the calorimeter.
- Each cluster had to have over 2.5GeV of energy deposited in the calorimeter.

The events that satisfied these requirements, about 6% of the input, were further tagged based on their E/P . Events with two tracks having an E/P over 0.75 were tagged as “2e”, only one track over 0.75 were tagged as “epi”, and events with two track below 0.75 were tagged as “2pi”. One event in every 250 inputted events was automatically accepted

as a “random accept”. Randomly accepted events were used to study the efficiency of the Level 3 code. Trigger 3 required the same L3 requirements, and performed the same tagging, with exception of the number of clusters. It required there to be 3 or 4 clusters. The Level 3 code for Trigger 3 reduced the rate of events to 3.4% of incoming L2. Table 3.1 enumerates the Trigger rates at all stages. These numbers are corrected for dead time. The rate for Trigger 3 in 1999 is different due to a prescale of 5 that was put in due to the lack of Level 2 TRD Trigger requirement.

Trigger	L1 Rate(kHz)	L2 Rate(kHz)	L3 Rate(kHz)
97 All	57	11	1.24
97 1	22	2.1	0.13
97 3	29	2.9	0.10
99 All	74	8	1
99 1	18	1.5	0.11
99 3	12	0.6	0.02

Table 3.1: Trigger Rates at various levels. The beam intensity for the 97 numbers is 4×10^{12} protons per spill, while 99 numbers are for 8×10^{12} protons per spill.

3.6 Data Reduction

The amount of data produced during the running was enormous. As mentioned above in section 3.5, the data from all triggers was written to DLTs. There were 950 raw data tapes in 1997 and 1045 in 1999. The tapes used in 1999 are 50% larger than those used in 1997. That works out to a formidable 30 Terabytes of Data. It was not feasible to run on 30 Terabytes worth of data for an analysis, so the the data was reduced in order to make it easier to analyze.

3.6.1 E799 Split

The first step in the data reduction scheme was splitting the raw data into its component trigger elements. This was done after data taking for 1997 data set. An effort that required 6 months, and in the end produced 96 DLT-III for Trigger 1 and 63 tapes for Trigger 3. This represented 1.6 Terabytes of data. Further reduction was required.

The 6 months of time it took to split the data offline was considered to be much

too long. Thus, for the 1999 data set, an online splitting system was implemented. A copy of the data being written to raw data tapes was sent to a disk. When a sufficient amount of data was accumulated, it was then written to a separate DLT-IIIXT. This reduced the amount of overhead greatly. In 1999, there are 134 tapes for Trigger 1 and 23 tapes for Trigger 3. This totaled to 2.3 Terabytes of data for the 1999 data set and 3.9 for the entire set.

3.6.2 Crunch

The next step was reducing the Trigger 1 data into separate data sets. This was done by a crunch, which took an analysis program and reconstructed the data. The reconstruction is discussed in depth in Chapter 4 and more details of the code can be found in [1]. The crunch divided the data into 10 separate subsections, with various amounts of overlap between them. Of interest to this thesis are only two, the 4TRACK and the 3PI0D sub-sets. The crunch as a whole required that there be two good tracks, which pointed to clusters, and came from a common vertex. Further, cuts were made to ensure that the data was good, *i.e.* that all detectors were functioning and their output was uncorrupted. If an event was to fall in the 3PI0D grouping, then it was further required to not have a 4 track vertex, both tracks had an E/P greater than 0.9, and that the clustering found 7 clusters. For the data to satisfy the 4TRACK requirements it only needed to have a good 4 track vertex, all the tracks have an $E/P > 0.9$ and the tracks matched to clusters in the calorimeter. This reduced the number of 4 track, 4 cluster events (where the $K_L \rightarrow e^+e^-e^+e^-$ events will be found) to 160000 or just over 1 Gb of data. The number of 4 track, 8 cluster events (the home of $K_L \rightarrow \pi^0\pi^0\pi^0 \rightarrow (\gamma\gamma)(e^+e^-\gamma)(e^+e^-\gamma)$ events) is 740000 or about 5 Gb. The number of events in the 3PI0D set (where the $K_L \rightarrow \pi^0\pi^0\pi_D^0 \rightarrow (\gamma\gamma)(\gamma\gamma)(e^+e^-\gamma)$ dwell) to 75 million or 495 Gb.

A similar process was done for the Trigger 3 data. The crunch basically required two good tracks with an $0.9 < E/P < 1.1$, three clusters and uncorrupted data. This resulted in a total of 2.8 million events at 170 Gb. This was a large amount of data, but it could be put on disk.

Sample	1997 # events	1999 # events	Total # events	Size Gb
2 Track, 3 Cluster	18573900	6482900	25056800	165.4
2 Track, 7 Cluster	28759100	46289700	75048800	495.3
4 Track, 4 Cluster	47778	109718	157496	1.04
4 Track, 8 Cluster	266754	474588	741342	4.89

Table 3.2: The number and size of events of interest.

Chapter 4

Event Reconstruction

Once the data has been read out, it was reconstructed and analyzed. The reconstruction took information saved at L2 and performed algorithms on it to determine particle identification, position, momentum, and energy of the decay particles and their parent. There was on average 6.5 kilobytes of data in the raw form saved. The code written to perform this task is FORTRAN code based off of routines in the KTEVANA package v6.00.

4.1 Tracking

Finding the position and momentum of tracks in the spectrometer is an important part of reconstructions. Good DC hits are used to form track segments which form track candidates, which are matched to clusters in the calorimeter. Once good tracks are found then the momentum can be calculated and the vertex found.

4.1.1 Good DC Hits

Hit reconstruction starts with looking at hits in plane pairs. The TDC values from the DC wires are converted into a distance from the wire using the $X(t)$ constants mentioned in section 2.3.3. If multiple hits occur on a wire that are in the in-time window, then only the earliest hit is used. If two wires are hit, one in the upstream plane and one in the downstream plane of a plane-pair, then they form a hit pair. If there is only one in-time wire hit, then it is referred to as an isolated single. The classification of a hit pair is based on the sum-of-distance (SOD). This is the distance of the track to one wire of the pair added to the distance to the second wire. Ideally, the SOD should

be equal to separation of the wires (*i.e.* 6.35mm). However, due to resolution effects anything with a SOD between 5.35 and 7.35mm is counted as a good SOD, see figure 4.1. Because of the large angles that can result from the bending in the analysis magnet, a good SOD can be between 4.85 and 7.85mm for DC 3X and DC 4X. Low SODs can result from multiple tracks in the same cell or from delta rays. High SODs can occur when a track passes closely to a wire and is mismeasured due to resolution. High SOD pairs are separated into a pair of isolated singles. This separation is done to reduce accidental inefficiency. Figure 4.2 illustrates the different classifications of tracks.

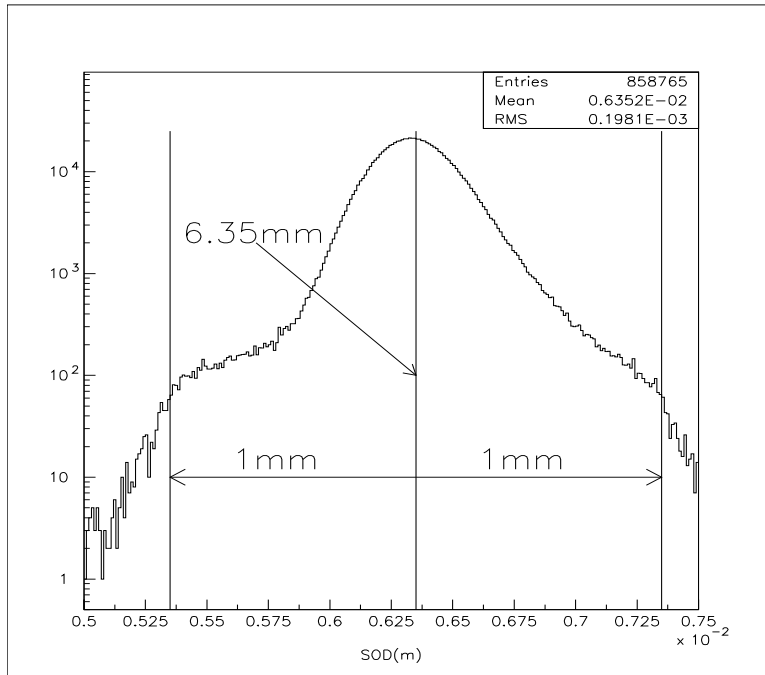


Figure 4.1: Sum of Distance. x view hits on tracks in $Ke3$ from the 1999 run period.

4.1.2 Tracks

The algorithm that finds tracks associated with hits begins by looking for y track candidates. The first step is to take all identified hits in DC 1Y and match them to hits in DC 4Y to form a line. Hits in DC 2Y and DC 3Y within 5mm of that line are then looked for. If such hits are found in all chambers then a straight line is fit to them. A χ^2 per degree-of-freedom is formed based on the distance of the hits compared to the

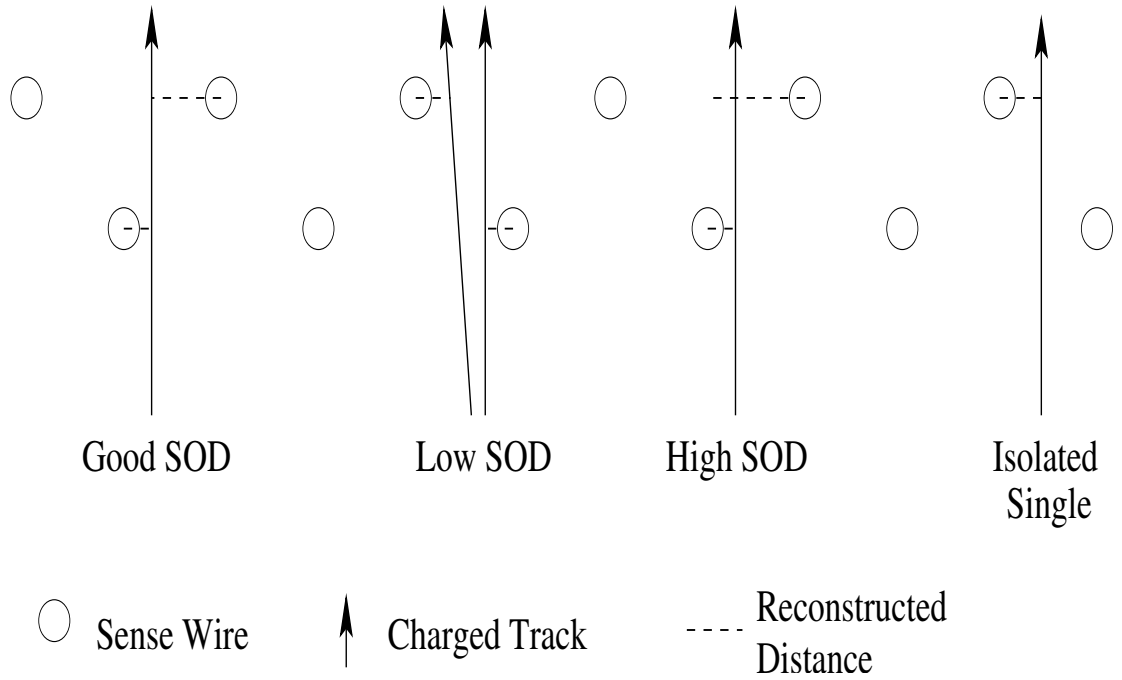


Figure 4.2: Sum of Distance scenarios.

extrapolated position of the fit line. The candidate is kept only if the χ^2 per degree-of-freedom is less than 4. The quality of hits, based on the SOD mentioned above, also determines whether or not the candidate is kept. Most of the hits must be from good SOD pairs. However, up to two hits from low SODs or one low SOD and an isolated single is allowed. If there are two or more track candidates, then they must be checked to see if they share hits. Generally they are not allowed to share any hits, however, one plane-pair can have a single shared hit in one of the two planes.

Next, x tracks are looked for. The analysis magnet bends tracks in this plane, complicating things. The first step is to look for segments upstream and downstream of the magnet. Identified hits are used in DC 1X and DC 2X to form upstream lines. Only candidates that form an angle with the z axis that is less than 100mrad are considered. The same is done for the downstream segment, except that the angle with the z axis must be less than 150mrad. All pairs of segments are extrapolated to the magnet bend plane at $z = 170.0m$ and if a given pair do not intercept the plane within 6mm of each other then they do not form a candidate x track. A similar coexistence check is made

and two exclusive x tracks are required. Figure 4.3 shows two views of the detector, a top-down view and a side view. Hits in Drift Chambers, and the best set of track candidates are seen.

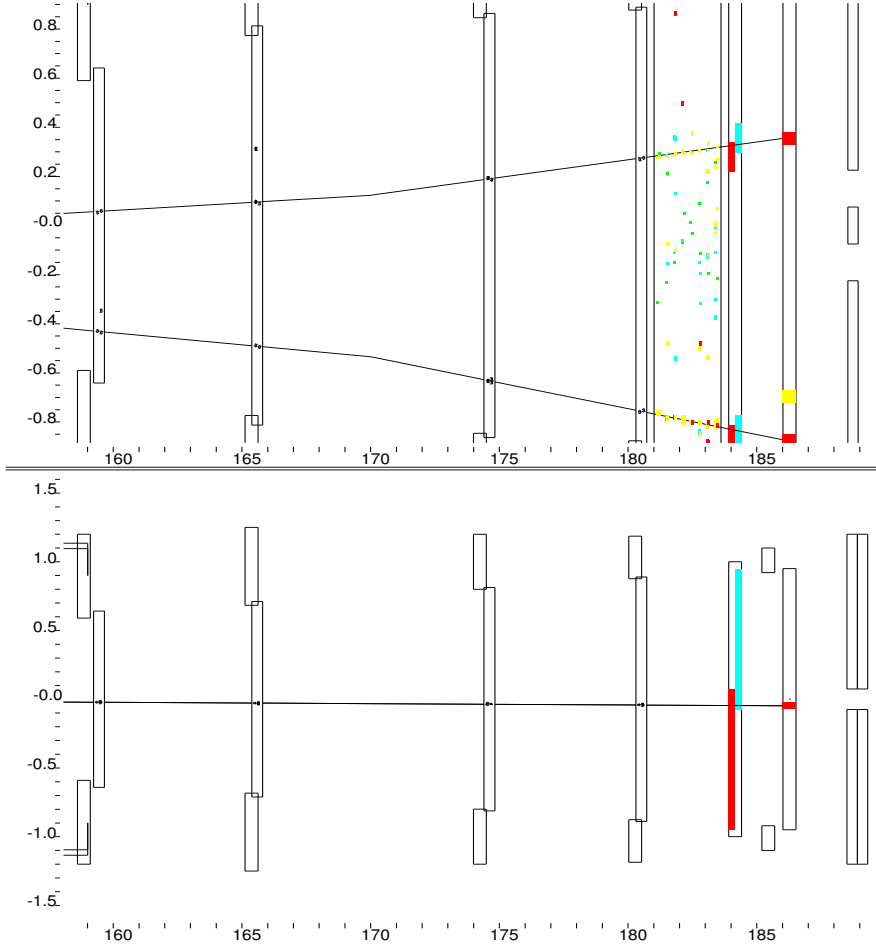


Figure 4.3: Hits in the Drift Chambers showing the Best Fit Track, the Matching Clusters, Hits in Trigger Hodoscope, and Hits in the TRDs. Top is downward looking view shown the x plane, the other showing y plane of the same event.

4.2 Clusters

An important step in the reconstruction is finding cluster positions and energies in the CsI calorimeter. This is a two step process, first the energy is found and then the position is calculated. A whole slew of corrections are included to better simulate the response of the calorimeter.

4.2.1 Energy

As mentioned in section 2.6.3, the energy of each crystal is calculated from the charge of a capacitor. The constants necessary for this transformation come out of the special runs, laser scans, and calibration jobs. The energy for a crystal is summed over 4 or 6 RF buckets, 4 in the 1997 period and 6 in the 1999. The first, or in-time, bucket corresponds to the one with the largest amount of energy seen by a crystal. Figure 4.4 shows the results of this calculation for several crystals forming a cluster.

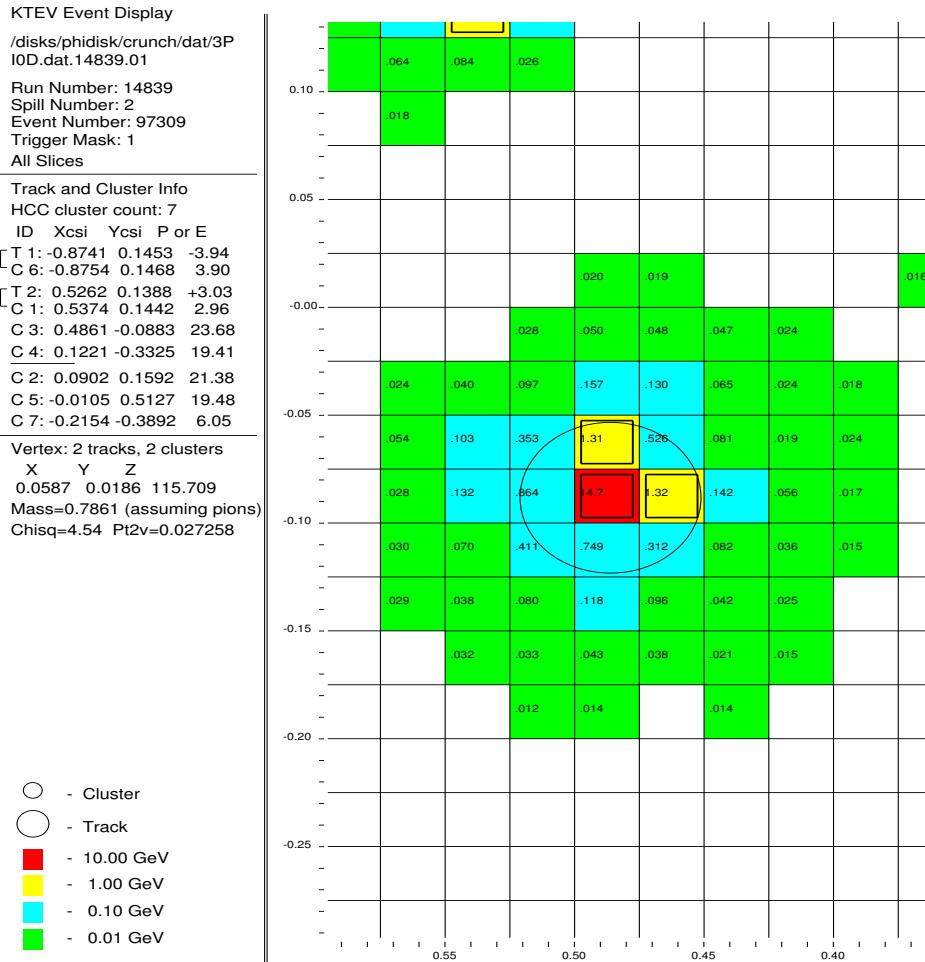


Figure 4.4: Energy of Individual Clusters. Shading indicates energy in logarithmic steps from 0.01GeV-0.1GeV, 0.1-1.0GeV, 1.0-10.0GeV and more then 10.0GeV. The bold boxes indicate that the HCC bit is on. The circles are where the reconstruction algorithm found a seed.

The next step is to find “seed” blocks, or the local maximum in energy. First, only

crystals with the HCC bit turned on are considered, the process for that is discussed in 3.3.1. The requirement of an HCC bit suppresses out-of-time clusters. Each crystal's energy is compared to the neighboring crystals. If its energy greater than all of its neighbors, it is flagged as a seed block. After the cluster seeds are found the “raw” energy is calculated by summing the energy in the crystals around the seed. Small crystals sum over an array of 7×7 crystals, large crystals sum a 3×3 array. If a cluster is on the boundary between large and small crystals, then the summing is done over an array of 3×3 large crystals but 4 small crystals are combined to make a pseudo large crystal.

Software clusters are used to identify the position of minimum ionizing particles such as muons. The particles typically leave about 320 MeV of energy in the CsI. Since these particles do not turn on any HCC bits, the software clustering algorithm looks for in-time energy over a preset threshold of about 50MeV. Hardware clusters are excluded and the software cluster only counts if the total energy of a cluster is about 100MeV. This analysis does not make use of software clusters.

4.2.2 Position

The position of a cluster is calculated by first summing the energy of different rows and columns from a 3×3 array centered on the seed crystal. Two ratios are formed for each coordinate. For example, the energy of the column of the $+x$ is divided by the energy of the seed column making R_+ and the ratio of the $-x$ column to the seed column makes R_- . The quantities R_+ and R_- are then used by a look-up table which returns a x position. The same procedure is used to find the position in y . The look-up tables are formed by using photon clusters from $K \rightarrow \pi^0 \pi^0 \rightarrow \gamma \gamma \gamma \gamma$ decays. The distribution of R_+ and R_- for these events are used to form the table and are checked with $Ke3$ decays. There are different tables for large and small crystals, and they are binned in energy bins with lower bounds of 0, 2, 4, 8, 16, and 32 GeV.

4.2.3 Corrections

Two sets of corrections are performed to adjust the energy of a cluster. The first set adjust the energy in individual crystals; the second modify the energy of whole

clusters. These corrections are necessary to account for various small effects in the calorimeter.

Overlap

An overlap correction is necessary to separate the energies of clusters that shared crystals, for example see figure 4.5. The energy of all the common crystals is divided between the clusters. Using this, new positions and energies are calculated for each cluster. This process is repeated until 20 iterations are done, or the energy and position converge.

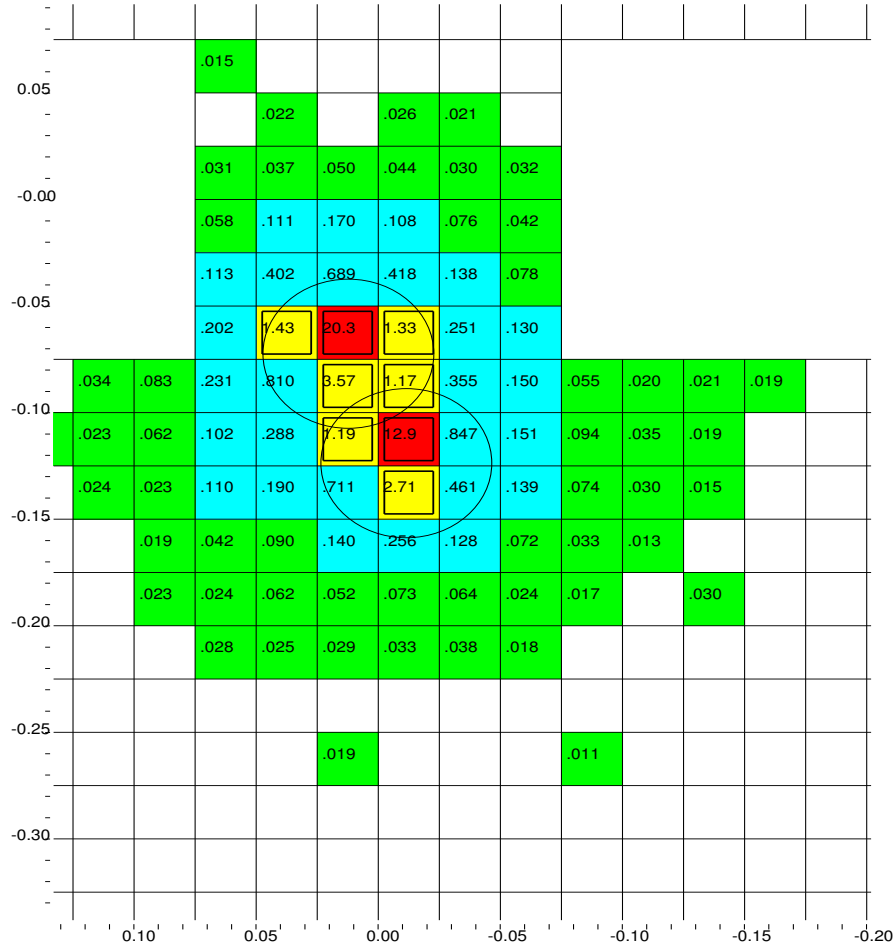


Figure 4.5: Picture of the Energy for Clusters in the CsI. These clusters overlap. Shading indicates energy in logarithmic steps from 0.01GeV-0.1GeV, 0.1-1.0GeV, 1.0-10.0GeV and more then 10.0GeV. The bold boxes indicate that the HCC bit is on. The circles are where the reconstruction algorithm found a cluster.

Neighbor

There are events where no common crystals are shared by two clusters, but energy from one cluster still invades the crystals of another cluster. As can be seen in figure 4.4, the size of a cluster can extend beyond the boundaries of the 7×7 array. If a highly energetic cluster is near a lower energy cluster, then contamination can be particularly significant. To account for this, shower shapes from a GEANT simulation are used to calculate the transverse shower profile for clusters in a 13×13 array of small blocks. The shape is then used to predict the amount of energy that could leak into neighbor cluster. This amount is subtracted off when appropriate.

Missing Block

Clusters that border the edge of the calorimeter can lose some of their energy out of the detector, *e.g.* see the top cluster in figure 4.5. Using the same transverse shower shapes as used in neighbor corrections discussed above, the missing energy is estimated and added to the cluster energy. This provides a more accurate measurement of the total energy.

Sneaky Energy

If a cluster is particularly close to the edge of the calorimeter, then the energy of a shower can cross the beam hole and infect crystals on the opposite side. This “sneaky energy” can increase the total energy of a cluster on the other side. The amount of energy that could “sneak” across is calculated by looking at $Ke3$ events with a cluster near the edge. The fraction of energy observed in a C shaped region on the opposite side of the hole from the cluster is then used as a template for correction. A library of energy deposits for the C shaped region is formed and stored to be used to calculate the level of the energy that needs to be subtracted.

Threshold

The amount of information that could be produced by the CsI is truly staggering, as there are 3100 crystals and multiple slices of information per crystal. If the energy of a crystal was below a threshold it was not read out. The output was sparsified. Some of these channels might have been on the outer edges of a cluster, so removing them shifts

the average energy of a cluster down. Special runs were made with no sparification in the CsI readout to determine the effect of this threshold cutoff. The energy correction is calculated as a function of distance from the center and the total energy of the cluster and then added back in.

Intrablock

The scintillation light produced by a particle hitting a crystal proved to be a function of the transverse position over the face. That is, the energy of a cluster varied depending on where it struck the face of the crystal. Thus, an intra-block correction is necessary. The correction is determined by dividing each crystal into 25 bins. The E/P response is then measured as a function of these bins using $Ke3$ electrons. This produced a map that is used to form a multiplicative factor to the cluster energy.

Non-linearity

A correction is necessary to remove residual variation in the longitudinal response of the crystals. This non-linearity correction is estimated by combining information from GEANT studies to actual measured longitudinal variations for each crystal. The depth of the shower depends on the energy of the incoming particle so the correction is binned in energy with lower bounds of 2, 4, 8, 16, 32, and 64 GeV.

Fudge

In a truly linear calorimeter, all the above corrections should produce a situation where the value of E/P is not a function of P . However, a very small residual variation of E/P as a function of P is still observed. This residual variation is corrected separately for large and small crystals after all other corrections had been made. This correction removes the variations in E/P as a function of P explicitly.

4.3 TRD Identification

The energy deposited by electrons on wires in the TRD is greater on average than the energy deposited by pions, as discussed previously in sections 2.4 and 3.3.5. A plot of the energy of the wires in the form of ADC counts is shown in figure 4.6(from

[1]). In this plot, the pions and electrons come from $Ke3$ decays from a limited number of runs in the Winter period. The identification of electrons are those particles with $0.95 < E/P < 1.05$ and pions have an $E/P < 0.8$.

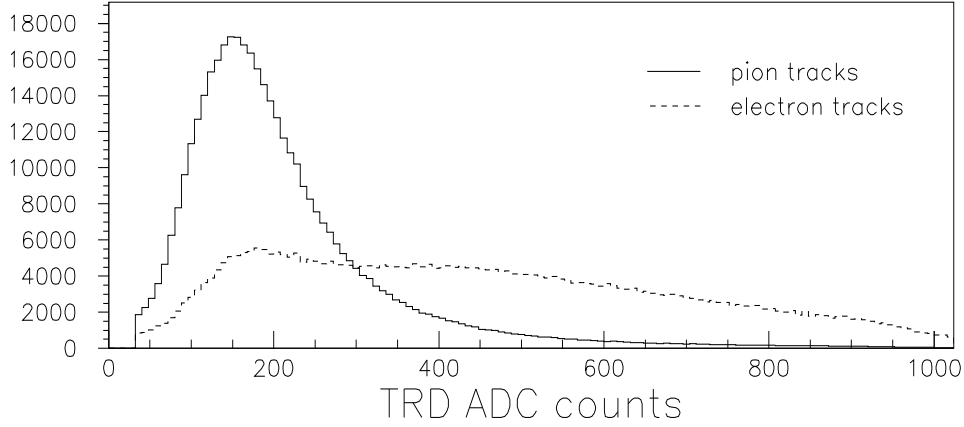


Figure 4.6: TRD ADC Values for Pions and Electrons from runs 8384, 8387, and 8397 for a Single Chamber [1].

The difference in the distributions of pions and electrons in figure 4.6 can be used to construct a confidence level that a particular ADC value, x , comes from a pion,

$$\psi(x) = \int_x^{\infty} \phi(y) dy, \quad (4.1)$$

where $\phi(x)$ is the probability of x coming from a pion. It is fairly obvious that one chamber does not provide much discriminating power between pions and electrons. However, the TRD system consists of 8 chambers or 16 wire planes, that when combined can provide much greater discrimination. The algorithm will only consider hits on a wire plane if no other tracks pass within 5mm, the track does not go through the deadened beam region, or exits the chamber. Therefore, there can be 1 to 16 wire planes with usable hits, each with a $\psi(x_i)$.

The combined TRD pion probability, Π_{TRD} , for a track with N ADC values is

$$\Pi_{TRD} = \left(\prod_{j=1}^N \psi(x_j) \right) \sum_{i=0}^N \frac{[-\ln(\prod_{j=1}^N \psi(x_j))]^i}{i!}, \quad (4.2)$$

where $\psi(x_j)$ is the confidence level for an ADC value x_j . The total Π_{TRD} is the confidence level of the hypothesis that the track was from a charged pion. Figure 4.7 shows the distribution of Π_{TRD} for the same events in figure 4.6. Saving 90% of the electrons provides rejection of pions of $276 \pm 38 : 1$. The rejection factor varied over the course of the run due to drifting voltages in the TRD chambers and calibrations but it was always better then 200:1 [47].

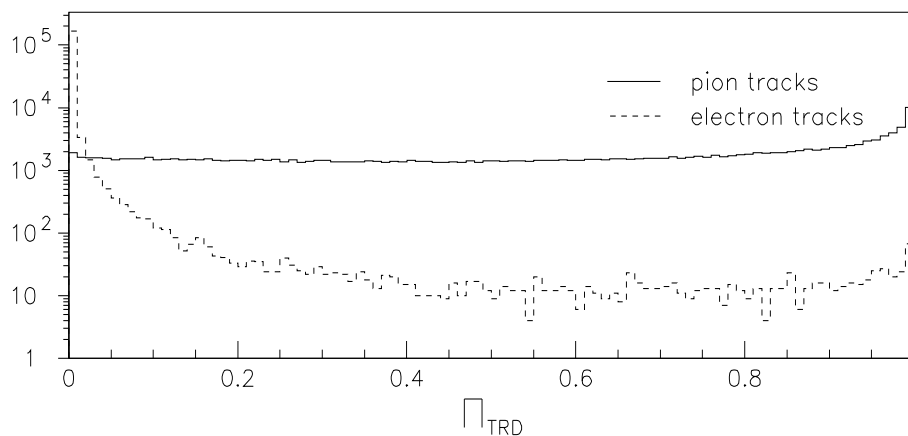


Figure 4.7: Π_{TRD} Values for Pions and Electrons from runs 8384, 8387, and 8397 [1].

4.4 Vertexing

All charged tracks should point back to a common decay vertex, marking the location at which the K_L decayed. The process for finding this vertex begins by extrapolating the track candidates found previously at 4.1.2 in the Drift Chambers. The process starts by looping over track candidates, starting with Y and going to X. The minimum z , the nominal z as determined by the average of X and Y z 's and a weight are all calculated using the values and errors of the slopes and intercepts for a track pair. The weight is equal to the difference in slopes squared and used for averaging x and y intercepts. If the z positions of the intercepts for both x and y candidates are compatible and sensible (*i.e.* $z > 0$), then a vertex candidate is formed and a new

nominal z is formed from the individual weighted z 's.

4.4.1 Track-Cluster Matching

The next step in this process is matching x and y track candidates. There is some ambiguity in this matching since the x and y views are independent, requiring the CsI calorimeter to resolve it. The cluster positions found by the clustering algorithms discussed in section 4.2 are compared to the extrapolated position of a track candidate at the CsI. If the difference between the cluster position and the extrapolated track position is less than 7cm, then the track can be matched to the cluster. This is done for all track candidates and all clusters, with the smallest difference of positions used to resolve any ambiguity. Thus, if an x and y track are matched to the same cluster then they are matched to each other. The extrapolated positions of the x and y tracks are then further required to be within 1.5cm of each other for a valid matching. Figure 4.8 shows the face of the calorimeter with two of the three clusters matched to two tracks. Tracks that point down the beam hole are not required to be matched to a cluster. Unmatched clusters are extra and will be treated as photons for the rest of the analysis.

4.4.2 Vertex Selection

A final vertex must be selected from all the vertices formed by track candidates. A figure of merit is calculated for each vertex candidate which will be used in the final determination. Before that is done, several corrections are made to track hits, much the same as what was done to the energy of clusters in section 4.2.

The first set of corrections takes into account the transit time of the signals from the wires to the discriminators. This correction uses the x and y hits from the best fit track line as input and changes the DC hit positions. Another correction is applied if a track is moving through the chamber at an angle. In that case the SOD will not be 6.35mm, so the correction is made to account for the angle. Another correction modifies the hit positions in DC 2 and DC 3 due to the fringe fields from the analysis magnet. If two tracks share a hit (*i.e.* there are three neighboring hits in the two planes of DC view), then the track with the best SOD keeps two hits and the other track only gets an isolated single.

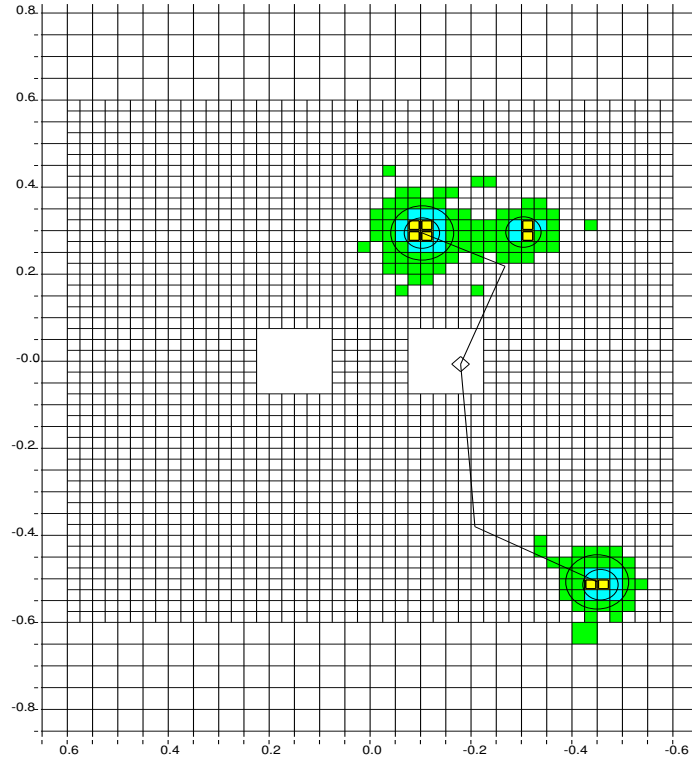


Figure 4.8: Hits in the CsI, lines show the path of the tracks in x and y projected onto the face of the CsI. The Diamond is the best fit vertex.

All these corrections are to the SODs. With them in place, the classification of hits is readdressed. Now, good SOD pairs have to be within 0.6mm of 6.35mm instead of the 1mm used in section 4.1.1. Those hit pairs with SODs outside this region are split into isolated singles, with the hit that gives the smallest difference between upstream and downstream segments being assigned to the track. This procedure is done so that tracks with delta rays can still be used.

Using the corrected positions, the current candidates are refit to track lines. This fit depends on the resolution of individual hits which vary as a function of run range and plane of wires. There is also a dependence from multiple scattering which comes into the DC resolutions. An iterative approach is used, where a vertex position from the intersection of the tracks is calculated, the average vertex position of X and Y tracks is then used to modify the slopes of the tracks. The combination of tracks is weighted by the momentum of the particle in the track (high momentum tracks have less multiple

scattering, so greater hit resolution). This iteration continues until the change of the z position of the vertex changes by less than 1mm. The process generally converges very quickly. The best vertex candidate is then chosen by taking the sum of several things. A χ^2 based on the y and x vertices, a χ^2 based the upstream and downstream segments matching at the magnet plane, and the quality of hits that make up the track (*i.e.* the number of good SOD hits) all enter into the sum. The vertex that minimizes this sum is chosen as the best vertex. Figure 4.9 shows two views of the detector, including the Drift Chambers and the decay volume. This plot shows the best fit vertex candidate and the resulting tracks, which are matched to clusters in the calorimeter.

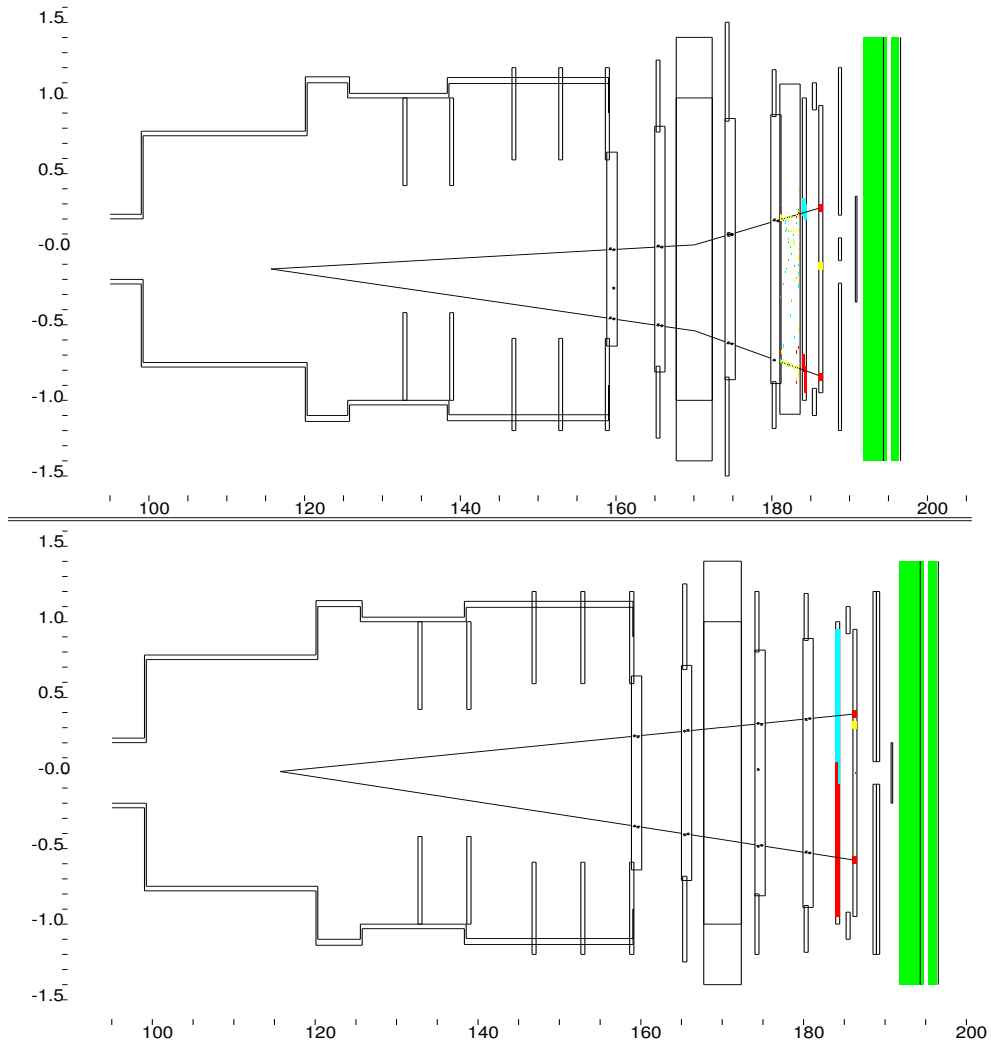


Figure 4.9: View of Hits in the Drift Chambers showing the Best Fit Track, the Matching Clusters, Hits in Trigger Hodoscope, Hits in the TRDs and the Common Vertex. Top plot is a downward looking view showing the x plane, the other plot shows y plane.

Chapter 5

Event Simulation

A crucial element in the analysis is a detailed understanding of the detector. A Monte Carlo simulation (MC) is used to generate kaons at the target and simulate the performance of the detector for various decays. The MC provides information about the acceptance of various decays modes. The acceptance is defined as the number of MC events after all cuts and simulations over the number of generated events. The acceptance for most modes is on the order of a few percent. The acceptance of background modes allows for an estimation of the level of contamination in the signal sample. The acceptance of the signal mode is essential for the calculation of branching ratios and form factors. The MC is also used to measure the level of understanding of the geometry and resolution of various detector elements. In the case of disagreements of these quantities between the MC and the data, it can be used to estimate systematic effects. Much effort was put forth to make the MC simulate the data as well as possible.

5.1 Kaon Production

The MC starts with the production of $K^0 - \bar{K}^0$ at the BeO target. The production is based off the Malensek spectrum [48]. This spectrum is based on a study with charged kaons (K^\pm), but by counting valence and sea quark contributions, an educated guess can be made for neutral kaon production,

$$\sigma(K^0) \approx \frac{\sigma(K^+) + \sigma(K^-)}{2} \quad (5.1)$$

$$\sigma(\bar{K}^0) \approx \sigma(K^-), \quad (5.2)$$

where the σ here refers to a cross section. The spectrum is parameterized by four parameters K , D , M , and A which were fit in the charged kaon data and have the form:

$$\frac{d^2N}{dP d\Omega} = KP \frac{(1-x)^A (1+5e^{-Dx})}{(1+P_t^2/M^2)^4}, \quad (5.3)$$

where P is the lab frame momentum of the produced particle, x is the ratio of P to the momentum of the protons on the target and P_t is the transverse momentum of the kaons to the momentum of the incoming protons. This predicts a mix of about 55% K^0 and 45% \bar{K}^0 . The parameters are tweaked to match the spectrum from actual $K_L \rightarrow \pi^+\pi^-$ events from KTeV.

The kaon is produced over a momentum range of 20 to 220 GeV and at an angle of 4.8mrad. It is then traced to the decay region of 90 to 160m. Figure 5.1 shows the generated momentum and decay vertex. As the kaon moves through the NM2 enclosure (see section 2.1.2) it is allowed to scatter off various elements or it is terminated if it hits something. For example the primary collimator can cause the kaon to be absorbed or scatter.

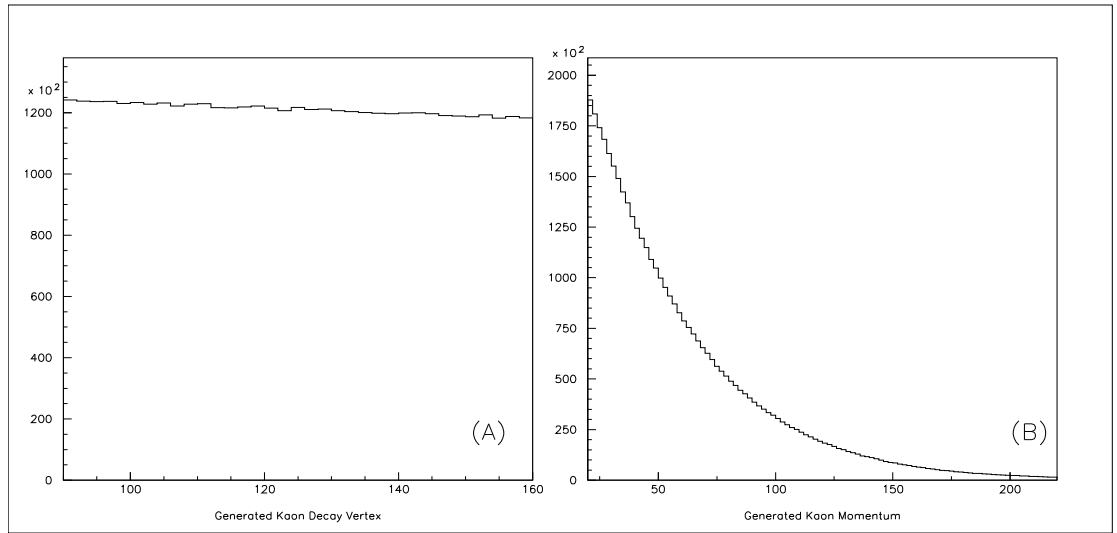


Figure 5.1: Plot A is the Decay Vertex at Generation of the Kaon. Plot B is the Generated Kaon Momentum.

5.2 Kaon Decay

Once the kaon reaches the decay region it is forced to decay. The various background, signal, and normalization modes all decay in different ways, using appropriate theories to parameterize each decay. A normalization mode is a decay that is similar to the signal mode in form, but has greater statistics. It is used to calculate the flux (the total number of K_L decays). By choosing a mode similar to the signal, it is hoped that most systematic effects cancel in the branching ratio calculation.

5.2.1 $K_L \rightarrow \gamma\gamma$ Generator

The $K_L \rightarrow \gamma\gamma$ decay is a relatively common mode, having a branching ratio of $(5.86 \pm 0.15) \times 10^{-4}$ [15]. This mode can be a source of background to both the $K_L \rightarrow e^+e^-\gamma$ and the $K_L \rightarrow e^+e^-e^+e^-$ signal modes. As the photons pass through the material in the detector, they can convert into a e^+e^- pair. The probability for conversion is about $\sim 0.3\%$ which means that the rate of $K_L \rightarrow \gamma(\gamma \rightarrow e^+e^-)$ is about 3.5×10^{-6} . This rate is within an order of magnitude of the expected branching ratio of $K_L \rightarrow e^+e^-\gamma$. Both photons convert at a rate of 5.2×10^{-9} , which is within an order of magnitude of the expected $K_L \rightarrow e^+e^-e^+e^-$ rate. So this mode is an important background for both signal modes.

The basic generator uses a two body phase space model to generate the momenta and the directions of the decay products (*i.e.* the two γ 's). Since the chance of conversions is only $\sim 0.3\%$, the amount of $K_L \rightarrow \gamma\gamma$ that would have to be generated to get a statistical sample is very large. To increase efficiency, the generator forces 1 or 2 conversions to happen with a 100% probability. The location of the conversion is a function of the radiation length of the material, thus most of the conversions happen at the vacuum window (see table 5.2). To further enhance the efficiency the conversions are confined to occur from the vacuum window up to the analysis magnet. This requirement comes from the fact that conversion events will only be reconstructed as signal if the conversion happens upstream of DC 1. Once generated, the two photons as a system are randomly rotated and boosted into the lab frame. From there the photons are traced through the detector.

5.2.2 $K_L \rightarrow e^+e^-\gamma$ Generator

As discussed in section 1.4, the MC includes all QED processes up to second order in α_{EM} . This includes one loop terms, such as those seen in figure 1.8, that interfere with the tree level diagram (figure 1.6). It also includes the radiative diagrams like that in figure 1.7. Both types of graphs are necessary in order to cancel out the divergences that arise. The loop graphs produce a negative infinity which is canceled by the infrared, positive divergence from the radiative graphs. The sum of the graphs is finite. There is a continuum of energies from the radiated photons from graphs like 1.7. A threshold in the radiated photon energy is used to set the scale of hard radiation and soft radiation. The threshold is set so that soft radiation cannot be distinguished from the non-radiative process.

The MC sets the threshold at $m_{\gamma\gamma} = 1\text{MeV}$. This results in about 27.82% of the kaon Dalitz decays produce $K_L \rightarrow e^+e^-\gamma\gamma$ instead of $K_L \rightarrow e^+e^-\gamma$. The MC also uses a form factor based on the Bergström, Massó, and Singer (BMS) model, discussed in section 1.5.2. For the generation, a value of the free parameter α_{K^*} is chosen that corresponded approximately with the measured value from KTeV for $K_L \rightarrow \mu^+\mu^-\gamma$. That is $\alpha_{K^*} = -0.16$ was used in the form factor. Figure 5.2 shows the two phase space variables that describe the system(see equation 1.13) at generation. The value of the form factor as a function of the phase space variable x and the free parameter α_{K^*} is illustrated in figure 5.3. The system of three or four particles are randomly rotated and boosted into the lab frame. The form factor can then be measured by analyzing the shape of the x distribution. However, the one loop and radiative terms also have an effect on the shape of x , as is illustrated in figure 5.4. For the analysis of the form factor, radiative corrections are included.

The mode $K_L \rightarrow e^+e^-\gamma$ can also be a source of background for $K_L \rightarrow e^+e^-e^+e^-$. As with the $K_L \rightarrow \gamma\gamma$, the photon can convert into an e^+e^- pair by interaction with the material in the detector. The rate for $K_L \rightarrow e^+e^-\gamma$ has been measured before and is $(10.0 \pm 0.05) \times 10^{-6}$ from a world average [15], combined with the conversion probability of ~ 0.3 , the rate for $K_L \rightarrow e^+e^-(\gamma \rightarrow e^+e^-)$ is then about 3×10^{-8} very close to the predicated rate for $K_L \rightarrow e^+e^-e^+e^-$. This is a major background, as it has the same final state as the signal. To generate these events with converted photons, the

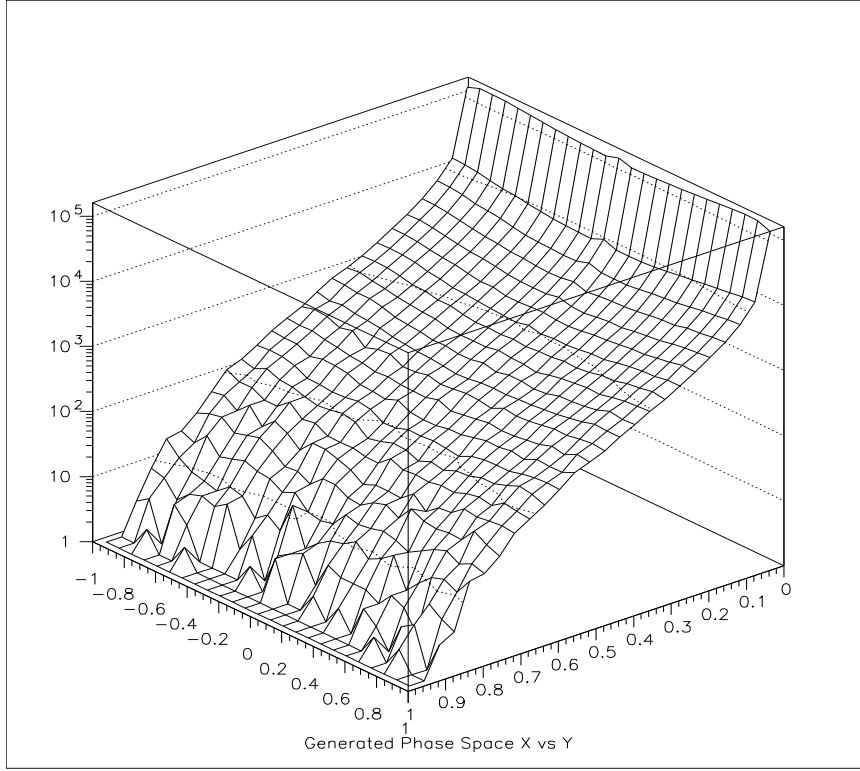


Figure 5.2: Generated Phase Space for $K_L \rightarrow e^+e^-\gamma$. X ranges from 0.0 to 1.0 and Y ranges from -1.0 to 1.0. The Z-axis is the number of events at generation.

MC forces conversion in the same manner as is described in section 5.2.1.

5.2.3 $K_L \rightarrow e^+e^-e^+e^-$ Generator

The decay $K_L \rightarrow e^+e^-e^+e^-$ is a kaon double Dalitz decay and it is discussed in section 1.4. The MC includes the QED tree level and one loop contributions. The tree level graphs (figure 1.10) are $\mathcal{O}\alpha_{EM}^2$, the loop diagrams are $\mathcal{O}\alpha_{EM}^4$ (figure 1.12), and the radiative graphs are $\mathcal{O}\alpha_{EM}^3$ (figure 1.13). Again, both the loop and radiative graphs are necessary to cancel out the divergences (*i.e.* positive and negative infinities) that arise. As for radiative terms for $K_L \rightarrow e^+e^-\gamma$, a threshold is set to make the distinction between hard and soft radiation.

The energy of the radiated photon is used as the threshold for the QED calculation, and is set at 400keV for kaons in the MC. The cutoff is closely related to a variable called $X_{4e} = m_{eeee}^2/M_K^2$, where m_{eeee} is the invariant mass formed by the four leptons.

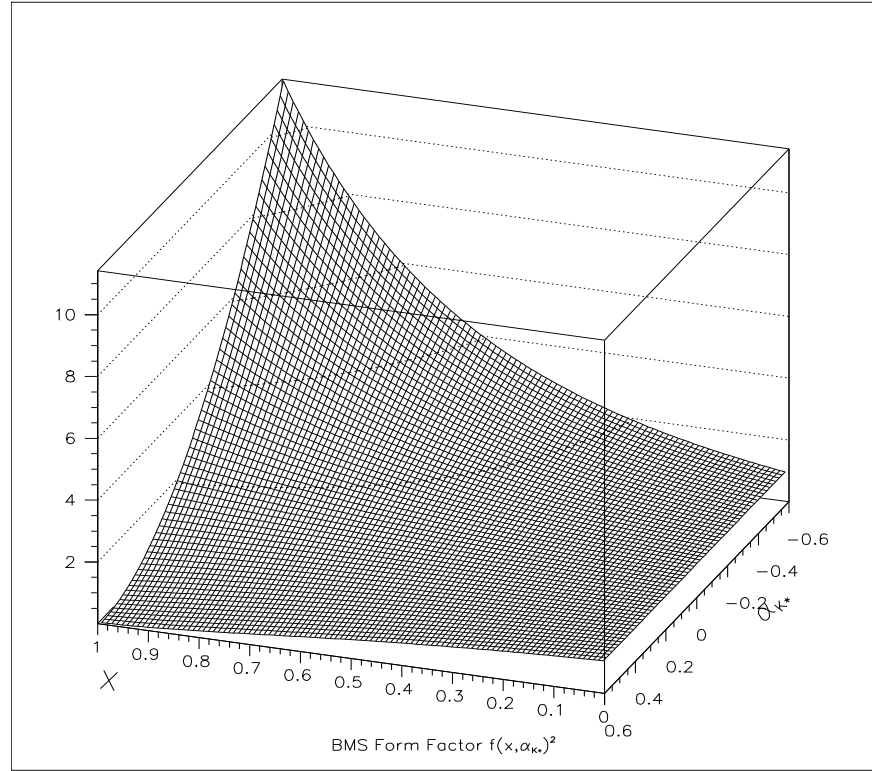


Figure 5.3: BMS form factor squared as a function of phase space variable x and the parameter α_{K^*} .

Figure 5.5 shows the variable X_{4e} at generation. This figure shows the tree level events in the peak at $X_{4e} = 1$, with a falling tail representing the radiative events with every harder radiated photons. The rise near zero is due to the diagrams like that in figure 1.13 on the right, where a lepton is internally radiating a photon than converts into an e^+e^- pair. The 400keV cutoff corresponds to an $x_{4e} = 0.9985$. Equation 1.18 defines the five phase space variables. Figures 5.6, 5.7, and 5.8 show the distribution of those variables at generation. The final state has two pairs of identical photons, so it is useful to have a prescribed way of pairing the leptons. The pairing with the minimum product of x 's is chosen with the additional requirement that $x_{11} < x_{22}$. This pairing is then used to define the y_{11} and y_{22} and ϕ . The plots actually show $\cos(\theta_{11})$ and $\cos(\theta_{22})$ which are related to the y 's as follows:

$$y_{11} = \lambda(1, x_{+1}, x_{-1}) \cos(\theta_{11}) \quad (5.4)$$

$$y_{22} = \lambda(1, x_{+2}, x_{-2}) \cos(\theta_{22}), \quad (5.5)$$

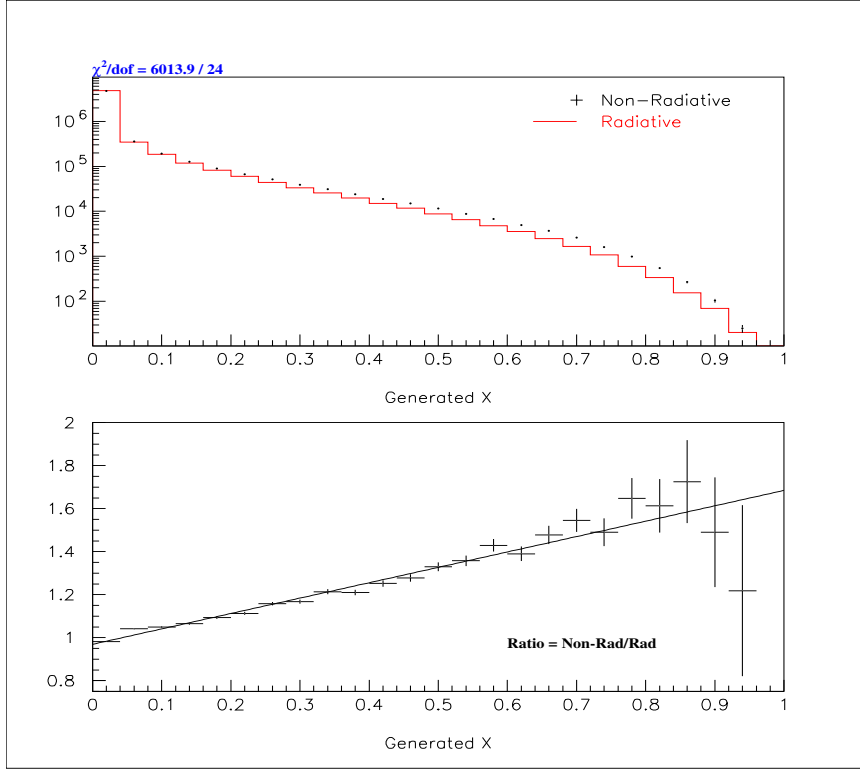


Figure 5.4: Generated Phase Space. Comparing x for Tree Level graphs to Tree Level plus One Loop and Radiative Graphs.

where $x_{+1} = m_{e^+}^2/m_{e_1^+e_1^-}^2$, $x_{-1} = m_{e^-}^2/m_{e_1^+e_1^-}^2$, $x_{+2} = m_{e^+}^2/m_{e_2^+e_2^-}^2$, $x_{-2} = m_{e^-}^2/m_{e_2^+e_2^-}^2$, and $\lambda(1, x_{+1}, x_{-1})$ is the same function as is defined in equation 1.16. Equations 1.18 - 1.23 also refer to the phase space variables. With the above pairing, x_{+1} would be the positron with momentum p_1 (see figure 1.10), $x_{-1} \rightarrow p_2$, $x_{+2} \rightarrow p_3$, and $x_{-2} \rightarrow p_4$.

In addition to the QED process, there is a form factor included at generation. The D'Ambrosio, Isidori and Portolés model is used (see section 1.5.3). There are two parameters in the model, and they have been set to reasonable values, $\alpha_{DIP} = -1.0$ and $\beta_{DIP} = +1.0$. Figures 5.9 and 5.10 show the effect of having different values of α_{DIP} and β_{DIP} in the form factor. As in the $K_L \rightarrow e^+e^-\gamma$ the radiative and one loop terms alter the shape of the phase space variables. Figure 5.11 and 5.12 compare the variables that are affected by the addition of higher-order terms.

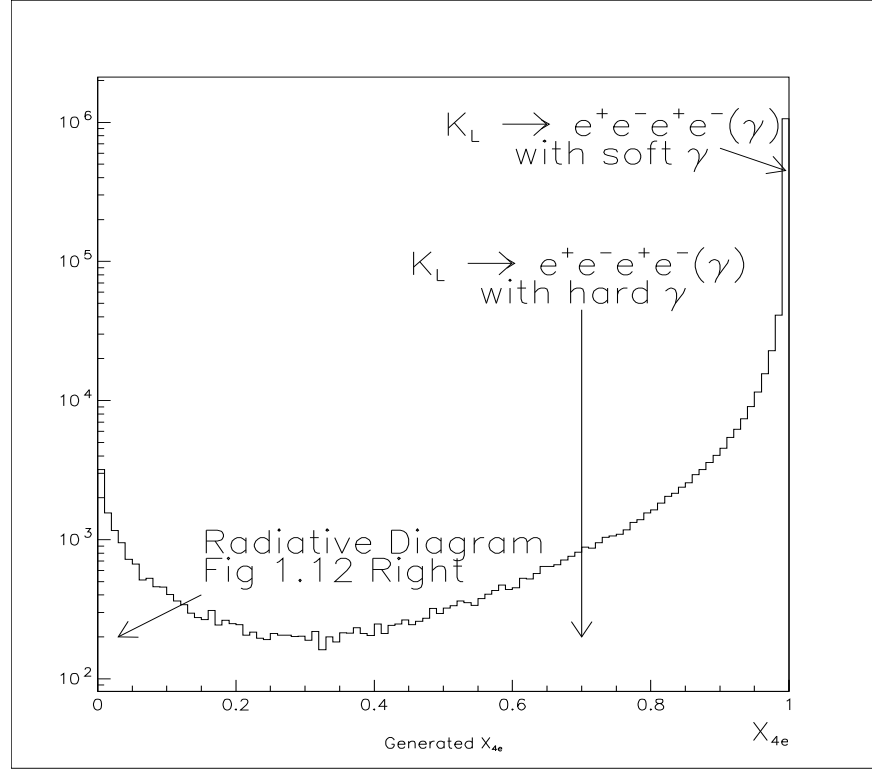


Figure 5.5: $X_{4e} = m_{eeee}^2/M_K^2$ for $K_L \rightarrow e^+e^-e^+e^-$.

5.2.4 $K_L \rightarrow \pi^0\pi^0\pi^0$, $K_L \rightarrow \pi^0\pi^0\pi_D^0$ and $K_L \rightarrow \pi^0\pi_D^0\pi_D^0$ Generator

The decays $K_L \rightarrow \pi^0\pi^0\pi_D^0$ and $K_L \rightarrow \pi^0\pi_D^0\pi_D^0$ are used as normalization modes in the calculations of the branching ratios for $K_L \rightarrow e^+e^-\gamma$ and $K_L \rightarrow e^+e^-e^+e^-$. These decays are nearly the same. Both start with the decay of $K_L \rightarrow \pi^0\pi^0\pi^0$. The generation of this decay is based off of a flat 3 body phase space. Immediately after the π^0 has been generated, it is forced to decay.

The decay of $K_L \rightarrow \pi^0\pi^0\pi_D^0$ has two of the π^0 going into the $\gamma\gamma$ final state and last π^0 undergoing a Dalitz decay (*i.e.* $\pi^0 \rightarrow e^+e^-\gamma$), the basic process is illustrated in figure 5.13. The $\pi^0 \rightarrow \gamma\gamma$ decay uses a simple two body phase space. The $\pi_D^0 \rightarrow e^+e^-\gamma$ uses the same method as the $K_L \rightarrow e^+e^-\gamma$ decay, following QED. Feynman diagrams just like those in figures 1.6, 1.8, and 1.7 are used with the K_L being replaced by a π^0 . As with the kaon the one loop and radiative graphs are included. The radiated photon has a threshold set at $M_{\gamma\gamma} = 1\text{MeV}$. This results in 16.18% of the π^0 Dalitz

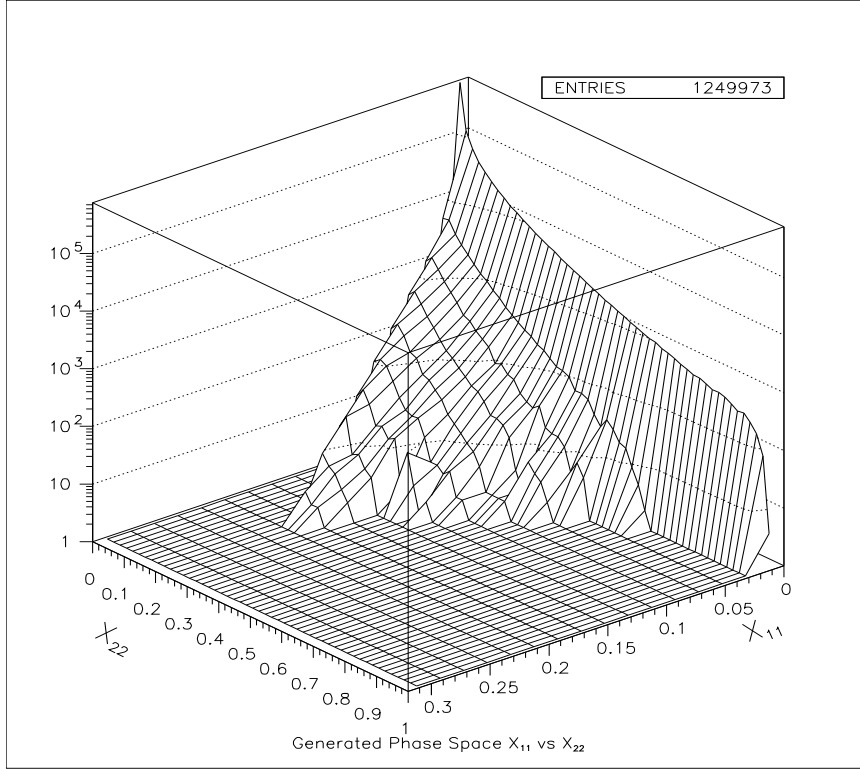


Figure 5.6: X_{11} versus X_{22} Phase Space Variables for $K_L \rightarrow e^+e^-e^+e^-$ at Generation.

decays having a radiated photon. The Dalitz decay also contains a form factor term

$$f(x) = 1 + a \cdot x, \quad (5.6)$$

where $x = m_{ee}^2/M_{\pi^0}^2$ and a is a constant. The value of a was taken from the world average [15] and is 0.032.

The decay of $K_L \rightarrow \pi^0\pi_D^0\pi_D^0$ has two of the π^0 undergoing Dalitz decays and the remaining π^0 going to $\gamma\gamma$, as is illustrated in figure 5.14. The pion decays are identical to those described above. The branching ratios for these two decays can be calculated using the world averages [15] of the component decays and any combinatoric factors. The world average branching ratios are listed in table 5.1 and the formula for calculating the branching ratios is given by 5.7 and 5.8. Finally, all the decay products as a system are randomly rotated and boosted into the lab frame.

$$BR(K_L \rightarrow \pi^0\pi_D^0\pi_D^0) = 3 \cdot BR(K_L \rightarrow \pi^0\pi_D^0\pi_D^0) \cdot BR(\pi^0 \rightarrow e^+e^-\gamma) \cdot BR(\pi^0 \rightarrow \gamma\gamma) \quad (5.7)$$

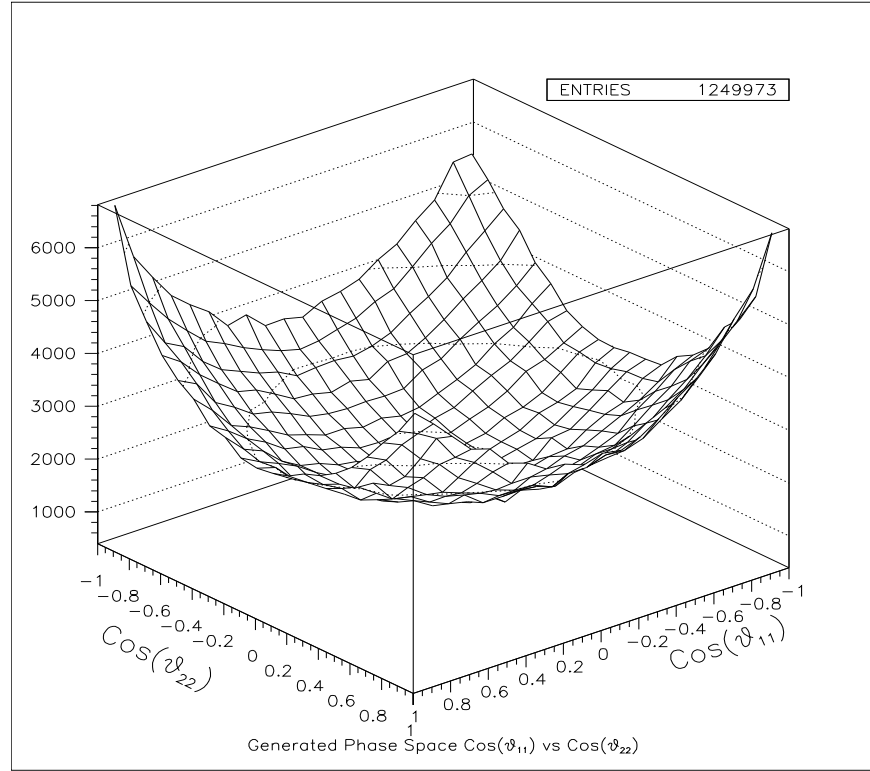


Figure 5.7: $\cos(\theta_{11})$ versus $\cos(\theta_{22})$ Phase Space Variables for $K_L \rightarrow e^+e^-e^+e^-$ at Generation.

Decay	Branching Ratio [15]
$K_L \rightarrow \pi^0\pi^0\pi^0$	0.2113 ± 0.0027
$\pi^0 \rightarrow \gamma\gamma$	0.98798 ± 0.00032
$\pi^0 \rightarrow e^+e^-\gamma$	0.01198 ± 0.00032

Table 5.1: Independently Measured Branching Ratios for π^0 and K_L Decays of Interest.

$$= (7.41 \pm 0.22) \times 10^{-3}$$

$$\begin{aligned}
 BR(K_L \rightarrow \pi^0\pi_D^0\pi_D^0) &= 3 \cdot BR(K_L \rightarrow \pi^0\pi^0\pi^0) \cdot BR(\pi^0 \rightarrow e^+e^-\gamma)^2 \cdot BR(\pi^0 \rightarrow \gamma\gamma) \\
 &= (8.99 \pm 0.49) \times 10^{-5}
 \end{aligned}$$

5.3 Particle Tracing

Once the kaon has decayed, the products of the decay are traced through the remaining parts of the detector. From here they are traced in bins of z through

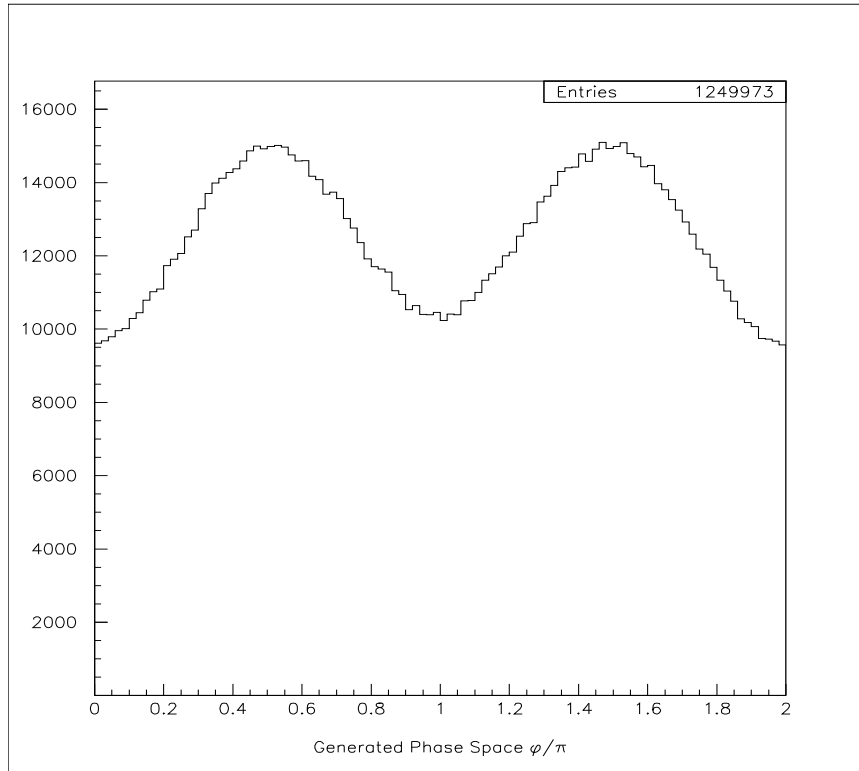


Figure 5.8: ϕ/π Phase Space Variable for $K_L \rightarrow e^+e^-e^+e^-$ at Generation.

the detector. If a particle leaves the detector, it is no longer traced and considered lost. As the particle progresses it can undergo multiple scattering for charged particles, bremsstrahlung if it is a lepton or charged pion, or conversion into e^+e^- if it is a photon. The tracing ends when the particle reaches the CsI (for photons, electrons and some pions) or possibly the HA. If the particle is a muon it passes all the way through without stopping. As it passes through each of the elements of the detector a response is simulated, adding in resolution and subtler effects.

5.3.1 Decay Product Interaction with Material

The MC divides the detector into several chunks, each chunk representing an amount of material with which a particle can interact. At each section, the MC checks to see what, if anything happened to the particle. All of these interactions are based on the amount, density and type of the material in question. The experiment was designed to minimize the amount of material that needed to be passed through by each

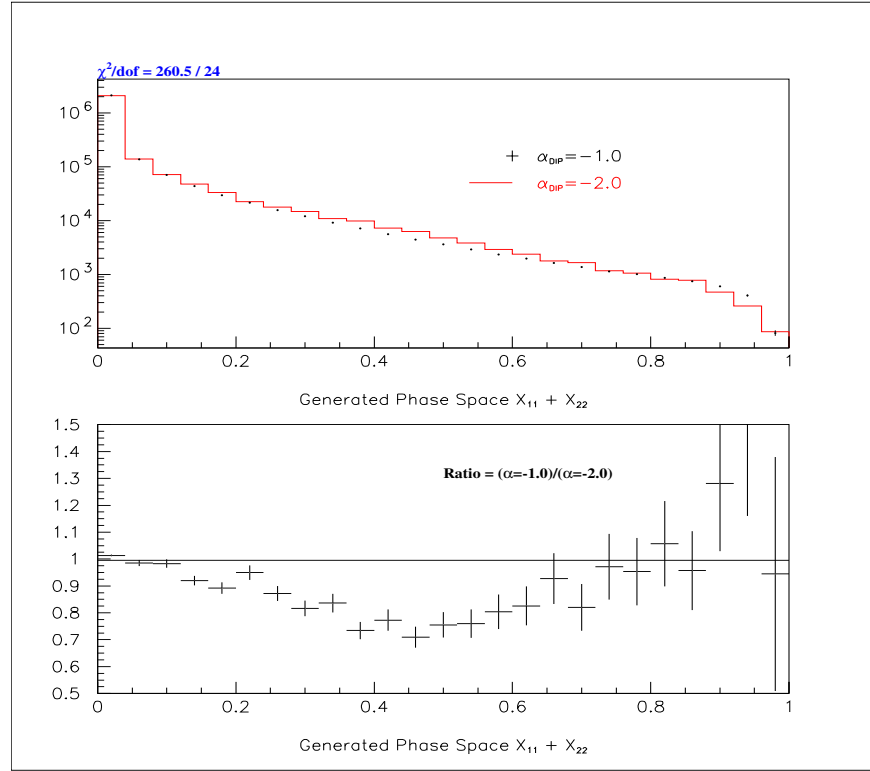


Figure 5.9: $x_{11} + x_{22}$ comparing Two Values of α_{DIP} at Generation. β_{DIP} is set to +1.0 for both sets.

decay product (thus, Helium bags were placed throughout the spectrometer). However, physical detectors dictate that some material be present.

Material Calculations

The material upstream of the analysis magnet is of the most interest. After the magnet, a photon conversion will not form a track and the electrons will be close enough together to form only one cluster, bremsstrahlung photons will land directly on top of the electron cluster that spawned them, etc. These events will usually reconstruct as if they had never been altered. However, upstream of the magnet, things are different. There is enough time for some separation to occur, plus, the magnet can create even more separation. If a $K_L \rightarrow \gamma\gamma$ has one of the photons convert at the vacuum window, then it can mimic a $K_L \rightarrow e^+e^-\gamma$ decay. The $K_L \rightarrow e^+e^-\gamma$ analysis in particular is sensitive to the upstream material. Diagram 5.15 is a zoomed view of the upstream

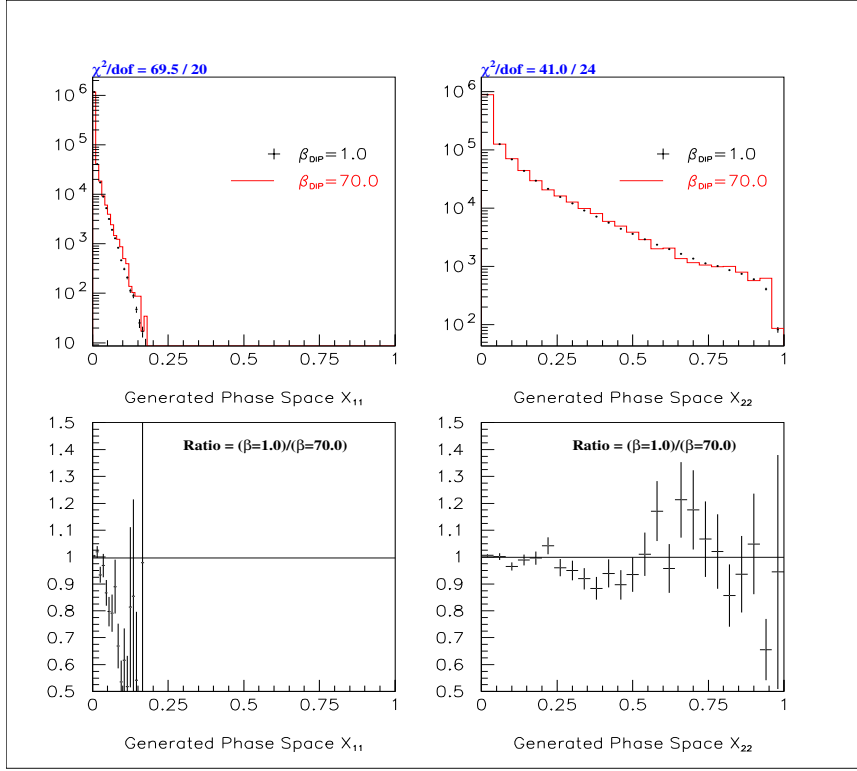


Figure 5.10: x_{11} and x_{22} comparing Two Values of β_{DIP} during Generation. α_{DIP} is set to -1.0 for both sets.

component of the detector. It shows the vacuum window, helium bags and the drift chamber. Helium bag 1b, the mylar chamber windows and the chamber gas plus wires are referred to as “DC1U”.

A special run at the very end of the 1997 period was performed to calculate the amount of material upstream of the magnet [49]. This run looked at $K_L \rightarrow 3\pi^0$ decays reconstructing them using only the calorimeter. If the conversion of a photon occurred then it would leave very close tracks (*i.e.* one measurable track). By counting the number of tracks over the total number of reconstructed decays a conversion probability could be found. One of the things discovered by this run was that the conversion probability was higher than estimated based on the putative amount of material, and was indeed consistent with the hypothesis that Helium Bag 1a was full of air. This study was more than adequate for most analyses, but not for $K_L \rightarrow e^+e^-\gamma$. Another study is necessary and is described in full in appendix B. In essence it looks at the

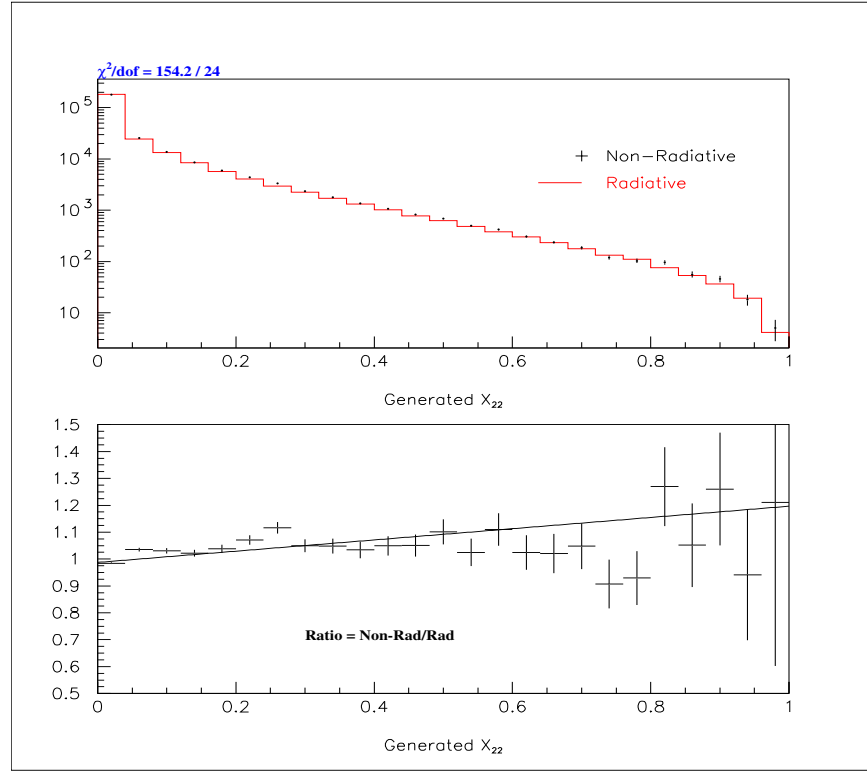


Figure 5.11: $x_{11} + x_{22}$ Comparing Tree Level graphs to Tree Level plus One Loop and Radiative Graphs.

difference in the vertex z positions formed by the x and y upstream track segments. The result of this study is that the bags were not full of air for the full run, but that they slowly filled with air as a function of time. In 1999 this bag was replaced and filled with helium. Table 5.2 lists the amount of material that is important to these analyses. The numbers for the wire include the probability of hitting a field wire or a sense wire (0.7% and 9.9% respectively). A particle actually hitting a wire has a very high chance of interacting compared to everything else.

Multiple Scattering

Every charged particle that passes through matter is scattered via Coulombic interactions with nuclei. In the MC, the particles direction is altered by an angle θ rotated randomly around the original direction. The angle θ is generated by using a Gaussian with a width of θ_0 and a mean of 0, where θ_0 is given by the Molière distribution

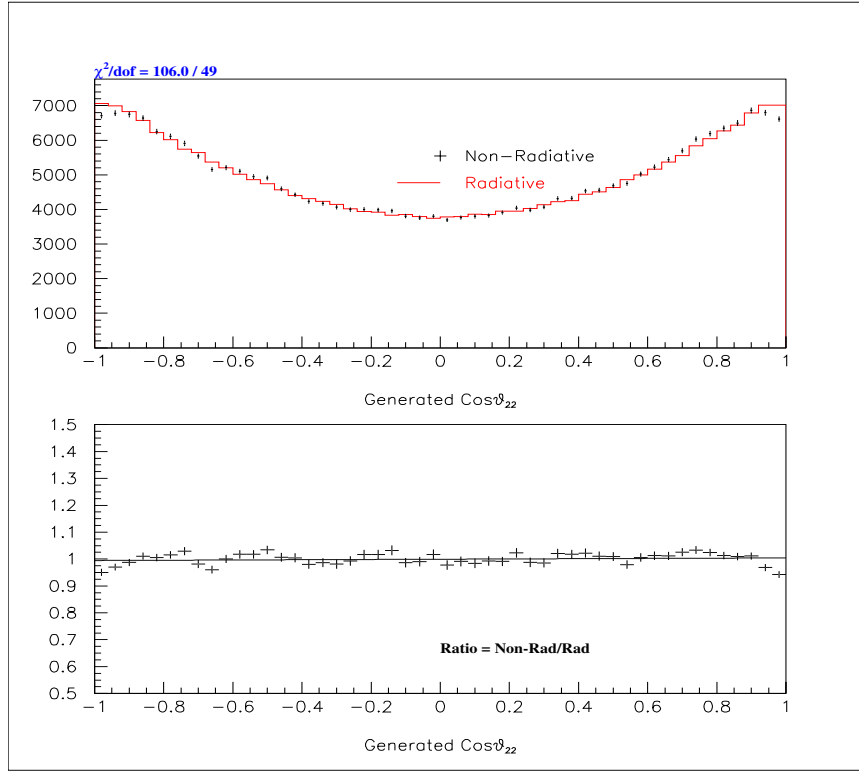


Figure 5.12: $\cos(\theta_{11}) + \cos(\theta_{22})$ Comparing Tree Level graphs to Tree Level plus One Loop and Radiative Graphs.

Detector Element	Composition	Radiation Length X/X_0
Vacuum Window	kevlar, mylar	0.00156
Helium Bag 1a 1997	mylar, air	0.00107
Helium Bag 1a 1999	mylar, helium	0.00074
“DC1U”	mostly mylar	0.00050
DC field wire	aluminum	0.00089
DC field wire	gold	0.00062
DC sense wire	tungsten	0.00570
Helium Bag 2	helium	0.00162
TRD Chamber	(Sect. 2.4)	0.01760
TRD Beam Hole	(Sect. 2.4)	0.00510

Table 5.2: Material in the Upstream segment of the detector. X is the path length of the material and X_0 is the characteristic radiation length of the material.

[15]:

$$\theta_0 = \frac{13.6\text{MeV}}{\beta cp} Z \sqrt{\frac{X}{X_0}} \left[1 + 0.038 \ln \left(\frac{X}{X_0} \right) \right], \quad (5.9)$$

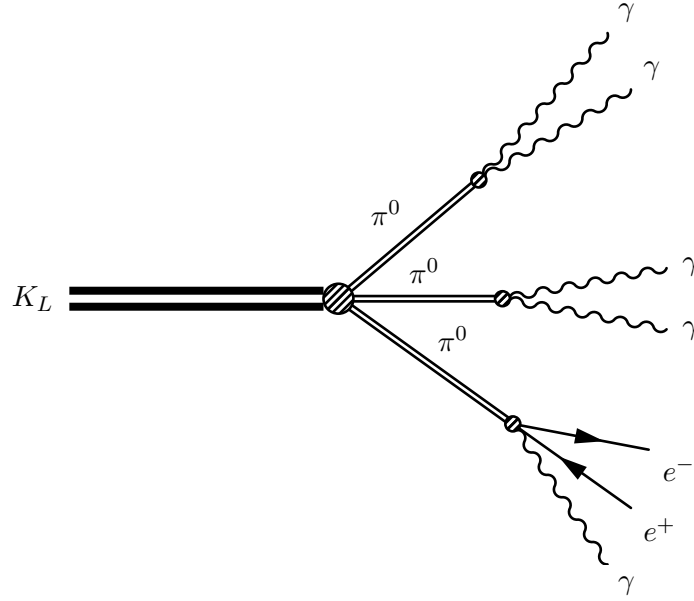


Figure 5.13: Feynman Diagrams for Three π^0 Single Dalitz decay, $K_L \rightarrow \pi^0 \pi^0 \pi_D^0 \rightarrow (\gamma\gamma)(\gamma\gamma)(e^+e^-\gamma)$.

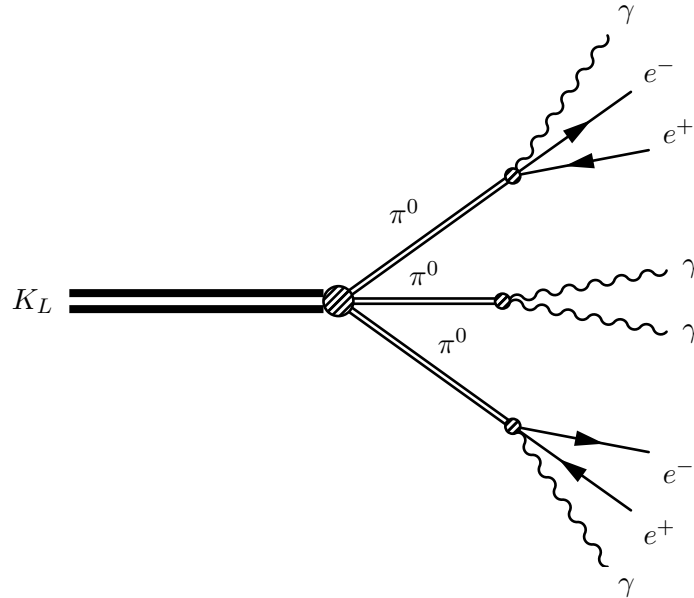


Figure 5.14: Feynman Diagrams for Three π^0 Double Single Dalitz decay, $K_L \rightarrow \pi_D^0 \pi^0 \pi_D^0 \rightarrow (e^+e^-\gamma)(\gamma\gamma)(e^+e^-\gamma)$.

where p is the momentum, βc is the velocity, and Z is the charge of the scattered

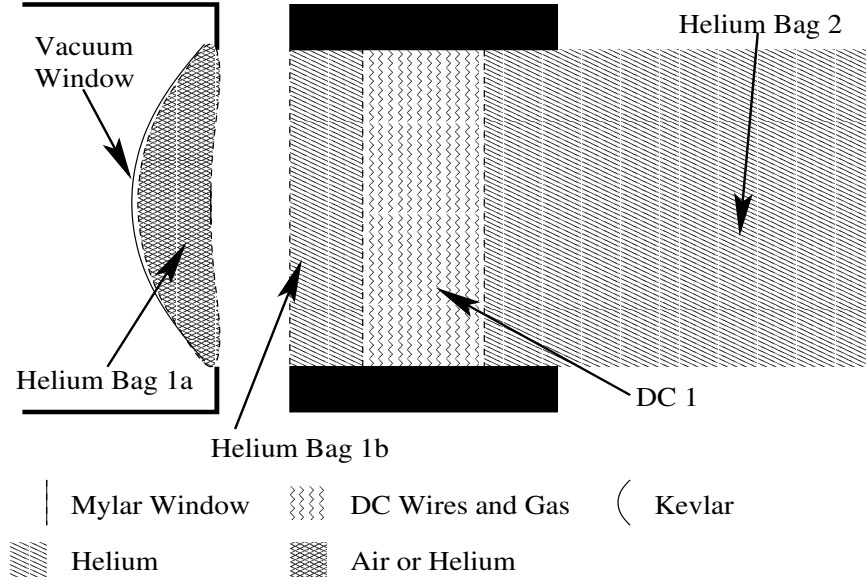


Figure 5.15: Picture of the Upstream Detector Elements showing the Vacuum Window, Helium Bags, and DC 1.

particle.

Photon Conversion

Each photon in a decay can convert into an electron-positron pair as it interacts with matter. In the MC, any photon over a 100 MeV is given a chance to convert as it passes through a detector. The probability of conversion is given by:

$$P(\gamma \rightarrow e^+e^-) = 1 - e^{-\frac{7}{9}\frac{X}{X_0}}. \quad (5.10)$$

The z position of a conversion was determined randomly with a flat spectrum within a volume (*i.e.* a subsection of the detector). The distribution of the energy between the electron and positron is given by the Bethe-Heitler spectrum:

$$P(E_{e^+}, E_{e^-}) \sim \left(\frac{E_{e^+}}{E_\gamma}\right)^2 + \left(\frac{E_{e^-}}{E_\gamma}\right)^2 + \left(\frac{2}{3} - \frac{1}{9Z}\right) \frac{E_{e^+}E_{e^-}}{E_\gamma^2}, \quad (5.11)$$

where E_{e^\pm} is the energy of the electron/positron, E_γ is the energy of the parent photon and Z is constant equal to 3.74059. The products of the decay have the same direction as the photon offset by a small angle given by the EGS4 code [50]. This angle is a function of the photon's energy, the energy of the e^\pm , and the composition of the

material that spawned the conversion. Lastly, the plane of the pair is rotated randomly around the direction of the photon. The probability of a single conversion from the upstream material is $\sim 0.24\%$.

Bremsstrahlung

Electrons and positrons are allowed to radiate bremsstrahlung photons as they pass through material. By assuming that the incoming particle is ultra-relativistic and that the Born approximation holds, then the probability of a photon emission is given by

$$P_{k>k_0} = \frac{X}{X_0} \frac{1}{(18\zeta + 1)} \left[2(12\zeta + 1) \left(\frac{k_0}{E_0} - \ln \left(\frac{k_0}{E_0} \right) - 1 \right) + 9\zeta \left(1 - \left(\frac{k_0}{E_0} \right)^2 \right) \right], \quad (5.12)$$

where k is the momentum of the photon, k_0 is a threshold momentum, E is the final energy of the electron, E_0 is the initial energy of the electron, and X/X_0 is the radiation length of the material. The term ζ is equal to $\ln(183/Z_{eff}^{1/3})$, where Z_{eff} is the effective Atomic number [1]. The threshold momentum, k_0 is set to $0.001E_0$ for the MC. Table 5.3 gives the Z_{eff} and probabilities for various components of the detector.

The MC does not apply this correction everywhere. In order to save on computer computation time, bremsstrahlung is applied only to those detector elements upstream of the analysis magnet and where the $E_\gamma > 1.5\text{GeV}$. The first requirement is made so that there is enough separation of the photon and electron that they can form distinct clusters in the calorimeter. The second requirement is made so that the photon cluster will have a chance of triggering the HCC. Assuming these conditions, then the spectrum of momentum for the photon is given by

$$\frac{d\sigma}{dk} = 4\alpha_{EM} Z^2 r_0^2 \frac{1}{k} \left[\left(1 + \left(\frac{E}{E_0} \right)^2 - \frac{2}{3} \frac{E}{E_0} \right) \zeta + \frac{1}{9} \frac{E}{E_0} \right], \quad (5.13)$$

where $r_0^2 = e^2/m_e c^2$ is the classic electron radius and Z is the atomic number.

δ Rays

When charged particles pass through a gas, electrons from molecules of the gas can be knocked free, creating a delta ray (δ ray). The electrons typically leave at high angles from the direction of the charged track, and can be energetic enough to leave a

Detector	Z_{eff}	Probability
Vacuum Window	5.556	0.01313
Helium Bag 1a 1997	7.799	0.00825
Helium Bag 1a 1999	7.799	0.00587
“DC1U”	5.737	0.00421
DC field wire(Al)	13.501	0.00745
DC field wire(Au)	79.555	0.00518
DC sense wire	74.554	0.04804
Helium Bag 2	2.452	0.01364

Table 5.3: Probability of bremsstrahlung for upstream detector elements.

secondary ionization trail, producing its own hit information in the spectrometer. The MC simulates the production of delta rays by producing them with a probability

$$P_{T>T_0} = (15400\text{keVcm}^3/\text{gram}) \frac{Z}{AE} \rho d \quad (5.14)$$

where T is the energy of the δ ray, T_0 is a cut-off energy, Z is the Atomic Number, A is the Atomic Weight, ρ is the density of the source material, d is the distance traveled in source material, and E is the energy of the incoming track. The source material is assumed to be Argon ($Z = 18$, $A = 39.9$, and $\rho = 1.66\text{gram/liter}$). If a δ ray is produced, its direction is perpendicular to the incoming track, the energy is chosen to conform to a T^{-2} spectrum as is suggested in [15] and the electron is allowed to travel only one cell. The transverse momentum imparted to the parent track is assumed to be small enough to be ignored.

5.3.2 Detector Simulation

Each detector element had it’s own peculiarities when it came to simulating the response to particles. An overview of the techniques used in the MC are discussed below.

Photon Vetoes

If a particle is traced to the physical space occupied by any of the photon vetoes (*i.e.* the RCs, SAs, CIA, CA or BA see sections 2.2.1, 2.3.4 and 2.6.4) then it is terminated. If the particle is a photon or electron then it deposits its energy in the detector, smeared by a Gaussian based on the resolution of that detector. These

resolutions were determined by a calibration [42] from special runs.

Spectrometer

The MC simulates each of the 16 planes of the charged spectrometer individually for all of the charged decay products. The first step is to find the closest wire and the distance of closest approach from the charged particle. This distance is smeared by a gaussian with the measured hit resolution as the sigma. The hit resolution is a function of plane and time period. Additional smearing is added for tracks depending on their position in the plane (*i.e.* within the region which the neutral beam passes or further away). An inefficiency due to discriminator response is also simulated, causing any additional hit within 45ns of a previous hits to be lost. Discrete ionization of the gas causes a small amount of hit position smearing.

The smeared distances are used to create a sum-of-distance (SOD, see section 4.1.1) and are converted into TDC values. By inverting the $X(t)$ function, discussed in section 2.3.3, a TDC count is created. The propagation time is also added, the $T0$ discussed in 2.3.3. A small additional amount of time can be added to simulate the additional high side tail in the SOD distribution. Finally, a small amount of time is added if the particle is heavier than an electron to account for a difference seen in the data from $Ke3$ events. Finally if a delta ray is produced then it is allowed to interfere with creation of other hits, as it would in the data, creating a low side tail on the SOD distribution and hit inefficiencies from hitting the wire within 45ns of the primary hit. A transverse kick is applied in the x direction from the analysis magnet as the particle passes through 170.0m in the z direction.

DC Inefficiency Maps

After the DC hit simulations some low level discrepancy between remains the data and the MC. In particular, the simulated hit positions show that the MC efficiency for reconstructing hits in the beam region (defined as the area where the neutral beam passes through spectrometer) is greater than the data efficiency, see left two plots in 5.16. An attempt to fix this is made by the creation of so-called DC inefficiency maps. These maps are created by using $Ke3$ events in the data to look for missing hits in a specific plane. Tracks were reconstructed using information from all of the DC planes

except one (*e.g.* 1X') and then looking to see how often a hit is seen on the test plane corresponding to the predicted position. The ratio of the number of tracks with missing hits over the number of tracks with good hits is the isolated single inefficiency (*i.e.* missing hit). The inefficiency is calculated for each wire and in bins of position along the wire. Near the beam region the position along the wire was divided into 1cm segments, growing into larger segments as the statistics dwindled. A similar process is followed, but instead of looking for missing hits, hits with high SODs are counted. Figure 5.17 shows the maps that are determined for the 1997 data set. It is evident from this figure that there were “spots” of very high isolated single inefficiencies, caused by defects in the wire. It is also evident that there was a higher chance of having high SODs formed by tracks passing through the beam regions of the DC. This is attributed to radiation damage on the wires. An effort was made before the 1999 running to clean chamber wires and enhance the gain of the electronics in order to reduce these inefficiencies. Figure 5.18 shows the results of this effort. The high SOD inefficiency was greatly reduced, but the inefficiency from missing hits is not greatly affected. The maps are produced for electrons and pions separately and are allowed to change as a function of time. No noticeable difference is seen between electrons and pions for the maps. The effect of these maps can be seen by comparing the right hand plots in figure 5.16 to the left hand plots. The MC used for this analysis increased the size of the inefficiency maps such that the illumination was flat. A systematic uncertainty was assigned that corresponded to the difference between using the nominal maps compared to the maps that gave a flat distribution.

Trigger Hodoscope

Charged particles traced to the trigger hodoscope and photons that convert there, interact with the detector. An inefficiency based on calibration data is simulated. If the particle is traced to a crack in between paddles, again no hit is simulated. The position of the particle determines which paddle is hit as well as the scintillation light propagation time. There is a small chance that pions will shower as they interact with VV' , this affect is not simulated, but is not of consequence to this analysis.

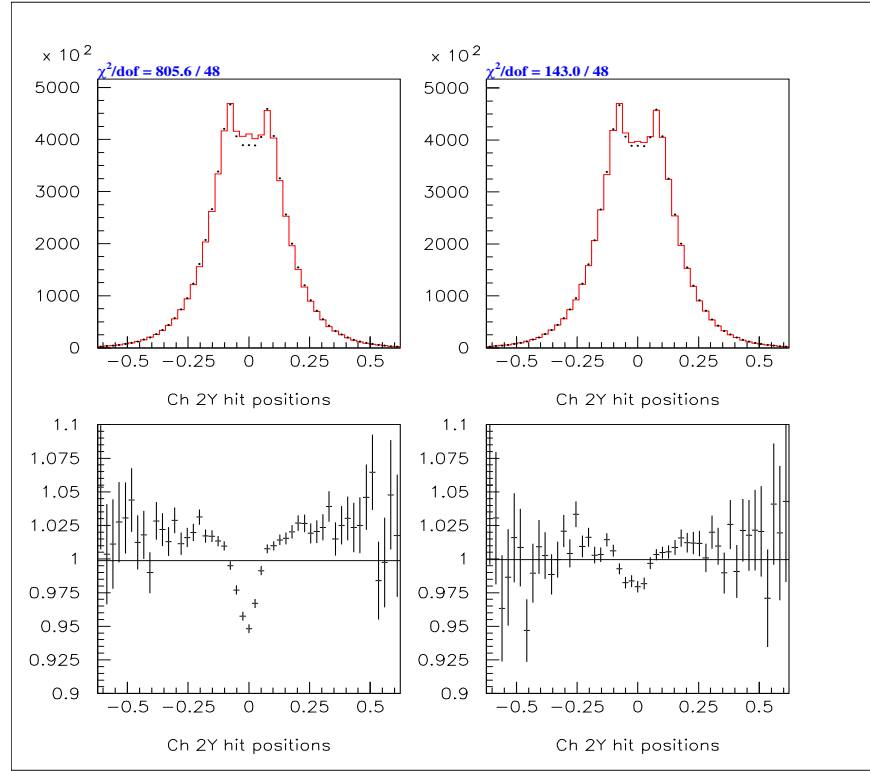


Figure 5.16: Comparison of Data (Dots) to MC (Histogram) DC 2Y Hit Positions in the DC for $K_L \rightarrow \pi^0 \pi^0 \pi_D^0$ Charged Tracks. The plots on the left use a MC without a DC Map, the right with the DC Map. The top plot of the pair is Data, MC overlay, the bottom is a ratio.

Calorimeter

Electrons and photons that are traced to the face of the calorimeter are terminated. The MC response of the CsI begins with a shower simulation. The mean depth of shower maximum is found to be different for γ and e^\pm ,

$$z_{e^\pm} = 0.11 + 0.18 \ln E_{e^\pm} \quad (5.15)$$

$$z_\gamma = 0.12 + 0.18 \ln E_\gamma, \quad (5.16)$$

where z is the mean position in meters and E is the energy in GeV. A shower library created from the GEANT simulation package is consulted. The library is binned in energy (with upper bounds of 2, 4, 8, 16, 32 and 64 GeV) and in x and y position at the mean z . Each shower spans an array of 32.5×32.5 cm, or an array of 13×13 small crystals. The showers themselves are also segmented into 25 bins in mean z . This

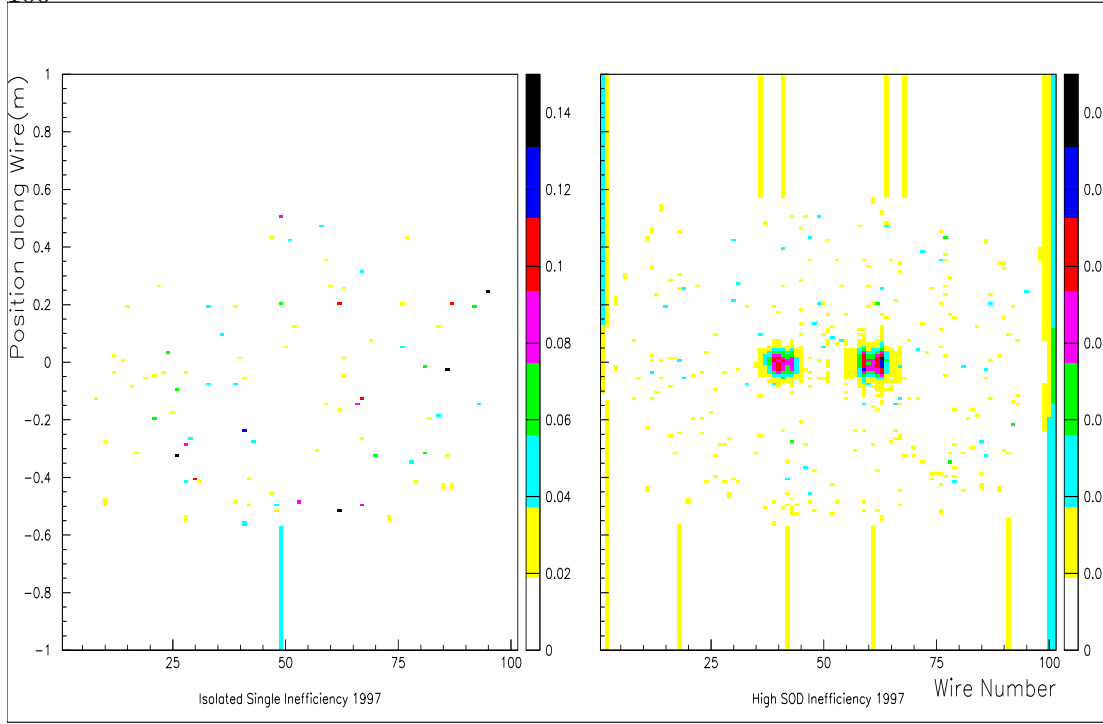


Figure 5.17: Map of the Single Hit and High SOD Inefficiency for DC 1X from the 1997 data set. Vertical axis is a position along the wire, horizontal axis is the wire number.

allows them to be scaled to match the longitudinal responses measured in the individual crystals.

The deposited energy is smeared to match the resolutions found in the data. This means that the smearing is a function of time, large versus small crystals, and position in the entire calorimeter. This smeared energy is used to select a shower. The shower is then scaled to match the energy of the incoming particle. Now, each crystal has a base amount of energy. If the shower is near the edge of the calorimeter and it extends beyond the boundaries of the crystals, then some energy is lost. If the shower is near a beam hole then some energy is allowed to sneak across the beam hole using the special library described above. Finally, some energy is subtracted to simulate a low-energy tail observed in electron E/P distributions. If there are multiple particles interacting in the calorimeter, then energy combined for crystals hit by multiple showers. A shower can deposit energy even beyond the edge of a 13×13 array, so crystals can get a small amount of extra energy from far-away clusters. This is simulated by extending the

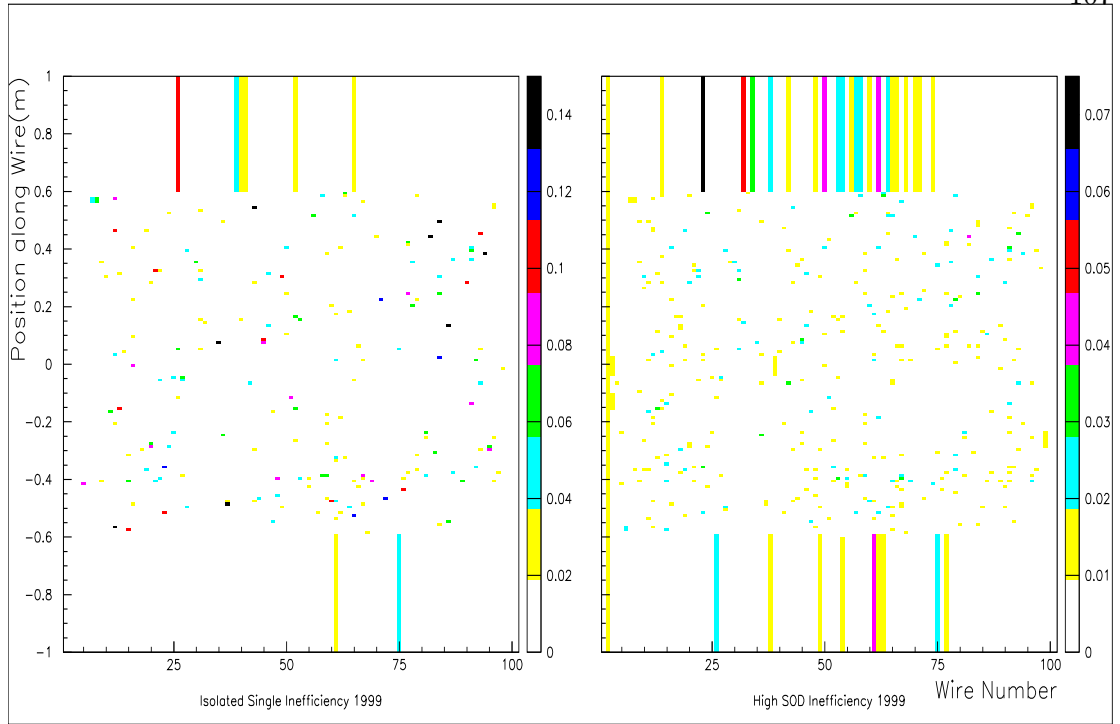


Figure 5.18: Map of the isolated single and high SOD Inefficiency for DC 1X from the 1999 data set. Vertical axis is a position along the wire, horizontal axis is the wire number.

13×13 to a 27×27 using an exponential transverse function. This summing of energy in a crystal from multiple showers is not performed if there is already a sneaky energy correction.

Pions are handled only a little differently than the electrons and photons. A GEANT simulation created a shower library for pions. The shower is considerably larger in size: 41×41 small crystals or 102.5×102.5 cm in size. However, the process of handling and selecting the shower is the same as for electromagnetically showering particles. Pions only hadronically shower about $\sim 70\%$ of the time, the rest of the time they are treated as Minimum Ionizing Particles (MIPs), where they leave only 320 MeV in the calorimeter. Muons are also minimum ionizing and the deposit energy according to the Bethe-Bloch distribution [46].

Electronics

The goal of the MC is to produce a data format that is as much like the real data

as possible. Therefore, all of the information is digitized and the hardware is simulated. The energy deposited in a photon veto is compared to a threshold energy, and if it is greater, then a L1 source bit is set that corresponds to the detector. The trigger hodoscopes, as previously mentioned, turn on source bits if there is enough in-time scintillation light. The TDC times calculated for the spectrometer are digitized as they were in the data and create DC-OR signals.

The Kumquat signals are created by taking the DC TDC values, comparing them to the in-time window of the Kumquats and using the same hit-counting algorithm as was discussed before. The Bananas also use the DC TDC times. Because the Banana count is different from the TDC count, it must be converted. Then the counts are used to look for in time pairs as described above. Again, once valid hits are found, the same hit counting is done. As is mentioned in [1], the Banana in-time window is larger than the DC TDC in-time window. That means that the trigger accepts more events than the MC would simulate. However, the Trigger requirements are loose enough that this should not be a problem.

The energy in each crystal of the calorimeter is determined, and is then converted to a simulated charge. This is the exact opposite of what is done in 4.2.1. The charge is spread out over several time slices using pulse shapes measured from the data. A smearing is added to reflect photostatistical effects seen in the data. The DPMT logic is then simulated and used. The same threshold for readout was applied to the MC. The E-Total system (see section 3.2.3) is simulated by measuring the thresholds from *Ke3* data. Radiation damage caused these thresholds to shift as a function of time, so measuring from the data is necessary. A simulation of the HCC logic is then used and the L2 source bits can be calculated. More information on the finding of the thresholds can be found in [46].

5.4 Accidental Overlays

One very important thing has been left out so far. The events so far are “clean”. There is no simulation of electronic noise in the various detector elements, no cosmic rays or various other junk. A special trigger was in place that took on-spill data which would include this accidental activity. Every event that is generated had one of these

accidentals overlayed on top of it. This could produce extra energy in a photon veto, or extra hits in the spectrometer or even additional energy in the calorimeter. Thus, it is crucial that the accidental activity be included before the trigger simulation, which is what was done. It should be noted that these accidental events could include real tracks and clusters as well as noise.

As is mentioned in section 2.1.1, a special trigger was in place that recorded off-spill information. This trigger somewhat randomly took a snap-shot of the detector with beam. The information at that moment was recorded into a data file. Each file corresponds to a separate run. These files are identical in format to a standard data file. A separate Multiple Run (MRN) file contains the location of each of these accidental files and the fraction of generated events that should correspond to each of these runs. The fraction was determined by looking at a run-by-run flux analysis using $K_L \rightarrow \pi^0 \pi^0 \pi_D^0$ events.

The format of these accidental events is not ideal. First the files were written out in a time ordered fashion. This is a problem if the number of generated events is smaller than the number of accidental events. A condition that occurred later in the run might not be simulated. Second, the accidental rate was not necessarily the same as the kaon rate. Thus, each accidental file was processed in such a way as to eliminate these problems.

A random prescale factor, r_i was applied to each file, where

$$r_i = \frac{A_{max}}{N_{max}} \frac{N_i}{A_i}. \quad (5.17)$$

Here A_i is the number of accidentals recorded for run i and N_i is the flux of that run (the same as the number used for the MRN file). A_{max} is the run with largest number of accidentals recorded and N_{max} is the flux for that run. This makes the ratio of A/N be a constant for each run. To account for the second problem the events were written out in a round-robin fashion to 10 separate files. This made a set of 10 small, time-ordered files. The number of generated events was forced to correspond to a number that would use each file an integer number of times.

The MRN file not only provided the number events generated for each run, but also the run number that is used to determine which constants are used in the simulation

(as most detectors had a time dependence in their performance). It also provided the spill number.

5.5 Trigger

The output of all this is a data format that is identical to the real data. DC TDC information, L1 source bit, trigger bits, etc. are included. That means that the same reconstruction code (*e.g.* the L3 code) can be run on the MC without any changes.

The hardware trigger logic conditions are applied in an identical manner on the MC. L1 sources are turned on, HCC clusters are counted, and the spectrometer hits are counted. The MC then can figure out if conditions are met to turn on various trigger bits, in an identical manner to those discussed in Chapter 3. After this, the identical code used for the L3 Trigger is run on the MC data. The code is the same, and the constants used are those used while the data is being taken.

Chapter 6

General Event Selection

This thesis deals with reconstruction and study of events from four different decay modes. The modes in question come from two different triggers and have anywhere from three to eight final state particles consisting of electrons and photons. Despite these differences, there are still a number of selection criteria that are common to all the modes. This includes things like selection of good runs, cuts on the fiducial volume of the detector, cuts to verify the trigger, and identification of particles.

6.1 Bad Spills

An effort is made to eliminate runs in which there are major problems with a detector element. However, a component can fail while a run was ongoing. This could mean that the first 4 hours or so of a run were of good quality, but the last few minutes (or spills) had problems. Sometimes a problem would exist for most of a run, but wouldn't be noticed. It is wasteful to throw out an entire run if only a part of it had problems. Therefore, a database exists that contains information on the failures of various detector elements as a function of time (measure in spills and run number). This is accomplished by carefully combing through the log books and by early analysis of the data.

A mask can be formed where various bits represent particular problems with the detector. If the database of bad spills indicates a problem, then it can be compared to the mask and the event thrown out if there is a match. It is set up in this way, because not all analyses are sensitive to all types of failures. For example, the Transition Radiation Detectors are not used in the analysis of $K_L \rightarrow e^+e^-e^+e^-$, so failures in those detectors

need not be considered. Table 6.1 lists the various bits and if they were used in each analysis.

Bit	Problem	$K_L \rightarrow e^+e^-e^+e^-$ On?	$K_L \rightarrow e^+e^-\gamma$ On?
1	Trigger	Yes	Yes
2	DPMT Pedestal Exponent > 0	Yes	Yes
3	Bad DPMT Capacitor	Winter Only	Winter Only
4	Blown QIE Comparator	Yes	Yes
5	Misc. Dead DPMT	Yes	Yes
6	DPMT Pedestal Drift	No	No
7	DPMT Gain Drift	Yes	Yes
8	Broken DPMT Dynode	Yes	Yes
9	CsI Pipeline Problems	Yes	Yes
10	Global CsI Problems	Yes	Yes
11	E-Total Trigger Problems	Yes	Yes
12	FERA ADC	Yes	Yes
13	Drift Chamber	Yes	Yes
14	Photon Veto	Yes	Yes
15	Trigger Hodoscope	Yes	Yes
16	Muon Veto/Counter	runs < 8577	runs < 8577
17	HCC Trigger	runs > 8245	runs > 8245
18	Hit Counting Problems	Yes	Yes
19	TRD Trigger	No	No
20	Hyperon Trigger	No	No
21	DAQ/L3	Yes [†]	Yes [†]
22	non-799 run(<i>i.e.</i> Special Run)	Yes	Yes
23	Short Run	Yes	Yes
24	Non-Standard TRD Voltage	No	No
25	1 Dead TRD Plane	No	No
26	>1 Dead TRD Plane	No	Only in 1997
27	TRD Voltage Sag	No	No
28	Severe TRD Problem	No	Only in 1997
29	Beam Problem	Yes	Yes
30	unused	No	No
31	unused	No	No
32	Miscellaneous	No	No

Table 6.1: Bad Spill Summary. [†] refers to the cutting only on certain CPUs for this bit.

There are some interesting features in table 6.1, a brief explanation follows. Trigger 3 used the TRD trigger, so one would expect to cut on bit 19, however, this bit was never set. Therefore, not using it is of no consequence. The muon vetoes were only used in the early part of the Winter running, so problems with the muon detector system can be safely ignored after that. The problems with the HCC for runs 8088 to 8245

were eventually understood to be the result of a swapped cable. The effects of this are simulated in the MC for those runs. As well, the summer DPMT Capacitor problems were figured out and are simulated in the MC. A dead TRD plane is not a severe problem because of the redundancy of the system. However, more than one dead plane was a severe problem. In the 1999 data-taking period a strange problem, whose source was never discovered, caused the calorimeter information to become corrupted during the L3 processing. This corruption is isolated to certain Level 3 CPUs, so instead of cutting out all events when this problem occurred, a routine exists that cuts out events only in the affected spills and on the affected CPUs. The TRDs are not used in the 1999 analysis of $K_L \rightarrow e^+e^-\gamma$ as they are not in the 1999 trigger (see 3.3.5). Figure 6.1 shows the distribution of bits for $K_L \rightarrow \pi^0\pi^0\pi_D^0$ events after the crunch stage. The bad spill bits most often set in 1997 came from bit 24, bit 3, bit 25, and bit 17. Bits 24 and 25 are not used in any analysis. Most of bit 3 comes from the runs 8088 to 8245, where it is not actually cut on, so only $\sim 5\%$ of that bin is cut out. Similarly bit 17 comes mainly from the Summer period and only $\sim 13\%$ of the bin is thrown out. Thus, the majority of the event are cut due to bit 26 followed by bit 2. In the 1999 period the majority of events were lost due to bit 21, but cutting out only the problematic CPUs reduces most of these problems.

Further studies revealed runs with bad spills that are not in the bad spill database. These studies resulted in only a minor loss of events and are not included above. Table 6.2 lists the runs and spills that are cut in addition to the bad spill cuts above. When all of these cuts are applied an idea of how many events are lost after the crunch can be gotten. Looking at $K_L \rightarrow \pi^0\pi^0\pi_D^0$ events after the crunch, the removal of the bad spills results in a reduction of $\sim 3.3\%$ of the events for the 1997 data and $\sim 2.7\%$ in the 1999 data, or a total of $\sim 2.9\%$ loss. This loss does not include entire runs that were thrown out for various reasons.

Run	Spills	Problems
8428	0-148	CA High Voltage is off
8453	120-200	Large CsI Gain Drift
10599	55-end	Stuck DPMT mantissa
10790	245-end	E-Total Controller Failure

Table 6.2: Additional Bad Spills and Reasons.

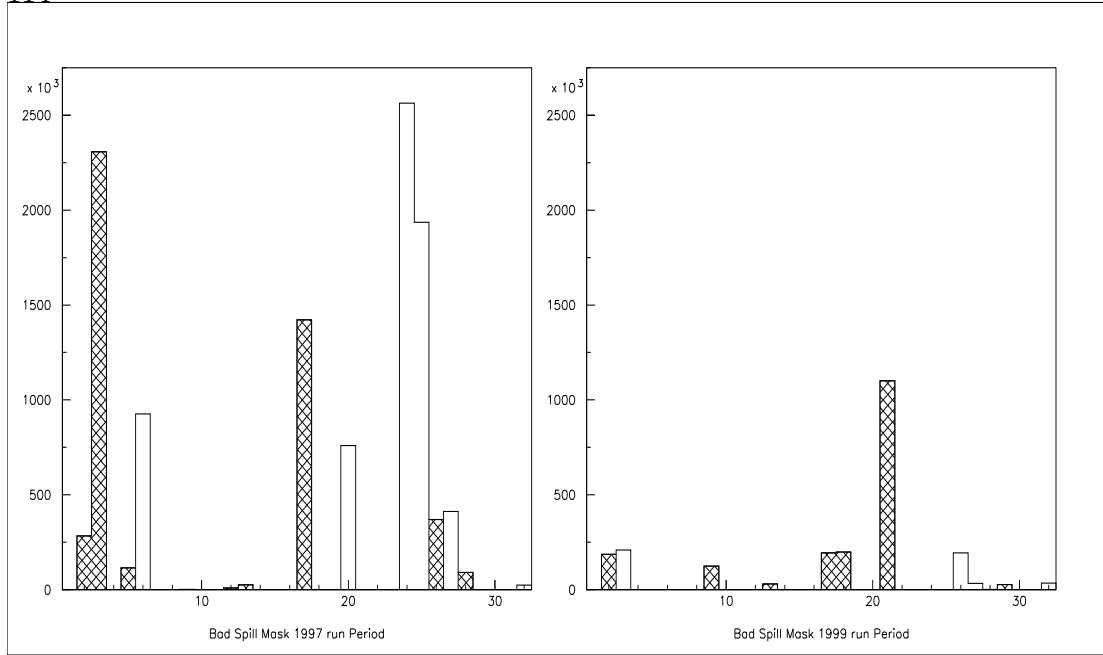


Figure 6.1: Bad Spill Bits for $K_L \rightarrow \pi^0 \pi^0 \pi_D^0$ Events. The cross hatched bins are ones in which that bit is cut on most of the time, open boxes are bits not used.

6.2 Fiducial Region

Cuts are made on the momentum of the kaon and the decay vertex in z . These cuts are made in order to be well removed from the edges of the MC generated distribution, see figure 5.1. The momentum cut is also made to be well removed from the edge caused by the E-Total threshold discussed in section 3.2.3. The cut on Kaon momentum is made between 40.0 and 200.0 GeV. The low end cut is made to be well above the E-Total threshold of 25GeV.

Reconstruction of the vertex z position using the Spectrometer is discussed section 4.4.2. A cut is made from 95.0m to 157.0m (94.0m to 158.0m for $K_L \rightarrow e^+ e^- e^+ e^-$ and $K_L \rightarrow \pi^0 \pi_D^0 \pi_D^0$) in order include the decay region, be well away from the vacuum window and the final sweeper magnet.

Both normalization modes include $\pi^0 \rightarrow \gamma\gamma$ decays. These decays can be used to calculate a neutral vertex position. To calculate a position using information just from the calorimeter, one needs the positions and energies of the various clusters, these are calculated as in section 4.2. Then one takes all combinations of photons (*i.e.* clusters

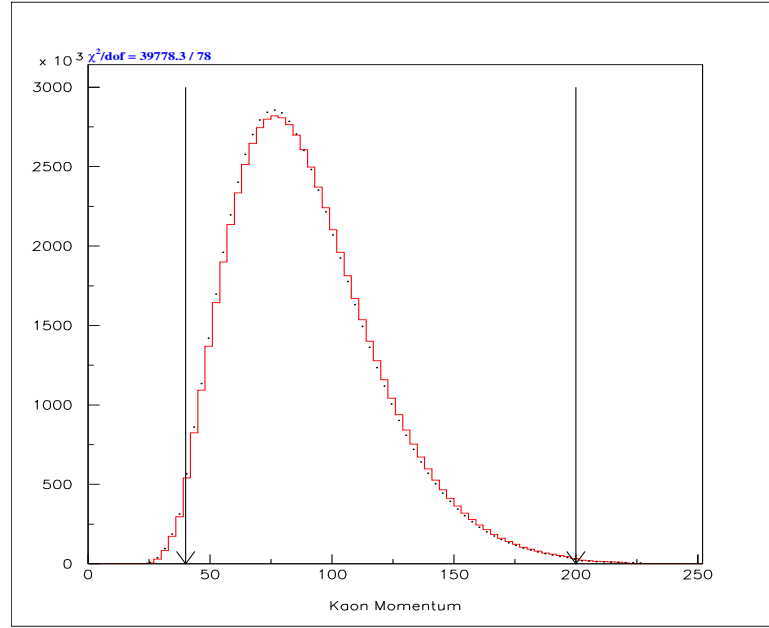


Figure 6.2: Energy of the $K_L \rightarrow \pi^0 \pi^0 \pi_D^0$ data (Dots) compared to MC (Histogram) requiring only two good tracks and 7 hard ware clusters.

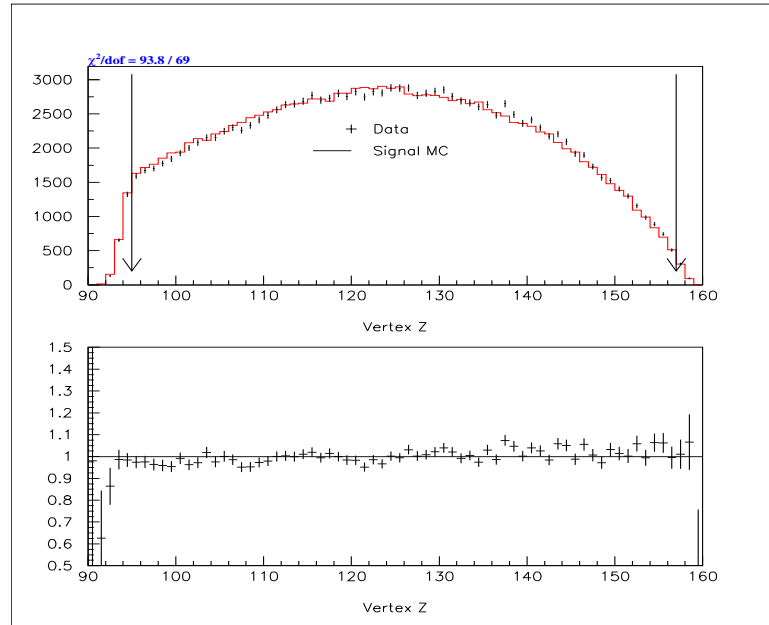


Figure 6.3: Vertex Z of the $K_L \rightarrow \pi^0 \pi_D^0 \pi_D^0$ data (Dots) compared to MC (Histogram) after all cuts. Lower plot is the ratio.

not matched to tracks) and forms a quantity called $ZM = \sqrt{k_1 k_2 r^2}$, where k_i is the energy of a photon cluster and r^2 is the distance between the two clusters. The pairing (there are 15 possible pairings for $K_L \rightarrow \pi^0 \pi^0 \pi_D^0$ and 3 for $K_L \rightarrow \pi^0 \pi_D^0 \pi_D^0$) that has the minimum difference between neutral vertexes $Z_{neut} = ZM/M_{\pi^0}$ and the charge vertex is considered to be the best pairing. M_{π^0} is the π^0 mass of 134.9764 MeV from [15]. The resolution on the neutral vertex is typically better than the resolution on the charged vertex and uniform over the whole range of z vertex positions, as is shown in figure 6.4 and figure 6.2. The charged vertex has a resolution that improves as the vertex moves downstream in Z . This is due to the fact that upstream decays have smaller opening angles, so small errors result in a large uncertainty in the decay position. The neutral vertex is required to be within a looser requirement of 90.0m to 160.0m. It may seem strange to cut loosely on the neutral vertex and it has a better resolution, however, the signal modes for this analysis do not have a neutral vertex. In order to make the analysis of all the modes as similar as possible only a cut on the charged vertex is used.

Another fiducial cut is the one that required the decay to occur from one of the two neutral kaon beams. This is a cut on the vertex x and vertex y positions. The cut is made from -0.2 to 0.2m in x and -0.1 to 0.1m in y . Figures 6.6 and 6.7 show the comparison of data and MC for these distributions after complete reconstruction for the $K_L \rightarrow \pi^0 \pi^0 \pi_D^0$ data sample. The vertex y distribution for the MC was difficult to match to the data. Figure 6.8 shows the change in the size of the defining collimator that occurred during the Summer period (discussed in section 2.1.2. Also during this period the position of the defining collimator was not well known and had to be determined from the data. Figure 6.9 compares different sets of runs for the $K_L \rightarrow \pi^0 \pi^0 \pi_D^0$ data set during the Summer. The comparison is the Vertex y distribution projected backwards to the face of the defining collimator. As is clearly seen the position of the collimator was not fixed as a function of time.

6.3 Trigger Verification

All trigger elements were calibrated and monitored throughout the data taking. However, cuts were made that would eliminate the requirement that the MC be able to exactly reproduce the data at the Trigger level. The threshold of energy that turned

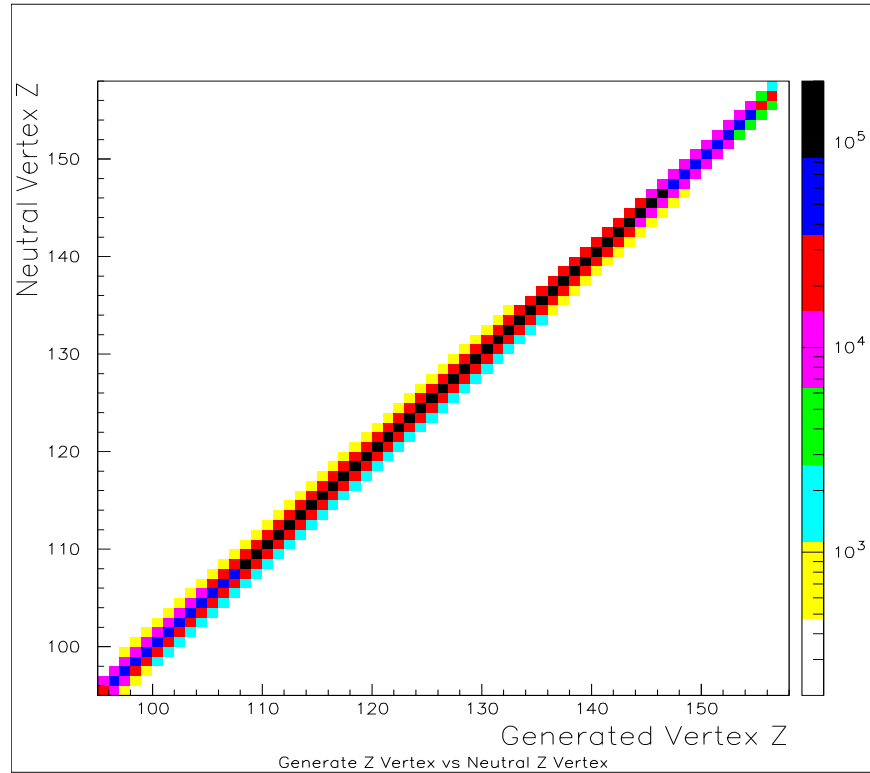


Figure 6.4: Vertex Z of the $K_L \rightarrow \pi^0 \pi^0 \pi_D^0$ MC, Generated versus Neutral Reconstruction.

on L1 source bits for the RCs and the SAs (see 3.2.1) shifted slightly over time. The same can be said for the E-Total thresholds. In order to be insensitive to these types of effects certain triggers were verified using data.

The individual energy deposited in each photon veto (*e.g.* RC6 or SA4) was written out. If the energy in any of the vetoes was greater than 150 MeV then the event was thrown out. This is well away from the thresholds of 400 and 500 MeV. Similarly, the energy deposited in the CsI was required to be greater than 40 GeV to be above the thresholds of E-Total system (see section 3.2.3).

The Trigger hodoscope system is also verified. The tracks from the spectrometer are projected back to the Hodoscope. If the tracks did not land within 5mm of the edge of the beam hole and would have produced the requisite number of hits, then the trigger is verified.

Section 4.2 discusses the finding of clusters using seed crystals. The number

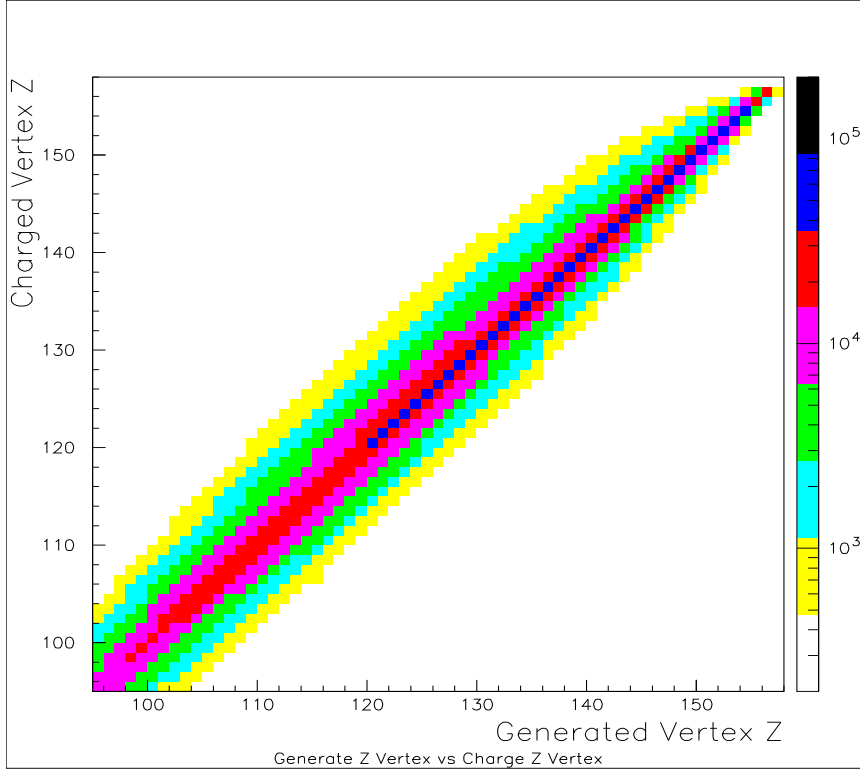


Figure 6.5: Vertex Z of the $K_L \rightarrow \pi^0 \pi^0 \pi_D^0$ MC, Generated versus Charge Reconstruction.

of clusters for each mode is required to be a specific number equal to the number of final state particles. The requirement also verifies the HCC trigger element implicitly. The number of clusters required for $K_L \rightarrow e^+ e^- \gamma$ is 3, for $K_L \rightarrow \pi^0 \pi^0 \pi_D^0$ is 7, for $K_L \rightarrow e^+ e^- e^+ e^-$ is 4 and for $K_L \rightarrow \pi^0 \pi_D^0 \pi_D^0$ is 8.

6.4 Calorimeter

The calorimeter is essential for reconstructing events in all modes discussed here. To ensure that only well-understood clusters are used, there are two cuts that can be made. The first is a cluster separation cut. A cut is made at 0.075m to provide a difference of at least two small crystals between cluster centers. Figure 6.10 shows that there is a small disagreement below 0.07m for $K_L \rightarrow \pi^0 \pi^0 \pi_D^0$ events. However, figure 6.11 shows that there is good agreement between data and MC for $K_L \rightarrow \pi^0 \pi_D^0 \pi_D^0$ mode all the way down. Thus, this cut is not made for $K_L \rightarrow e^+ e^- e^+ e^-$ studies.

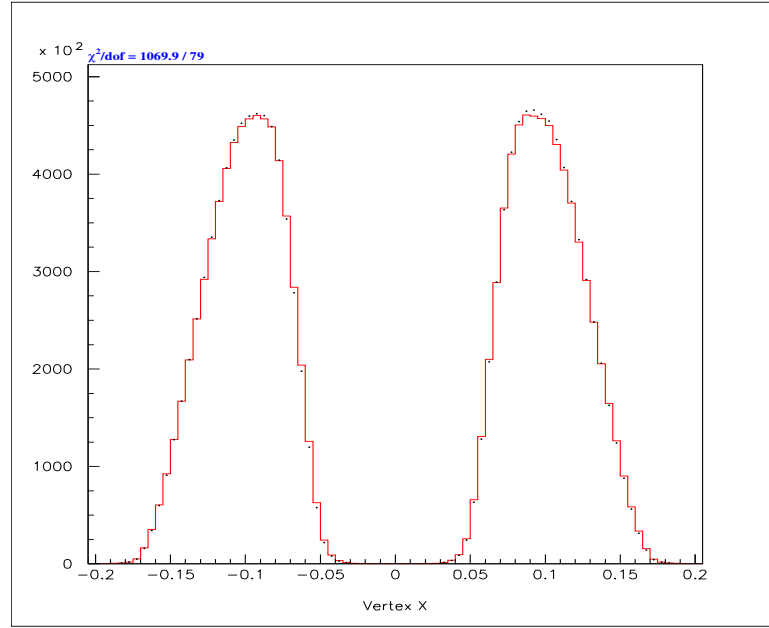


Figure 6.6: Vertex X of the $K_L \rightarrow \pi^0 \pi^0 \pi_D^0$ data (Dots) compared to MC (Histogram) after all cuts.

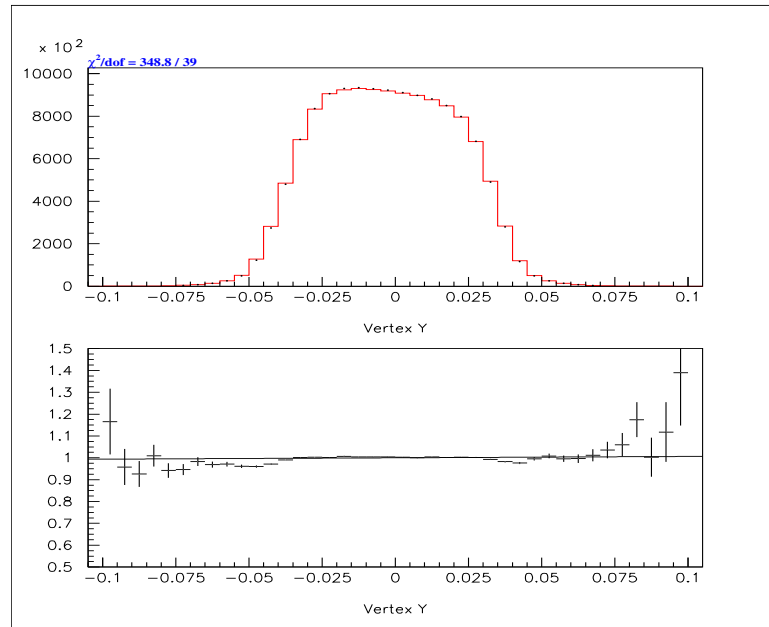


Figure 6.7: Vertex Y of the $K_L \rightarrow \pi^0 \pi^0 \pi_D^0$ data (Dots) compared to MC (Histogram) after all cuts. Lower plot is the ratio.

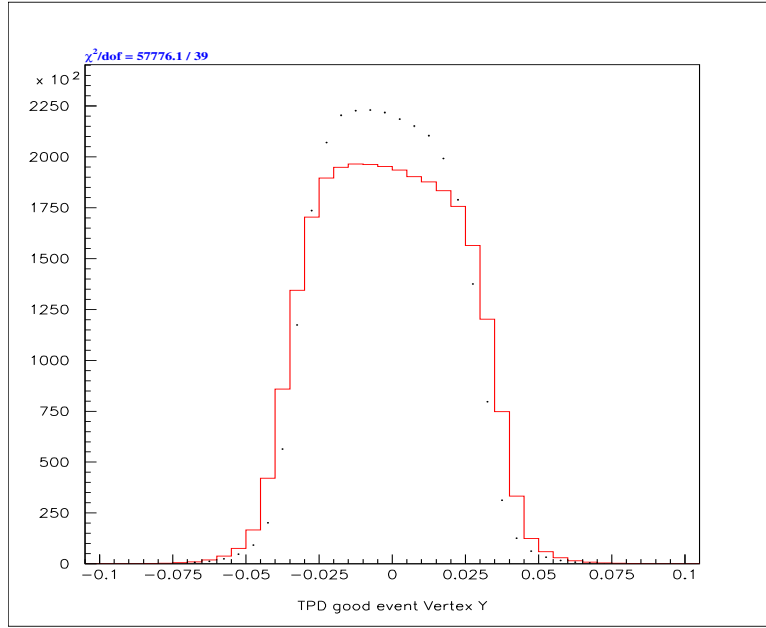


Figure 6.8: Vertex Y of the $K_L \rightarrow \pi^0 \pi^0 \pi_D^0$ data, Winter (Dots) compared to Summer (Histogram).

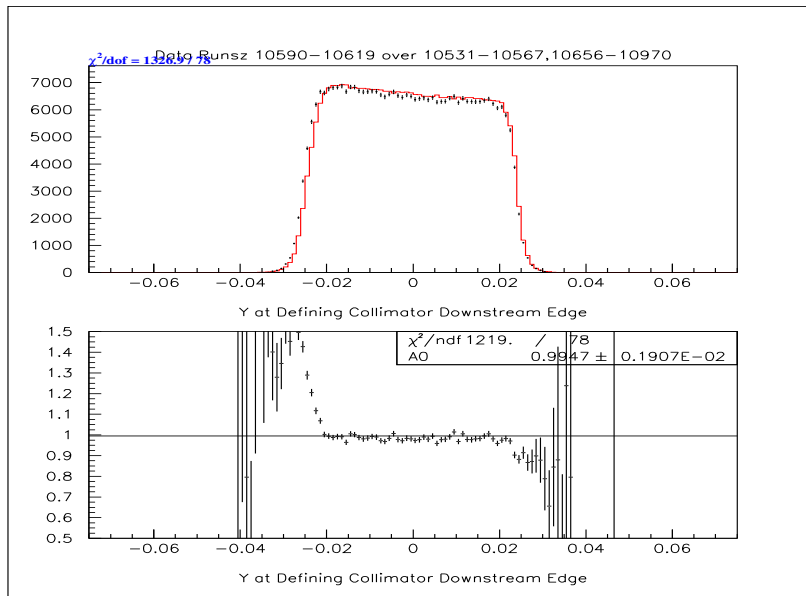


Figure 6.9: Vertex Y of the $K_L \rightarrow \pi^0 \pi^0 \pi_D^0$ data, Early Summer Runs (Dots) compared to Late Summer Runs (Histogram). Lower plot is the ratio.

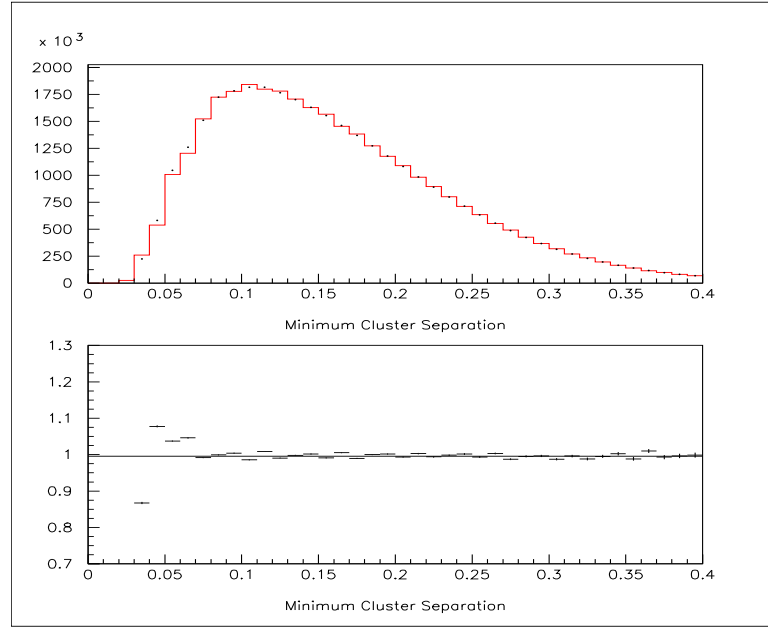


Figure 6.10: Distance between Clusters in the CsI measured in meters. Comparing $K_L \rightarrow \pi^0 \pi^0 \pi_D^0$ Data (Dots) and MC (Histogram) after all other cuts.

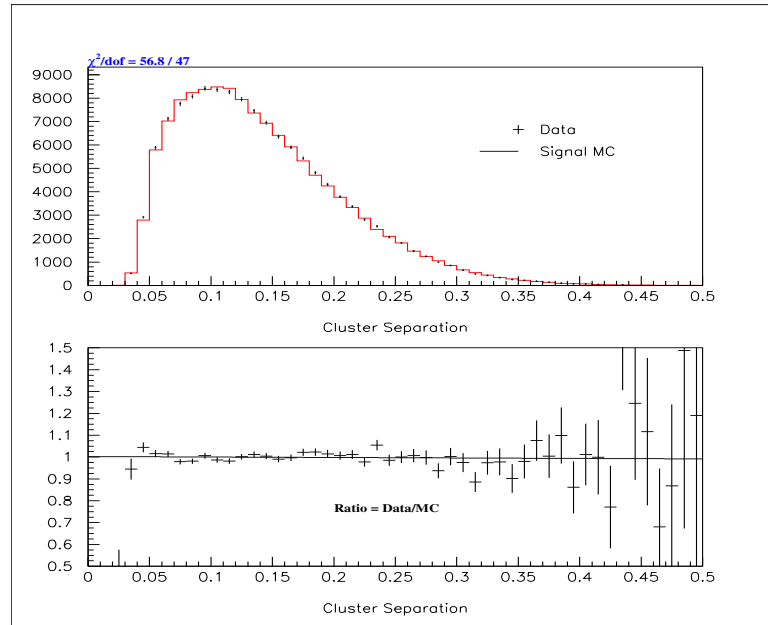


Figure 6.11: Distance between Clusters in the CsI measured in meters. Comparing $K_L \rightarrow \pi^0 \pi_D^0 \pi_D^0$ Data (Dots) and MC (Histogram) after all other cuts.

The second cut is a fiducial cut on the edges on the spectrometer. Events with clusters that are centered on the crystals at the edges of the calorimeter are cut out of the final sample. This includes the ring of small crystals around each of the two beam holes and the ring of large crystals at the outside edge of the CsI. Figure 6.12 is a two dimensional view of the cluster position for $K_L \rightarrow \pi^0 \pi^0 \pi_D^0$ Data events. The lines denote the cuts on the edge crystals.

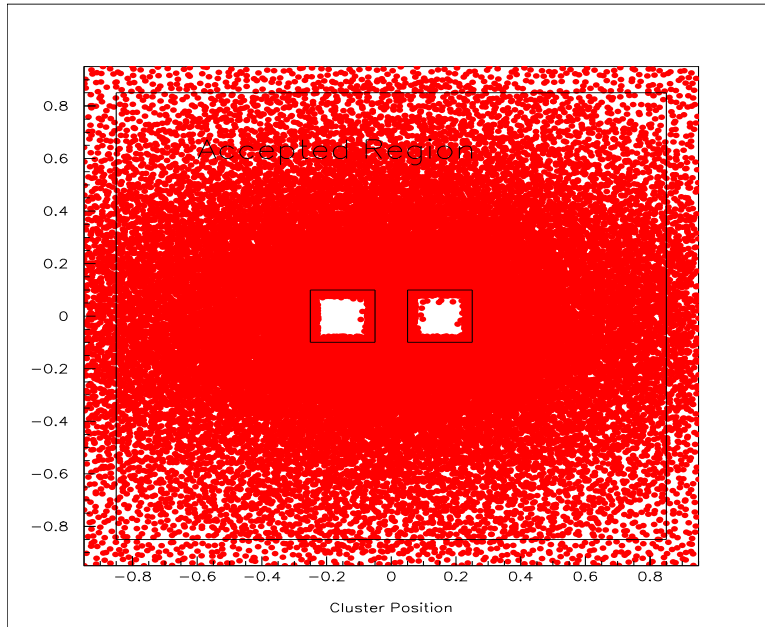


Figure 6.12: Two Dimensional View of the Face of the Calorimeter showing the Position of Clusters for $K_L \rightarrow \pi^0 \pi^0 \pi_D^0$ Data. Each event will have 7 clusters in this plot.

Finally a requirement is made to ensure that a cluster deposited enough energy in the CsI to fire the HCC. This cut is made at 2.75 GeV well away from the cut made by the L3 code (cut of 2.5 GeV, see 3.5). Figure 6.13 shows the distribution of cluster energy for the minimum energy per event for $K_L \rightarrow e^+ e^- \gamma$ events. Figure 6.14 shows the same thing for $K_L \rightarrow \pi^0 \pi^0 \pi_D^0$ events.

6.5 Spectrometer

The number of positively charged final state particles is equal to the number of negatively charged particles in all the modes of interest. A cut is made to remove events

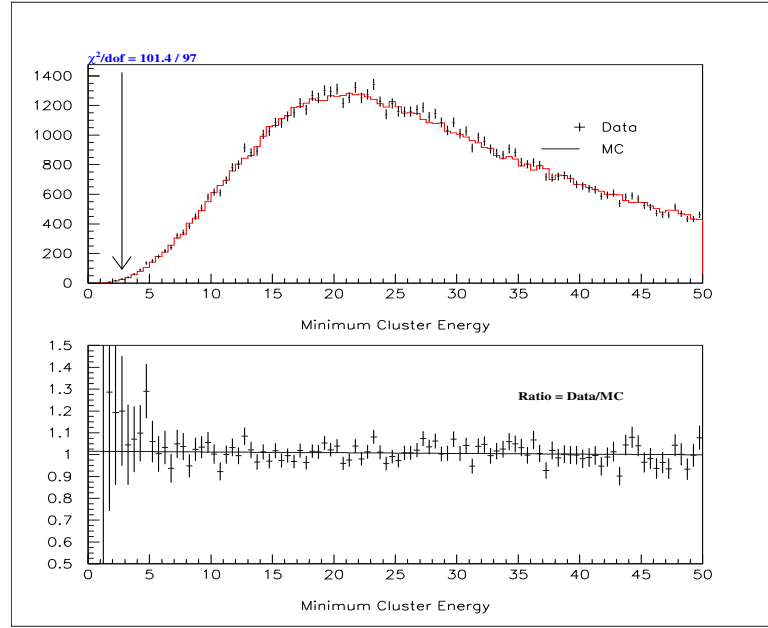


Figure 6.13: Minimum Cluster Energy for $K_L \rightarrow e^+e^-\gamma$ Data (Dots) compared to MC (Histogram) after all other cuts.

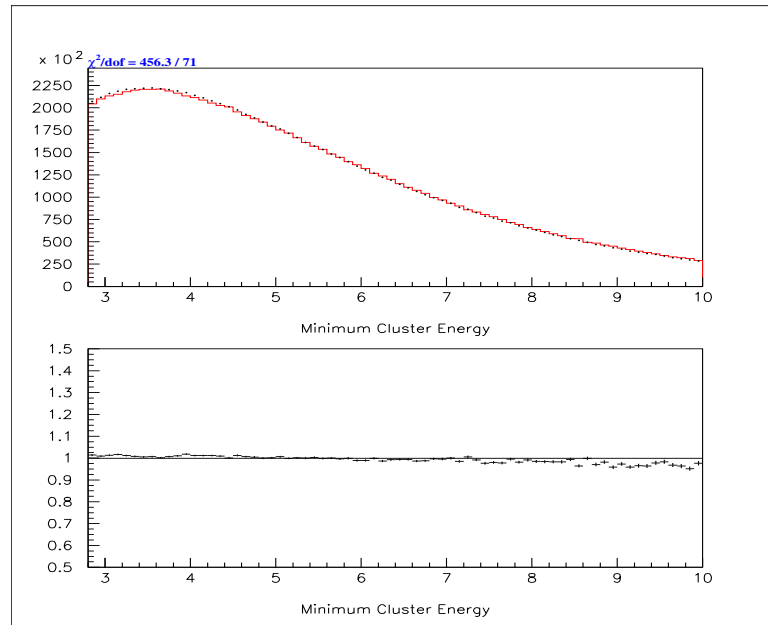


Figure 6.14: Minimum Cluster Energy for $K_L \rightarrow \pi^0\pi^0\pi_D^0$ Data (Dots) compared to MC (Histogram) after all other cuts.

where this is not the case.

There are two variables that determine the quality of the best fit decay vertex, the Vertex χ^2 and the Off-Magnet χ^2 . The Vertex χ^2 is a variable that compares how well the individual upstream track segments intersect at a common vertex. This χ^2 takes into account the resolution of the chambers and multiple scattering. Figure 6.15 shows the comparison of the vertex χ^2 for $K_L \rightarrow \pi^0 \pi_D^0 \pi_D^0$ events. Figure 6.16 shows the comparison of vertex χ^2 for $K_L \rightarrow e^+ e^- \gamma$ events. The means of these two distributions are quite different, however, in one mode there are only two tracks in the other there are four. The Off-Magnet χ^2 is a measure of how well all the track segments match up at the bend plane of the magnet. This quantity is a function of many things, such as the material in the downstream part of the detector and the details of the magnet field produced by the analysis magnet. Figure 6.17 shows a comparison of data and MC for $K_L \rightarrow \pi^0 \pi_D^0 \pi_D^0$ events, while figure 6.18 shows the similar plot for $K_L \rightarrow \pi^0 \pi^0 \pi_D^0$ events. Again the means are different due to the higher number of tracks in one mode. There is a substantial disagreement in this quantity, however, the cut on this variable is very loose, and a systematic by varying this cut over a large range is assigned.

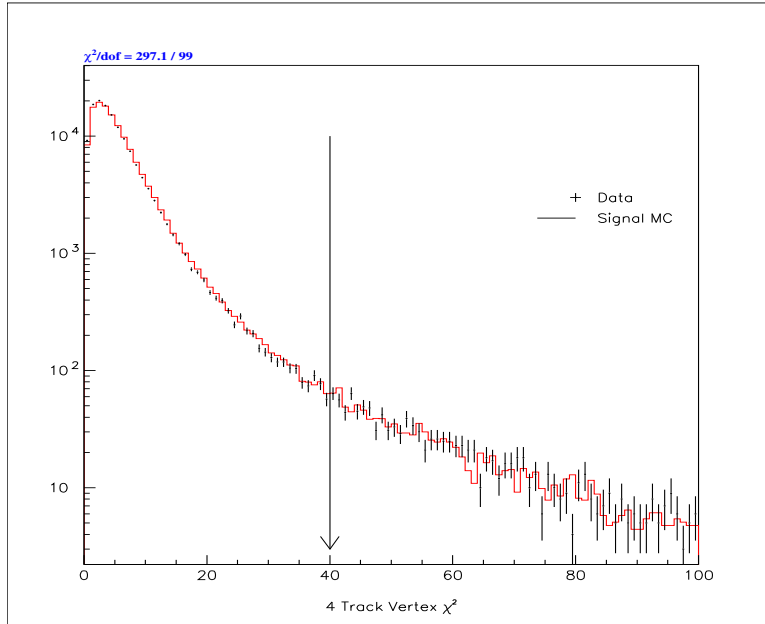


Figure 6.15: Vertex χ^2 for $K_L \rightarrow \pi^0 \pi_D^0 \pi_D^0$ Data (Dots) compared to MC (Histogram) after all other cuts.

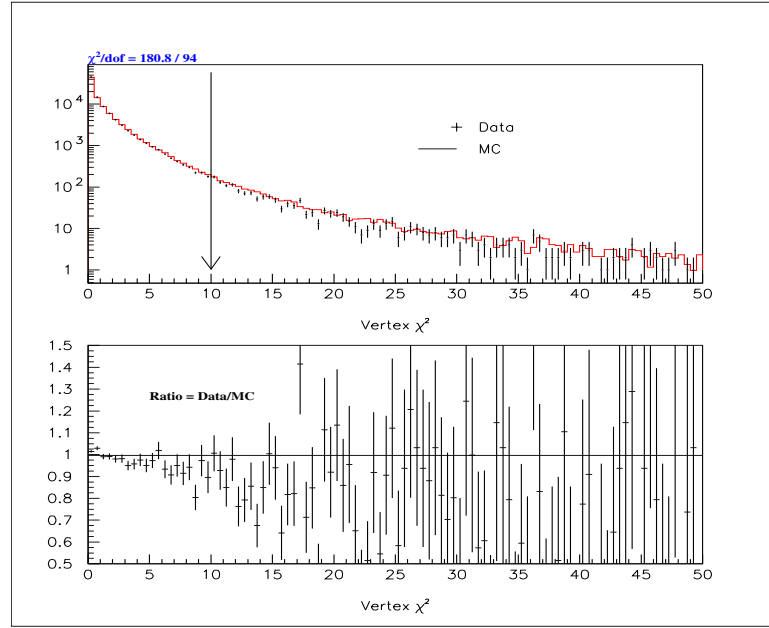


Figure 6.16: Vertex χ^2 for $K_L \rightarrow e^+e^-\gamma$ Data (Dots) compared to MC (Histogram) after all other cuts.

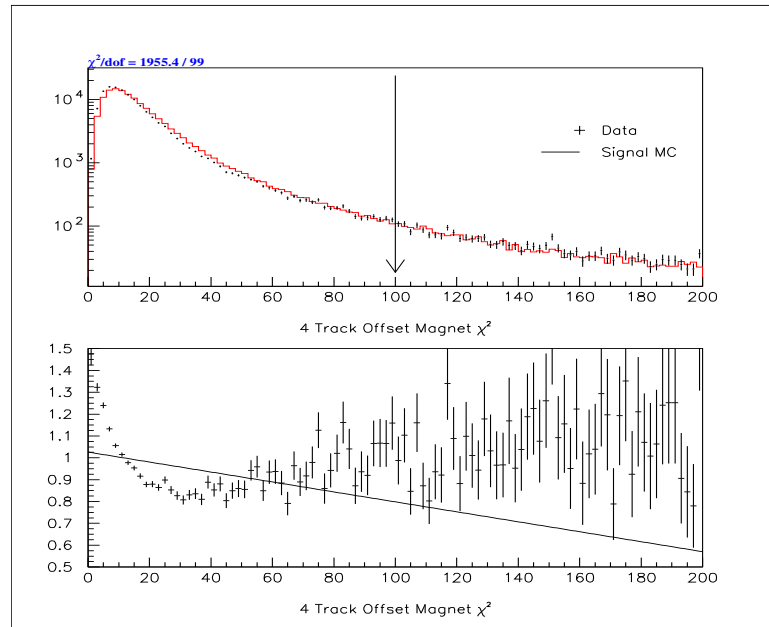


Figure 6.17: Off-Magnet χ^2 for $K_L \rightarrow \pi^0\pi_D^0\pi_D^0$ Data (Dots) compared to MC (Histogram) after all other cuts.

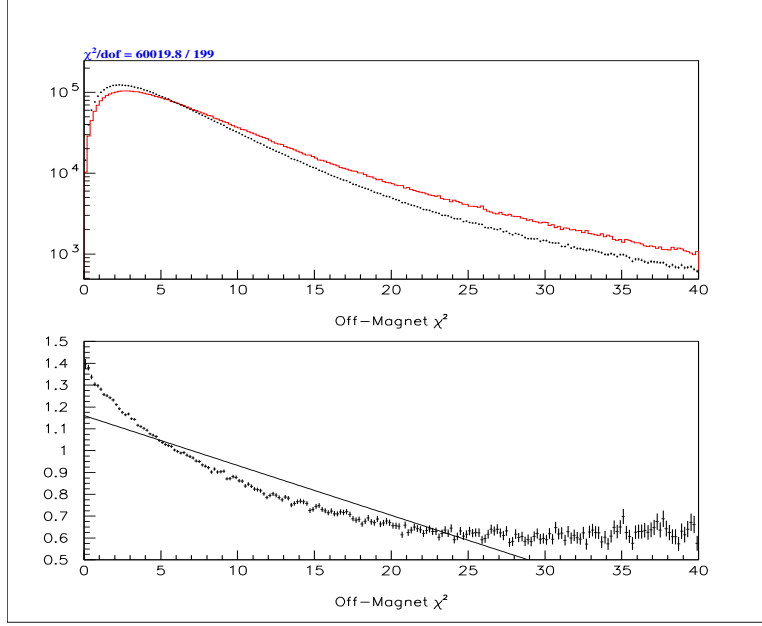


Figure 6.18: Off-Magnet χ^2 for $K_L \rightarrow \pi^0 \pi^0 \pi_D^0$ Data (Dots) compared to MC (Histogram) after all other cuts.

One of the most insidious backgrounds for the signal modes under study are the conversion backgrounds. These include $K_L \rightarrow \gamma\gamma$ with the conversion of one photon as a background to $K_L \rightarrow e^+e^-\gamma$ and with two conversions as a background to $K_L \rightarrow e^+e^-e^+e^-$. A $K_L \rightarrow e^+e^-\gamma$ decay with a photon conversion is yet another background to $K_L \rightarrow e^+e^-e^+e^-$. However, there is a powerful tool for removing this background. Conversion events are characterized by the e^+e^- pair being very close together. Figure 6.20 shows a comparison of separation of tracks in DC 1 the x view for data and signal MC using $K_L \rightarrow e^+e^-e^+e^-$ events after a complete reconstruction. One can see that there is a sizable disagreement in the first bin. Figure 6.21 shows a similar thing for $K_L \rightarrow e^+e^-\gamma$. By generating a sample of $K_L \rightarrow \gamma\gamma$ with two conversions and $K_L \rightarrow e^+e^-\gamma$ with one conversion one can study distributions of separation of tracks at DC 1 for these backgrounds as well. Figure 6.19 shows a comparison of the three sets of MC compared to the data. Here, it is made clear that the Conversion MC have very close track separation. One could cut on this quantity at about 0.001m and remove most of the background, which is done for $K_L \rightarrow e^+e^-\gamma$ sample. However, another quantity can be constructed called the Min-Maximum Separation. The Min-Maximum Separation is

formed by first finding the separation in the x and y planes of the DC for a combination of a positive and negative track. The greater of the two separations (*i.e.* either x or y) is then taken. The minimum of this maximum separation for all possible combinations of positive and negative tracks is the quantity Min-Maximum Separation. For conversion pairs, both the x and the y separations are very close together. Figure 6.22 shows the comparison of this quantity. By cutting on this Min-Maximum Separation, we retain 1056 signal events while allowing 4.4 ± 0.2 background events. If one cuts on the track separation alone, then there is only 640 events with 0.02 background. For this mode, the additional signal is better as the measurement is statistics limited. Figures 6.23 and 6.24 show how the conversion events (generated with $100\times$ the data flux) compare to data events for total mass and kaon energy. This shows that the conversion background looks quite a bit like the data.

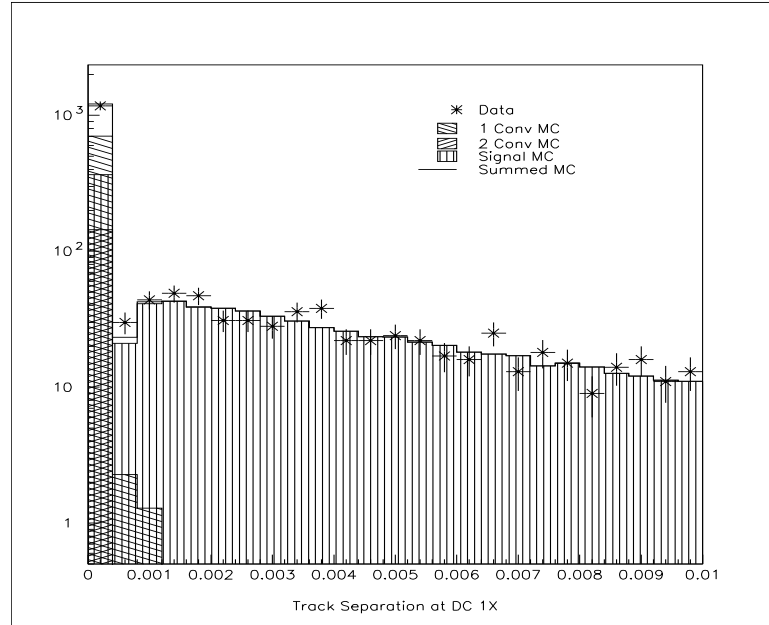


Figure 6.19: Distance between tracks in DC 1X measured in meters. Dots are $K_L \rightarrow e^+e^-e^+e^-$ data and histogram is signal and conversion background MC after a complete reconstruction.

However, there is one other variable that is different between signal and background. The mass of the pairs of electrons and positrons, m_{ee} , is correlated with the Track Separation. Figure 6.25 compares the m_{ee}^{11} spectrum for signal MC and conver-

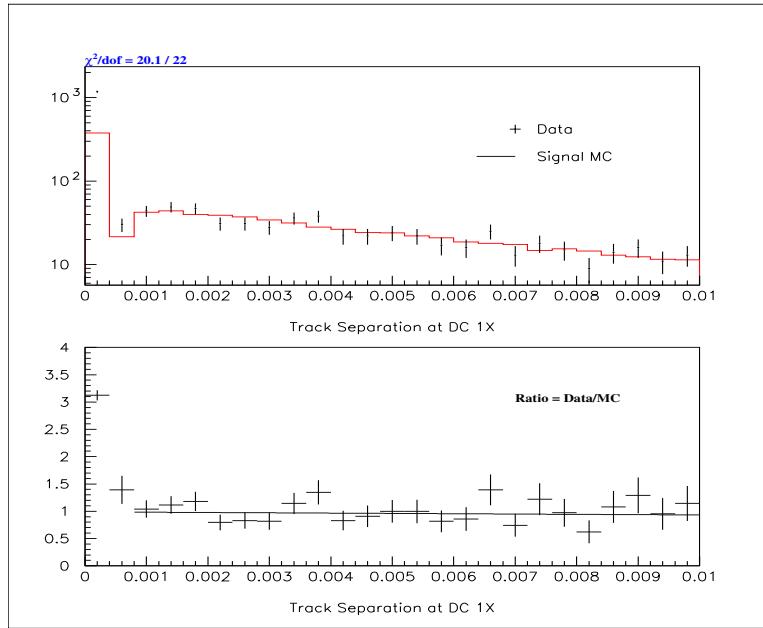


Figure 6.20: Distance between Tracks in DC 1X measured in meters. Dots are $K_L \rightarrow e^+e^-e^+e^-$ data and histogram is signal MC after a complete reconstruction. Lower plot is the ratio of the two.

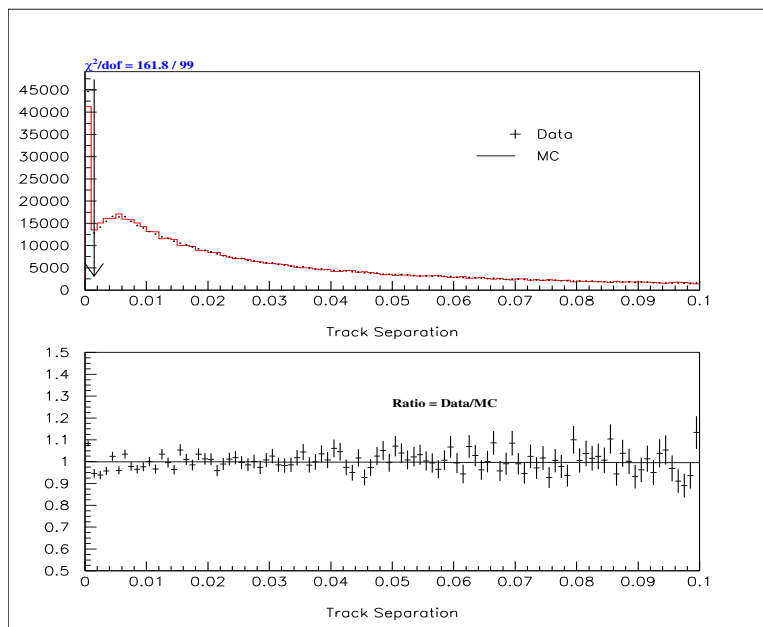


Figure 6.21: Distance between Tracks in DC 1X measured in meters. Dots are $K_L \rightarrow e^+e^-\gamma$ data and histogram is signal MC after a complete reconstruction. Lower plot is the ratio of the two.

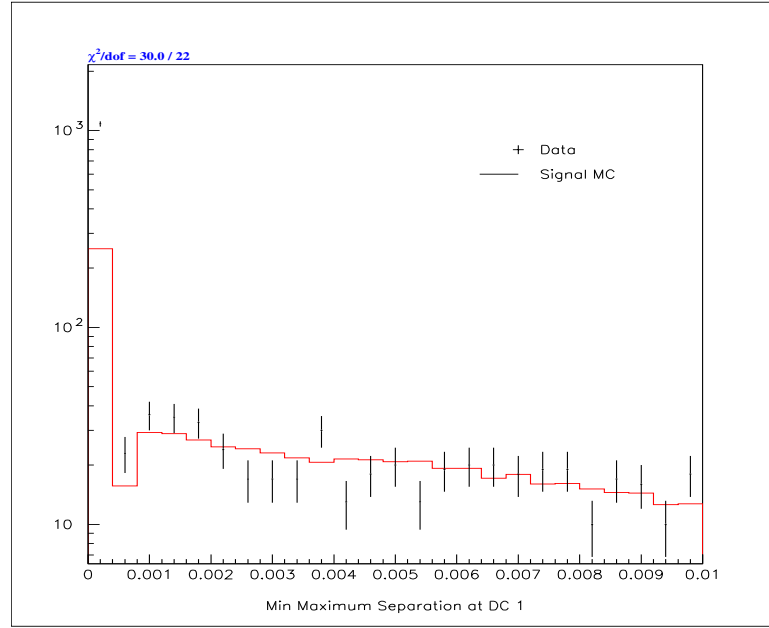


Figure 6.22: The Min-Maximum Track Separation in DC 1X measured in meters. Dots are $K_L \rightarrow e^+e^-e^+e^-$ Data and Histogram is Signal MC.

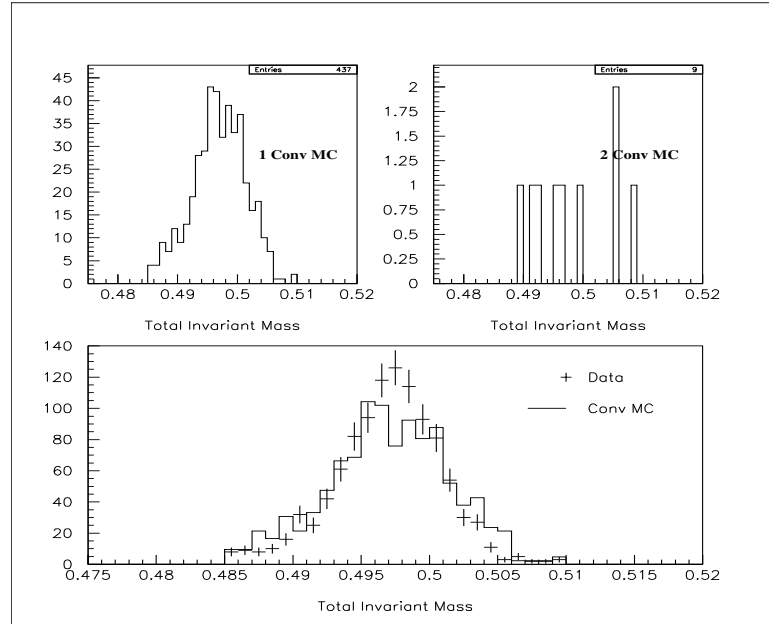


Figure 6.23: Total Mass measured in GeV after all cuts including a cut on Min-Maximum Separation. Dots are $K_L \rightarrow e^+e^-e^+e^-$ Data and Histogram is Conversion MC. The Conversion MC is approximately 100 times the data flux.

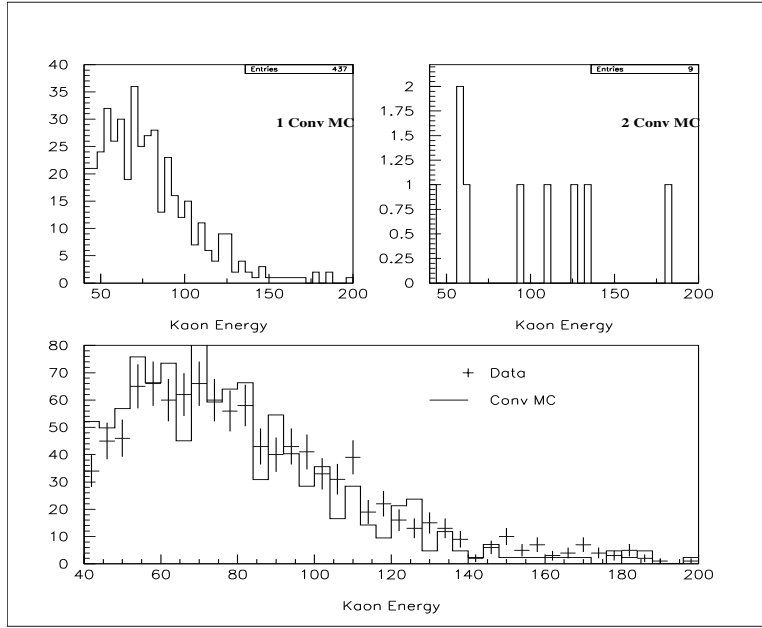


Figure 6.24: Kaon Energy measured in GeV after all cuts including a cut on Min-Maximum Separation. Dots are $K_L \rightarrow e^+e^-e^+e^-$ Data and Histogram is Conversion MC. The Conversion MC is approximately 100 fluxes worth of data.

sion MC. m_{ee}^{11} is defined using the pairing discussed in section 5.2.3 where the lepton pair that produces the smallest sum of masses is chosen and the 11 system is the smaller of those two. The line at 0.005GeV in figure 6.25 is a possible cut that would separate the background and signal. If this cut is used then 647 data events remain with 0.96 background events. Again the min maximum separation cut leaves more signal.

6.6 E/P

The primary method of particle identification for charged particles is using the combination of spectrometer measured momentum and the energy deposited in the CsI calorimeter. This is the E/P ratio that has been mentioned before in sections 2.3.3 and 2.6.3. The quantity E/P is the ratio of the energy of a cluster deposited in CsI calorimeter over the momentum of the track matched to the cluster as measured by the spectrometer. Nearly all electrons and photons deposit all of their energy in the crystals. By looking at the E/P spectrum for electrons from reconstructed $Ke3$ events in the 1997 period, Figure 6.26, the percentage of electrons that deposit less than all

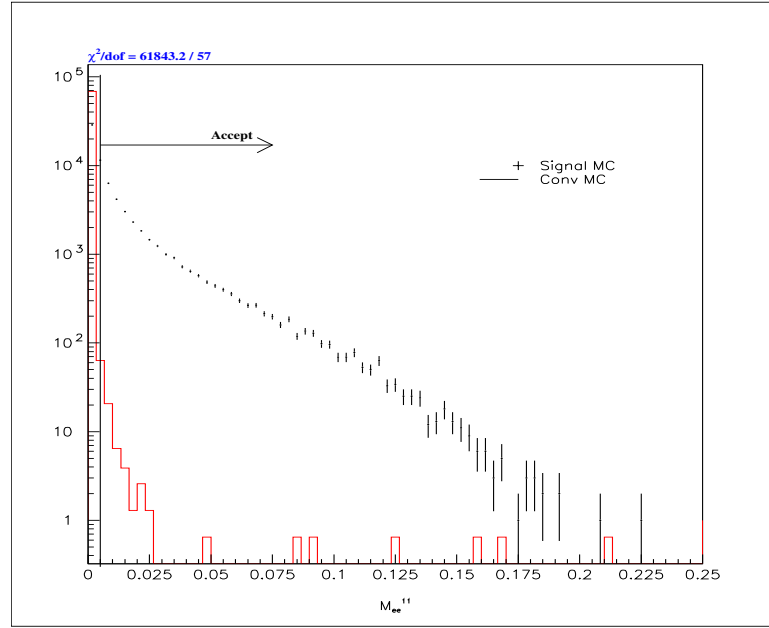


Figure 6.25: m_{ee}^{11} for $K_L \rightarrow e^+e^-e^+e^-$ signal MC (Dots) compared to Conversion background MC (Histogram). Also shown is a hypothetical cut at 5MeV, which is not made in the actually analysis.

of their energy can be seen [2]. The electrons are selected using a very tight cut on the quantity Π_{TRD} (defined in section 4.3). Figure 6.26 shows that less than 0.2% of electrons have an E/P less than 0.85 (well away from the peak which includes resolution effects).

Any particle with $0.925 < E/P < 1.075$ in this analysis is assumed to be a electron. If the particle went down a beam hole in the CsI, its E/P is set to be exactly 0. Muons and other minimum-ionizing particles have a very small E/P . Since about 70% of the pions interact hadronically with the CsI, they can leave a significant percentage of their energy in the CsI. Figure 6.27 shows the E/P of events with 4 good tracks forming a vertex at the level of the crunch in Trigger 1. The plot shows the peak with electrons, the continuum of small E/P events from pions and a peak at zero where one of the tracks points down the beam hole. It should be noted that at this level of the crunch there is a requirement that two tracks have an $E/P > 0.75$ (see section 3.5), which causes a bump at 0.75 seen in the plot.

All the modes of interest are required to have various numbers of electrons, so

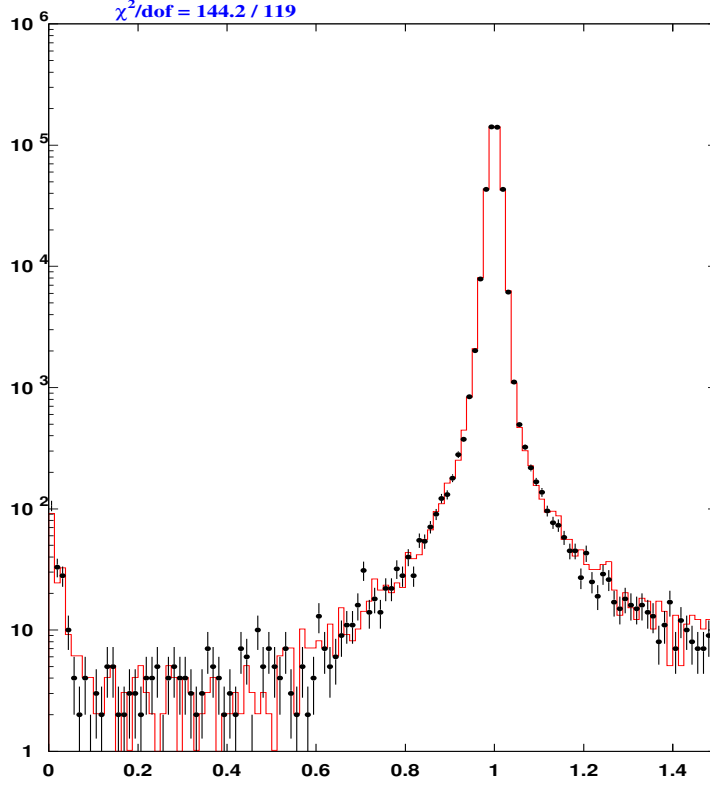


Figure 6.26: E/P for Data (dots) and MC (histogram) of electrons, using $Ke3$ decays. Electrons selected using Π_{TRD} (*i.e.* the TRD) [2].

all tracks are required to have an E/P between 0.925 and 1.075. This requirement also prevents tracks from going down the beam holes. For the $K_L \rightarrow e^+e^-e^+e^-$ and $K_L \rightarrow e^+e^-\gamma$ modes (the modes of interest), this beam hole requirement is necessary. Trigger 1 had a requirement of a minimum of 4 clusters in the CsI, Trigger 3 required at least 3 clusters (see Section 3.4 for Trigger definitions). Figure 6.28 is a comparison of E/P for data and Monte Carlo for $K_L \rightarrow e^+e^-\gamma$ events. There is some disagreement shown in this quantity between data and MC, probably due to some remaining energy resolution issues. The cut on this variable is fairly loose and a systematic has been assigned to cover any remaining disagreement.

6.7 Transition Radiation Detector

The $K_L \rightarrow e^+e^-\gamma$ signal mode comes from a trigger that uses the Transition Radiation Detector to cut back on background modes with π^\pm in the final state. Since the

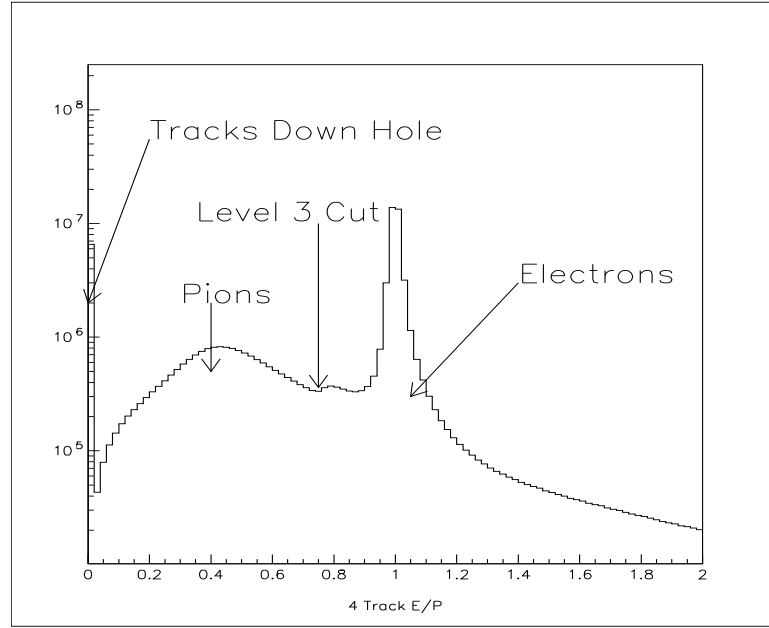


Figure 6.27: E/P for Data during the Crunch. Trigger 1, 4 Tracks. The drop off at 0.75 is due to the requirement that two of the tracks must have an $E/P > 0.75$ from the L3 Trigger.

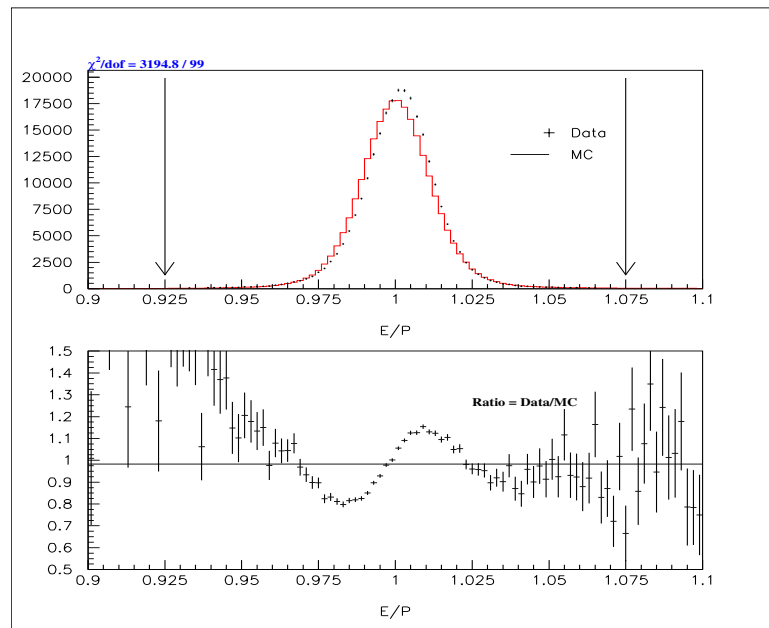


Figure 6.28: E/P for Data(dots) $K_L \rightarrow e^+e^-\gamma$ compared to MC(histogram after all cuts have been made. Top plot is an overlay, bottom is a ratio.

detector was used at the trigger level, further cuts were made to reject pion backgrounds and verify the trigger. The TRD Trigger element was reconstructed as is discussed in appendix A and section 3.3.5. The quantity of pion probability, Π_{TRD} , as defined in 4.3 for each of the charged particles is used to make further rejection. Figure 6.29 shows the pion probability of $K_L \rightarrow \pi^0 \pi^0 \pi_D^0$ events after most reconstruction. The top plot is the 1997 data set and the bottom is the 1999 data set. This also shows that the calibration of the TRD for the 1999 set is not finished. This is one of the reasons that this cut was not applied to all the data.

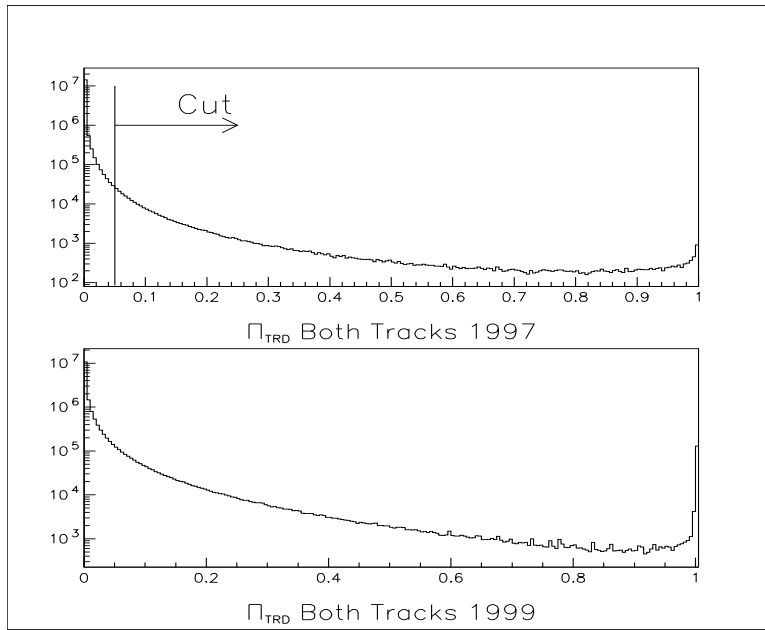


Figure 6.29: Π_{TRD} for both charged tracks for $K_L \rightarrow \pi^0 \pi^0 \pi_D^0$ events. The top plot is the 1997 data set, the bottom is 1999 data set.

6.8 Transverse Momentum

In order to reduce the amount of background from events with missing or extra particles, a quantity called the transverse momentum, \vec{P}_T , is constructed. The definition of transverse momentum is simply the amount of momentum perpendicular to the direction of flight the parent kaon for the combined system of reconstructed particles. The direction of flight of the kaon is calculated by pointing the decay vertex back to the target. The sum of momentum, \vec{P}_{sum} is just that, the sum of the momentum for

each individual particle of an event. The definition of \vec{P}_T is illustrated in Figure 6.30. The quantity most often used in these analyses is the square of the transverse momentum, \vec{P}_T^2 . For events where all the particles are detected and their momenta are well measured (*i.e.* little multiple-scattering and good resolution) then the \vec{P}_T^2 should be very close to zero. Figure 6.31 compares the data \vec{P}_T^2 distribution to the MC distribution for $K_L \rightarrow \pi^0 \pi^0 \pi_D^0$ events. There is a small disagreement that remains most likely from remaining biases in track resolution and/or material measurement. A systematic uncertainty is assigned to cover this.

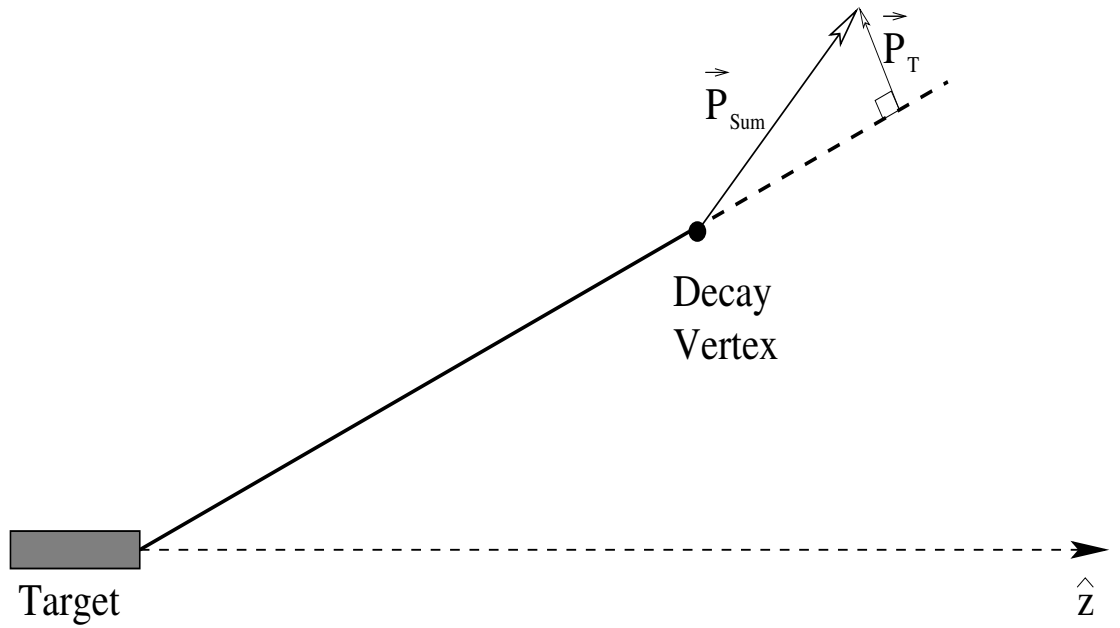


Figure 6.30: Defining the Quantity of Transverse Momentum \vec{P}_T .

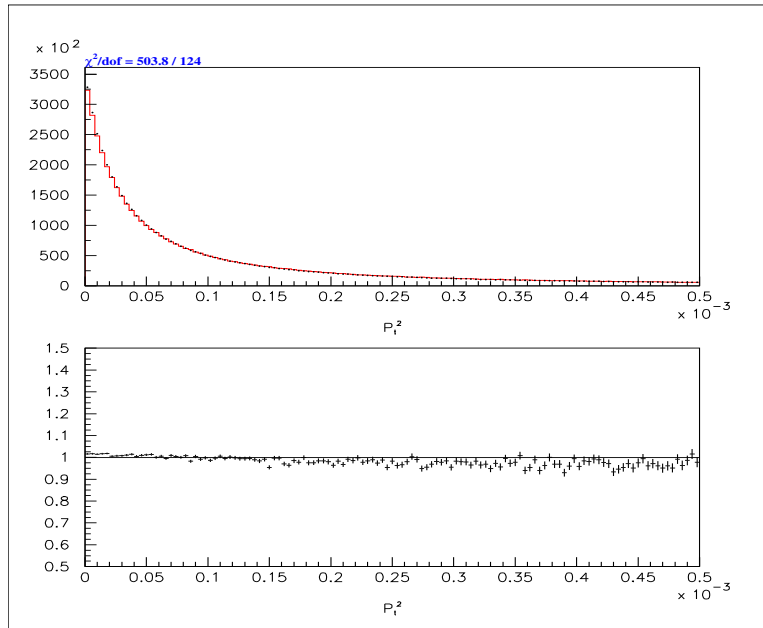


Figure 6.31: \vec{P}_T^2 for fully reconstructed $K_L \rightarrow \pi^0 \pi^0 \pi_D^0$ events where Data (dots) is compared to the MC (histogram). Lower plot is the ratio of Data over MC.

Chapter 7

$K_L \rightarrow e^+e^-\gamma$ Branching Ratio

One of the goals of the analysis is the measurement of the branching ratio for $K_L \rightarrow e^+e^-\gamma$. This branching ratio is calculated as follows:

$$BR(K_L \rightarrow e^+e^-\gamma) = \frac{N_{e^+e^-\gamma}^{obs}}{\epsilon_{e^+e^-\gamma} \cdot \mathcal{F}}, \quad (7.1)$$

where $N_{e^+e^-\gamma}^{obs}$ is the number of signal events with any background subtraction, $\epsilon_{e^+e^-\gamma}$ is the acceptance or efficiency of the detector, and \mathcal{F} is the flux of kaons, or number of kaons that decayed in the accepted region as defined in section 5.1, for the experiment.

The efficiency of the detector is calculated using Monte Carlo simulations of the detector. Therefore, the agreement of the MC with the Data for a variety of different kinematic and fundamental quantities is an important gauge for the degree of confidence of the result. The acceptance is calculated in the following manner:

$$\epsilon_{e^+e^-\gamma} = \frac{N_{e^+e^-\gamma}^{rec}}{N_{e^+e^-\gamma}^{gen}}, \quad (7.2)$$

where $N_{e^+e^-\gamma}^{gen}$ is the number of kaons generated and required to decay into the $e^+e^-\gamma$ final state and $N_{e^+e^-\gamma}^{rec}$ is the number of such events that are reconstructed by the analysis code, the same code used to find $N_{e^+e^-\gamma}^{obs}$.

The calculation of the flux is done by simultaneously analyzing a mode with a similar final state for which the branching fraction is accurately known. The mode chosen in this case, as was mentioned previously, is $K_L \rightarrow \pi^0\pi^0\pi_D^0$. The flux is calculated using the known branching ratio and the acceptance of the detector as simulated by the MC again. The following is the equation used

$$\mathcal{F} = \frac{N_{\pi^0\pi^0\pi_D^0}^{obs}}{\epsilon_{\pi^0\pi^0\pi_D^0} \cdot BR(K_L \rightarrow \pi^0\pi^0\pi_D^0)}, \quad (7.3)$$

where $N_{\pi^0\pi^0\pi_D^0}^{obs}$ is the number of normalization events with backgrounds subtracted, reconstructed from the data, $\epsilon_{\pi^0\pi^0\pi_D^0}$ is the acceptance from the MC and $BR(K_L \rightarrow \pi^0\pi^0\pi_D^0)$ is the independently measured branching ratio taken to be the world average from other experiments.

The study of backgrounds, the level of agreement between data and MC for both the signal mode and the normalization, and other sources give an estimate of the amount of uncertainty in the final result.

7.1 Data Selection

In order to get clean samples of the normalization and signal modes, cuts are made. Chapter 6 describes the trigger verification, fiducial and particle identification cuts. Table 7.1 gives the exact values for these cuts for both the signal and normalization modes. In most cases the normalization mode has exactly the same cuts, but a few more are necessary.

The signal and normalization modes each appear quite different to the detector. Figure 7.1 shows what is seen by the detector for a two track event with three clusters and two identified electrons. Similarly, figure 7.2 shows what is seen by the detector for a two electron track event with 7 clusters in the CsI. These initial views help in deciding what sort of cuts are necessary.

It should be noted here that the 99 data set will not be used for any of the results from $K_L \rightarrow e^+e^-\gamma$. The reasons for this are threefold. First, the results are already systematics limited, meaning that the systematic uncertainty is larger than the statistical. The 99 data set was prescaled, so it only adds a small number of events in any case. Second, there are some remaining, subtle discrepancies between data and MC that I have not had the time to explore at the level of detail needed for this analysis. Third, the amount of background in the 99 data set is much larger, since the TRD trigger was not used. An offline cut using the TRDs could not be done as the calibration was done in a different manner and not completed. The additional background can only make the systematic uncertainty larger.

Cut Variable	Accept Range	
	$K_L \rightarrow e^+e^-\gamma$	$K_L \rightarrow \pi^0\pi^0\pi_D^0$
CsI Clusters	3	7
Photon Veto	$< 0.15\text{GeV}$	$< 0.15\text{GeV}$
Minimum Cluster E	$> 2.75\text{GeV}$	$> 2.75\text{GeV}$
Distance to VV' hole	$> 0.005\text{m}$	$> 0.005\text{m}$
Distance to CsI Hole	$> 0.025\text{m}$	$> 0.025\text{m}$
Distance to Outer CsI Edge	$> 0.05\text{m}$	$> 0.05\text{m}$
Vertex X	$-0.2\text{m to } +0.2\text{m}$	$-0.2\text{m to } +0.2\text{m}$
Vertex Y	$-0.1\text{m to } +0.1\text{m}$	$-0.1\text{m to } +0.1\text{m}$
Vertex Z	$95.0\text{m to } 157.0\text{m}$	$95.0\text{m to } 157.0\text{m}$
Track Separation @ DC1	$> 0.0015\text{m}$	$> 0.0015\text{m}$
Vertex χ^2	< 10.0	< 10.0
Magnet Offset χ^2	< 40.0	< 40.0
Total Kaon Energy	$40.0\text{GeV to } 200.0\text{GeV}$	$40.0\text{GeV to } 200.0\text{GeV}$
E/P	$0.925 \text{ to } 1.075$	$0.925 \text{ to } 1.075$
Minimum # of TRD planes	> 8	> 8
Π_{TRD}	< 0.05	< 0.05
TRD beam hole planes	> 0	> 0
Total Mass	$0.475\text{GeV to } 0.520\text{GeV}$	$0.485\text{GeV to } 0.510\text{GeV}$
P_t^2	$< 0.0005\text{GeV}^2$	$< 0.0005\text{GeV}^2$
Dalitz χ^2	-	< 10.0
$\pi^0 \rightarrow e^+e^-\gamma$ Mass	-	$0.1275 \text{ to } 0.1425 \text{ GeV}$
Neutral Vertex Z	-	$90.0\text{m to } 160.0\text{m}$

Table 7.1: $K_L \rightarrow e^+e^-\gamma$ Cuts.

7.1.1 Backgrounds

Backgrounds to the signal mode can come from several sources. Similar modes with accidental activity (*i.e.* $K_L \rightarrow e^+e^-$ with an accidental photon), similar modes with misidentified particles (*i.e.* $Ke3$ with the pion reconstructed as an electron), similar modes with missing particles (*i.e.* $K_L \rightarrow \pi^0\pi_D^0$ with two missing photons, and decays with the same final state (*i.e.* $K_L \rightarrow \gamma\gamma$ with an external conversion of one of the photons).

Figure 7.3 is plot of the total invariant mass of all of the final state particles versus the \vec{P}_T^2 for 1997 data. It is useful to look at this plot to determine the nature of some of the backgrounds. A cluster of events is located at the kaon mass and low \vec{P}_T^2 , which corresponds to events with the same final state particles as the signal. A vertical strip of events at the pion mass corresponds to $K_L \rightarrow \pi^0\pi^0\pi_D^0$ events where two

/disks/upsilondisk/jladue/ee
g97.dat.10732.1

Run Number: 10732

Spill Number: 0

Event Number: 6722

Trigger Mask: 4

All Slices

Track and Cluster Info

HCC cluster count: 3

ID Xcsi Ycsi P or E

T 1: -0.8074 0.0565 +4.26

C 3: -0.8107 0.0555 4.13

T 2: 0.0349 0.0122 -38.48

C 1: 0.0365 0.0126 36.04

C 2: -0.3276 0.2994 12.18

Vertex: 2 tracks

X Y Z

-0.1007 -0.0115 106.341

Mass=0.4659 (assuming pions)

Chisq=0.14 Pt2v=0.005012

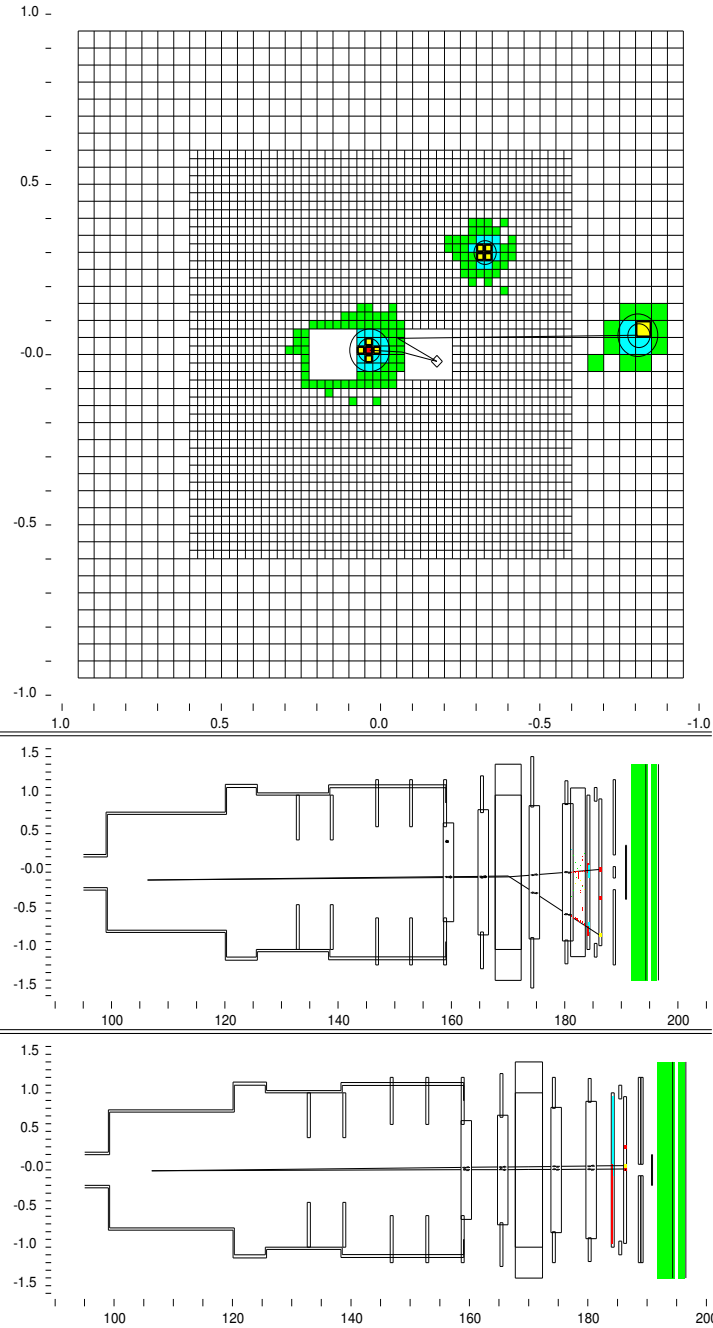


Figure 7.1: A Detector picture showing a $K_L \rightarrow e^+e^-\gamma$ event.

of the π^0 have been lost, thus its flatness with respects to the \vec{P}_T^2 . Figure 7.4 shows the projection of figure 7.3 plot onto the mass axis. The hatched histogram is the same plot but with the \vec{P}_T^2 cut applied. The events that lie between the pion mass and

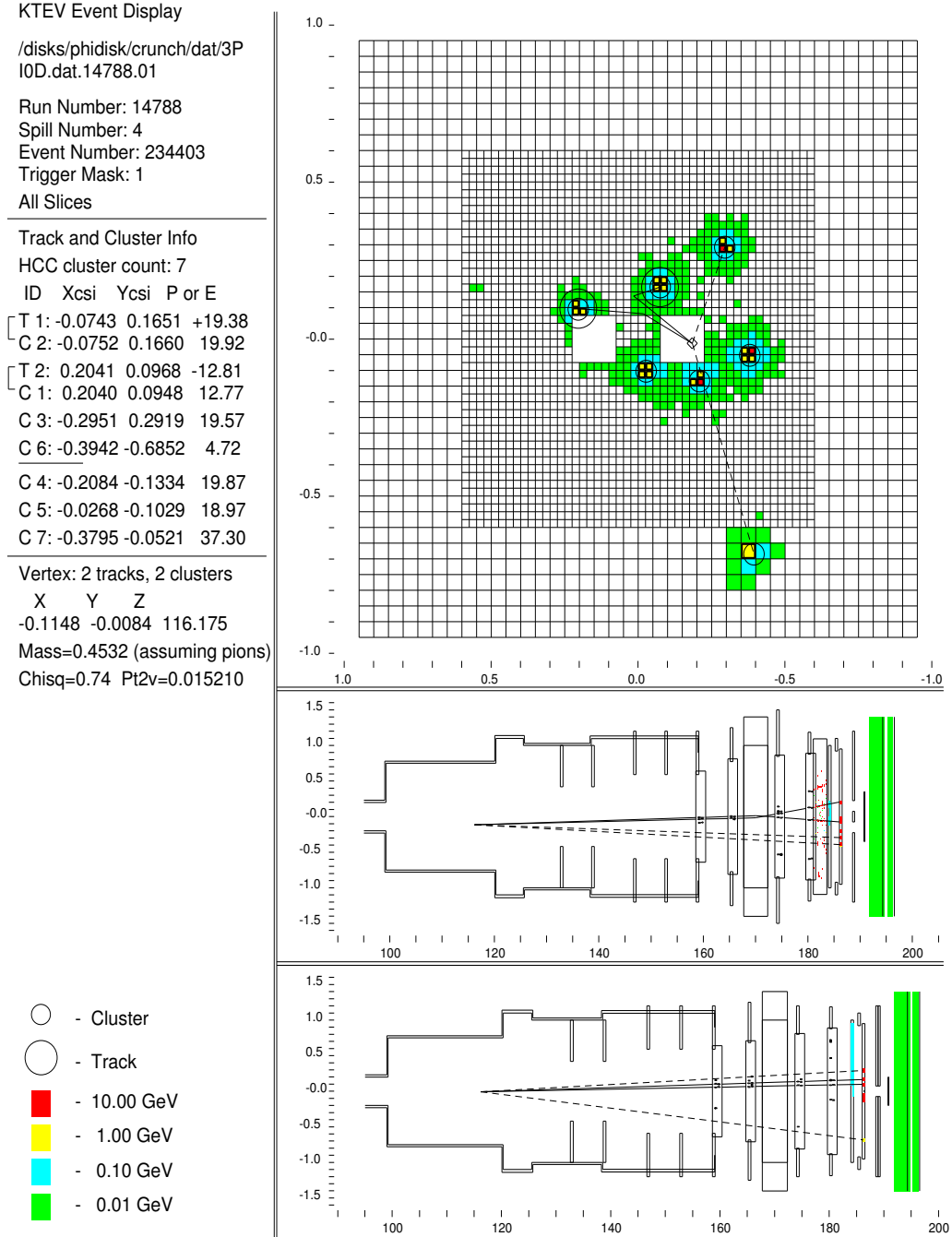


Figure 7.2: A Detector picture showing a $K_L \rightarrow \pi^0 \pi^0 \pi_D^0$ event.

the kaon mass come primarily from $Ke3$ decays with misidentified π^\pm . These decays reconstruct with a low total mass because the actual particle is a π^\pm , but it is treated as if it were an electron. The drop off of the background at about 0.43GeV in mass is

a kinematic limit due to using the electron mass instead of the pion mass. Figure 7.5 shows a plot of the mass for 1997 data set, but the cut on Π_{TRD} has been removed. This illustrates that some of the background contains charged pions. As mentioned previously, the \vec{P}_T^2 cut is used to remove events with missing or added particles. This includes the majority of backgrounds. A mass cut keeps only those events consistent with being exclusively reconstructed kaon decays. The remaining few events are the signal and subtler backgrounds.

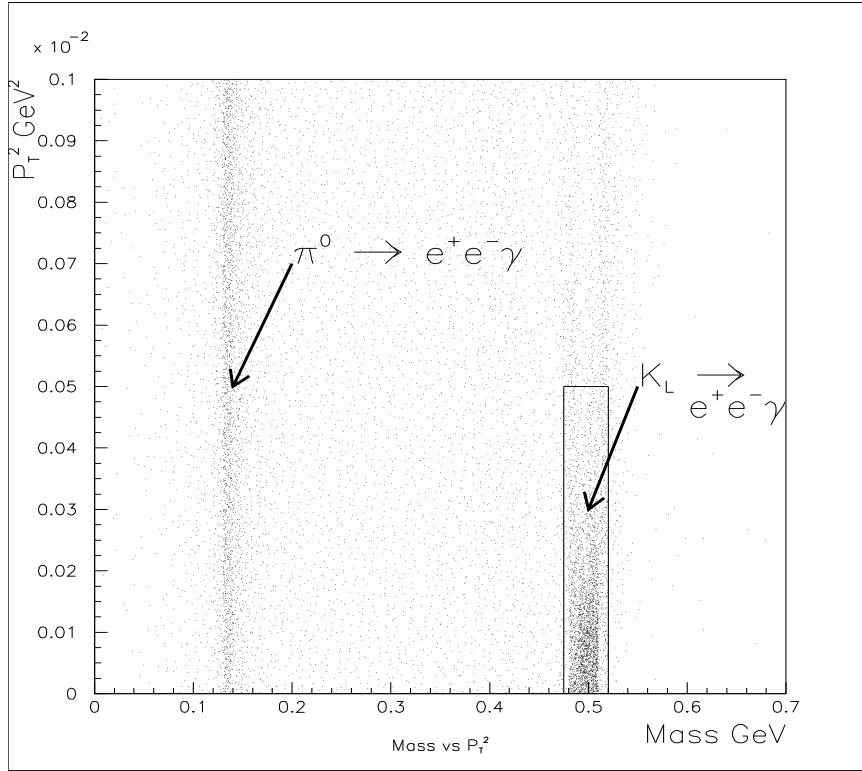


Figure 7.3: Total Invariant Mass versus \vec{P}_T^2 for $K_L \rightarrow e^+e^-\gamma$ Data events. Box defines the signal region.

In order to estimate the remaining amount of background a fit is performed to the data. Figure 7.6 shows the total mass near the kaon mass for 1997 period data only. An exponential fit to the mass distribution is performed from 0.4425 to 0.4575 MeV. This exponential is then extrapolated into the signal region and integral of the curve in that region is taken as an estimate of the remaining background. The result of the fit is 79 events. These events are subtracted from the nominal signal. Given

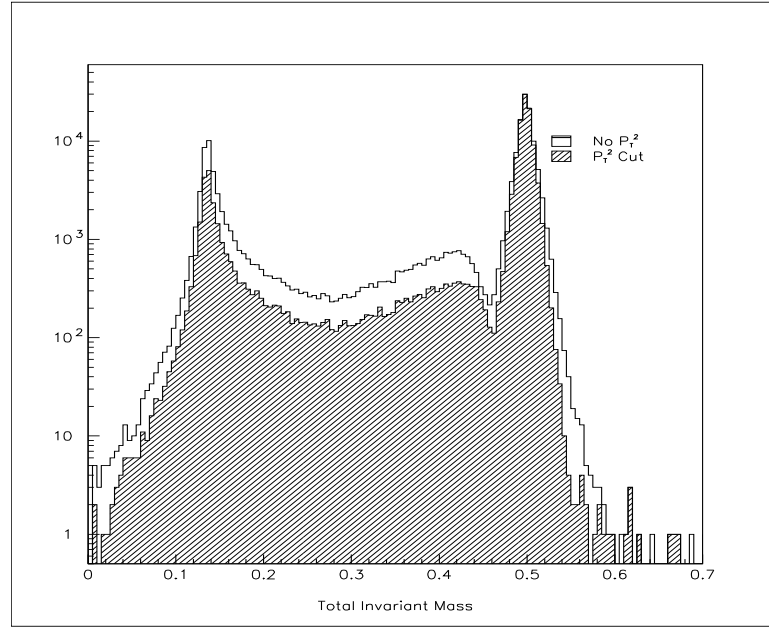


Figure 7.4: Total Invariant Mass for $K_L \rightarrow e^+e^-\gamma$ Candidate events for Data events. The hatched plot overlaid is the same mass after a \vec{P}_T^2 cut is made.

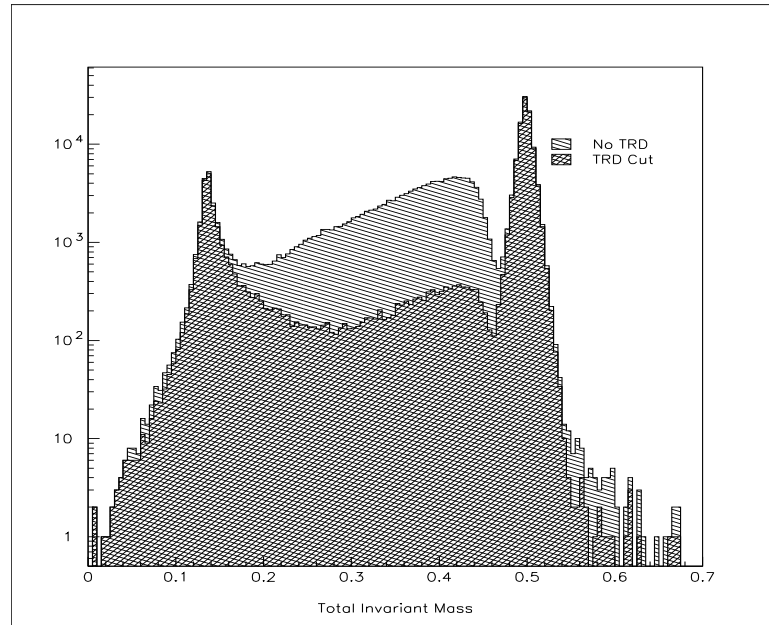


Figure 7.5: Total Invariant Mass for $K_L \rightarrow e^+e^-\gamma$ Candidate events for Data events. The hatched plot overlaid is the same mass after a Π_{TRD} cut is made.

that the fall off is due to a kinematic limit, 100% of the background was taken as a systematic uncertainty. In the 1999 data set, there is no TRD trigger and no TRD cuts made. Not surprisingly, the amount of background is much larger. Figure 7.7 shows the background fit for the 1999 period. From this fit one estimates that there is about 467 events in the signal region. The level of signal to background goes from 0.08% for 1997 to 1.41% for the 1999 set.

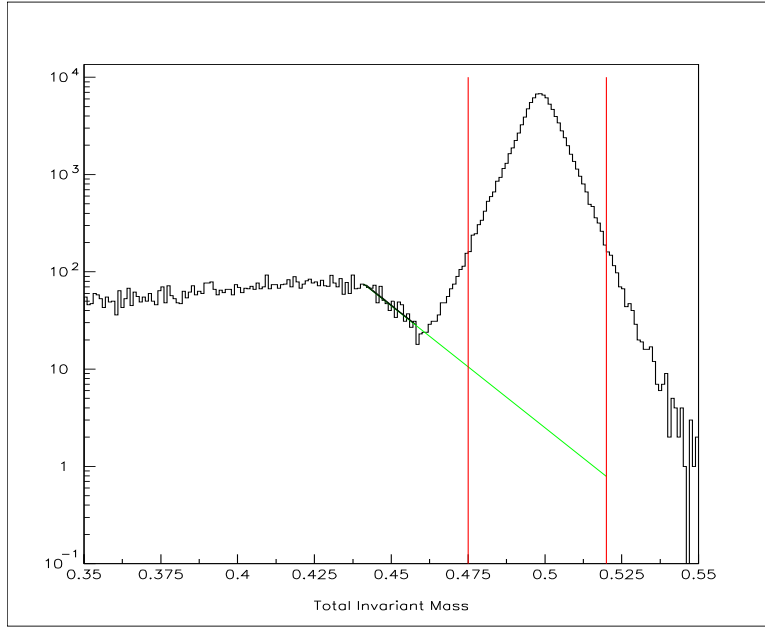


Figure 7.6: Total Invariant Mass for 1997 $K_L \rightarrow e^+e^-\gamma$ Candidate events for Data events. A fit is performed for the exponentially falling edge between 0.4425 and 0.4575 MeV, then extrapolated into the signal region denoted by the vertical lines. The number of events from this fit is 79.

A Monte Carlo is used to simulate the amount of background from conversion events. A sample of $K_L \rightarrow \gamma\gamma$ with forced conversions (see section 5.2.1) is used. The sample generated consists of ~ 10 times the data flux. No events can be found after all cuts are applied. The “killer” cut in this case is the Track Separation at DC 1. The variation of this cut described below provides a systematic check on the amount of background.

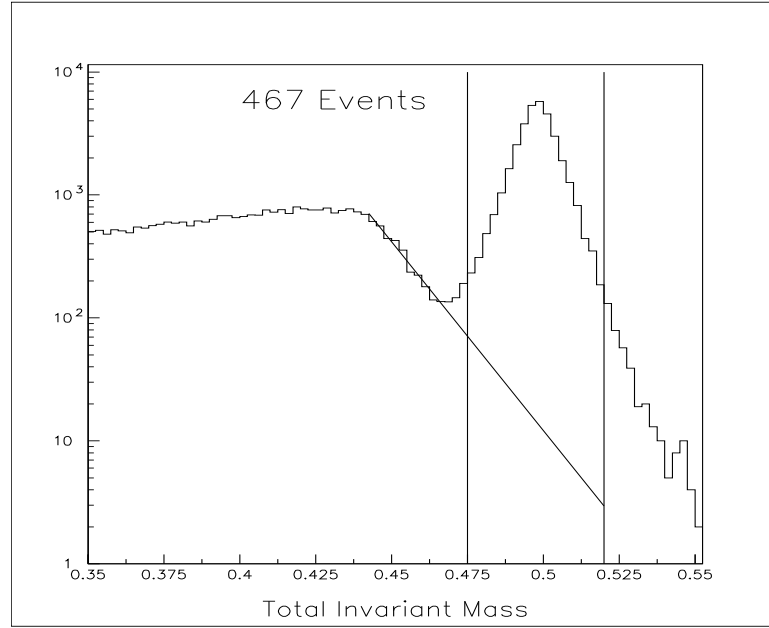


Figure 7.7: Total Invariant Mass for 1999 $K_L \rightarrow e^+e^-\gamma$ Candidate events for Data events. A fit is performed for the exponentially falling edge between 0.4425 and 0.4575 MeV, then extrapolated into the signal region denoted by the vertical lines. The number of events from this fit is 476.

7.1.2 Normalization Cuts

In order to assure that the 7 final state particles for $K_L \rightarrow \pi^0\pi^0\pi_D^0$ events came from intermediate pions more cuts are necessary. The first is a χ^2 and the second is a cut on the mass of the $e^+e^-\gamma$. Of course, a method for pairing the photons is needed, which is described in section 6.2. The pairing requires that there is a consistent vertex, with masses for 2 pairs of the 4 photons being near the π^0 mass. The odd photon is assigned to the e^+e^- to form the Dalitz state.

A χ^2 is constructed for the $K_L \rightarrow \pi^0\pi^0\pi_D^0$ decays using the assumption that there are three π^0 's of which two decay into $\gamma\gamma$ and one into $e^+e^-\gamma$. This Dalitz χ^2 depends on how well the π^0 match up to a common vertex (see section 6.2) and how close they match the π^0 mass. Figure 7.8 is a comparison of this variable between data and MC simulation. The arrow shows the cut that is made. A cut on this variable implicitly cuts on the mass of the $\pi^0 \rightarrow \gamma\gamma$. An explicit cut is made on the mass of the $\pi^0 \rightarrow e^+e^-\gamma$. Figure 7.9 shows a comparison of data and MC for the mass of the π^0 . There is some

disagreement in these two mass plots. This is most likely due to remaining uncertainty in the energy resolution, which has been assigned a systematic.

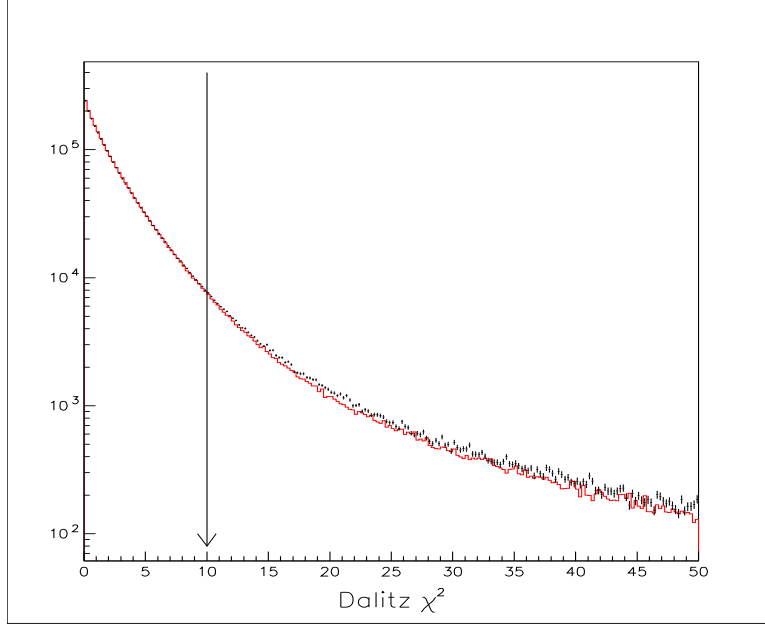


Figure 7.8: The Dalitz χ^2 for $K_L \rightarrow \pi^0 \pi^0 \pi_D^0$ events where Data (Dots) is overlaid with MC (Histogram).

There are few backgrounds to the decay $K_L \rightarrow \pi^0 \pi^0 \pi_D^0$ since there are few kaon decays with seven final state particles. Figure 7.10 is a plot of the total invariant mass of all particles versus the \vec{P}_T^2 , see section 6.8. From this plot it is obvious that there are very few backgrounds with missing particles or misidentified particles. The only backgrounds will be those with the same final state (*i.e.* conversion backgrounds). The conversion events come from $K_L \rightarrow \pi^0 \pi^0 \pi^0$ where all the π^0 's decay into $\gamma\gamma$ final states and a photon converts into an e^+e^- pair. Monte Carlo is used to predict the amount of events from this background. After generating a sample of MC equal to a data flux, no events were found from this background.

7.1.3 Data Numbers

The number of events that result from the reconstruction of data events and the application of cuts to eliminate backgrounds is listed in table 7.2 for the various data sets.

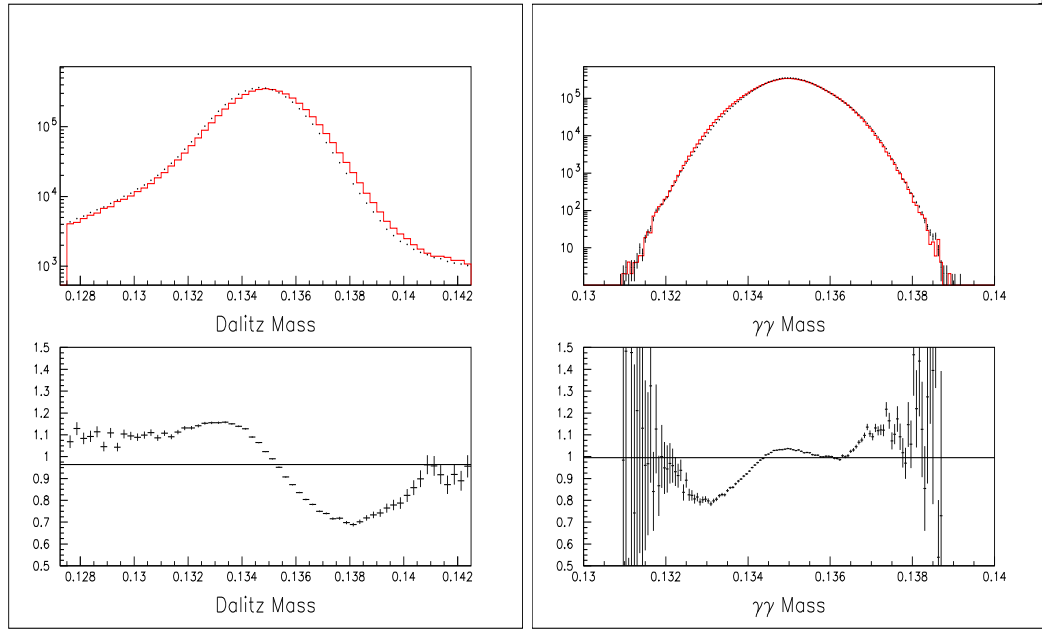


Figure 7.9: The π^0 Mass for $K_L \rightarrow \pi^0 \pi^0 \pi_D^0$ events where the Data (Dots) is overlaid on MC (Histogram). The plots on the left show the mass for $\pi^0 \rightarrow e^+ e^- \gamma$, Plots on the Right show mass for $\pi^0 \rightarrow \gamma \gamma$.

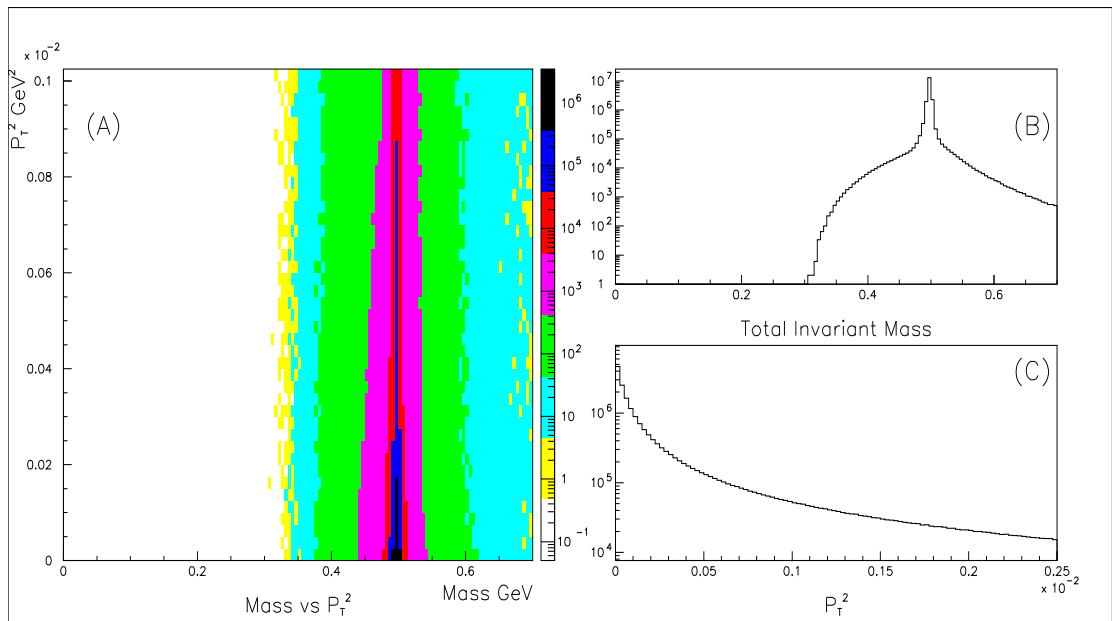


Figure 7.10: Total Invariant Mass versus \vec{P}_T^2 for $K_L \rightarrow \pi^0 \pi^0 \pi_D^0$ events, Plot (A). Plot (B) is the projection on the x-axis and (C) is the projection on y-axis.

Mode	Winter	Summer	1999
$K_L \rightarrow e^+e^-\gamma$	50487	41782	33879 [†]
$K_L \rightarrow \pi^0\pi^0\pi_D^0$	2778007	2023181	9729646

Table 7.2: The Number of Events in the Data for Signal and Normalization modes. [†] indicates that the estimated background of 476 events has been subtracted.

7.2 Monte Carlo Sample

The acceptance of our detector and reconstruction procedure was calculated using a Monte Carlo simulation, explained in chapter 5. In particular the $K_L \rightarrow e^+e^-\gamma$ and the $K_L \rightarrow \pi^0\pi^0\pi_D^0$ generators are of importance, from sections 5.2.2 and 5.2.4 respectively. Tables 7.3 and 7.4 lists the amount of MC generated and the amount left at various stages of the reconstruction and simulation. Also given is the acceptance with statistical errors.

Quantity	Winter	Summer
K_L Generated	7978720	5799330
MC after L1 simulation	1901400	1365534
MC after L2 simulation	1323209	1070069
MC after L3 simulation	985607	797020
MC after all cuts	257453	215930
$\epsilon_{e^+e^-\gamma}$	0.03228 ± 0.00005	0.03723 ± 0.00005

Table 7.3: The Monte Carlo Numbers and Acceptance for $K_L \rightarrow e^+e^-\gamma$ events. The errors are statistical.

Quantity	Winter	Summer
K_L Generated	562145920	406017400
MC after L1 simulation	55651823	39345576
MC after L2 simulation	42499790	31140695
MC after L3 simulation	21757954	15724675
MC after all cuts	1371152	1019088
$\epsilon_{\pi^0\pi^0\pi_D^0}$	0.002439 ± 0.000002	0.002510 ± 0.000002

Table 7.4: The Monte Carlo Numbers and Acceptance for $K_L \rightarrow \pi^0\pi^0\pi_D^0$ events. The errors are statistical.

A standard method of determining the quality of the simulation of the detector from the MC is to take histograms of various variables and comparing the distribution

from data and MC. Usually, one takes the ratio of the data over the MC distribution and looks for slopes or disagreements. Many of these ratios are scattered throughout this thesis, but figures 7.11, 7.12, 7.13, 7.14, and 7.15 are typical. There is some disagreement in the total invariant mass plot of the $K_L \rightarrow \pi^0 \pi^0 \pi_D^0$ events, which is most likely do to misunderstanding of the energy resolutions. This is covered in a systematic study.

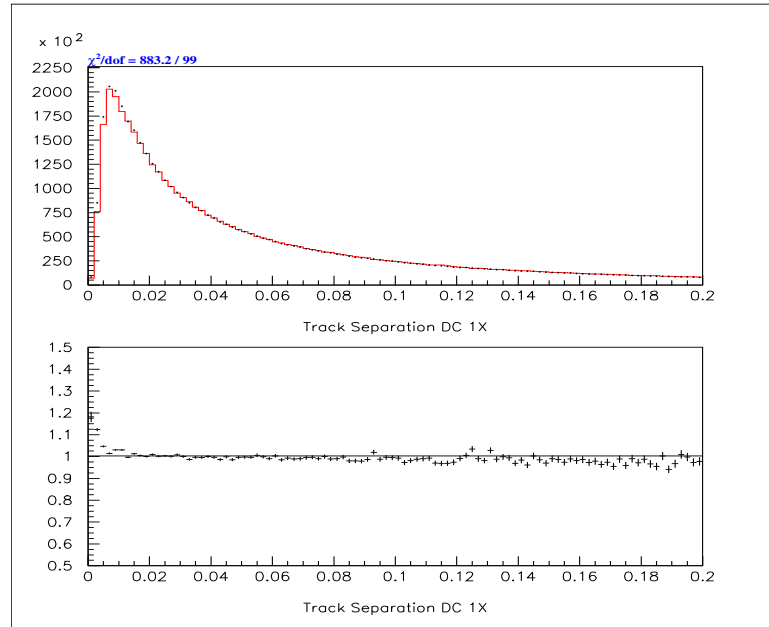


Figure 7.11: Track Separation at DC 1 x view, comparing Data (Dots) to MC (Histogram) for $K_L \rightarrow \pi^0 \pi^0 \pi_D^0$ events.

7.3 Flux

The normalization mode is used to calculate the flux of kaons produced during the running of the experiment. The equation used is defined in equation 7.3, and uses the acceptance, $\epsilon_{\pi^0 \pi^0 \pi_D^0}$, from table 7.4 and the branching ratio of $K_L \rightarrow \pi^0 \pi^0 \pi_D^0$ from equation 5.7. The result of this calculation is shown in table 7.5.

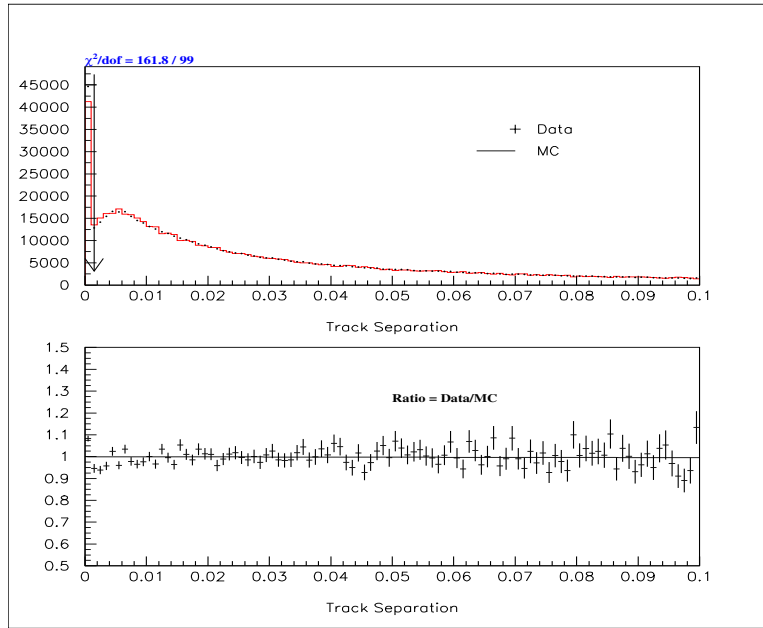


Figure 7.12: Track Separation at DC 1 x view, comparing Data (Dots) to MC (Histogram) for $K_L \rightarrow e^+e^-\gamma$ events.

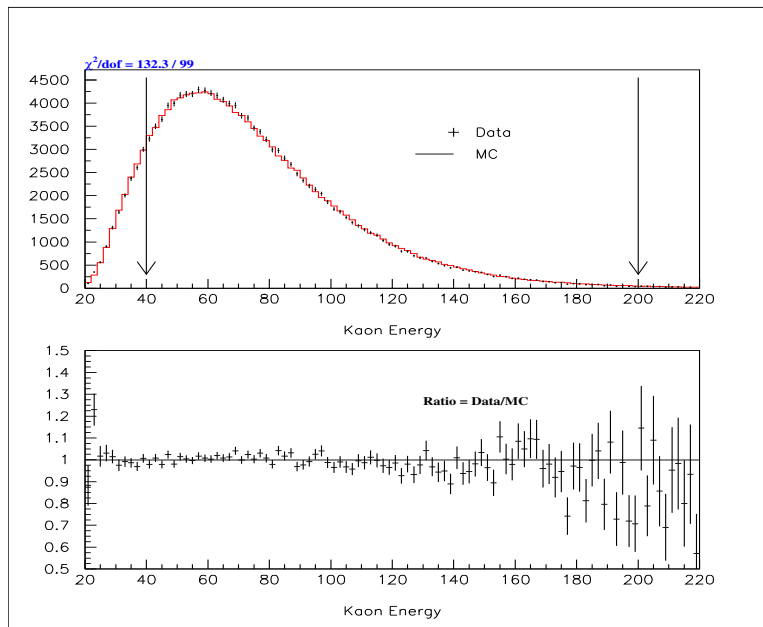


Figure 7.13: Kaon Energy for $K_L \rightarrow e^+e^-\gamma$ events, Comparing Data (Dots) to MC (Histogram) with the ratio shown below. The arrows show the region selected by the cut.

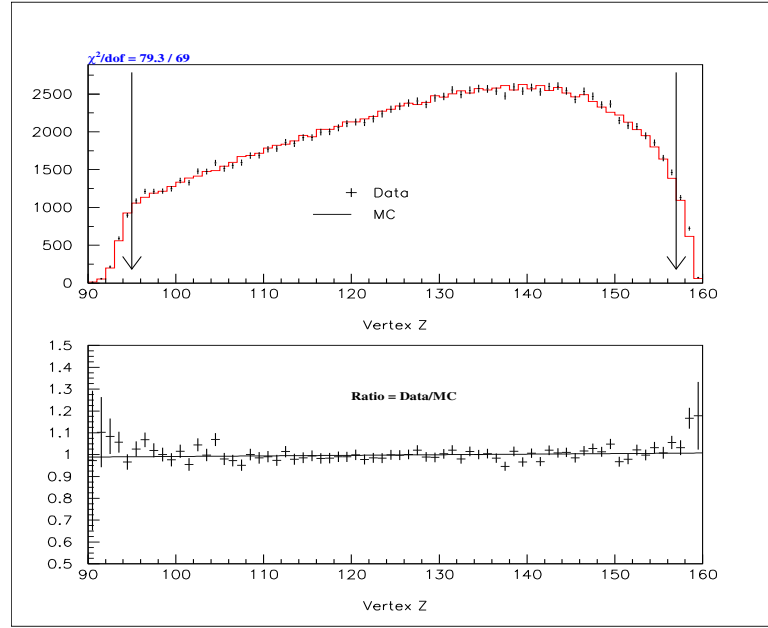


Figure 7.14: z Position of the Kaon Decay Vertex for $K_L \rightarrow e^+e^-\gamma$ events, Comparing Data (Dots) to MC (Histogram) with the ratio shown below. The arrows show the region selected by the cut.

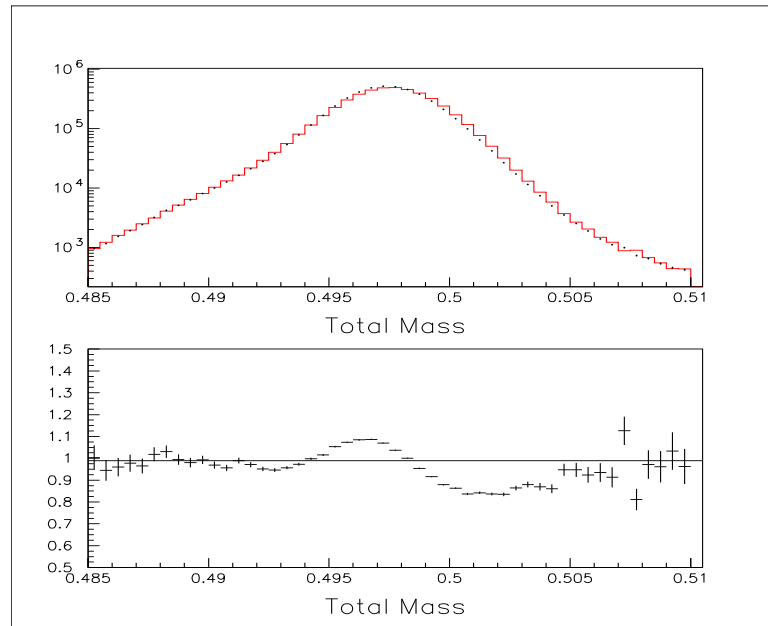


Figure 7.15: The Total Invariant Mass for $K_L \rightarrow \pi^0\pi^0\pi^0$ events where Data (Dots) is overlayed with MC (Histogram).

	1997 Winter	1997 Summer
\mathcal{F}	$(1.537 \pm 0.003) \times 10^{11}$	$(1.088 \pm 0.003) \times 10^{11}$

Table 7.5: The number of kaons produced from the Target in the specific region of energy and vertex z as discussed in section 5.1, for the two run periods. The errors are statistical.

7.4 Branching Ratio

The calculation of the $K_L \rightarrow e^+e^-\gamma$ branching ratio depends on the flux, calculated above, the signal mode acceptance (see table 7.3), and the number of events found. Table 7.6 is the result of the calculation using the numbers already provided. The errors here are purely statistical.

	1997 Winter	1997 Summer
$BR(K_L \rightarrow e^+e^-\gamma)$	$(10.177 \pm 0.049) \times 10^{-6}$	$(10.210 \pm 0.054) \times 10^{-6}$

Table 7.6: The Branching Ratio for $K_L \rightarrow e^+e^-\gamma$ as a function of run period. The errors are statistical.

7.5 Systematics

In addition to the statistical error associated with measurement of the branching ratio, there are systematic errors. These errors represent the limitations of the Monte Carlo in simulating the responses of the detector. Quite a bit of effort was put into making the MC as accurate as possible, but it is not perfect. The majority of the systematics come from studies on the spectrometer and the calorimeter.

7.5.1 Varying Sets Of Cuts

A useful test of the quality of the Monte Carlo simulation of the data is the variation of cuts. Each cut was defined at a nominal value in table 7.1, however, table 7.7 defines another set of reasonable cuts on these variables. An uncertainty was determined by taking the larger difference between the branching ratios calculated using the loose cut values or the tight cut values. The largest difference was between the loose and nominal values and resulted in a change of the branching ratio equal to 0.33%.

Cut	Loose Value	Tight Value
Vertex X	−0.22m to 0.22m	−0.18m to 0.18m
Vertex Y	−0.11m to 0.11m	−0.09m to 0.09m
Vertex Z	94.0m to 158.0m	96.0m to 156.0m
E/p	0.90 to 1.10	0.95 to 1.05
Photon Veto	<0.20GeV	<0.10GeV
$K_L \rightarrow e^+e^-\gamma$ Total Mass	0.470GeV to 0.525GeV	0.480GeV to 0.515GeV
$K_L \rightarrow \pi^0\pi^0\pi_D^0$ Total Mass	0.480GeV to 0.515GeV	0.490GeV to 0.505GeV
P_t^2	<0.0006GeV ²	<0.0004GeV ²
Minimum E_γ	>2.5GeV	>3.0GeV
Track Separation @ DC1	>0.001m	>0.002m
Pion Probability	<0.06	<0.04
Dalitz χ^2	<12.0	<8.0
E_{tot}	35.0GeV to 210.0GeV	45.0GeV to 190.0GeV
Vertex χ^2	<12.0	<8.0
Magnet Offset χ^2	<45.0	<35.0

Table 7.7: Definition of Loose and Tight Cut for $K_L \rightarrow e^+e^-\gamma$.

7.5.2 Upstream Detector Material

The amount of material in the upstream portion of the spectrometer is not perfectly known, as is discussed in appendix B. Ideally, one would generate MC at $\pm 1\sigma$ of the measured amount and then see the difference in the branching ratios using these different amounts. However, the statistical error associated with MC for each of these samples becomes important. One would need to generate a very large amount of MC to cause this error to become small enough. There is another method which makes one less sensitive to the statistics of the MC. Instead of generating at $\pm 1\sigma$ of the measured material, one generates at $\sim 7\sigma$ and interpolates back to the 1σ level. Figure 7.16 shows the effect of doing this with appropriate MC error bars. The black points are the branching ratio using the MC with different materials 7σ from nominal, the small vertical lines represent the 1σ change in the material, and the horizontal lines represent the maximum amount of change in the branching ratio for the 1σ change in material. The systematic that results is equal to 0.07% in the branching ratio.

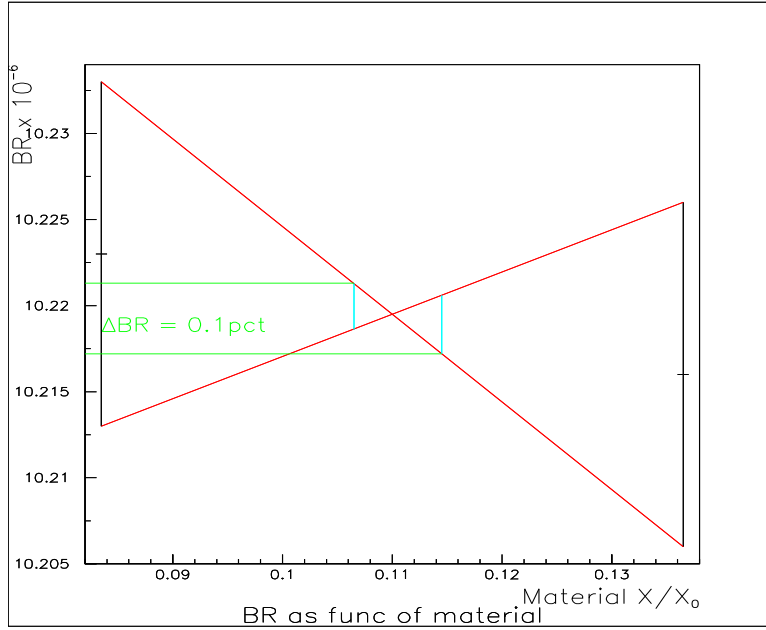


Figure 7.16: The Change in the Branching Ratio as a Function of Varying the Amount of Material in the Upstream part of the Detector.

7.5.3 Track Hit Inefficiency

As discussed in section 5.3.2, there is an inefficiency for detecting hits in the Drift Chamber. This inefficiency was measured and corresponding maps implemented in the MC, as shown in figure 5.16. A small discrepancy can still be observed in the beam region. By multiplying the size of the inefficiency maps by a factor of 1.4, an illumination plot like that shown in 7.17 can be obtained. Careful study of the level of the inefficiency as a function of the factor reveals that the best fit value is 1.40 ± 0.33 . The MC used for the calculation of the branching ratio used the best fit value for the map factor.

The systematic uncertainty on the branching ratio is figured by taking half the difference in branching ratio for events reweighted for a map factor of $\pm 1\sigma$ of the nominal (i.e. map weights of 1.07 and 1.73). Instead of generating MC with different map factors, the MC events were reweighted using a function based on their position in a chamber and the maps used in the MC. This means that if a MC event is located in a inefficient region of the chamber, then it was given a smaller or larger weight compared to other

events depending on the map factor (*i.e.* larger weight if the factor is less, smaller if the factor is larger). Figure 7.18 shows a comparison of this reweighting compared to two small samples of MC generated with the different factors. This plot is evidence that the reweighting of the MC events is equivalent to generating MC with different factors. The difference in branching ratios gives an uncertainty of 0.37%

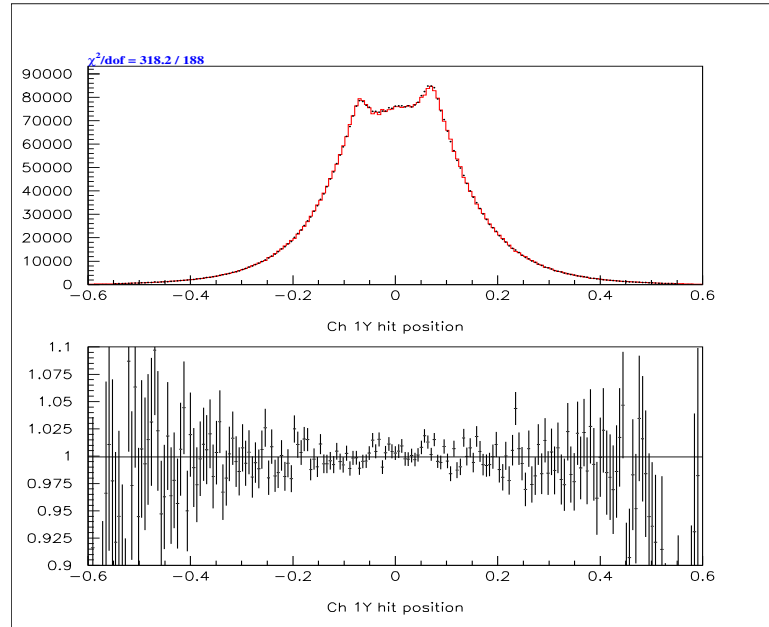


Figure 7.17: Drift Chamber 1 Y Illumination Plot (in meters) with DC Map \times Factor 1.4

7.5.4 Hit resolution

Discrepancies in the sum-of-distance (also called SOD see section 4.1.1) distributions are evidence of further disagreement between data and Monte Carlo. This can be seen in figure 7.19. The center of the SOD distribution is dependent on the intrinsic resolution of the drift chambers. By smearing hits in order to increase the width of the SOD distribution by 10% of itself, as indicated in figure 7.20, one can estimate the dependence of the branching ratio and form factor on the SOD distributions. Taking the difference of the branching ratio gives an uncertainty of 0.04%.

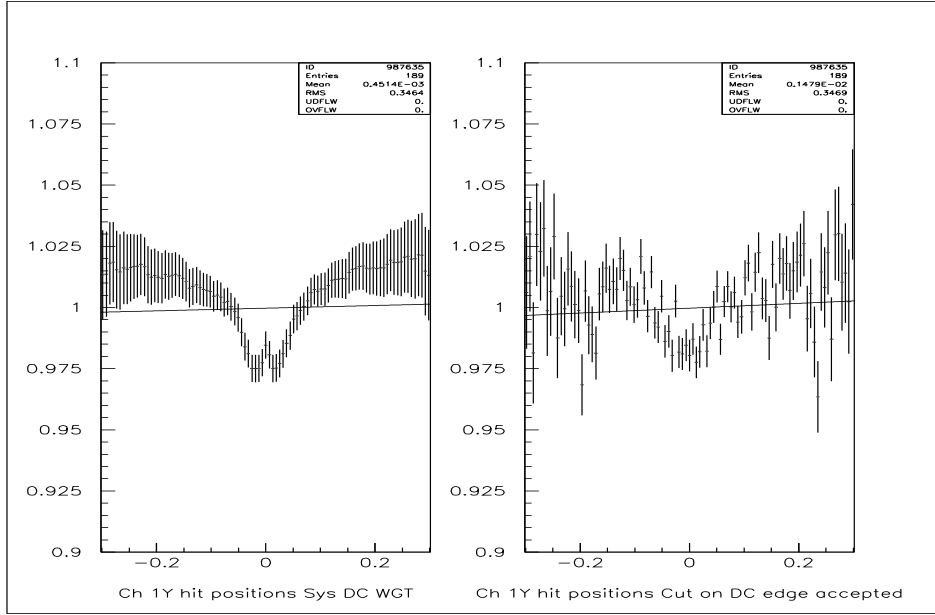


Figure 7.18: Drift Chamber 1Y Illumination Ratio of Monte Carlo with Map Weight of 1.0 compared to Map Weight of 1.4 using reweighting (left) and generated (right)

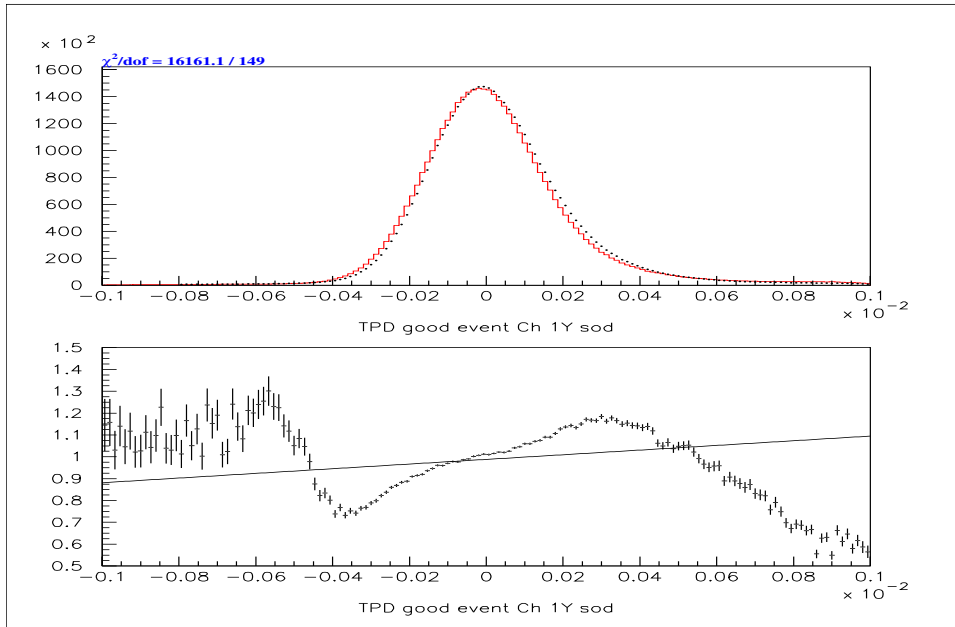


Figure 7.19: Drift Chamber 1Y Sum-of-Distance (SOD) minus 6.35mm comparing $K_L \rightarrow \pi^0 \pi^0 \pi_D^0$ Data (Dots) and MC (Histogram). Top plot is an overlay, bottom plot is a ratio of Data to MC.

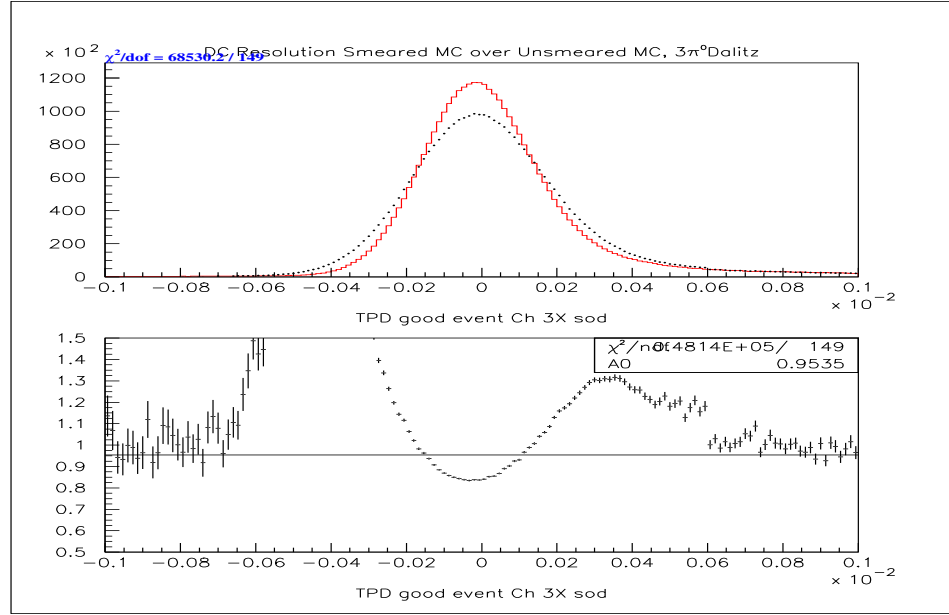


Figure 7.20: Drift Chamber 1Y Sum-of-Distance (SOD) minus 6.35mm comparing $K_L \rightarrow \pi^0 \pi^0 \pi_D^0$ Data MC with (Dots) and without (Histogram) an Additional Amount of Hit Smearing. Top plot is an overlay and the Bottom plot is a ratio of MC with additional smearing over MC without.

7.5.5 Energy Slope

Another discrepancy between data and MC can be seen in the kaon energy distribution. This can be seen in figure 7.21. By applying a fudge to the energy of the MC events in such a way to eliminate the slope, see figure 7.22, one can estimate an uncertainty associated with the discrepancy. The full difference between fixing the slope and using the default Monte Carlo is taken. This gives a difference of 0.23% in the branching ratio. The branching ratio calculation uses the fudged MC that has a flat energy ratio.

7.5.6 Energy resolution

The E/P (energy over momentum) distribution is sensitive to the energy resolution. As can be seen in figure 7.23, the RMS widths of the E/P distributions in the data and the default MC are significantly different. One can develop a “smearing” routine which will change the energy of MC events in order to increase the width of the MC E/P , the effects of which can be seen in figure 7.23. The energy resolution also

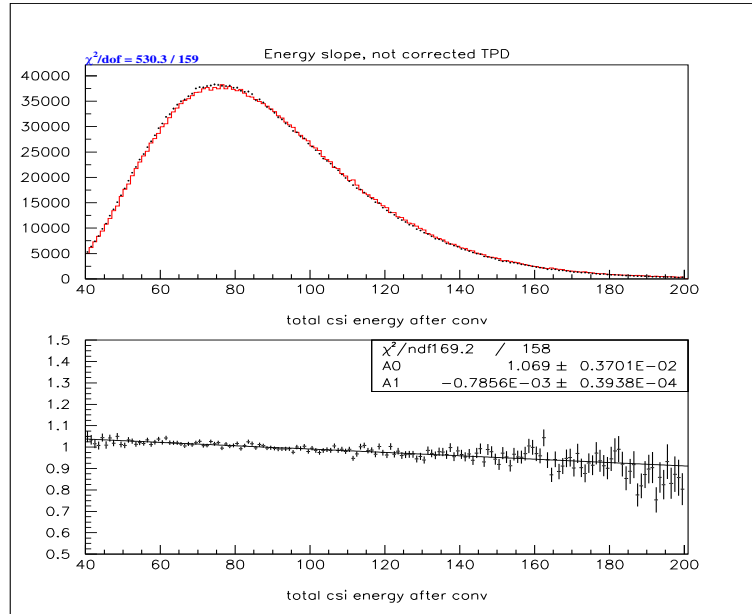


Figure 7.21: Total Kaon Energy after all cuts for $K_L \rightarrow \pi^0 \pi^0 \pi_D^0$ Data (Dots) compared to MC (Histogram). Top plot is overlay and the Bottom is the ratio of Data over MC.

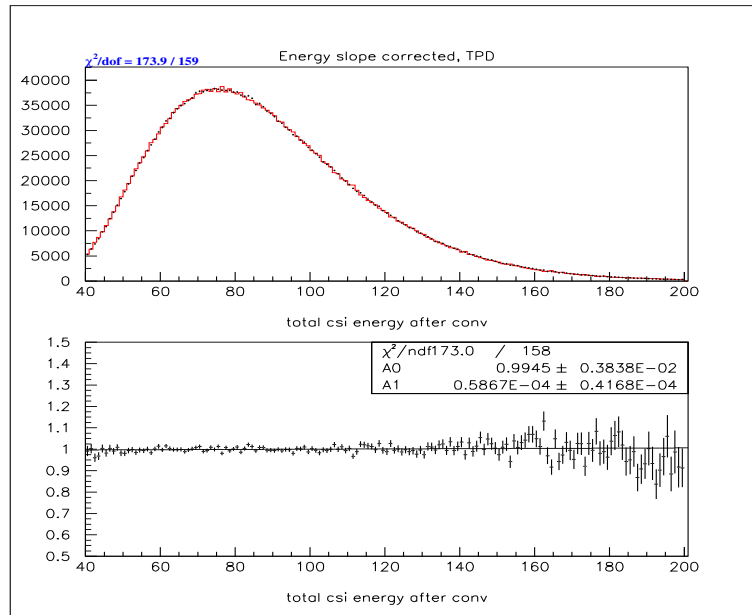


Figure 7.22: Total Kaon Energy after all cuts for $K_L \rightarrow \pi^0 \pi^0 \pi_D^0$ Data (Dots) compared to MC (Histogram) with reweighting applied. Top plot is overlay and the Bottom is the ratio of Data over MC.

affects the Dalitz χ^2 , defined in section 7.1.2 above, as shown in figure 7.24.

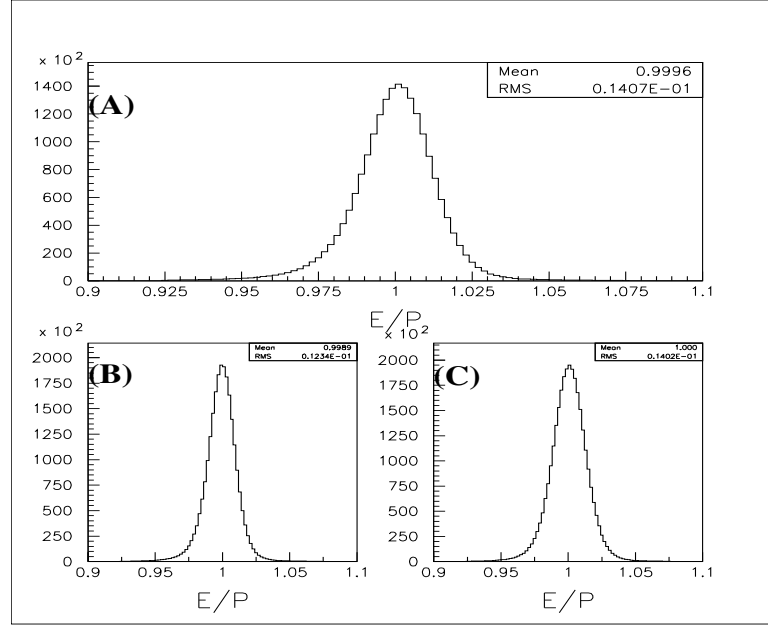


Figure 7.23: The E/P after all selection cuts for $K_L \rightarrow \pi^0 \pi^0 \pi_D^0$ events. Plot (A) is the data, plot (B) is the Default MC, and plot (C) has had the energy resolution smeared.

The amount of additional smearing is controlled by a parameter called δ . When δ is equal to zero then the default MC energy resolution is used, $\delta = 0.10$ implies that the resolution is degraded by an additional 10% of itself. I varied the parameter δ over a wide range, much larger than would seem reasonable by looking at the Dalitz χ^2 distribution. Varying δ by 0.01 implies that the energy resolution is known to 1% of itself, which is a reasonable amount. Figure 7.25 shows the dependence of the branching ratio as a function of the smearing parameter δ and the interpolation of the error assuming a 1% variation on δ . The uncertainty that results is 0.14%.

7.5.7 γ Inefficiency

One of the biggest differences between the signal and normalization modes is that the normalization mode has four more photons in the final state, $e^+e^-\gamma$ compared to $e^+e^-\gamma\gamma\gamma\gamma$. Thus, the absolute inefficiency for reconstructing photons is an important source of error. As there are five times as many photons in the normalization mode the effect does not cancel.

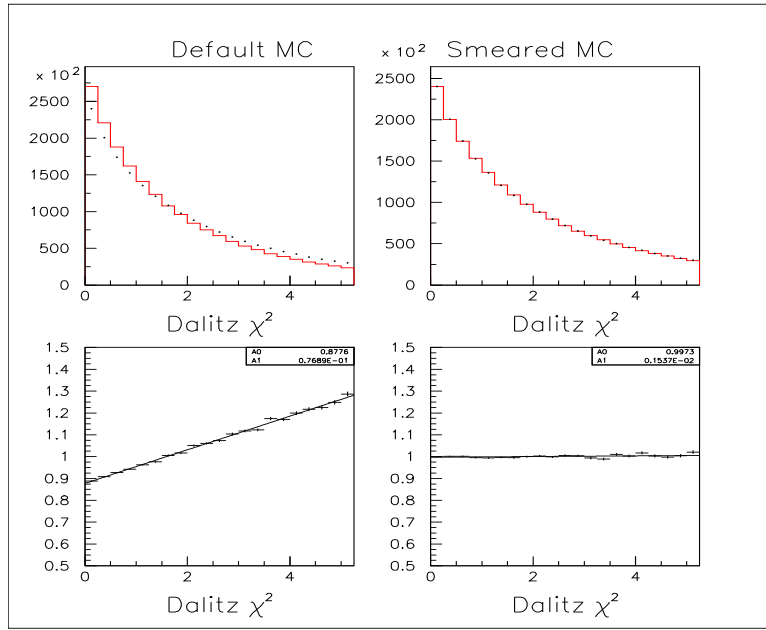


Figure 7.24: The Dalitz χ^2 for $K_L \rightarrow \pi^0 \pi^0 \pi^0$ events comparing the Data (Dots) to Default MC (Left Histogram) and the Smeared MC (Right Histogram). Plots on the Top are overlays while those on the bottom are ratios of Data over MC.

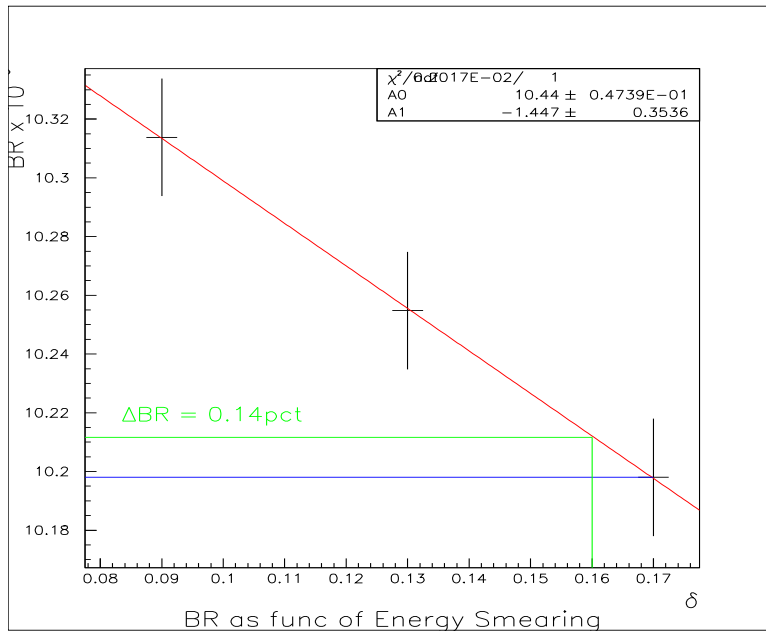


Figure 7.25: The Branching Ratio as a function of the Energy Smearing Parameter δ .

There are several ways of misreconstructing a photon. The simulation of the edge of the CsI detector can be imperfect. Thus, photons could be lost differently (*e.g.* by going down a beam hole) in the data and MC. A cut is made on the edges of the CsI Calorimeter, but by observing the affect on the branching ratio of changing the cut for just the normalization mode, one can get an idea of the possible systematic error. Figure 7.26 shows the smallest Distance to any CsI calorimeter edge for $K_L \rightarrow \pi^0 \pi^0 \pi_D^0$ Data and MC. Shifting the cut by 0.5mm for the Monte Carlo only, implying that the edge is not understood to within 0.5mm causes a change in the branching ratio of 0.226%.

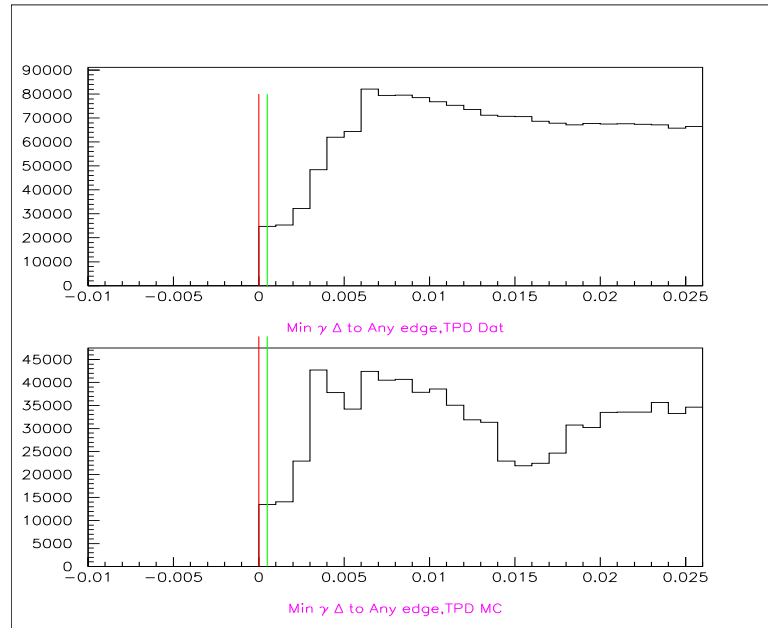


Figure 7.26: Top plot is the Position of the γ that is closest to a CsI Calorimeter Edge for the Data, the Bottom is the same for the MC. The first vertical line is the value of the nominal cut, the second is the value of the cut +5mm.

Another source of loss would be if the energy spectrum of photons was not well simulated in the MC. A cut is made at 2.75 GeV, but if the mean cluster energy for photons is off by 10MeV then the loss of events due to the cut could be different for data and MC. Figure 7.27 shows the smallest energy for all photons in $K_L \rightarrow \pi^0 \pi^0 \pi_D^0$ events for data and MC. A shift of 10MeV in the MC results in a branching ratio change of 0.219%.

Photons that hit the CsI are assumed to deposit all of their energy in the Calorime-

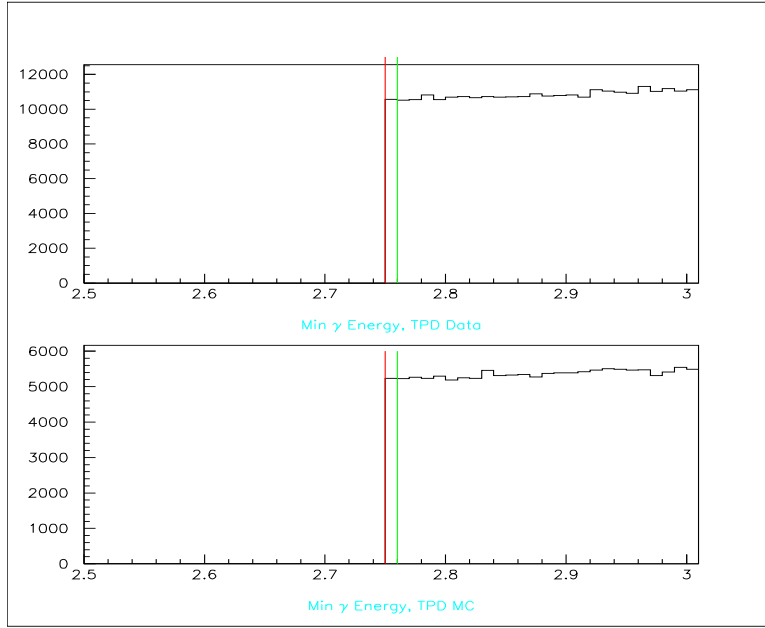


Figure 7.27: Top plot is the Energy of the γ with the Smallest Energy for the Data, the Bottom is the same for the MC. The first vertical line is the value of the nominal cut, the second is the value of the cut +10MeV.

ter, however, the reconstruction of all the energy is not always guaranteed. One can observe this effect by looking at the E/P distribution of well measured electrons. A source of these electrons is from $Ke3$ events where the Transition Radiation Detectors are used to identify the electron. Figure 6.26 shows the this distribution for Data and Monte Carlo events, with a clear low end tail. The default MC has a simulation of this tail, but a separate study using $K_L \rightarrow \pi^0 \pi^0 \pi^0$ events from the E832 data set [3] shows that the default tail was not sufficient. A new tail is produced from this data set, and the difference between the new tail and the default is taken as an uncertainty. Figure 7.28 shows the different functional forms used to study the systematic effects. Figure 7.29 compares the MC with the New Tail to the MC with the Default in the variable of the invariant mass of $\gamma\gamma$ pairs. The difference in branching ratios for the two sets is 0.288%.

The total change from these three sources added in quadrature is 0.43%. This is taken as the uncertainty due to photon losses.

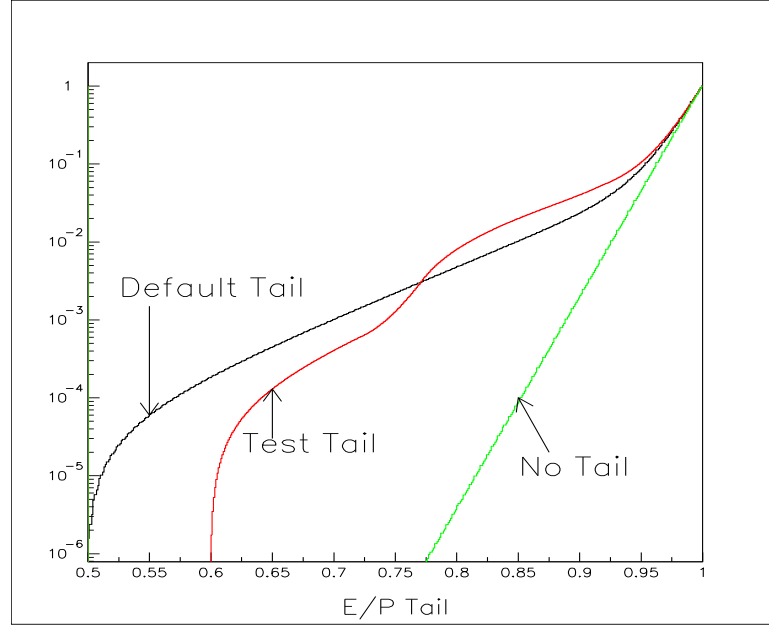


Figure 7.28: The functional dependence of the far E/P used in the MC generation for $K_L \rightarrow \pi^0 \pi^0 \pi_D^0$ events. The Test Tail was the best fit shape from a study of $K_L \rightarrow \pi^0 \pi^0 \pi^0$ events [3], the Default Tail is what was assumed, and the No Tail was from turning off all tails.

7.5.8 Radiative Corrections

Figure 7.30 compares the total invariant mass from MC with tree-level-only graphs to that from MC with one-loop and radiative corrections (see section 5.2.2). The default MC includes these corrections, but there are still higher order corrections that could be included, *e.g.* two loop corrections and one loop corrections to the radiative graphs. These corrections have not been calculated, but an estimate of the effect can be made. The difference in the branching ratio using MC with and without the corrections is equal to 1.7%. Assuming that the next order corrections would be another 1.7% of the existing 1.7% change, then there could be a change of 0.03% in the branching ratio.

7.5.9 Varying BMS Form Factor α_K^*

The form factor used by the Monte Carlo generation has a dependence on a free parameter (*e.g.* α_{K^*} for the BMS model). The acceptance of the signal mode depends to a small degree on this parameter. Therefore, by varying the best fit parameter by

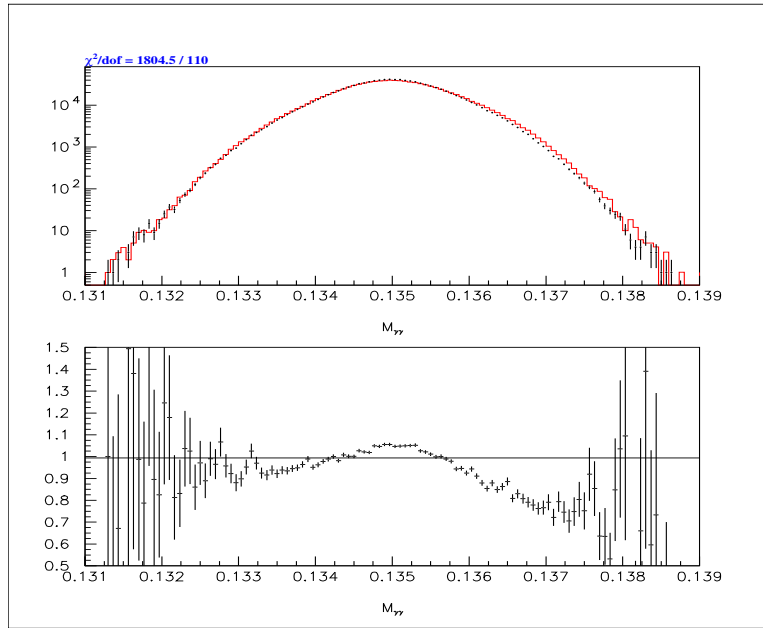


Figure 7.29: The ratio of MC with the Default E/P Tail (Dots) to MC (Histogram) with the New E/P Tail measured from $K_L \rightarrow \pi^0 \pi^0 \pi^0$ events [3]. Top plot is the overlay and the bottom is the ratio.

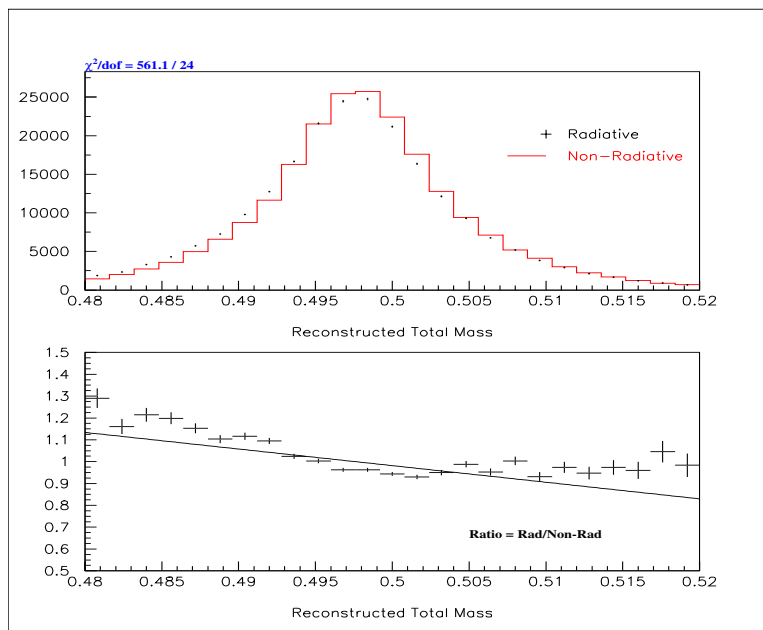


Figure 7.30: Total Invariant Mass for $K_L \rightarrow e^+ e^- \gamma$ MC events. The dots include one loop correction and radiative graphs and the histogram does not.

$\pm 1\sigma$ of its uncertainty, a change in the branching ratio can be found. The method of finding the best parameter is discussed in section 9.1. Figure 7.31 shows the ratio of m_{ee} spectrum for $+1\sigma$ over -1σ of the measured α_{K^*} for $K_L \rightarrow e^+e^-\gamma$. The change in the branching ratio is 0.03%

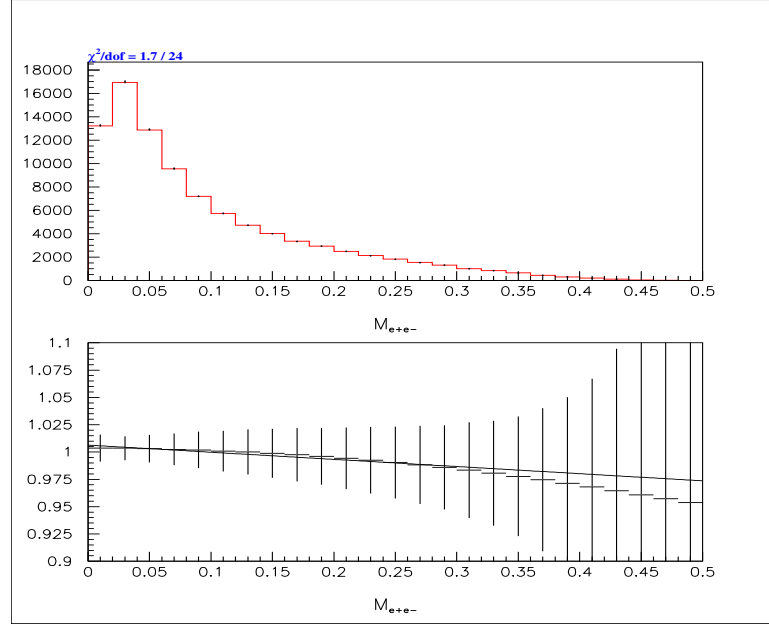


Figure 7.31: m_{ee} Ratio of Monte Carlo with $+1\sigma$ of best fit α_{K^*} over -1σ .

7.6 Result

Table 7.8 lists all of the sources of uncertainty for this analysis. The systematic uncertainties discussed above are combined in quadrature to form a total uncertainty. This gives an answer for the branching ratio with a list of uncertainties, see equation 7.4. The uncertainties here are split into a statistical component, the systematics discussed above and the uncertainty associated $K_L \rightarrow \pi^0\pi^0\pi_D^0$ branching ratio, labeled as the external systematic uncertainty. The largest component of the uncertainty comes from the uncertainty in $BR(\pi^0 \rightarrow e^+e^-\gamma)$.

The final result with all the errors is

$$BR(K_L \rightarrow e^+e^-\gamma) = (10.192 \pm 0.036_{\text{stat}} \pm 0.073_{\text{sys}} \pm 0.285_{\text{ext sys}}) \times 10^{-6}. \quad (7.4)$$

These results agree rather well with previously measured results. Table 1.3 lists

Uncertainty Source	% of Branching Ratio
Statistical	0.36%
$BR(K_L \rightarrow \pi^0 \pi^0 \pi_D^0)$ Uncertainty	2.85%
γ Inefficiency	0.43%
DC Inefficiency	0.37%
Cut Variations	0.33%
Energy Slope	0.23%
Energy Resolution	0.14%
Backgrounds	0.08%
Upstream Material	0.07%
DC Hit Resolution	0.04%
Radiative Corrections	0.03%
Form Factor Dependence	0.03%
Total Systematic	0.72%

Table 7.8: List of Sources of Uncertainty for the Branching Ratio measurement of $K_L \rightarrow e^+ e^- \gamma$.

the previously measured results and this result lies within the error bars of the previously measured values as is illustrated by figure 7.32. The result is systematically limited at this time.

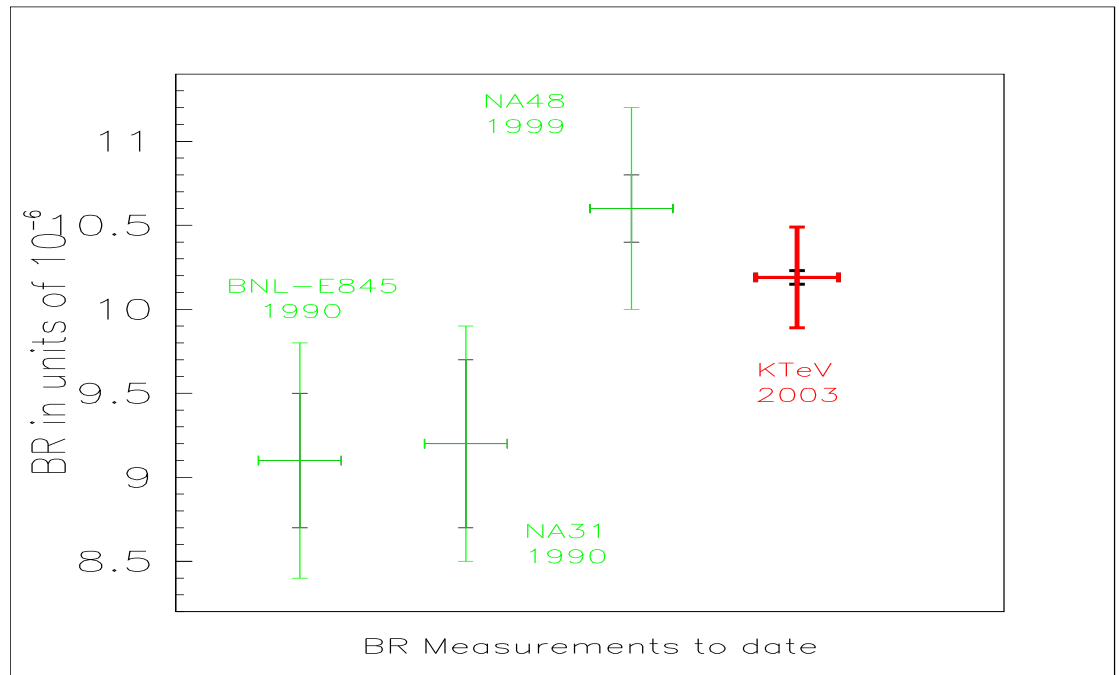


Figure 7.32: Previously measured values of the Branching Ratio of $K_L \rightarrow e^+e^-\gamma$ with the current measurement also shown.

Chapter 8

$K_L \rightarrow e^+e^-e^+e^-$ Branching Ratio

Another goal of the analysis is the measurement of the branching ratio for $K_L \rightarrow e^+e^-e^+e^-$. The method is the same as for the calculation of the $K_L \rightarrow e^+e^-\gamma$ branching ratio, with the exception that signal and normalization modes are different. This branching ratio is calculated as follows:

$$BR(K_L \rightarrow e^+e^-e^+e^-) = \frac{N_{4e}^{obs}}{\epsilon_{4e} \cdot \mathcal{F}}, \quad (8.1)$$

where N_{4e}^{obs} is the number of signal events with any background subtraction, ϵ_{4e} is the acceptance or efficiency of the detector, and \mathcal{F} is the flux of kaons for the experiment.

The efficiency of the detector is calculated using Monte Carlo simulations of the detector. Therefore, the agreement of the MC with the Data for a variety of different kinematic and fundamental quantities is an important gauge for the degree of confidence of the result. The acceptance is calculated in the following manner:

$$\epsilon_{4e} = \frac{N_{4e}^{rec}}{N_{4e}^{gen}}, \quad (8.2)$$

where N_{4e}^{gen} is the number of kaons generated and forced to decay into the $4e$ final state and N_{4e}^{rec} is the number of such events that reconstructed by the analysis code, the same code used to find N_{4e}^{obs} .

The calculation of the flux is done by simultaneously analyzing a mode with a similar final state. The mode chosen in this case, as was mentioned previously, is $K_L \rightarrow \pi^0\pi_D^0\pi_D^0$. The flux is calculated using the known branching ratio and the acceptance of the detector as simulated by the MC. The flux is given by

$$\mathcal{F} = \frac{N_{\pi^0\pi_D^0\pi_D^0}^{obs}}{\epsilon_{\pi^0\pi_D^0\pi_D^0} \cdot BR(K_L \rightarrow \pi^0\pi_D^0\pi_D^0)}, \quad (8.3)$$

where $N_{\pi^0\pi_D^0\pi_D^0}^{obs}$ is the number of normalization events reconstructed from the data, $\epsilon_{\pi^0\pi_D^0\pi_D^0}$ is the acceptance from the MC and $BR(K_L \rightarrow \pi^0\pi_D^0\pi_D^0)$ is the independently measured branching ratio.

The study of backgrounds, the level of agreement between data and MC for both the signal mode and the normalization, and other sources give an estimate of the amount of uncertainty in the final result.

8.1 Data Selection

Chapter 6 describes a variety of cuts that are used in this analysis. These cuts are mainly trigger verification, fiducial, and particle identification cuts. Table 8.1 contains the specific cuts used in the analysis for the $K_L \rightarrow e^+e^-e^+e^-$ branching ratio and form factor. In most cases the cuts are the same for signal and normalization modes, by design. However, a few more cuts are needed to get a clean sample of normalization mode events.

Cut Variable	Accept Range	
	$K_L \rightarrow e^+e^-e^+e^-$	$K_L \rightarrow \pi^0\pi_D^0\pi_D^0$
CsI Clusters	4	8
Photon Veto	$< 0.15\text{GeV}$	$< 0.15\text{GeV}$
Minimum Cluster E	$> 2.75\text{GeV}$	$> 2.75\text{GeV}$
Distance to VV' hole	$> 0.005\text{m}$	$> 0.005\text{m}$
Vertex X	$-0.2\text{m to }+0.2\text{m}$	$-0.2\text{m to }+0.2\text{m}$
Vertex Y	$-0.1\text{m to }+0.1\text{m}$	$-0.1\text{m to }+0.1\text{m}$
Vertex Z	$95.0\text{m to }158.0\text{m}$	$95.0\text{m to }158.0\text{m}$
Min-Maximum Separation	$> 0.001\text{m}$	$> 0.001\text{m}$
4 Track Vertex χ^2	< 40.0	< 40.0
4 Track Magnet Offset χ^2	< 100.0	< 100.0
Total Kaon Energy	$40.0\text{GeV to }210.0\text{GeV}$	$40.0\text{GeV to }210.0\text{GeV}$
E/P	$0.925 \text{ to } 1.075$	$0.925 \text{ to } 1.075$
Total Mass	$0.485\text{GeV to }0.510\text{GeV}$	$0.485\text{GeV to }0.510\text{GeV}$
P_t^2	$< 0.0003\text{GeV}^2$	$< 0.0003\text{GeV}^2$
Two Dalitz χ^2	-	< 12.0
Double Dalitz χ^2	-	> 12.0
$e^+e^-\gamma$ Mass	-	$0.1275 \text{ to } 0.1425 \text{ GeV}$
Neutral Vertex Z	-	$90.0\text{m to }160.0\text{m}$

Table 8.1: $K_L \rightarrow e^+e^-e^+e^-$ Cuts.

What the detector sees for each type of decay is illustrated with figure 8.1 for

$K_L \rightarrow e^+e^-e^+e^-$ and with figure 8.2 for $K_L \rightarrow \pi^0\pi_D^0\pi_D^0$ events. These figures are a first step in understanding the decays.

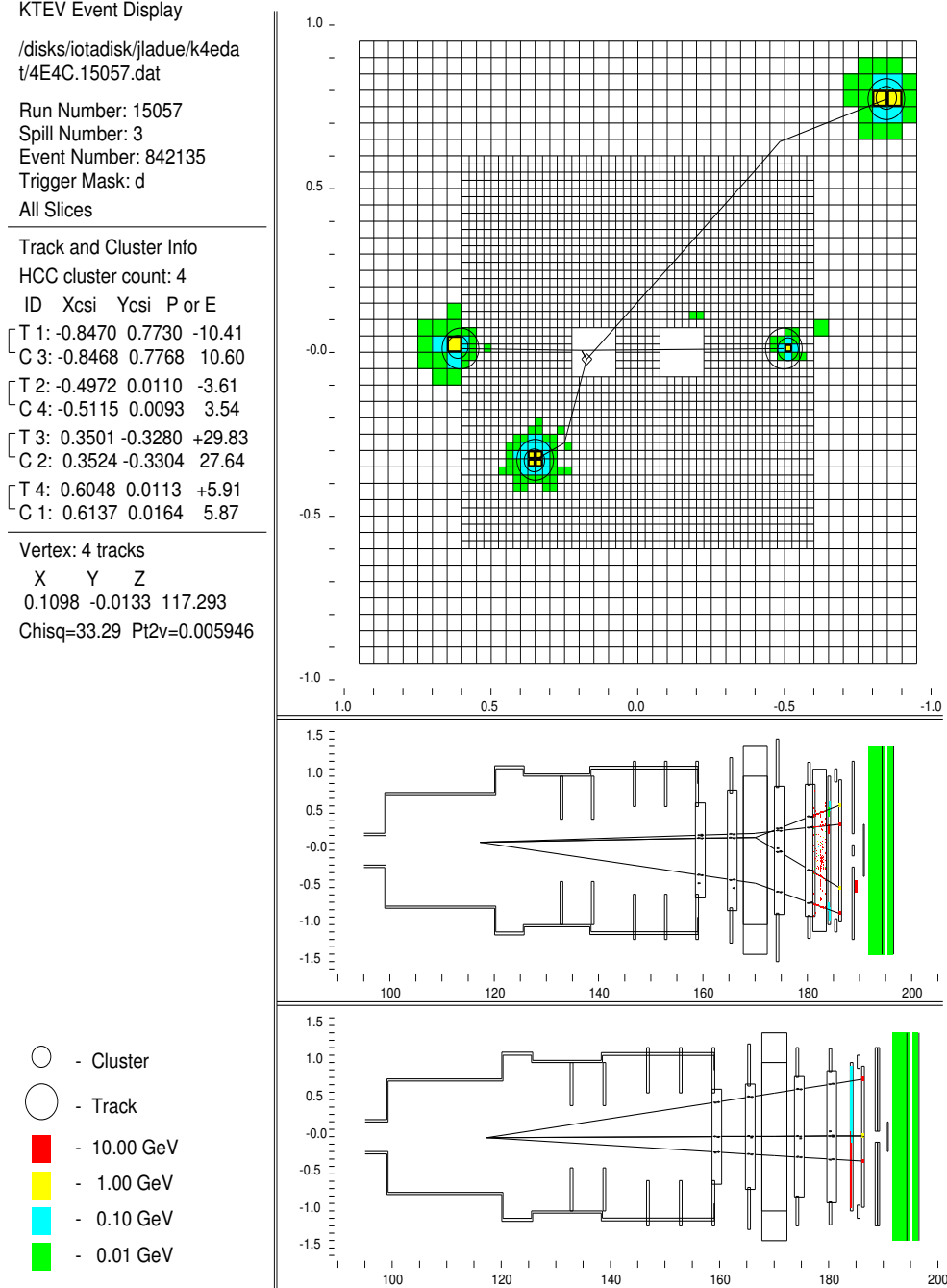


Figure 8.1: A Detector picture showing a $K_L \rightarrow e^+e^-e^+e^-$ event.

There are some differences between the cuts made for the $K_L \rightarrow e^+e^-\gamma$ branching

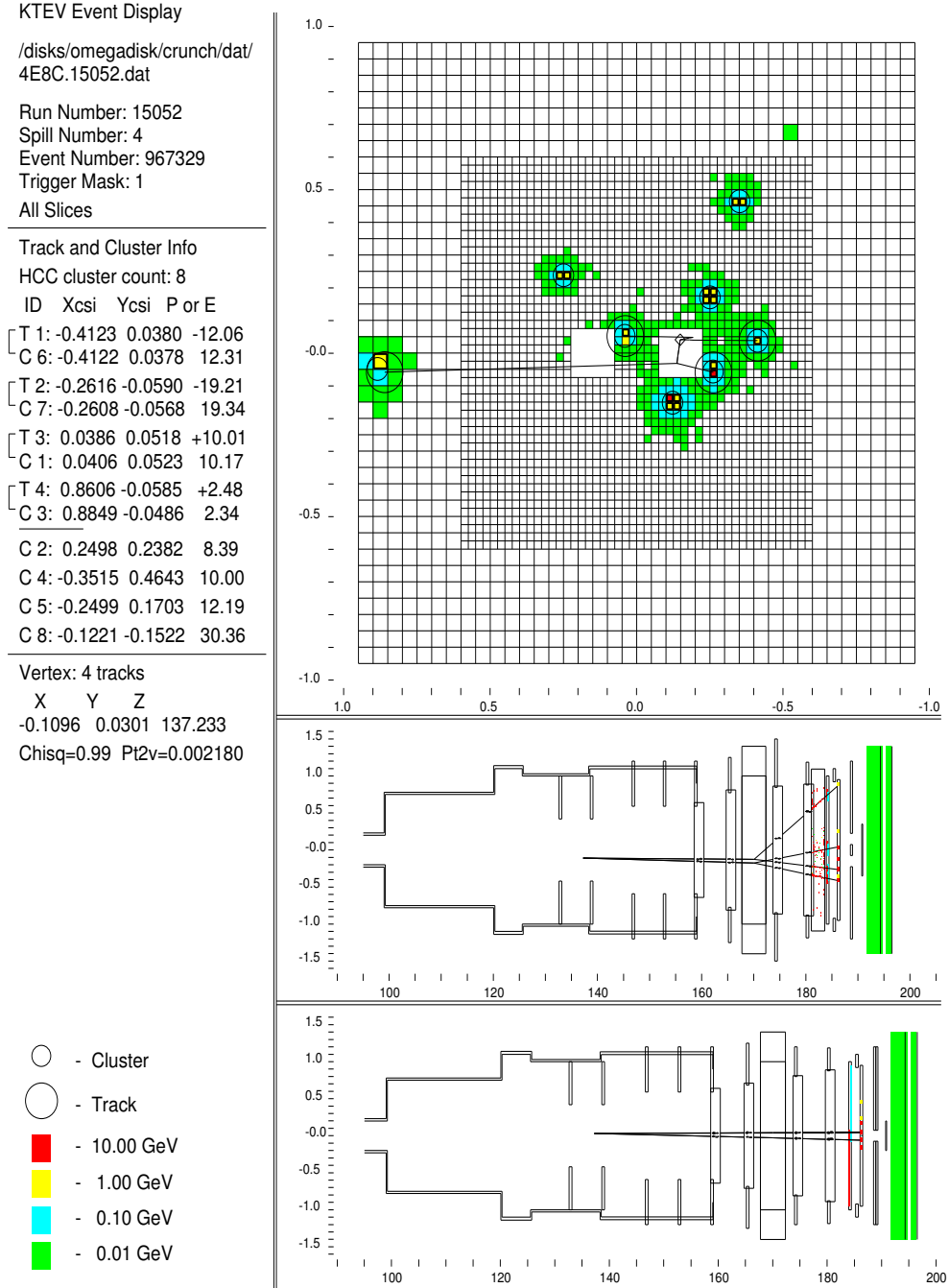


Figure 8.2: A Detector picture showing a $K_L \rightarrow \pi^0 \pi_D^0 \pi_D^0$ event.

ratio analysis and this one. In most cases the cuts here are looser. The reason for this is that the $K_L \rightarrow e^+ e^- \gamma$ analysis is systematics limited (*i.e.* the systematic error is larger than the statistical), so losing statistics is acceptable in order to obtain a sample

that is better understood systematically. The $K_L \rightarrow e^+e^-e^+e^-$ is, on the other hand, limited by the statistics.

8.1.1 Backgrounds

The requirement of having four tracks coming from a signal vertex, that each track has a good E/P and that the tracks match to clusters are all that is needed to see clear signals. Figure 8.3 shows the total invariant mass for all particles for 4 and 8 cluster events with these requirements. A clearly separate peak can be seen in the 4 cluster events at the kaon mass with lower mass backgrounds. The 8 cluster plot shows a peak at the kaon mass and no significant background at low or high mass.

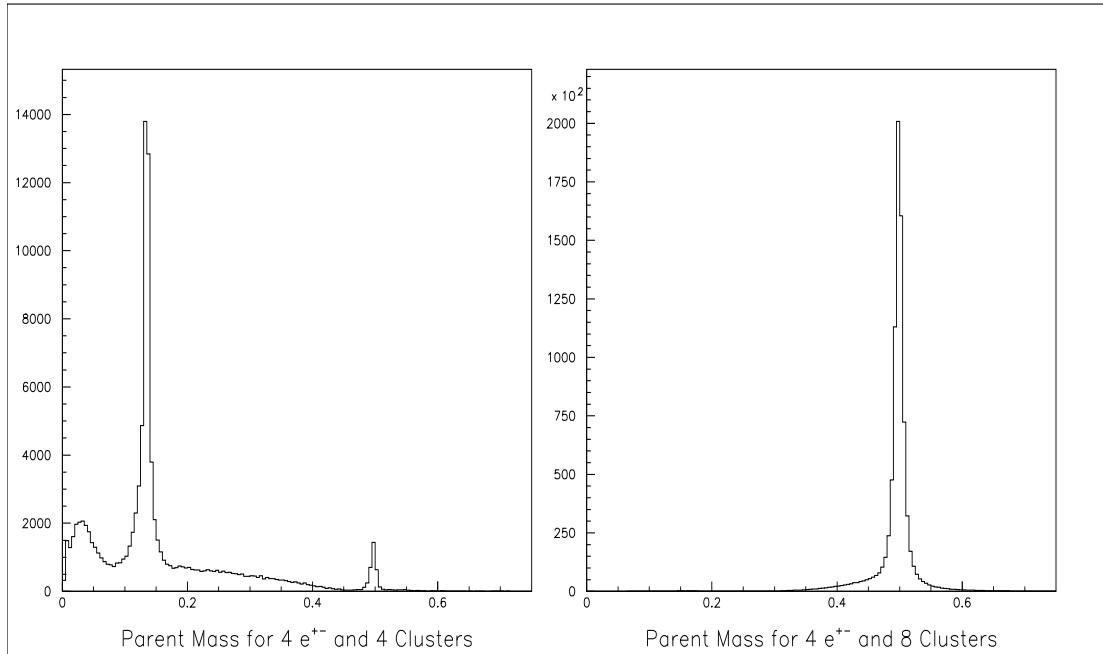


Figure 8.3: Total Invariant Mass for $4e^\pm$ Data events coming from a common vertex. The plot on the left is for 4 cluster events and the right is 8 cluster events.

After making the trigger verification, fiducial, track quality, and particle identification cuts, a plot of Total Mass versus \vec{P}_T^2 can be made, as is done in figure 8.4. In this plot one can see a cluster of events at low \vec{P}_T^2 and near the kaon mass corresponding to the signal $K_L \rightarrow e^+e^-e^+e^-$. A line of events with a mass near the π^0 and a wide range of \vec{P}_T^2 shows $K_L \rightarrow \pi^+\pi^-\pi^0$ events with one of the π^0 under going a double Dalitz

decay (*i.e.* $\pi^0 \rightarrow e^+e^-e^+e^-$) and the other two pions being lost entirely. Figure 8.5 shows a projection of this plot onto the Mass axis. The hatched histogram in that plot shows the 4e mass distribution for events passing the \vec{P}_T^2 cut.

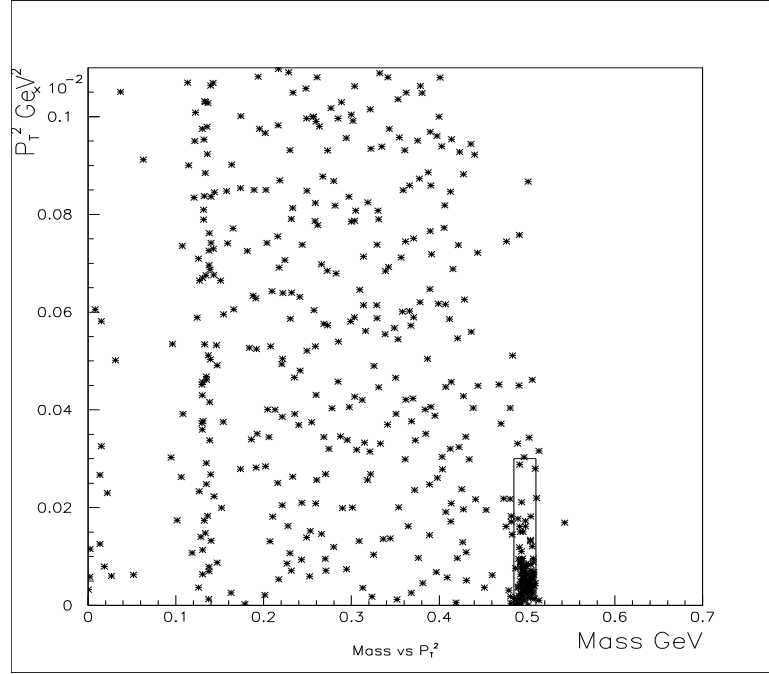


Figure 8.4: Total Invariant Mass versus \vec{P}_T^2 for $e^+e^-e^+e^-$ Data events. Box defines the signal region.

γ Conversion

The only remaining background comes from events with the same final state $e^+e^-e^+e^-$, the majority of these events are conversion events. That is $K_L \rightarrow \gamma\gamma$ and $K_L \rightarrow e^+e^-\gamma$ events where one or two of the photons convert into e^+e^- pairs as a result of interacting with matter. These events will have a good \vec{P}_T^2 and a kaon mass, since nothing is missing and the parent particle was a kaon. There is a good variable for removing these events as described in section 6.5, the Min-Maximum Separation. After applying this cut, the MC predicts that only 4.4 ± 0.2 conversion events remain. There appears to be very good agreement between data and MC in this variable as indicated by figure 8.6.

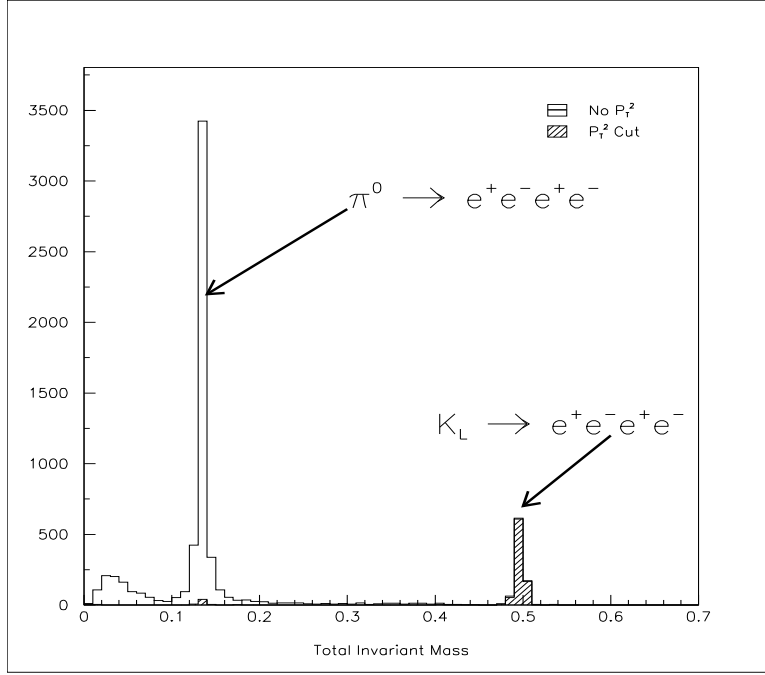


Figure 8.5: Total Invariant Mass for $e^+e^-e^+e^-$ events and the effect of a \vec{P}_T^2 cut on the data.

$$\underline{K_L \rightarrow e^+e^-e^+e^-}$$

Another source of background comes from the $K_L \rightarrow e^+e^-e^+e^- \gamma$ decay, the radiative partner of the $K_L \rightarrow e^+e^-e^+e^-$ decay. This mode can lose a photon (*e.g.* by going down a beam hole), have the photon land on top of an electron cluster, or have a photon whose energy is too small to produce a hardware cluster in the CsI. The MC generator simulates these events, so the MC can be used to predict the level of background. The quantity $X_{4e} = m_{eeee}^2/M_K^2$ is used to separate $K_L \rightarrow e^+e^-e^+e^-$ from $K_L \rightarrow e^+e^-e^+e^- \gamma$ events as is described in section 5.2.3. Any events in the MC with an X_{4e} smaller than 0.95 are $K_L \rightarrow e^+e^-e^+e^- \gamma$ events that have show how made it into the final sample. The value of 0.95 in X_{4e} corresponds approximately to the total mass cut made by this analysis. Figure 8.7 shows the distributions of generated X_{4e} for MC after all selection cuts are made. Since there is $\sim 50\times$ the data generated, the figure implies that the number of background events from $K_L \rightarrow e^+e^-e^+e^- \gamma$ events faking as $K_L \rightarrow e^+e^-e^+e^-$ is 2.1 ± 0.2 .

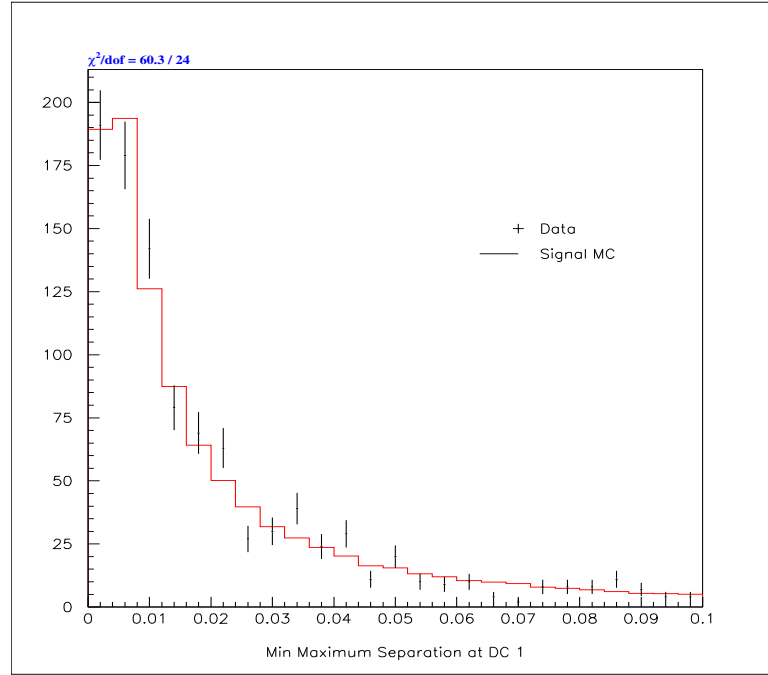


Figure 8.6: Min-Maximum Separation at DC 1 x view, comparing Data (Dots) to MC (Histogram) for $K_L \rightarrow e^+e^-e^+e^-$ events.

Source	# of Background events	Percentage of Signal
γ Conversion	4.4 ± 0.2	0.42%
$K_L \rightarrow e^+e^-e^+e^-\gamma$	2.1 ± 0.2	0.20%
Total	6.5 ± 0.3	0.62%

Table 8.2: The Monte Carlo prediction of Background to $K_L \rightarrow e^+e^-e^+e^-$.

8.1.2 Normalization Cuts

The normalization mode is fairly clean. There are not many kaon decays that occur that have eight particles in the final state. Figure 8.8 is a plot of Total Mass versus \vec{P}_T^2 for $K_L \rightarrow \pi^0\pi_D^0\pi_D^0$ events after all cuts are made (except for the cuts on mass and \vec{P}_T^2). This plot shows a cluster of events near the kaon mass and at low \vec{P}_T^2 where the signal is expected to be. The fact that there is little else in the plot indicates that only modes with the same final state are a potential source of background. Figure 8.9 is a projection of the mass versus \vec{P}_T^2 plot onto the mass axis, with the hatching showing the plot after a the \vec{P}_T^2 cut has been applied.

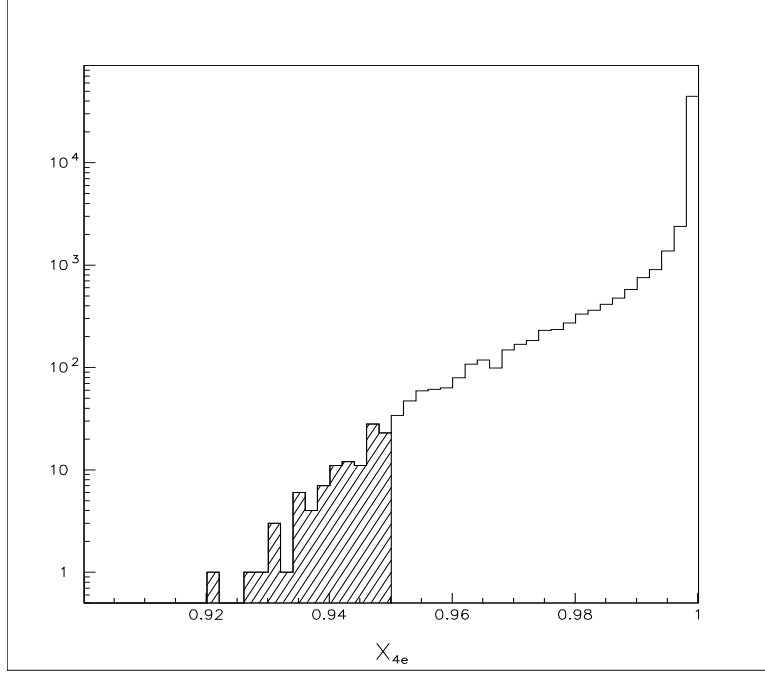


Figure 8.7: X_{4e} for Monte Carlo generated with $K_L \rightarrow e^+e^-e^+e^-$ and $K_L \rightarrow e^+e^-e^+e^-\gamma$ events. All events below 0.95 are considered to be $K_L \rightarrow e^+e^-e^+e^-$ events.

Pion Double Dalitz

There are not many backgrounds from a single decay that can fake a $K_L \rightarrow \pi^0\pi_D^0\pi_D^0$ event. However, there is one decay that has exactly the same final state particles as the normalization mode. This decay is K_L to three π^0 with two of the π^0 s decaying to two photons and the last π^0 undergoing a double Dalitz decay, (*i.e.* $K_L \rightarrow \pi^0\pi^0\pi_{DD}^0 \rightarrow (\gamma\gamma)(\gamma\gamma)(e^+e^-e^+e^-)$).

In order to separate the two modes a pair of Mass χ^2 are constructed. The 2-Dalitz χ^2 is given by equation 8.4. It tests the hypothesis that the decay products came from two single Dalitz decays and double Dalitz χ^2 tests for a single double Dalitz decay. There are 3 ways to pair up the final state particles to form a double Dalitz decay, the pairing with smallest double Dalitz χ^2 is selected. Equation 8.5 defines the double Dalitz χ^2 , where the mass of the π^0 is taken to be 135MeV [15].

$$2 - \text{Dalitz}\chi^2 = \frac{(M_{e^+e^-\gamma}^1 - M_{\pi^0})^2}{\sigma_{e^+e^-\gamma}^2} + \frac{(M_{e^+e^-\gamma}^2 - M_{\pi^0})^2}{\sigma_{e^+e^-\gamma}^2} + \frac{(M_{\gamma\gamma} - M_{\pi^0})^2}{\sigma_{\gamma\gamma}^2} \quad (8.4)$$

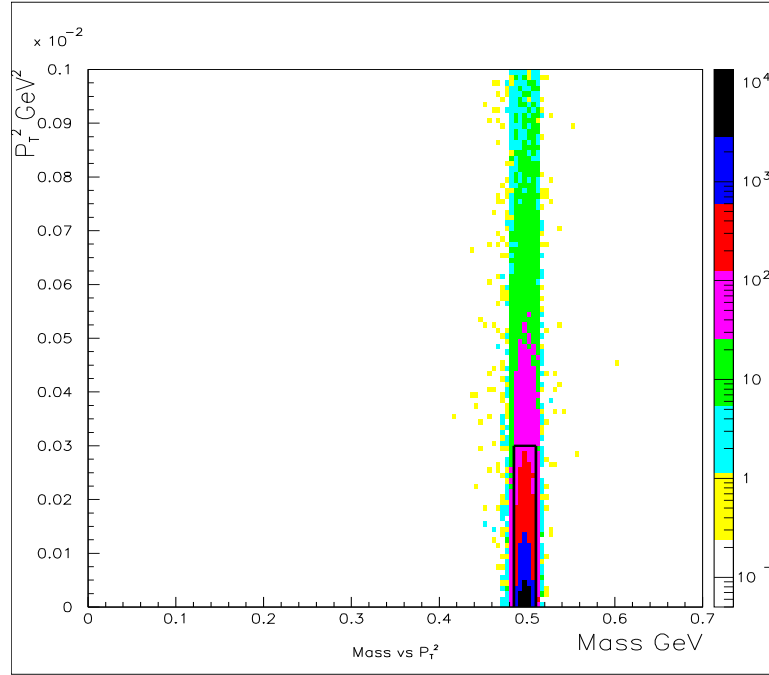


Figure 8.8: Total Invariant Mass versus \vec{P}_T^2 for $K_L \rightarrow \pi^0 \pi_D^0 \pi_D^0$ Data events. Box defines the signal region.

$$\text{doubleDalitz}\chi^2 = \frac{(M_{\gamma\gamma}^1 - M_{\pi^0})^2}{\sigma_{\gamma\gamma}^2} + \frac{(M_{\gamma\gamma}^2 - M_{\pi^0})^2}{\sigma_{\gamma\gamma}^2} + \frac{(M_{e^+e^-\gamma}^1 - M_{\pi^0})^2}{\sigma_{e^+e^-\gamma}^2} \quad (8.5)$$

There are 24 ways to pair up the final state particles to a 2-Dalitz decay; the one with the smallest 2-Dalitz χ^2 is chosen. If the 2-Dalitz χ^2 is smaller than the double Dalitz χ^2 then the event is classified as $K_L \rightarrow \pi^0 \pi_D^0 \pi_D^0$. A cut is then made on the masses of the $e^+e^-\gamma$ states, the 2-Dalitz χ^2 , and the double Dalitz χ^2 to further reduce the background. The cut on the 2-Dalitz χ^2 implicitly cuts on the mass of the paired $\gamma\gamma$. The cut on the double Dalitz χ^2 likewise implicitly cuts out the region where the M_{eee} is near the π^0 mass. Figure 8.10 shows a comparison of the 2-Dalitz χ^2 for data and MC after all cuts. Figures 8.11 and 8.12 show the Masses of the π^0 s, comparing data and MC. There is a small disagreement in the tails of these two plots, most likely due to energy resolution in the MC. There is a systematic uncertainty that includes this level of disagreement.

A Monte Carlo sample of pion double Dalitz decays (*i.e.* $K_L \rightarrow \pi^0 \pi_D^0 \pi_D^0$) is used to predict the amount of background to the double single Dalitz mode. After all cuts, the MC predicts a total of 100 ± 16 background events from this source.

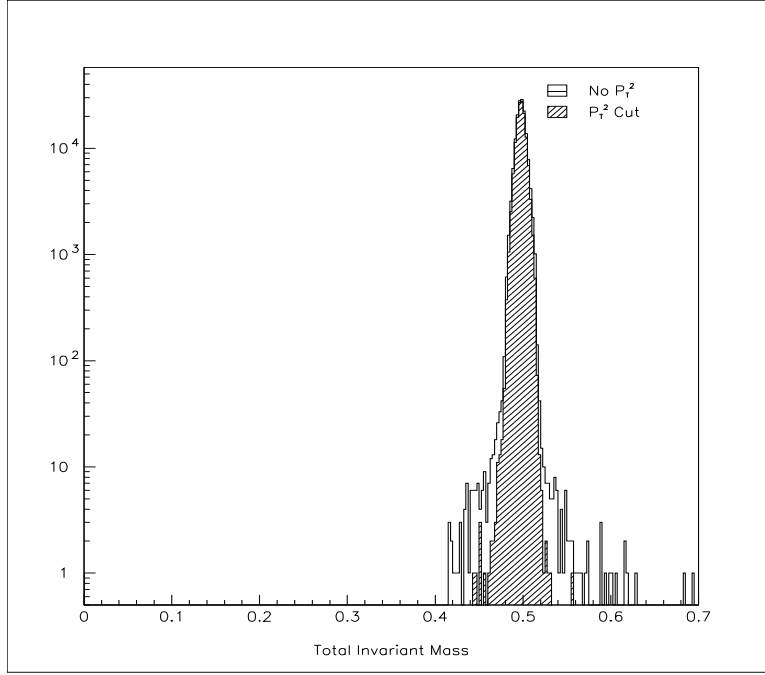


Figure 8.9: Total Invariant Mass for $K_L \rightarrow \pi^0 \pi_D^0 \pi_D^0$ Data events showing the effect of a \vec{P}_T^2 cut on the data.

γ Conversion

As in the $K_L \rightarrow e^+ e^- e^+ e^-$ case, there is a background to the normalization mode from conversion of photons into $e^+ e^-$ pairs as a result of interaction with the material. Both $K_L \rightarrow \pi^0 \pi^0 \pi^0$ events with two photon conversions from different π^0 's and $K_L \rightarrow \pi^0 \pi^0 \pi_D^0$ events with one conversion from a non-Dalitz π^0 can fake $K_L \rightarrow \pi^0 \pi_D^0 \pi_D^0$ events. MC with forced conversions is analyzed to determine the level of this background. After the Min-Maximum Separation cut the MC predicts a total of 3666.2 ± 38.5 events from either 1 or 2 conversions of photons. A summary of the backgrounds is listed in table 8.3.

Source	# of Background events	Percentage of Signal
γ Conversion	3666 ± 38	2.25%
Double Dalitz	100 ± 16	0.06%
Total	3766 ± 37	2.31%

Table 8.3: The Monte Carlo prediction of Backgrounds to $K_L \rightarrow \pi^0 \pi_D^0 \pi_D^0$.

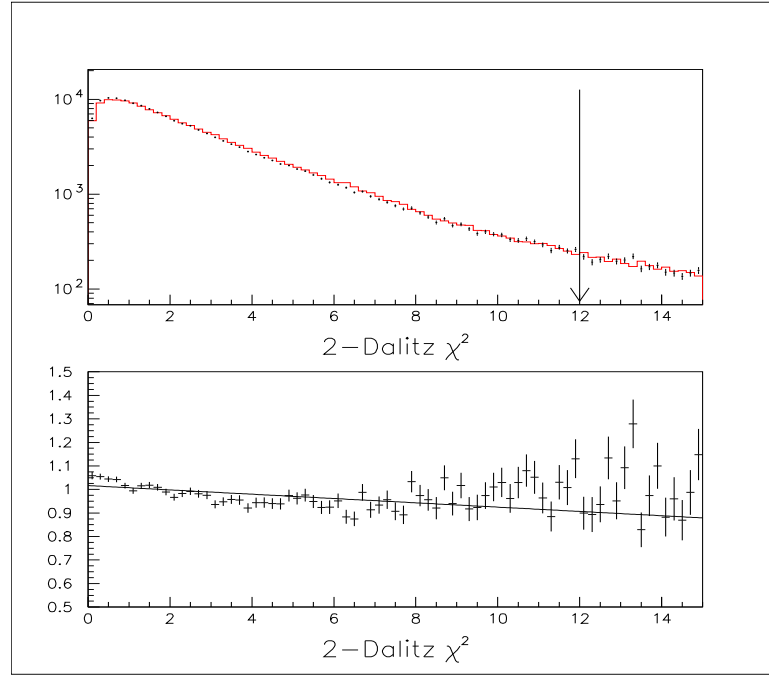


Figure 8.10: 2-Dalitz χ^2 comparing Data (Dots) with MC (Histogram) for $K_L \rightarrow \pi^0 \pi_D^0 \pi_D^0$ events. The arrow shows the location of the cut.

8.1.3 Data Numbers

After reconstructing and using the selection cuts mentioned above, the number of data events for each mode is found. These numbers are listed in table 8.4.

Mode	Winter	Summer	1999
$K_L \rightarrow e^+ e^- e^+ e^-$	223	159	674
$K_L \rightarrow \pi^0 \pi_D^0 \pi_D^0$	29454	22938	110720

Table 8.4: The number of events in the data for signal and normalization modes.

8.2 Monte Carlo Sample

Using the code explained in chapter 5 and in particular the generators for the $K_L \rightarrow e^+ e^- e^+ e^-$ (section 5.2.3) and the $K_L \rightarrow \pi^0 \pi_D^0 \pi_D^0$ (section 5.2.4), Monte Carlo simulated events were generated in order to model the acceptance of the detector. Table 8.5 lists the amount of MC at each stage and the acceptance for $K_L \rightarrow e^+ e^- e^+ e^-$ events divided up into run periods. Table 8.6 is the same thing for $K_L \rightarrow \pi^0 \pi_D^0 \pi_D^0$ MC.

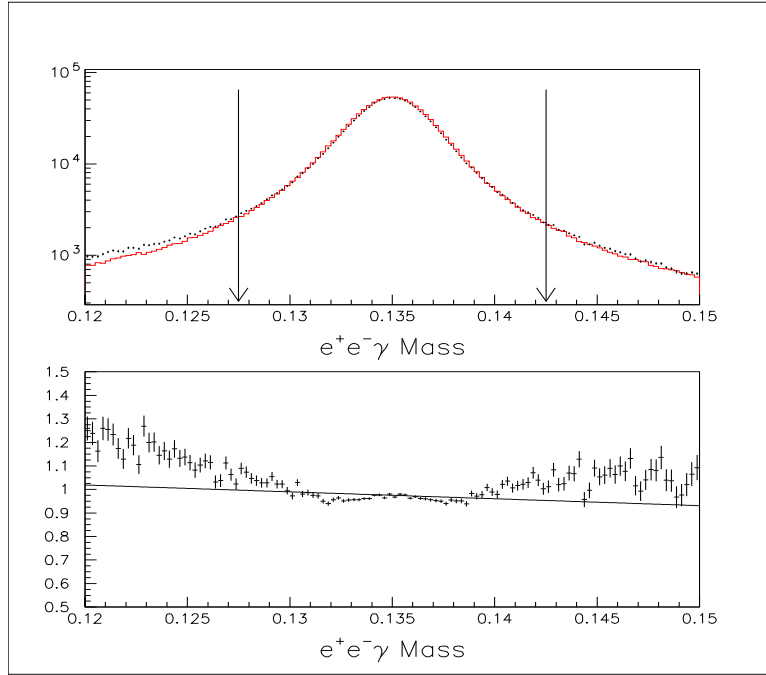


Figure 8.11: $\pi^0 \rightarrow e^+e^-\gamma$ Mass comparing Data (Dots) to MC (Histogram) for $K_L \rightarrow \pi^0\pi_D^0\pi_D^0$ events. The arrows show the location of the cut.

Quantity	Winter	Summer	1999
K_L Generated	305330	219888	724792
MC after L1 simulation	76237	53201	197855
MC after L2 simulation	44896	33407	131948
MC after L3 simulation	31951	23726	95507
MC after all cuts	11332	8276	34533
ϵ_{4e}	0.0371 ± 0.0003	0.0376 ± 0.0004	0.0476 ± 0.0003

Table 8.5: The Monte Carlo simulation numbers and acceptance for $K_L \rightarrow e^+e^-e^+e^-$ events. The errors are statistical only.

Quantity	Winter	Summer	1999
K_L Generated	27499260	19797170	78028090
MC after L1	2621525	1753540	8507422
MC after L2	2524582	1709799	8220372
MC after L3	1748160	1202069	6111494
MC after all cuts	62308	45594	281918
ϵ_{dsd}	0.002266 ± 0.000009	0.002303 ± 0.000011	0.00361 ± 0.000007

Table 8.6: The Monte Carlo simulation numbers and acceptance for $K_L \rightarrow \pi^0\pi_D^0\pi_D^0$ events.

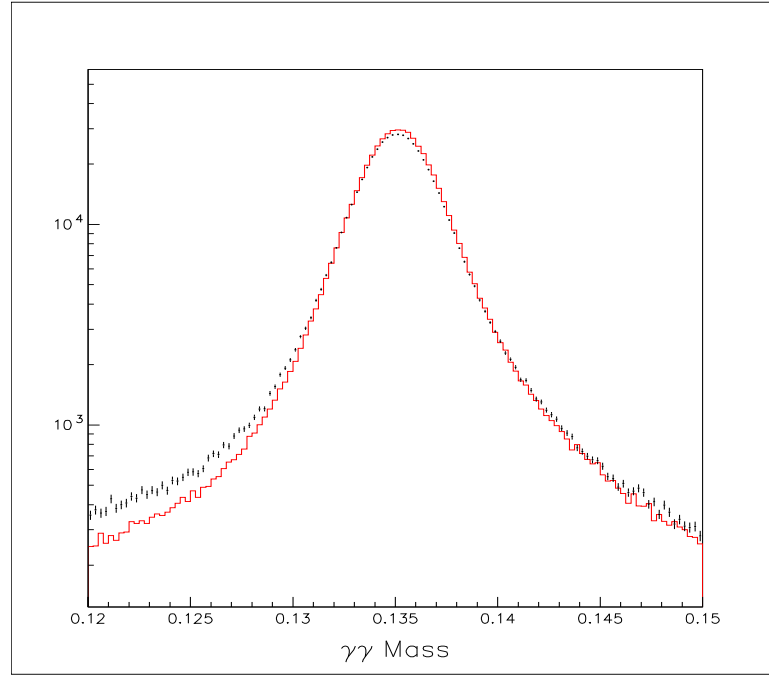


Figure 8.12: $\pi^0 \rightarrow \gamma\gamma$ Mass comparing Data (Dots) to MC (Histogram) for $K_L \rightarrow \pi^0 \pi_D^0 \pi_D^0$ events.

8.3 Flux

The number of kaons that decayed during the running of the experiment is calculated using the normalization mode information from equation 8.3. The acceptance comes from the MC, see table 8.6, and table 8.4 gives the number of events in the data. The branching ratio for $K_L \rightarrow \pi^0 \pi_D^0 \pi_D^0$ is $(8.99 \pm 0.36) \times 10^{-5}$, see 5.8 [15]. The result of this calculation is given in table 8.7. There is a significant difference between the flux measured by $K_L \rightarrow \pi^0 \pi_D^0 \pi_D^0$ and $K_L \rightarrow \pi^0 \pi^0 \pi_D^0$ for the 1997 data set. This difference is most likely due to the level of understanding of the absolute tracking efficiency.

	1997	1999
$K_L \rightarrow \pi^0 \pi_D^0 \pi_D^0$	51379	108117
\mathcal{F}	$(2.505 \pm 0.013) \times 10^{11}$	$(3.329 \pm 0.012) \times 10^{11}$

Table 8.7: The Background Subtracted Number of $K_L \rightarrow \pi^0 \pi_D^0 \pi_D^0$ Events and The Number of Kaons produced from the Target for the two run periods. The errors are statistical. The 1997 flux agrees within errors with the flux found from $K_L \rightarrow \pi^0 \pi^0 \pi_D^0$.

8.4 Branching Ratio

Equation 8.1 is used to get the branching ratio for $K_L \rightarrow e^+e^-e^+e^-$. The acceptance, ϵ_{4e} is located in table 8.5 and the flux from table 8.7. The number of events from the data include a subtraction of the expected backgrounds listed in table 8.2 and the events found, see table 8.4.

	1997	1999
$K_L \rightarrow e^+e^-e^+e^-$ Events	380.1	669.4
$BR(K_L \rightarrow e^+e^-e^+e^-)$	$(4.06 \pm 0.21) \times 10^{-8}$	$(4.22 \pm 0.17) \times 10^{-8}$

Table 8.8: The number of $K_L \rightarrow e^+e^-e^+e^-$ events after background subtraction and the Branching Ratio as a function of run period. The errors are statistical.

The average branching ratio is

$$BR(K_L \rightarrow e^+e^-e^+e^-) = (4.16 \pm 0.13_{\text{stat}} \pm 0.17_{\text{ext sys}}) \times 10^{-8}, \quad (8.6)$$

where the first error is from the statistics of the modes involved (including MC statistics) and the second error comes from the previously measured branching ratio of $K_L \rightarrow \pi^0\pi_D^0\pi_D^0$ which is dominated by the $\pi^0 \rightarrow e^+e^-\gamma$ branching ratio error, see table 5.1.

8.5 Systematic Uncertainty

The effects considered for the branching ratio of $K_L \rightarrow e^+e^-e^+e^-$ are similar to those discussed previously for $K_L \rightarrow e^+e^-\gamma$. In most cases the study was performed in the same way, except that different modes were considered. The uncertainties are reported as a percentage of the nominal branching ratio, see section 8.6.

8.5.1 Varying Sets Of Cuts

The cut variations for the $K_L \rightarrow e^+e^-e^+e^-$ branching ratio are handled in a slightly different manner than for the $K_L \rightarrow e^+e^-\gamma$ branching ratio. It was done this way in order to get a systematic that could be separated from the statistical fluctuations due to adding and removing data. Each variation is taken separately and the effects of statistics is subtracted off. The cuts studied and different values for tight and loose are given in table 8.9. Figure 8.13 shows the effect of each cut studied individually, taking

Cut Variable	Loose	Tight
Vertex X	-0.22m to +0.22m	-0.18m to +0.18m
Vertex Y	-0.11m to +0.11m	-0.09m to +0.09m
Vertex Z	94.0m to 158.0m	100.0m to 152.0m
Vertex χ^2	< 60.0	< 20.0
Magnet Offset χ^2	< 125.0	< 75.0
E/P	0.915 to 1.085	0.935 to 1.065
P_t^2	< 0.0002GeV ²	< 0.0004GeV ²
Total Mass	0.480GeV to 0.5125GeV	0.490GeV to 0.5075GeV
Min-Max Sep	> 0.0005m	> 0.002m
Total Kaon Energy	35.0GeV to 210.0GeV	45.0GeV to 200.0GeV
Two Dalitz χ^2	< 15.0	< 10.0
Δd CsI Edge	> 0.0125m	0.0375m
Cluster Separation	> 0.05m	0.1m
M_{ee}	> 0.000GeV	0.005GeV

Table 8.9: Definition of Loose and Tight Cuts for $K_L \rightarrow e^+e^-e^+e^-$.

into account that most events are the same from changing to tight and loose. The first bin is the effect when all cuts are varied at the same time.

The systematic error was calculated by taking the difference in the branching ratios for varying each cut separately and summing in quadrature. This produces an estimated systematic uncertainty of 2.1%.

8.5.2 Upstream Detector Material

As with the study of $K_L \rightarrow e^+e^-\gamma$, the amount of material is varied by 7σ and the change in the branching ratio was interpolated back to the 1σ level. Figure 8.14 shows the results of this interpolation and the change in the branching ratio. This gives an estimated systematic uncertainty of 0.6%.

8.5.3 Track Hit Inefficiency

The DC inefficiency and high-SOD maps for both the normalization and signal mode are varied in the same manner as described in 7.5.3. Half the difference of the branching ratio obtained using a map multiplied by 1.07 compared that found using a multiple of 1.73 is taken as the uncertainty. This result is a change in the branching ratio of 1.3%.

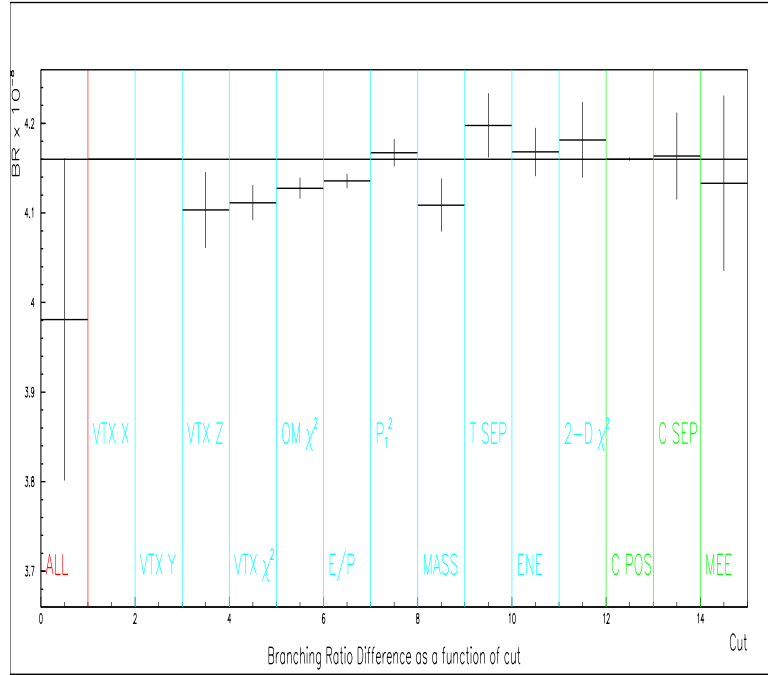


Figure 8.13: Change in the Measured Branching Ratio for $K_L \rightarrow e^+e^-e^+e^-$ between using the Tight and Loose Cut Values (Table 8.9) while keeping the rest of the Cuts at Nominal (Table 8.1). The error bars take into account the fact that most of the events are the same.

8.5.4 Hit resolution

As in section 7.5.4, the spectrometer hits are smeared in the MC by an additional factor. The factor is such that the width of the SOD distribution was increased by 10% of itself. This smearing results in a change of 0.4% in the branching ratio.

8.5.5 Energy Slope

The effect of removing the slope from the energy, as described in 7.5.5, is also evaluated. This results in a small systematic uncertainty of 0.8%

8.5.6 Energy resolution

Varying of the energy smearing factor, δ , between 0.17 and 0.09 as described in section 7.5.6 was done for the $K_L \rightarrow e^+e^-e^+e^-$ analysis as well. The effect of the entire variation between 0.17 and 0.09 results in a small systematic uncertainty of 0.8%.

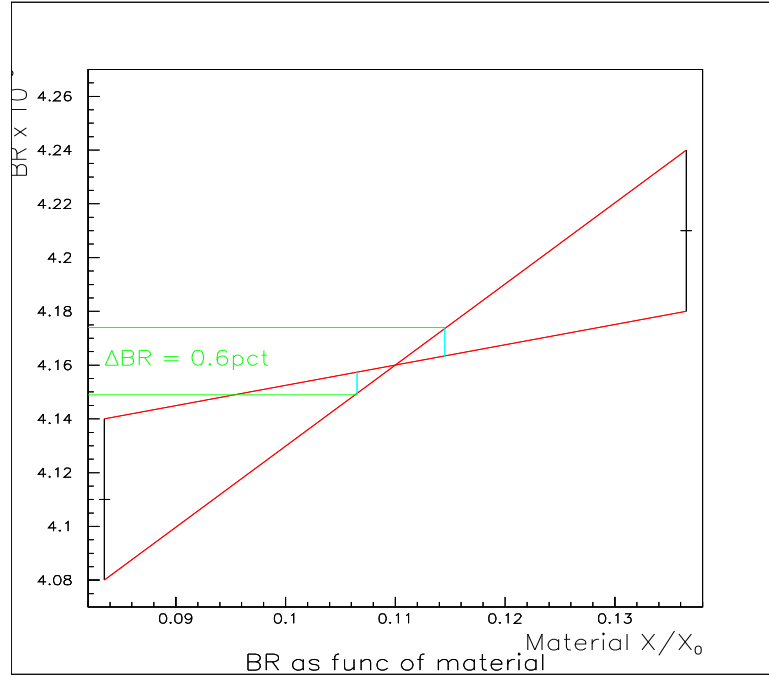


Figure 8.14: The change in the branching ratio as a function of varying the amount of material in the upstream part of the detector.

8.5.7 γ Inefficiency

There is a 4 photon difference between the normalization and the signal mode for this analysis as well. A study like the one done in section 7.5.7, with several different components, is done and resulted in a change of 0.4%.

8.5.8 Radiative Corrections

As is mentioned in section 7.5.8, there are higher order graphs that could be added to the MC generation. To estimate the potential size of those corrections, we note that the one-loop corrections change the branching ratios by 9.4%. We approximate the next order effect as $(9.4\%)^2 = 0.9\%$.

8.5.9 Varying the Form Factor

Chapter 9 discusses the process of finding the best fit to the form factor parameters. By changing the parameters by 1 sigma of the measured amount in α_{DIP} and

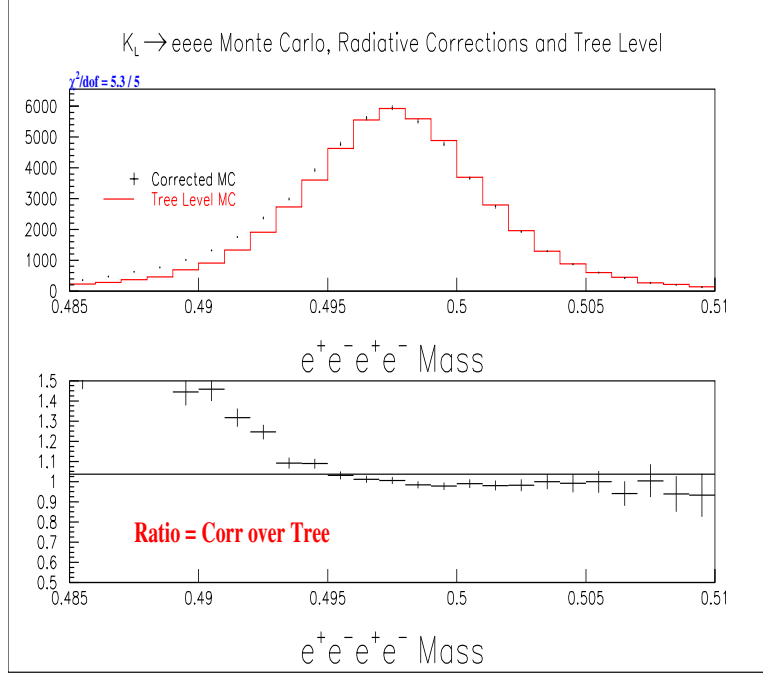


Figure 8.15: Total Invariant Mass for $K_L \rightarrow e^+e^-e^+e^-$ MC where the Dots have One Loop Corrections and Radiative Diagrams and the Histogram is Tree Level.

β_{DIP} , there is a corresponding change in the acceptance of the MC. This change was of the order of 0.9% for varying α_{DIP} and 0.2% for varying β_{DIP} . Together, the change in the branching ratio is 0.94%

8.6 Result

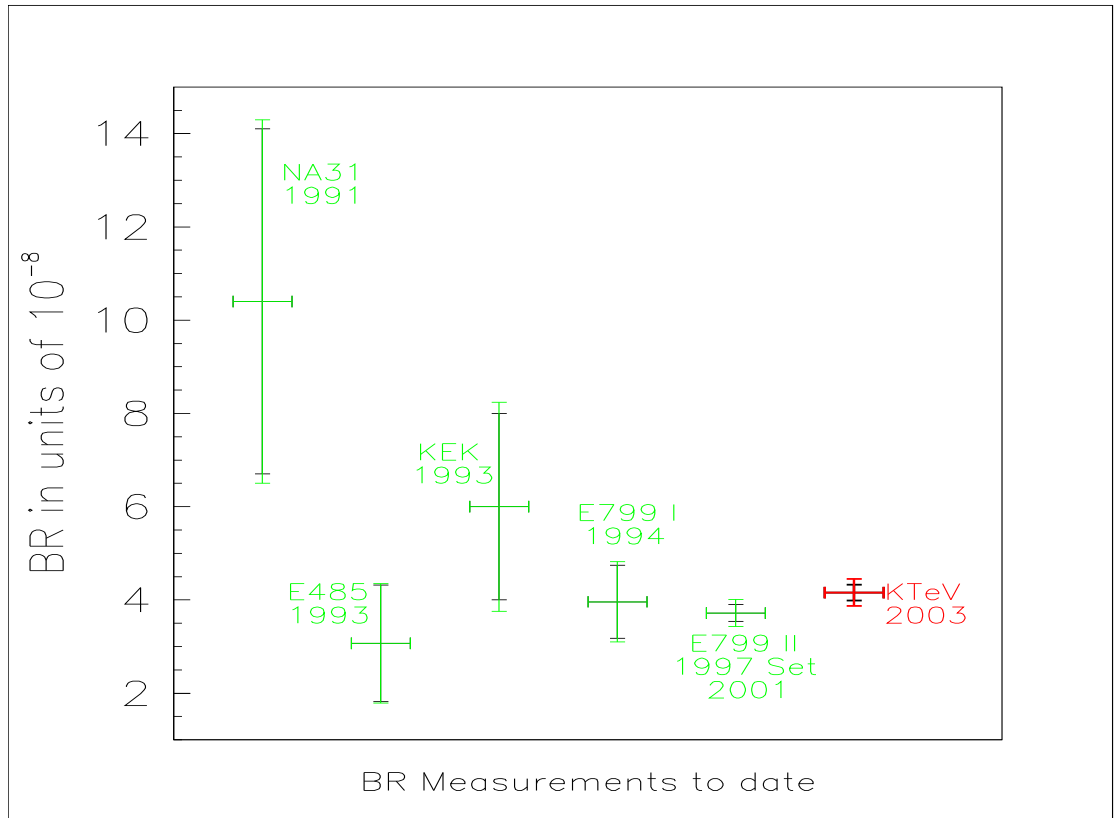
The uncertainties from the systematic studies are combined by adding them in quadrature, see table 8.10. This can then be combined with the information from equation 8.6 to calculate the branching ratio for $K_L \rightarrow e^+e^-e^+e^-$. The branching ratio with the statistical, external systematic (*i.e.* $BR(K_L \rightarrow \pi^0\pi_D^0\pi_D^0)$ uncertainty), and internal systematic uncertainties is:

$$BR(K_L \rightarrow e^+e^-e^+e^-) = (4.16 \pm 0.13_{\text{stat}} \pm 0.13_{\text{sys}} \pm 0.17_{\text{ext sys}}) \times 10^{-8} \quad (8.7)$$

This result is consistent with previously measured results, as given in table 1.4. Figure 8.16 shows the previously measured results with their error bars along with the newly measured value from this work.

Uncertainty Source	% of Branching Ratio
Statistical	3.1%
$BR(K_L \rightarrow \pi^0 \pi_D^0 \pi_D^0)$ Uncertainty	5.5%
Cut Variations	2.1%
DC Inefficiency	1.3%
Form Factor Dependence	0.9%
Radiative Corrections	0.9%
Energy Slope	0.8%
Energy Resolution	0.8%
Upstream Material	0.6%
DC Hit Resolution	0.4%
γ Inefficiency	0.4%
Total Systematic	3.1%

Table 8.10: List of Sources of Uncertainty for the Branching Ratio measurement.

Figure 8.16: Previously measured values of the Branching Ratio of $K_L \rightarrow e^+e^-e^+e^-$ with the current measurement also shown.

Chapter 9

Form Factor Measurements

One of the goals of this analysis is the measurement of the form factor dependence of the modes of interest. The $K_L \rightarrow \gamma^* \gamma$ form factor can be probed with the study of the $K_L \rightarrow e^+ e^- \gamma$ mode and the $K_L \rightarrow \gamma^* \gamma^*$ with the $K_L \rightarrow e^+ e^- e^+ e^-$ mode. The details of the form factor are discussed in section 1.5. In particular two parametrizations are studied in this analysis, the Bergström, Massó, and Singer (BMS) and the D'Ambrosio, Isidori and Portolés (DIP) forms. These models are discussed in sections 1.5.2 and 1.5.3 respectively.

The form factor affects the shape of the x or m_{ee} distributions. Thus, one has sensitivity to the form factor by studying the shape of these distributions in the data. Two methods were used to obtain results for the form factor parameters in both the BMS and the DIP models. A shape- χ^2 method was used for the $K_L \rightarrow e^+ e^- \gamma$ mode and a log likelihood for the $K_L \rightarrow e^+ e^- e^+ e^-$ mode.

9.1 Shape χ^2 Fit

One can form a χ^2 by comparing the shape of a binned m_{ee} distribution from the data to a similar one from the Monte Carlo using the equation below,

$$\chi^2 = \sum_{\text{bins}, i} \frac{(n_i - m_i)^2}{\sigma^2(n_i) + \sigma^2(m_i)} = \sum_{\text{bins}, i} \frac{(n_i - m_i)^2}{n_i}, \quad (9.1)$$

where n_i is the number of data in bin i , m_i is the scaled number of MC events in bin i , $\sigma(n_i) = \sqrt{n_i}$, $\sigma^2(\chi^2) = \sum_{\text{bins}, i} \frac{(n_i^2 - m_i^2)^2}{n_i^3}$. The MC events need to be scaled in order to have the same number of events as the data (*i.e.* if there was 1000 events in the MC and 100 events in the data, each bin would multiplied by 0.1). The error for each bin in

the MC is equal to the square root of the number of MC events in that bin, and $\sigma(m_i)$ is this uncertainty times the scale factor, so $\sigma(m_i) \propto 1/\sqrt{N_{MC}}$. For large N_{MC} , $\sigma(m_i)$ can be safely neglected. The assumption is made that the $\sigma(n_i)$ is much larger than the $\sigma(m_i)$. Here, $\sigma(\chi^2)$ represents how much spread would be expected to appear in a distribution of χ^2 if E799 were to be repeated very many times. This $\sigma(\chi^2)$ is only used while fitting a parabola to $\chi^2(\alpha_{K^*})$.

This can then be repeated for different values of α_{K^*} by reweighting a Monte Carlo generated with a known value form factor by $(f(x, \lambda)/f(x, \lambda_{GEN}))^2$ where $f(x, \lambda)$ is the tested form factor, $f(x, \lambda_{GEN})$ is the generated form factor and $x = m_{ee}^2/M_K^2$ is a phase space variable. Figure 9.1 compares the data m_{ee} distribution to the MC with various factors of the BMS form factor free parameter α_{K^*} . This plot shows the sensitivity to the form factor. Figure 9.2 shows the result of such a fit performed on Monte Carlo with a generated $\alpha_{K^*} = -0.10$. Its success in reproducing the input value implies that the implementation was not flawed. Figure 9.3 shows the result for the fit performed on data using the BMS form factor model. A similar process can be used using the DIP form factor model with the result shown in figure 9.4.

9.1.1 Systematics

The process for evaluating the systematics for the α_{K^*} is essentially identical to that used for determining the systematics for the branching ratio measurement of $K_L \rightarrow e^+e^-\gamma$. In almost all cases, the process is the same, except that the response of the normalization mode is not a factor, as the form factor analysis does not need a flux calculation. The errors are reported as an absolute error not a relative error. The value $\alpha_{K^*} = 0$ has no special significance.

Table 7.7 gives a set of reasonable cuts for the $K_L \rightarrow e^+e^-\gamma$ analysis. Each of these cuts is varied individually between loose and tight and the greater change is noted. If that change is larger than would be expected from just statistics, it is taken as an uncertainty. All the uncertainties are then summed in quadrature giving a total uncertainty of 0.0052 in α_{K^*} . The amount of material in the upstream part of the detector is varied by $\sim 7\sigma$ from the measured value and then interpolated back to the 1σ level. Figure 9.6 shows the interpolation of the errors, and gives a difference of

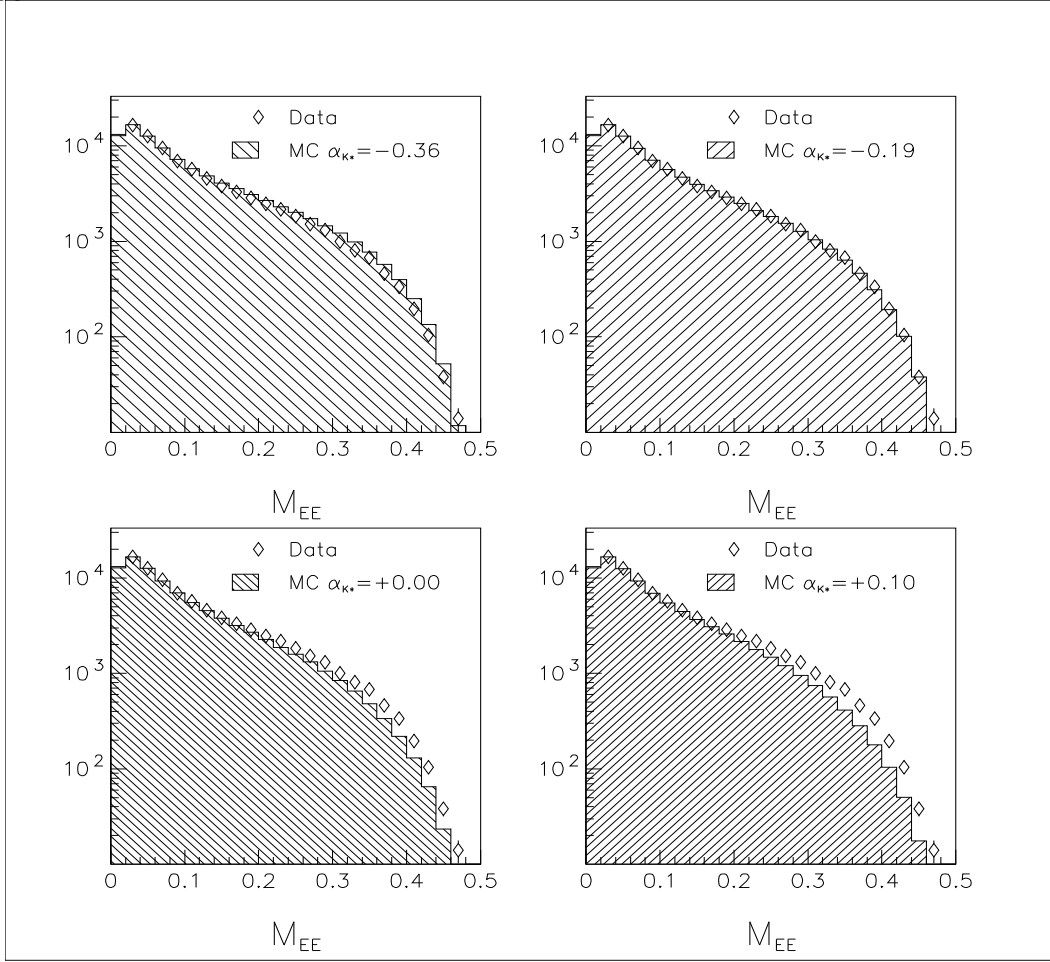


Figure 9.1: Shape χ^2 fit for the BMS parameter α_{K^*} with $K_L \rightarrow e^+e^-\gamma$ events from the 97 MC with a Generated Value of $\alpha_{K^*} = -0.10$.

0.003 in α_{K^*} . The uncertainty in inefficiency maps is handled in exactly the same way as in section 7.5.3, and the variation of α_{K^*} is seen to be 0.0036. The hit positions are smeared as in 7.5.4 resulting in a change of 0.0008. The energy slope was removed and the difference in the measured α_{K^*} was seen to be 0.0045. The smearing of the energy resolution is done in same way as described in 7.5.6, with the exception that no interpolation was performed because the error was so small to begin with. The change in α_{K^*} from varying the δ by 0.08 is 0.0003. Finally, the addition of higher order graphs is estimated by looking at the change in m_{ee} distribution between Monte Carlo made with only tree level graphs and MC with one loop graphs. The change in α_{K^*} between using the two different MC sets is 0.060 and the m_{ee} distribution changes by 5%, so

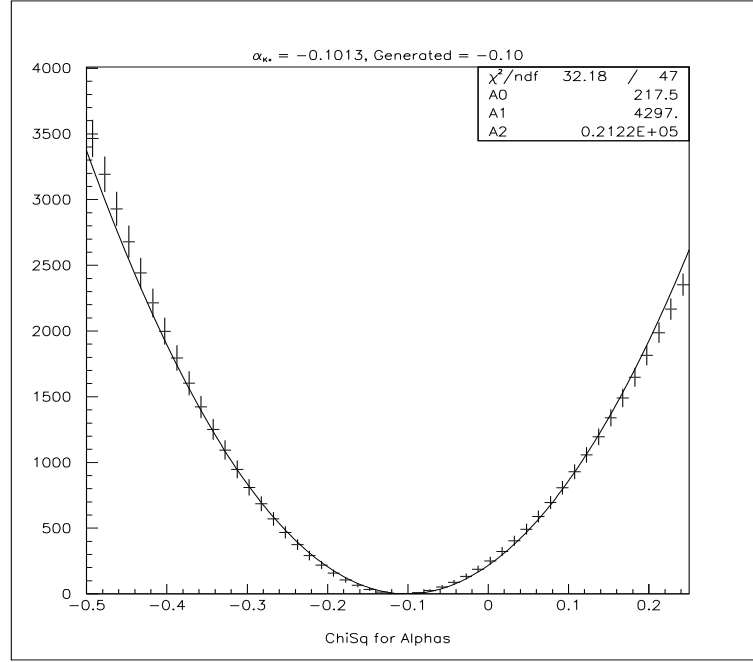


Figure 9.2: Shape χ^2 fit for the BMS parameter α_{K^*} with $K_L \rightarrow e^+e^-\gamma$ events from the 97 MC with a generated value of $\alpha_{K^*} = -0.10$.

if the higher order graphs are 5% of the first order change then the difference in α_{K^*} would be 0.0003. Table 9.1 lists all of the systematic uncertainties for the measurement of α_{K^*} and α_{DIP} from $K_L \rightarrow e^+e^-\gamma$ studies and the total.

Uncertainty Source	Change in α_{K^*}	Change in α_{DIP}
Statistical	0.0109	0.038
Cut Variations	0.0052	0.016
Energy Slope	0.0045	0.014
DC Inefficiency	0.0036	0.011
Radiative Corrections	0.0030	0.009
Upstream Material	0.0030	0.009
DC Hit Resolution	0.0008	0.003
Energy Resolution	0.0003	0.001
Total Systematic	0.0089	0.028

Table 9.1: List of sources of uncertainty for the $K_L \rightarrow e^+e^-\gamma$ form factor measurement.

A final value for the measurements of α_{K^*} and α_{DIP} is summarized in table 9.2. Equation 1.33 relates the DIP form factor parameter α_{DIP} to the BMS parameter α_{K^*} .

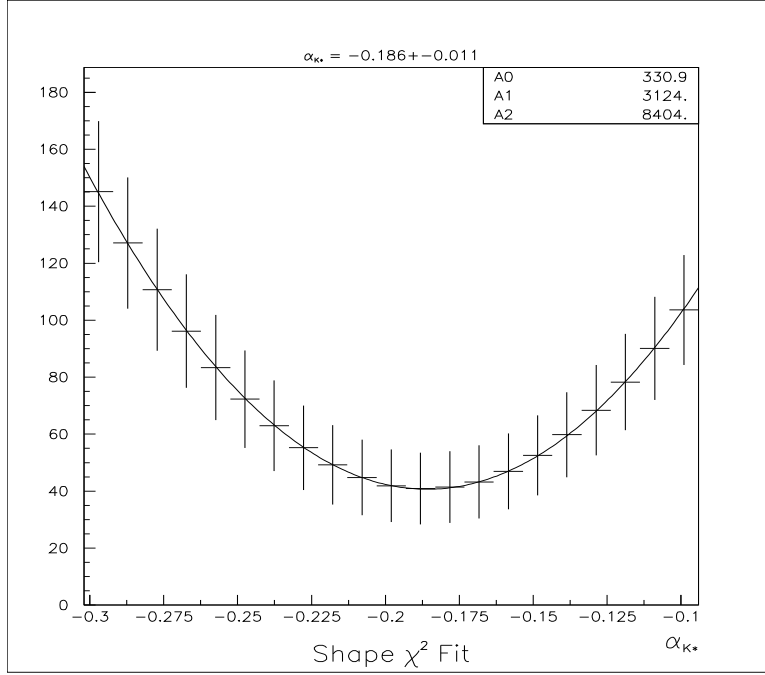


Figure 9.3: Shape χ^2 fit for the BMS parameter α_{K^*} with $K_L \rightarrow e^+e^-\gamma$ events from the 97 run period.

Using this equation and the measured value of α_{K^*} , one gets an estimated value of $\alpha_{DIP} = -1.6 \pm 0.1$, in good agreement with the measured value.

	α_{K^*}	α_{DIP}
1997 Data	$-0.186 \pm 0.011_{\text{stat}} \pm 0.009_{\text{sys}}$	$-1.630 \pm 0.038_{\text{stat}} \pm 0.028_{\text{sys}}$

Table 9.2: Measurements of the α_{K^*} and α_{DIP} from the $K_L \rightarrow e^+e^-\gamma$ mode with all uncertainties.

9.2 Log Likelihood

In order to make the optimal use of the limited statistics in the $K_L \rightarrow e^+e^-e^+e^-$ mode, an unbinned log likelihood method is used to fit for the form factor. The log likelihood is a function that uses a weight for each event based on the phase space variables to test different values of the form factor. The sum of all these weights is the log of a joint probability estimate [15]. The function is corrected for the acceptance of the detector. The QED calculation of the rate for $K_L \rightarrow e^+e^-e^+e^-$, as is discussed

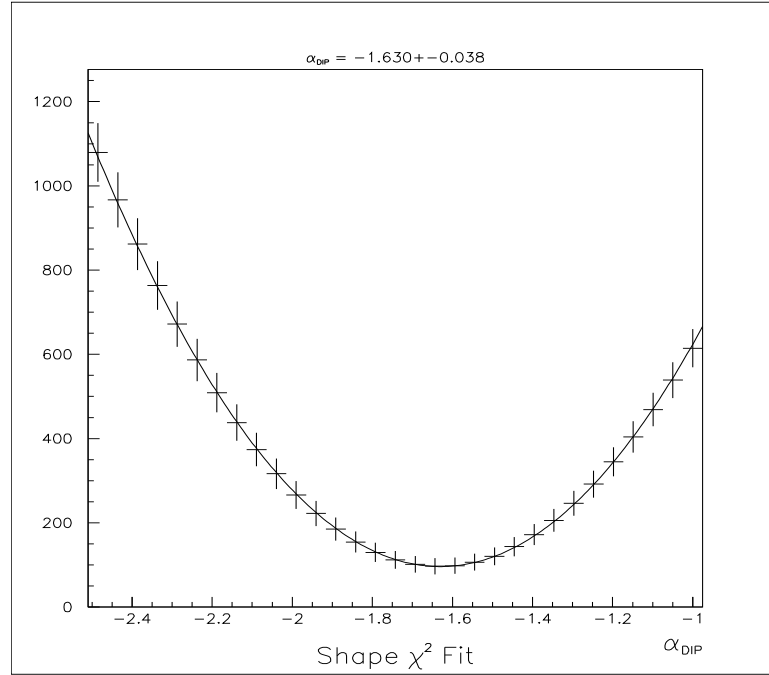


Figure 9.4: Shape χ^2 fit for the DIP parameter α_{DIP} with $K_L \rightarrow e^+e^-\gamma$ events from the 97 run period.

in section 1.4, gives the weight of each event as a function of the phase space and the form factor. Thus, the same function that is used to generate events for the MC can be used here.

A few definitions are required before an exact discussion of the log-likelihood function can be made.

x_i : Phase Space variables (there are five) for $e^+e^-e^+e^-$ event i .

k_i : Additional Phase Space variables (there are three more) for $e^+e^-e^+e^-\gamma$ event i

λ : Form Factor parameters (there is one or two).

λ_{GEN} : Form Factor parameters used to generate MC sample.

$W^{4e}(x_i, \lambda)$: Weight of tree level $K_L \rightarrow e^+e^-e^+e^-$ process based on standard QED process [18], includes phase space and form factor, (*i.e.* uses graphs like those in figure 1.10). An integral of this over the phase space gives the decay rate.

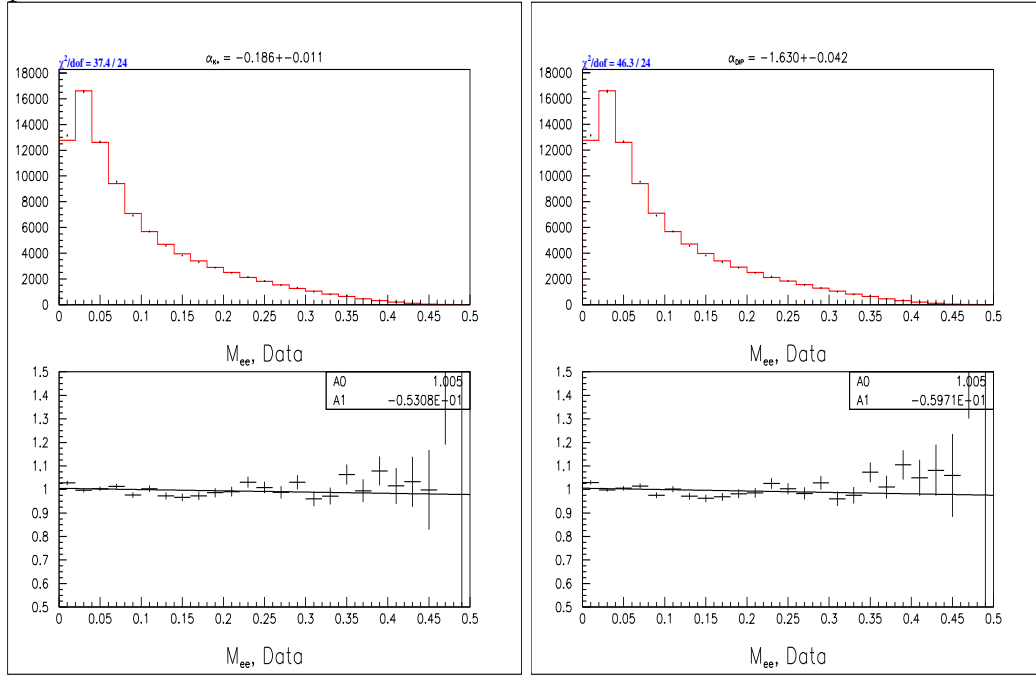


Figure 9.5: Comparison of Data (Dots) and MC (Histogram) m_{ee} distribution for 97 $K_L \rightarrow e^+e^-\gamma$ events, where the best fit value of α_{K^*} (on the right) and the best fit α_{DIP} on the left is used in the MC. Top plot is the overlay, while the bottom is the ratio.

$W^{4er}(x_i, \lambda)$: Weight of $K_L \rightarrow e^+e^-e^+e^-$ events with one loop corrections and tree level based on standard QED process, (*i.e.* uses graphs like those in figure 1.12).

$W^{4e\gamma}(x_i, k_i, \lambda)$: Weight of $K_L \rightarrow e^+e^-e^+e^-\gamma$ based on standard QED process, (*i.e.* uses graphs like those in figure 1.13).

N^{4e} : Number of generated $e^+e^-e^+e^-$ events.

N_{OBS}^{4e} : The number of MC $e^+e^-e^+e^-$ events observed after applying reconstruction and selection cuts.

N_{DAT}^{4e} : Number of $e^+e^-e^+e^-$ observed in the data after applying reconstruction and selection cuts.

$\mathcal{A}^{4e}(x_i, \lambda)$: Squared amplitude of tree level $K_L \rightarrow e^+e^-e^+e^-$ process (*i.e.* the part of the weight which contains λ dependence).

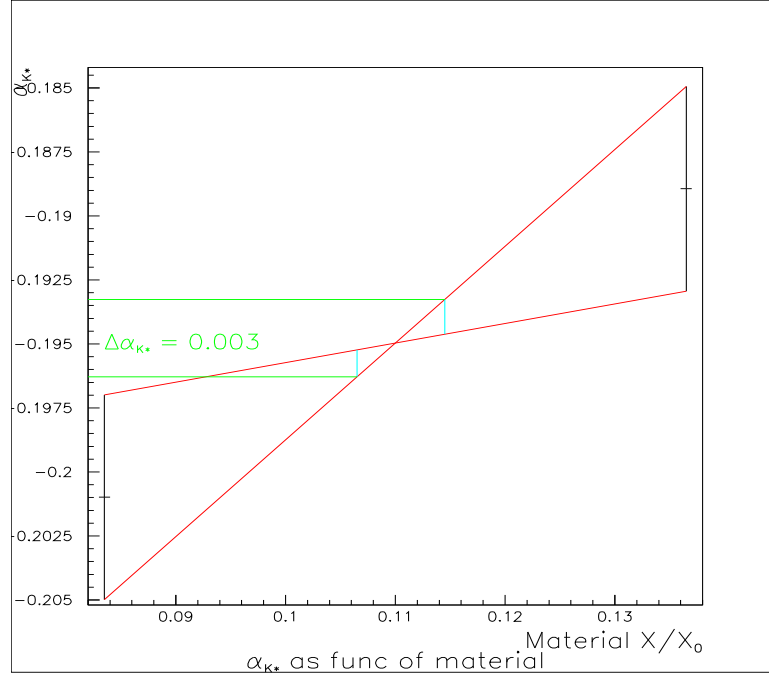


Figure 9.6: The change in the α_{K^*} parameter as a function of varying the amount of material in the upstream part of the detector.

$\mathcal{A}^{4er}(x_i, \lambda)$: Squared amplitude of $K_L \rightarrow e^+e^-e^+e^-$ with tree level and one loop corrections (*i.e.* the part of the weight which contains λ dependence).

$\mathcal{A}^{4e\gamma}(x_i, k_i, \lambda)$: Squared amplitude of radiative, $K_L \rightarrow e^+e^-e^+e^-\gamma$ process (*i.e.* the part of the weight which contains λ dependence).

Initially, consider the case where only tree level amplitudes are considered. The differential partial width for a given point in phase space is $d\Gamma^{4e}(x_i, \lambda)$. This is related to the squared amplitude \mathcal{A}^{4e} in equation 9.2, where $PS(x)$ is the phase space and $\Gamma_{\gamma\gamma}$ is the QED rate for $K_L \rightarrow \gamma\gamma$. The integrated rate is Γ^{4e} .

$$d\Gamma^{4e}(x_i, \lambda) = \mathcal{A}^{4e}(x_i, \lambda) \cdot PS^{4e}(x) \cdot \Gamma_{\gamma\gamma} \quad (9.2)$$

$$\Gamma^{4e}(\lambda) = \int d\Gamma^{4e}(x, \lambda) dx \quad (9.3)$$

The partial width for reconstructed events, $d\Gamma_{OBS}^{4e}$, is related to $d\Gamma^{4e}$ by the acceptance, ϵ^{4e} as is shown in equation 9.4.

$$d\Gamma_{OBS}^{4e}(x_i, \lambda) = d\Gamma^{4e}(x_i, \lambda) \cdot \epsilon^{4e}(x_i) \quad (9.4)$$

The probability of observing a given point in phase space is $f(x_i, \lambda)$ defined in equation 9.5. The log-likelihood function is defined in terms of this f and is shown in equation 9.6. The last two terms are not a function of λ so they can be ignored.

$$f(x_i, \lambda) = \frac{d\Gamma^{4e}(x_i, \lambda) \cdot \epsilon^{4e}(x_i)}{\int d\Gamma^{4e}(x, \lambda) \cdot \epsilon^{4e}(x) dx} \quad (9.5)$$

$$\begin{aligned} \mathcal{L}(\lambda) &= - \sum_i^{N_{DAT}^{4e}} \ln[f(x_i, \lambda)] \\ &= - \sum_i^{N_{DAT}^{4e}} \ln[\mathcal{A}^{4e}(x_i, \lambda)] + N_{DAT}^{4e} \ln \left[\int d\Gamma^{4e}(x, \lambda) \cdot \epsilon^{4e}(x) dx \right] \\ &\quad - \sum_i^{N_{DAT}^{4e}} \ln[\epsilon(x_i) \cdot PS(x_i)] - N_{DAT}^{4e} \ln \Gamma_{\gamma\gamma} \end{aligned} \quad (9.6)$$

The Monte Carlo does the integration for the total rate by summing over a large number of weights that span the phase space. The partial width is the weight (*i.e.* $W^{4e}(x_i, \lambda) = d\Gamma^{4e}(x_i, \lambda)$), and the total rate is defined in equation 9.7.

$$\Gamma^{4e}(\lambda) = \frac{1}{N^{4e}} \sum_i^{N^{4e}} W^{4e}(x_i, \lambda) \quad (9.7)$$

The observed rate is related to the total rate times an average acceptance, $\bar{\epsilon}^{4e}(\lambda)$, as is shown in equation 9.8.

$$\begin{aligned} \Gamma_{OBS}^{4e}(\lambda) &= \bar{\epsilon}^{4e}(\lambda) \cdot \Gamma^{4e}(\lambda) \\ &= \frac{1}{N^{4e}} \frac{\sum_i^{N_{OBS}^{4e}} W^{4e}(x_i, \lambda)}{\sum_i^{N^{4e}} W^{4e}(x_i, \lambda)} \sum_i^{N^{4e}} W^{4e}(x_i, \lambda) \\ &= \frac{1}{N^{4e}} \sum_i^{N_{OBS}^{4e}} W^{4e}(x_i, \lambda) \end{aligned} \quad (9.8)$$

In order to test new values of λ , we do not generate a new MC, instead we reweight existing Monte Carlo. This is illustrated in equation 9.9, where a new weight is calculated.

$$W^{4e}(x_i, \lambda) = \frac{\mathcal{A}^{4e}(x_i, \lambda)}{\mathcal{A}^{4e}(x_i, \lambda_{GEN})} W^{4e}(x_i, \lambda_{GEN}) \quad (9.9)$$

$$\Gamma_{OBS}^{4e}(\lambda) = \frac{1}{N^{4e}} \sum_i^{N_{OBS}^{4e}} \frac{\mathcal{A}^{4e}(x_i, \lambda)}{\mathcal{A}^{4e}(x_i, \lambda_{GEN})} W^{4e}(x_i, \lambda_{GEN}) \quad (9.10)$$

This is all true for the tree level calculation. However, there are additional complications since the $K_L \rightarrow e^+e^-e^+e^-$ MC is generated with $\mathcal{O}(\alpha_{EM})$ corrections and includes radiative events, see section 5.2.3. Thus the log-likelihood function must include both events with radiation and without. The variable N^{4er} is the number of events generated as $e^+e^-e^+e^-$ events with tree level and one-loop graphs with a certain infrared cutoff. $N^{4e\gamma}$ is the number of $e^+e^-e^+e^-\gamma$ events for the same infrared cut-off. The ratio of $N^{4e\gamma}$ to the sum of the two should be equal to the probability of radiation above that cutoff (represented here as P_{rad} and is equal to 24.59%) for a cutoff of 400keV. Equation 9.13 is the observed rate seen from the MC. In order to test different values of the form factor parameters, the quantity \mathcal{N} is constructed, see equation 9.15. It is related to Γ_{OBS}^{TOT} with the addition of a reweighting for different values of the form factor parameters made explicit and the constant N^{tot} is dropped. Finally, the log-likelihood as a function of λ can be formed, as is done in equation 9.16. For the calculation of \mathcal{N} , the photon is not detected (because it did not have enough energy or it was lost). However, the production of the photon is still known and the information at generation is used in the calculation. For the log-likelihood, the information is limited. If the photon was not detected, then there is no information, so we use a higher energy cut-off in the \mathcal{A} to reflect this.

$$N^{4er} = (1 - P_{rad})N^{tot} \quad (9.11)$$

$$N^{4e\gamma} = P_{rad}N^{tot} \quad (9.12)$$

$$\Gamma_{OBS}^{TOT}(\lambda) = \Gamma_{OBS}^{4er}(\lambda) + \Gamma_{OBS}^{4e\gamma}(\lambda) \quad (9.13)$$

$$= \frac{1}{N^{tot}} \left(\frac{1}{(1 - P_{rad})} \sum_i^{N_{OBS}^{4er}} W^{4er}(x_i, \lambda) + \frac{1}{P_{rad}} \sum_i^{N_{OBS}^{4e\gamma}} W^{4e\gamma}(x_i, \lambda) \right) \quad (9.14)$$

$$\begin{aligned} \mathcal{N}(\lambda) &= \frac{1}{1 - P_{rad}} \sum_i^{N_{OBS}^{4er}} \frac{\mathcal{A}^{4er}(x_i, \lambda, E_\gamma)}{\mathcal{A}^{4er}(x_i, \lambda_{GEN}, E_\gamma)} W^{4er}(x_i, \lambda_{GEN}) \\ &+ \frac{1}{P_{rad}} \sum_i^{N_{OBS}^{4e\gamma}} \frac{\mathcal{A}^{4e\gamma}(x_i, k_i, \lambda)}{\mathcal{A}^{4e\gamma}(x_i, k_i, \lambda_{GEN})} W^{4e\gamma}(x_i, k_i, \lambda_{GEN}) \end{aligned} \quad (9.15)$$

$$\mathcal{L}(\lambda) = - \sum_i^{N_{DAT}^{4e}} \ln \left(\frac{\mathcal{A}^{4er}(x_i, \lambda)}{\mathcal{N}(\lambda)} \right) \quad (9.16)$$

The minimum of the log likelihood as a function of λ gives the form factor parameters that best fit the data. There are some assumptions made for this calculation. First, the QED cut-off used in $\mathcal{L}(\lambda)$ is set much higher ($E_\gamma = 12.5\text{MeV}$ as opposed to $E_\gamma = 0.4\text{MeV}$ used for the generation of events). The higher cut-off is used because our detector can only find photons above a certain threshold (determined by the hardware cluster finding routine). The average detector threshold is about 12.5MeV in the center-of-mass frame. Second that the λ dependence comes mainly from the tree level graphs. The one loop correction diagrams do contain some λ dependence, but it is assumed to be the same as the tree level. Figure 9.7 shows the log-likelihood as a function the form factor parameters of α_{DIP} and β_{DIP} for $K_L \rightarrow e^+e^-e^+e^-$ data events.

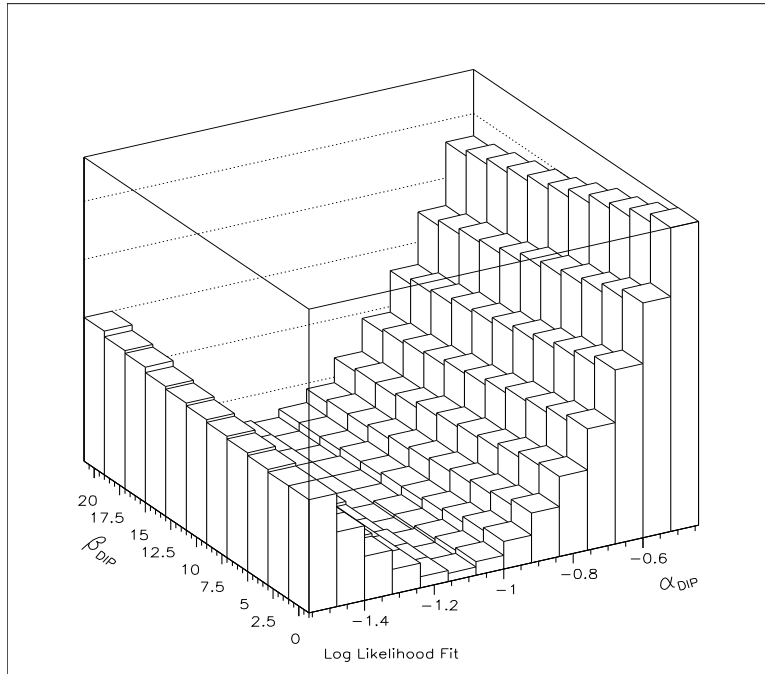


Figure 9.7: Log-Likelihood as a Function of the Fit Parameters α_{DIP} and β_{DIP} near the region of the minimum for $K_L \rightarrow e^+e^-e^+e^-$ data.

A test was performed in which the log likelihood function was applied to MC generated with known values of the form factor parameters. If the process is valid, the output should be the same as the input within statistical uncertainties. Figure 9.8 shows the one dimensional slices of the log likelihood where the DIP model is being tested. The outputs of the fit are at an $\alpha_{DIP} = -1.057 \pm 0.057$ and $\beta_{DIP} = 0.3 \pm 7.7$

for a MC generated with $\alpha_{DIP} = -1.0$ and $\beta_{DIP} = +1.0$, which is acceptable.

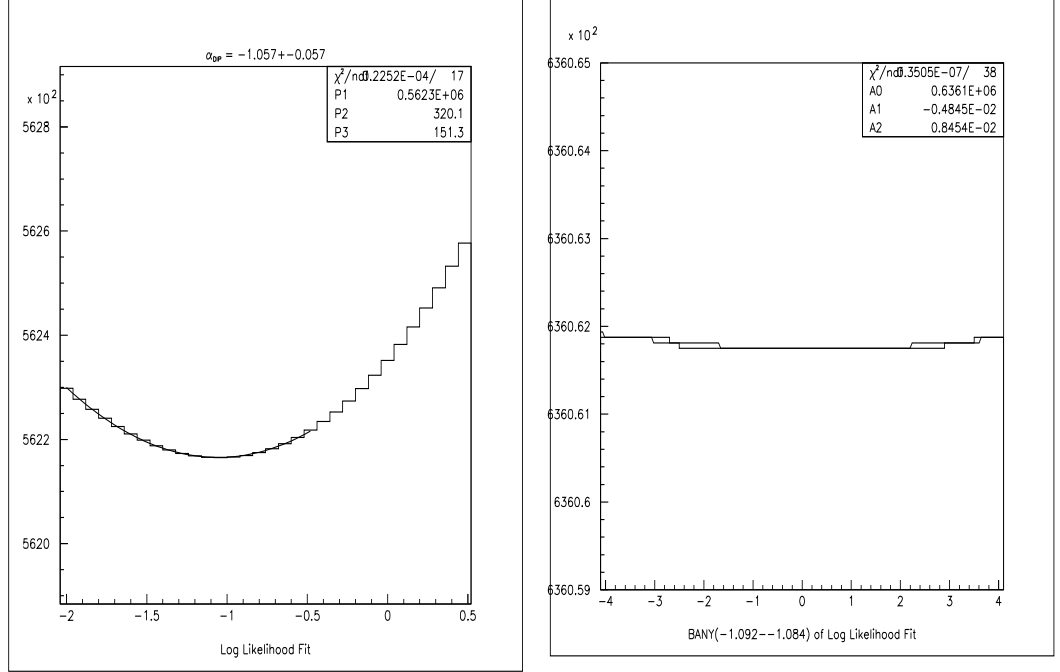


Figure 9.8: 1-dimensional Log-Likelihood as a Function of the Fit Parameter $\alpha_{DIP}(\beta_{DIP})$ at the minimum $\beta_{DIP}(\alpha_{DIP})$ for the Plot on the Left(Right) found for $K_L \rightarrow e^+e^-e^+e^-$ MC with an input of value of $\alpha_{DIP} = -1.0$ and $\beta_{DIP} = +1.0$.

Figure 9.9 shows the slices of the log likelihood found for the data. The best fit results corresponds to a $\alpha_{DIP} = -1.08 \pm 0.41$ and $\beta_{DIP} = 13 \pm 54$ when testing the DIP form factor. A similar process can be used to test the BMS model and it gives $\alpha_{K^*} = -0.03 \pm 0.13$. These results are summarized in table 9.4.

9.2.1 Systematics

The process for evaluating the systematics for the form factor parameters is essentially identical to that used for determining the systematics for the branching ratio measurement of $K_L \rightarrow e^+e^-e^+e^-$. Varying the value of cuts one at a time gives a set of different form factor measurements. The quadrature sum of these differences gives an uncertainty of 0.11 in α_{DIP} . Varying the amount of material gives a change of 0.03 in α_{DIP} . Varying the amount of track inefficiency produces a change of 0.05 in α_{DIP} ; and smearing hit positions gives an uncertainty of 0.02. Summing in quadrature the differ-

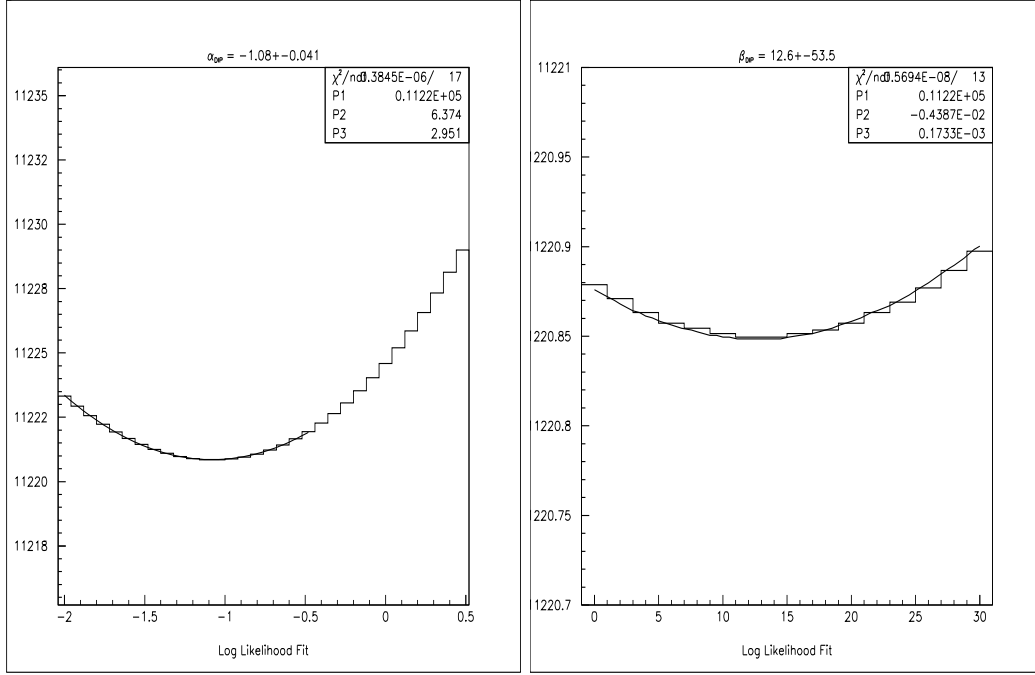


Figure 9.9: 1-dimensional Log-Likelihood as a Function of the Fit Parameter $\alpha_{DIP}(\beta_{DIP})$ at the Minimum $\beta_{DIP}(\alpha_{DIP})$ for the plot on the Left(Right) found for $K_L \rightarrow e^+e^-e^+e^-$ Data.

ence caused by removing the energy slope and increasing the energy resolution gives a difference of 0.01. The Monte Carlo includes by default corrections up to $\mathcal{O}(\alpha_{EM})$, but higher order corrections could have an effect. The change in the shape of the m_{ee}^{11} and m_{ee}^{22} spectrum between using just tree level and with one loop corrections and radiation is shown on the left hand side of figure 9.10. Assuming that higher order terms give a similar difference squared, then it would produce a shape like that shown on the right hand side of figure 9.10. This change in shape corresponds to a difference in α_{DIP} of 0.04. Table 9.3 lists and totals all the errors mentioned above. Table 9.4 lists the final results of the form factor measurements for the $K_L \rightarrow e^+e^-e^+e^-$ analysis with uncertainties.

9.3 Results

The form factor measurement are listed in tables 9.2 and 9.4. They can be compared with previous measurements of the same modes and with similar measurements

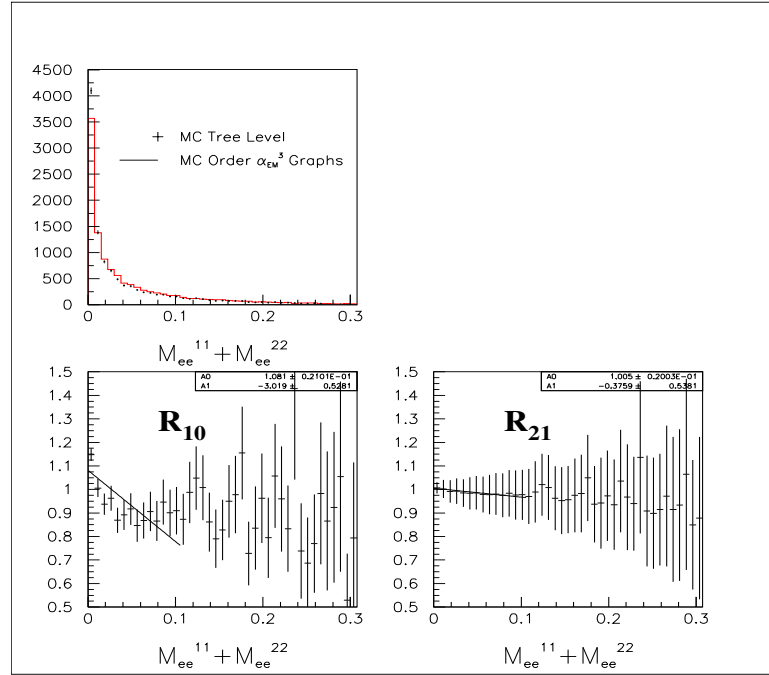


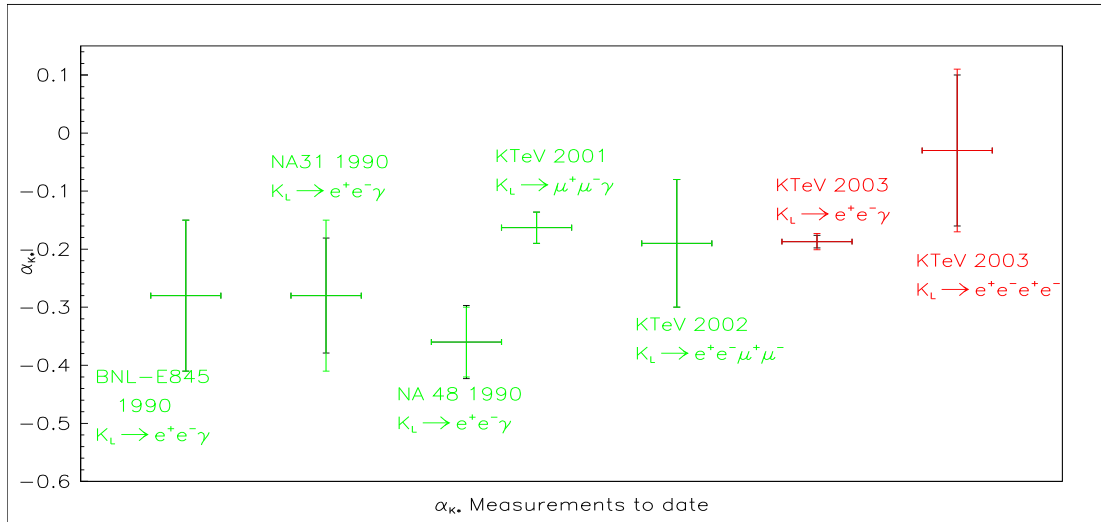
Figure 9.10: Left hand side, first plot is a comparison $m_{ee}^{11} + m_{ee}^{22}$ for Tree Level Monte Carlo with $\mathcal{O}(\alpha_{EM}^3)$ Monte Carlo. The second plot on the left hand side is R_{10} the ratio of the $\mathcal{O}(\alpha_{EM}^3)$ MC over the Tree Level MC. The third plot represents an estimate of the possible size of $\mathcal{O}(\alpha_{EM}^4)$ corrections. The quantity R_{21} plotted there is defined as $R_{21} = 1 - (R_{10} - 1)^2$. That is, we estimate the fractional effect of the second order correction to be the square of the fractional effect of the first order corrections.

Uncertainty Source	Change in α_{DIP}	Change in α_{K^*}	Change in β_{DIP}
Statistical	0.41	0.132	54
Cut Variations	0.11	0.035	32
DC Inefficiency	0.05	0.016	1
Radiative Corrections	0.04	0.013	2
Upstream Material	0.03	0.010	2
DC Hit Resolution	0.02	0.006	29
Energy Resolution	0.01	0.003	1
Total Systematic	0.13	0.043	43

Table 9.3: List of Sources of Uncertainty for the $K_L \rightarrow e^+e^-e^+e^-$ Form Factor Measurement.

for different modes. This is illustrated in figures 9.11 and 9.12. All the measurements seem to agree, except the NA48 result of $\alpha_{K^*} = -0.36 \pm 0.06$, where there is a $\sim 3\sigma$ difference between it and the α_{K^*} measured by this analysis.

	α_{K^*}	α_{DIP}	β_{DIP}
1997	$-0.05 \pm 0.28_{\text{stat}}$	$-1.13 \pm 0.70_{\text{stat}}$	$18 \pm 91_{\text{stat}}$
1999	$-0.02 \pm 0.15_{\text{stat}}$	$-1.06 \pm 0.51_{\text{stat}}$	$11 \pm 68_{\text{stat}}$
All	$-0.03 \pm 0.13_{\text{stat}} \pm 0.04_{\text{sys}}$	$-1.08 \pm 0.41_{\text{stat}} \pm 0.13_{\text{sys}}$	$13 \pm 54_{\text{stat}} \pm 43_{\text{sys}}$

Table 9.4: Measurements of α_{K^*} , α_{DIP} , and β_{DIP} .Figure 9.11: Previously measured values of the BMS parameter α_{K^*} with the newly measured result.

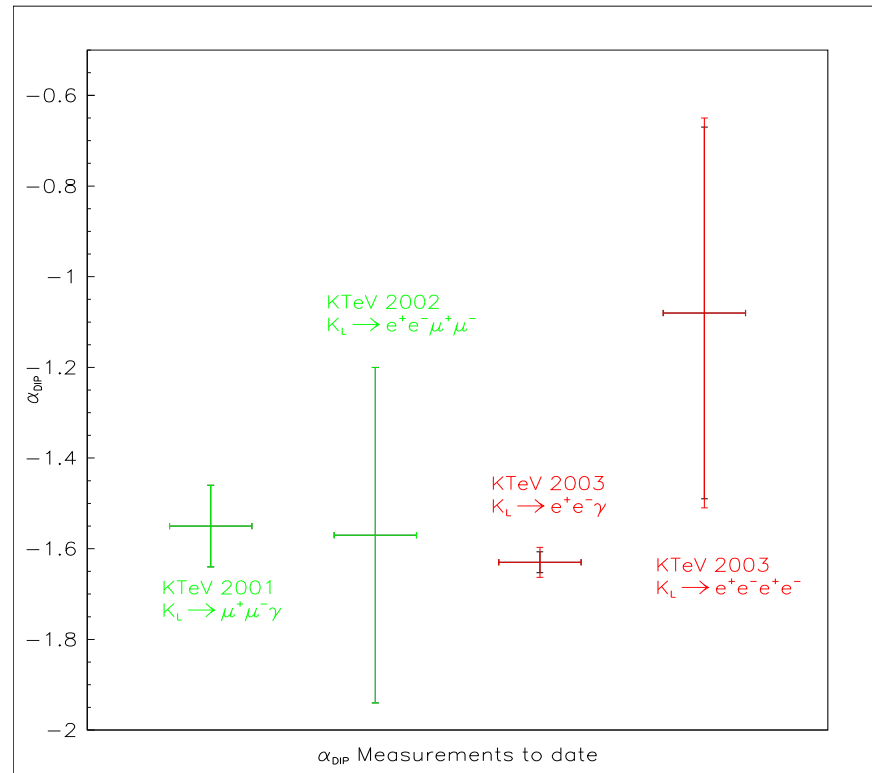


Figure 9.12: Previously measured values of the DIP parameter α_{DIP} with the newly measured result.

Bibliography

- [1] P. Mikelsons. Search for the Decay $K_L \rightarrow \pi^0 e^+ e^-$ and Study of the Decay $K_L \rightarrow e^+ e^- \gamma \gamma$. PhD thesis, The University of Colorado, Boulder, 1999.
- [2] Hogun Nguyen. Long write-up for the measurement of δ_l in 1997 kteV data (version 1). Technical report, KTeV Internal Note 0751, 2000.
- [3] Rick Kessler. "private communication". 2003.
- [4] C.S. Wu *et al.* Experimental test of parity conservation in beta decay. Phys. Rev., 105:1413, 1957.
- [5] V.L. Fitch J.H. Christenson, J.W. Cronin and R. Turlay. Evidence for the 2π decay of the K_2^0 meson. Phys. Rev. Lett., 13:562, 1964.
- [6] M. Gell-Mann and A. Pais. Behavior of neutral particles under charge conjugation. Phys. Rev., 97:1387, 1955.
- [7] K. Lande *et al.* Observations of long-lived neutral ν particles. Phys. Rev., 103:1901, 1956.
- [8] P. Ko. $K_L \rightarrow \mu^+ \mu^-$, the top-mass, and other related topics. Phys. Rev. D, 45:174, 1992.
- [9] G. Buchalla and A.J. Buras. The rare decays $K^+ \rightarrow \pi^+ \nu \bar{\nu}$ and $K_L \rightarrow \mu^+ \mu^-$ beyond leading logarithms. Nucl. Phys B, 412:106, 1994.
- [10] K. Kumericki J.O. Eeg and I. Picek. On the dispersive two-photon $K_L \rightarrow \mu^+ \mu^-$ amplitude. Eur. Phys. J C, 1:531, 1998.
- [11] G. Isidori G. D'Ámbrosio and J. Portolés. Short-distance information from $B(K_L \rightarrow \mu^+ \mu^-)$. Phys. Lett. B, 423:385, 1998.
- [12] G. Belanger and C.Q. Geng. New range of mixing parameters and rare K decays. Phys. Rev. D, 43:140, 1991.
- [13] G. D'Ámbrosio and D. Espriu. Rare decay modes of the K -mesons in the chiral langrangian. Phys. Lett. B, 175:237, 1986.
- [14] L. M. Sehgal. Electromagnetic contributions to the decays $K_S \rightarrow \bar{l} l$ and $K_L \rightarrow \bar{l} l^*$. Phys. Rev., 183:1511, 1969.

- [15] D.E. Groom *et al.* Particle data group. Eur. Phys. J. C, 15:395, 2000.
- [16] D. Ambrose *et al.* Improved branching ratio measurement for the decay $K_L^0 \rightarrow \mu^+ \mu^-$. Phys. Rev. Lett., 84:1389, 2000.
- [17] R. H. Dalitz. On an alternative decay process for the neutral π -meson. Proc. Phys. Soc. (London) A, 64:667, 1951.
- [18] A. Barker *et al.* Radiative corrections to double dalitz decays: Effects on invariant mass distributions and angular corrections. Phys. Rev. D, 67:033008, 2003.
- [19] T. Miyazaki and E. Takasugi. Internal conversion of psuedoscalar mesons into lepton pairs. Phys. Rev. D, 8:2051, 1973.
- [20] K.O. Mikaelian and J. Smith. Radiative corrections to the decay $\pi^0 \rightarrow \gamma e^+ e^-$. Phys. Rev. D, 5:1763, 1972.
- [21] C. Quigg and J.D. Jackson. Decays of neutral pseudoscalar mesons into lepton pairs. preprint 18487, UCRL:unpublished, 1968.
- [22] L. Zhang and J.L. Goity. Decays $K_L \rightarrow l^+ l^- l^+ l^-$ reexamined. Phys. Rev. D, 57:7031, 1998.
- [23] E. Massó L. Bergstrom and P. Singer. Testing the origin of the $\delta i = 1/2$ rule through K_L decays. Phys. Lett. B, 131:229, 1983.
- [24] R.F. Sarraga and H.J. Munczek. Weak-electromagnetic K -meson decays. Phys. Rev. D, 4:2884, 1971.
- [25] K.E. Ohl *et al.* Measurement of the branching ratio and form factor for $K_L \rightarrow e^+ e^- \gamma$. Phys. Rev. Lett., 65:1407, 1990.
- [26] G.B. Quinn. A Measurement of the Branching Ratio and Form Factor of $K_L \rightarrow \mu^+ \mu^- \gamma$. PhD thesis, University of Chicago, 2000.
- [27] A.I. Vainshtein M.A. Shiffman and V.I. Zakharov. Asymptotic freedom, light quarks and the origin of the $\delta t = \frac{1}{2}$ rule in the non-leptonic decays of strange particles. Nucl. Phys. B, 120:316, 1977.
- [28] A.S. Carroll *et al.* Observation of the dalitz decay modes of the K_L^0 . Phys. Rev. Lett., 44:525, 1980.
- [29] G.D. Barr *et al.* Measurement of the rate of the decay $K_L \rightarrow e^+ e^- \gamma$ and observations of a form factor in this decay. Phys. Lett. B, 240:283, 1990.
- [30] V. Fantil *et al.* Measurement of the decay rate and form factor parameter α_{K^*} in the decay $K_L \rightarrow e^+ e^- \gamma$. Phys. Lett. B, 458:553, 1999.
- [31] G.D. Barr *et al.* Observations of the decay $K_L^0 \rightarrow e^+ e^- e^+ e^-$. Phys. Lett. B, 259:389, 1991.
- [32] G.D. Barr *et al.* Measurement of the branching ratio of the double dalitz decay $K_L \rightarrow e^+ e^- e^+ e^-$ and the cp parity of the K_L -meson. Z. Phys. C, 65:361, 1995.

- [33] M.R. Vagins *et al.* Measurement of the branching ratio for $K_L \rightarrow e^+e^-e^+e^-$. Phys. Rev. Lett., 71:35, 1993.
- [34] T. Akagi *et al.* Estimation of the branching ratio of the decay $K_L^0 \rightarrow e^+e^-e^+e^-$ from the $K_L^0 \rightarrow e^+e^-x$ process. Phys. Rev. D, 47:2644, 1993.
- [35] P. Gu *et al.* Measurement of the branching ratio and a study of cp for the leptonic decay $K_L \rightarrow e^+e^-e^+e^-$. Phys. Rev. D, 47:2644, 1993.
- [36] A. Alavi-Harati *et al.* Measurements of the rare decay $K_L \rightarrow e^+e^-e^+e^-$. Phys. Rev. Lett., 86:5425, 2001.
- [37] E. Halkiadakis. Measurements of Neutral Kaon Decays to Two Electron-Positron Pairs. PhD thesis, Rutgers State University of New Jersey, 2001.
- [38] A. Alavi-Harati *et al.* Measurement of the branching ratio and form factor of $K_L \rightarrow \mu^+\mu^-\gamma$. Phys. Rev. Lett., 87:71801, 2001.
- [39] A. Alavi-Harati *et al.* Measurements of the decay $K_L \rightarrow e^+e^-\mu^+\mu^-$. Phys. Rev. Lett., 90:141801, 2003.
- [40] A. Alavi-Harati *et al.* A measurement of the branching ratio of $K_L \rightarrow e^+e^-\gamma\gamma$. Phys. Rev. D, 64:12003, 2001.
- [41] J. Graham. Measurements of the Direct CP -Violating Parameter $\text{Re}(\epsilon'/\epsilon)$ and the Kaon Sector Parameters Δm , τ_S , and ϕ_\mp . PhD thesis, University of Chicago, 2001.
- [42] K. Hanagaki. Search for the Decay $K_L \rightarrow \pi^0\nu\bar{\nu}$. PhD thesis, University of Osaka, Japan, 1998.
- [43] Nick Solomey *et al.* Development and performance of the ktev transistion radiation detector systme. Nucl. Inst. Meth. A, 419:637, 1998.
- [44] A. Roodman. The ktev pur csi calorimeter. In Proceedings of the VII International Conference on Calorimetry, Tuscon, Arizona. World Scientific, 1998.
- [45] P. Shawhan. Observation of Direct CP Violation in $K_{S,L} \rightarrow \pi\pi$ Decays. PhD thesis, The University of Chicago, 2000.
- [46] J. Hamm. Study of the Rare Decay $K_L \rightarrow e^+e^-\mu^+\mu^-$ at KTeV. PhD thesis, The University of Arizona, 2002.
- [47] G. Graham. First Observation of the rare decay $K_L \rightarrow \pi^0\gamma e^+e^-$. PhD thesis, The University of Chicago, 1999.
- [48] A.J. Malensek. "empirical formula for thick target particle production". Fermilab Report FN-341, 1981.
- [49] E. Zimmerman. Measurement of the Branching Ratio of the $\pi^0 \rightarrow e^+e^-$ Using $K_L \rightarrow 3\pi^0$ Decays in Flight. PhD thesis, University of Chicago, 1999.
- [50] A.F. Bielajew. "improved angular sampling for pair production in the egs4 code system". PIRS-0287, 1991.

- [51] L. Bergstrom *et al.* Radiative and muonic decays of K_L . implications for top mass. Phys. Lett. B, 249:141, 1990.
- [52] L. Bergstrom *et al.* $K_L \rightarrow \mu^+ \mu^-$, top mass and bottom lifetime. Phys. Lett. B, 134:373, 1984.
- [53] A. Bevan *et al.* Recent rare kaon decay results from NA48. J. Phys. G: Nucl. Part. Phys., 27:1161, 2001.

Appendix A

TRD Trigger Studies

The normalization of the decay $K_L \rightarrow e^+e^-\gamma$ is the the decay $K_L \rightarrow \pi^0\pi^0\pi_D^0$. These two data samples come from different triggers, Trigger 3 and Trigger 1 respectively. One of the largest differences between these two triggers is the TRD requirements placed in Trigger 3, see section 3.3.5. The following is a discussion of the efficiency of this L2 Trigger element and the effect it has on measurements.

A.1 Trigger Definition

The first part of the trigger required that there is a low threshold hit in TRD chamber 1 or 2. This formed the front seed. Similarly there was a back seed formed from the OR of low threshold hits in either TRD chamber 7 and 8. A line was drawn from the back seed to the front seed, as long as both existed. At least four out of eight TRD chambers were required to have high threshold hits along this line. The number tracks that satisfied those criterion was counted to be used by the trigger. A diagram illustrating an example of the the trigger can be seen in figure 3.11.

A.2 TRD Trigger Efficiency

The signals from the TRD chambers went to both FERA ADCs, where pulse height information was stored in the form of counts, and to Kumquat(KQ) latches. One can form an efficiency by looking at ADC spectrum from $K_L \rightarrow \pi^0\pi^0\pi_D^0$ events with the latch on to events were it did not turn on. In this way, one can determine the any errors associated with this trigger.

A.3 Efficiency Curves

Comparing the ADC spectrum for events that do and do not have a Kumquat latch set gives one an efficiency curve. These curves can give one insight into the details of the TRD Trigger. Figure A.1 shows such an ADC spectrum for low threshold data. Similarly figure A.2 shows the ADC spectrum for high threshold, and figure A.3 and A.4 are the corresponding efficiency curves.

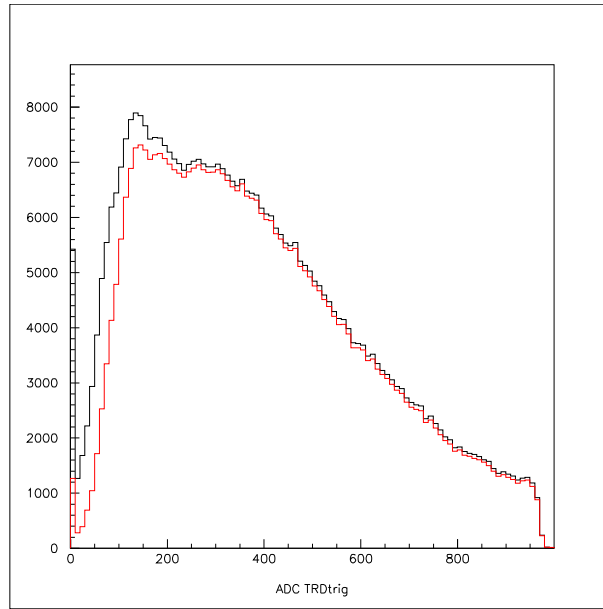


Figure A.1: Black is ADC spectrum, Red is Spectrum with the Low Threshold Kumquat bit set.

There are a number of interesting features that can be seen in the the efficiency curves. The most notable is that the curves seem to head downward at high ADC values. A hypothesis was formed to account for this feature. If there were multiple pulses on the wire (possibly from out of time activity), such that it could look like figure A.5, then it could account for the following:

- The efficiency curve not reaching one.
- The efficiency being worse at high ADC values.
- The efficiency effects above being worse for the Low Threshold curve.

The reason that multiple pulses could explain all these effects comes mainly from the

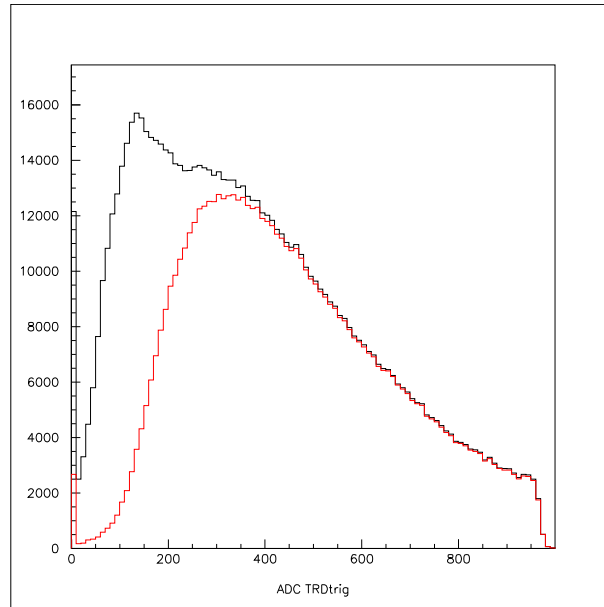


Figure A.2: Black is ADC spectrum, Red is Spectrum with the High Threshold Kumquat bit set.

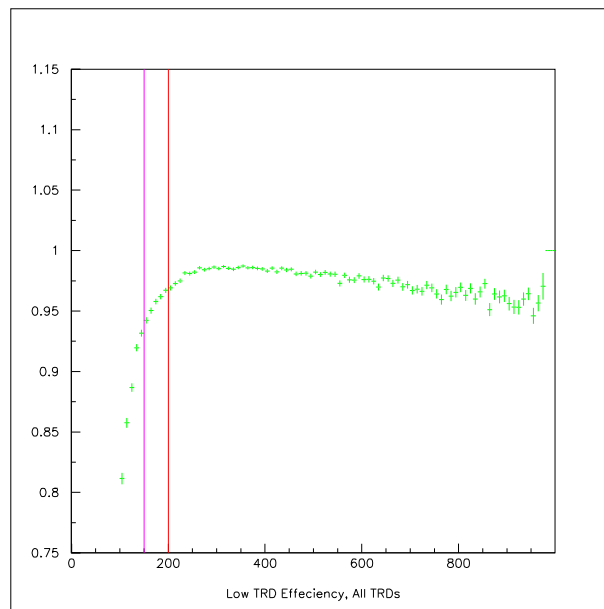


Figure A.3: Ratio of A.1. Efficiency curve for the Low Threshold.

fact that the Kumquat latch is turned on when the rising edge of the pulse crosses a certain threshold and it is in-time as is illustrated by the two vertical lines in figure A.5. An additional pulse can prevent a rising edge going over threshold in-time which

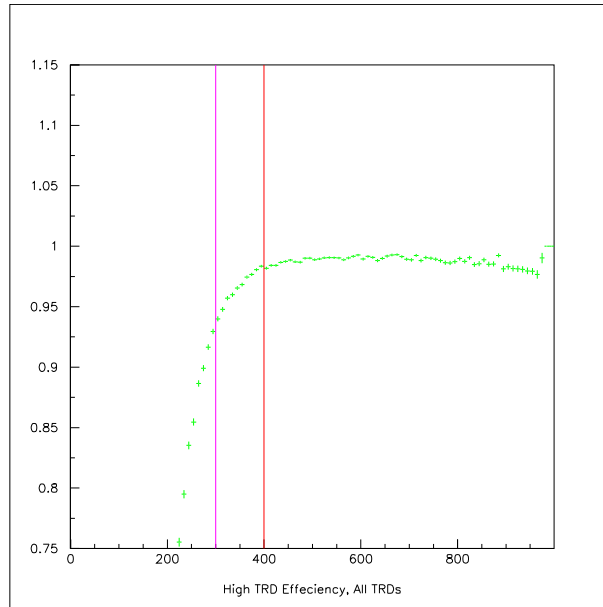


Figure A.4: Ratio of A.2. Efficiency curve for the High Threshold.

is illustrated for the low threshold in the figure (*i.e.* the rising edge only occurs out of time or it is above the low threshold). Larger ADC counts come from a large pulse, so it is easier for additional pulses to prevent an in-time rising edge. Finally, the effect is larger the lower the threshold.

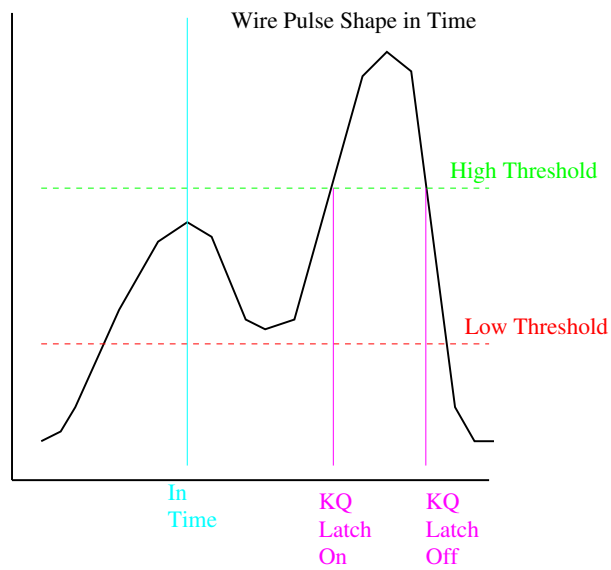


Figure A.5: Theoretical pulse shape, in time, for a TRD wire.

A.4 Simulating Curves

One can fit an efficiency curve, (eg fiure A.4 with a function in the $K_L \rightarrow \pi^0 \pi^0 \pi_D^0$ data set, figure A.6. This will give constants, P(1) is A, P(2) is B, etc.

$$A * \tanh\left(\frac{x - B}{C}\right) - D$$

Once the constants are known one can then use the same formula in the $K_L \rightarrow e^+ e^- \gamma$ data to form a probability that a track will pass high threshold requirements for each chamber. This probability can then be calculated for all TRD hits.

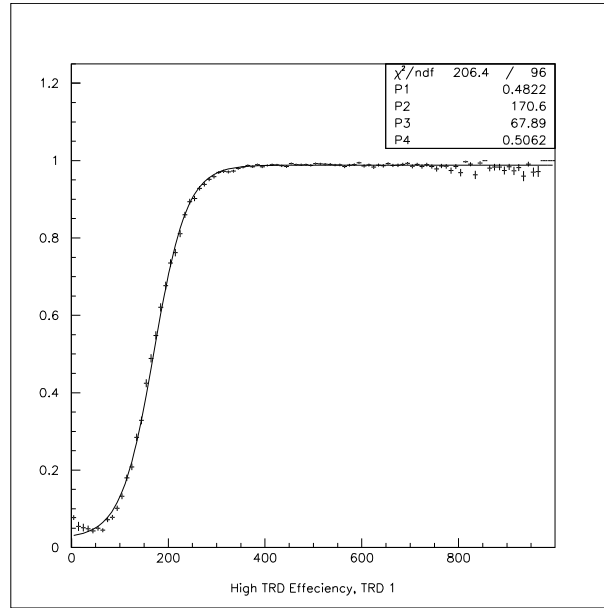


Figure A.6: Fit to the High Threshold efficiency curve.

For the purposes of this analysis it is obvious that the only point at which there is a substantial chance for a track to fail the TRD trigger is when it needs to find a coincidence of 4 hits that satisfy the High ADC Threshold. In that regard a probability of track satisfying 4 out of 8 High ADC Thresholds on a track was calculated, see figure A.7. Figure A.8 shows the ratio probability with and without the KQ latches being set. The fact that a track with a 4 of 8 probability of 70% has the latches set about 70% of the time is an indication that the probability is correctly calculated.

A cut on the 4 of 8 probability shown in figure A.7 is the best way to verify the TRD trigger. In order to evaluate a systematic uncertainty a “loose” and “tight” cut

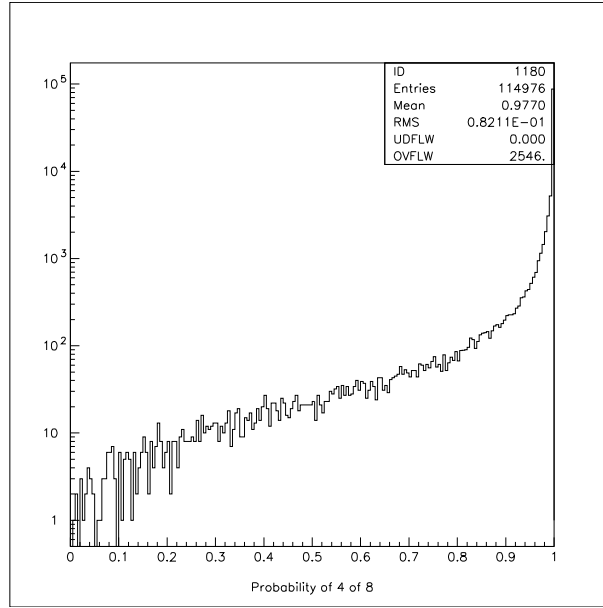


Figure A.7: Number of events versus the Probability that a Track has 4 out of 8 TRD hits that satisfy the High Threshold requirement.

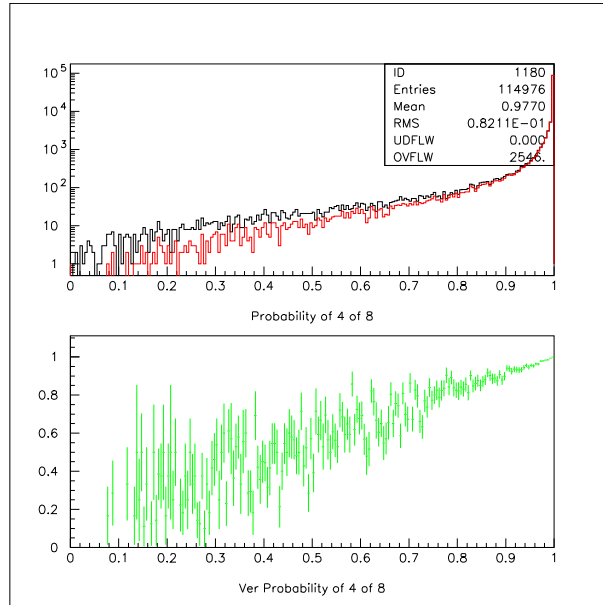


Figure A.8: 4 out of 8 probability ratio, total tracks over tracks with KQ latches on.

were also defined. The values of these cuts in the 4 out of 8 probability and the resulting change in α_{K^*} and the branching ratio are given in table A.1.

This shows a negligible systematic error, so no value was assigned to systematic

Cut Name	Value	$\Delta \alpha_{K^*}$	% Change in BR
Nominal Cut	0.90	-0.001	0.005
Loose Cut	0.80	0.000	0.004
Tight Cut	0.99	+0.001	0.011

Table A.1: Changes in the Branching Ratio and α_{K^*} measurement for $K_L \rightarrow e^+e^-\gamma$ due to the TRD Trigger element.

error.

Appendix B

Material Studies

The amount of material in the upstream segment of the detector has a large effect on the measurement of the form factor. The upstream segment in this case is defined to be the Vacuum Window, Helium Bag 1a, Helium Bag 1b, and Drift Chamber 1. This can be demonstrated by the looking at the minimum χ^2 per degree of freedom of the Data $M_{e^+e^-}$ over Monte Carlo $M_{e^+e^-}$ compared to a modified amount of material, figure B.1 and B.2.

A systematic method of determining the amount of material was obviously necessary. A collaborator, Jim Graham [41], had a method of doing just this using the width of the difference in the kaon vertex figured from the upstream X track segments and from the Y track segments as a function of 1 over the sum of track momentum squared. The difference in vertex location is normalized to make it dimensionless and referred to as the scaled Z. Figure B.3 is a two dimensional plot of scaled Z versus $1/P_1^2 + 1/P_2^2 = 1/P^2$.

Fitting the root mean squared (RMS) of the scaled Z in bins of $1/P^2$ for the $K_L \rightarrow \pi^0\pi^0\pi_D^0$ data set, figure B.4, one notices that the points nearly lie on a line. The slope of this line is sensitive to the amount of material and the intercept is sensitive to the intrinsic chamber resolution. By comparing the data to Monte Carlo generated with different amounts of upstream material, figure B.5 and B.6, it is evident that the slopes can be made to match. One process to do this is as follows: first generate three sets of Monte Carlo with the material significantly less than, greater than, and equal to the default amount of material (20%, 120%, and 100% material). Next, measure the slope of the RMS of scaled Z as a function of $1/P^2$ for each of the Monte Carlo simulations and for the data. Finally, plot the slopes of the Monte Carlos as a function

of the material and fit those points to a line and see where that line intersects with the slope from the data, figure B.7.

Figure B.4 shows that the RMS is not exactly linear in $1/P^2$, so the slope could be biased. To take this into account, one could repeat the above process fifty times, each time changing the range of the fit and/or the binning of the plot. Each time this is done a different optimal amount of material is found. If a plot of these measurements is made, the points are seen to form a nice Gaussian, figure B.8, with a RMS which is taken as a systematic error. Other sources of uncertainty include a rotation of the chambers with respect to each other and magnetic fields from the earth and the analysis magnet in the vacuum tank. Table B.1 lists all the sources of uncertainty for measuring material. Table B.2 lists the amount of material that I have measured for each of three periods of data taking (winter 97, summer 97 and 1999), see also figure B.9 . Note that the amount of material in the 1999 data set agrees with the estimate of all helium in Helium Bag 1a.

Table B.1: Uncertainties in Measuring the amount of Material.

Source	Amount
Statistical	0.000020
Varying Linear Fits	0.000025
Chamber Rotations and Vacuum Fields	0.000026
Total	0.000041

Table B.2: Amounts of Material.

	Vacuum Window+Air Gap
Estimate of all Air in Bag 1a	0.00156+0.00147
Estimate of all Helium in Bag 1a	0.00156+0.00072
	+
Winter Measurement	0.00156+0.00104
Summer Measurement	0.00156+0.00110
1999 Measurement	0.00156+0.00074

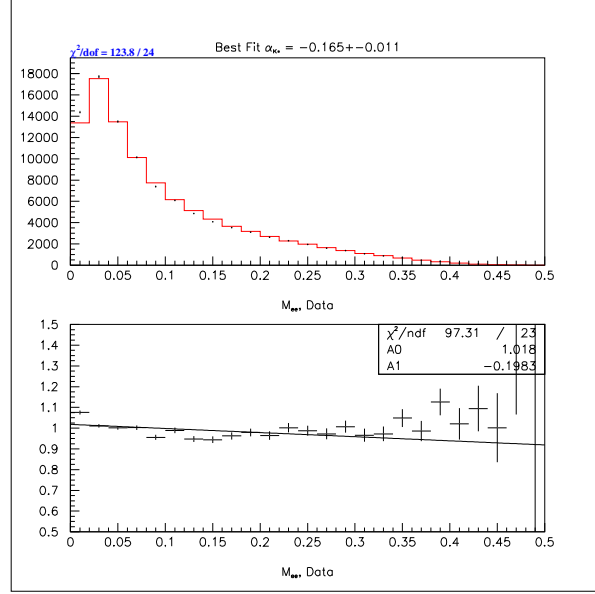


Figure B.1: $M_{e^+e^-}$ Data over Monte Carlo for $K_L \rightarrow e^+e^-\gamma$: Default Material.

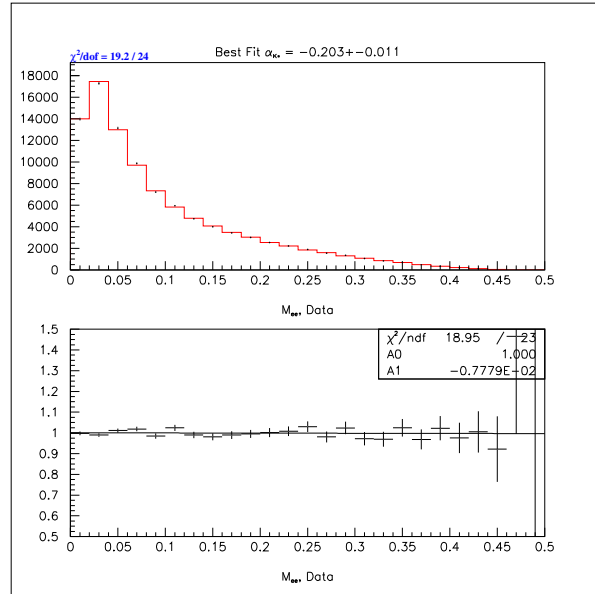


Figure B.2: $M_{e^+e^-}$ Subset of the Data over Monte Carlo for $K_L \rightarrow e^+e^-\gamma$: Modified Material.

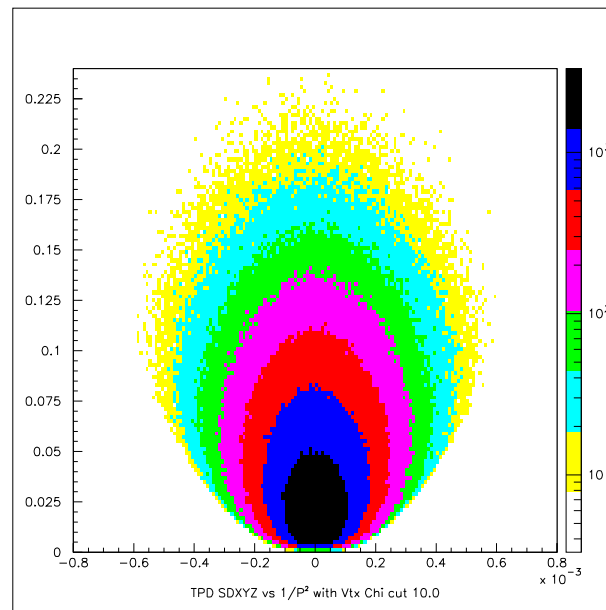


Figure B.3: Scaled Z versus $1/P^2$.

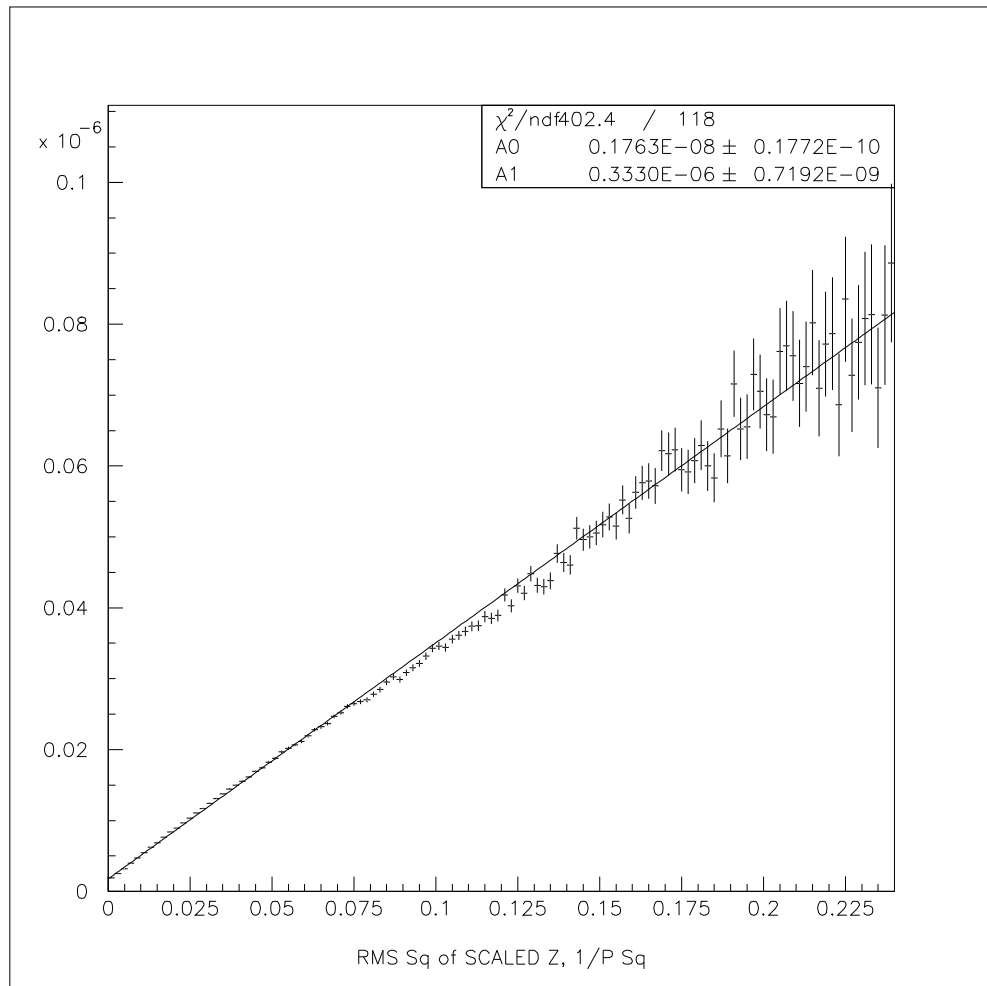


Figure B.4: RMS of Scaled Z in bins of $1/P^2$ for the normalization data.

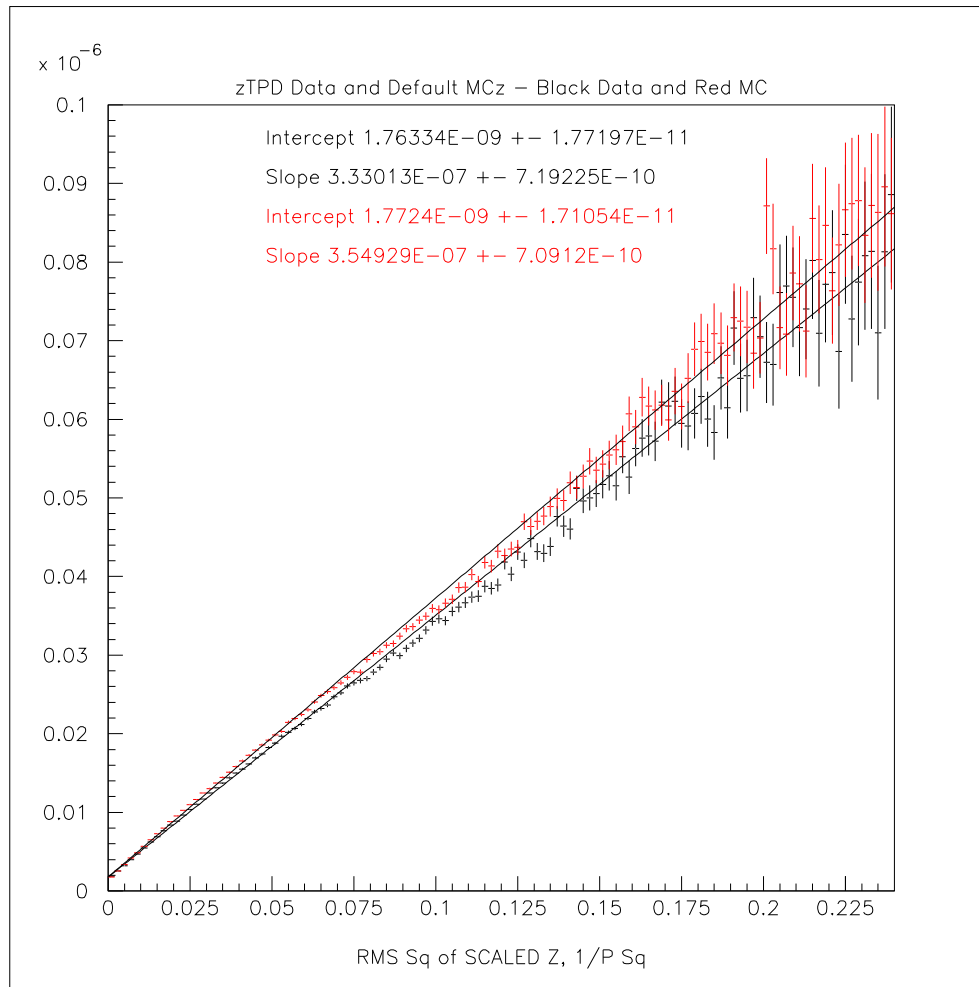


Figure B.5: RMS of Scaled Z in bins of $1/P^2$ for the normalization data and Monte Carlo with default material.

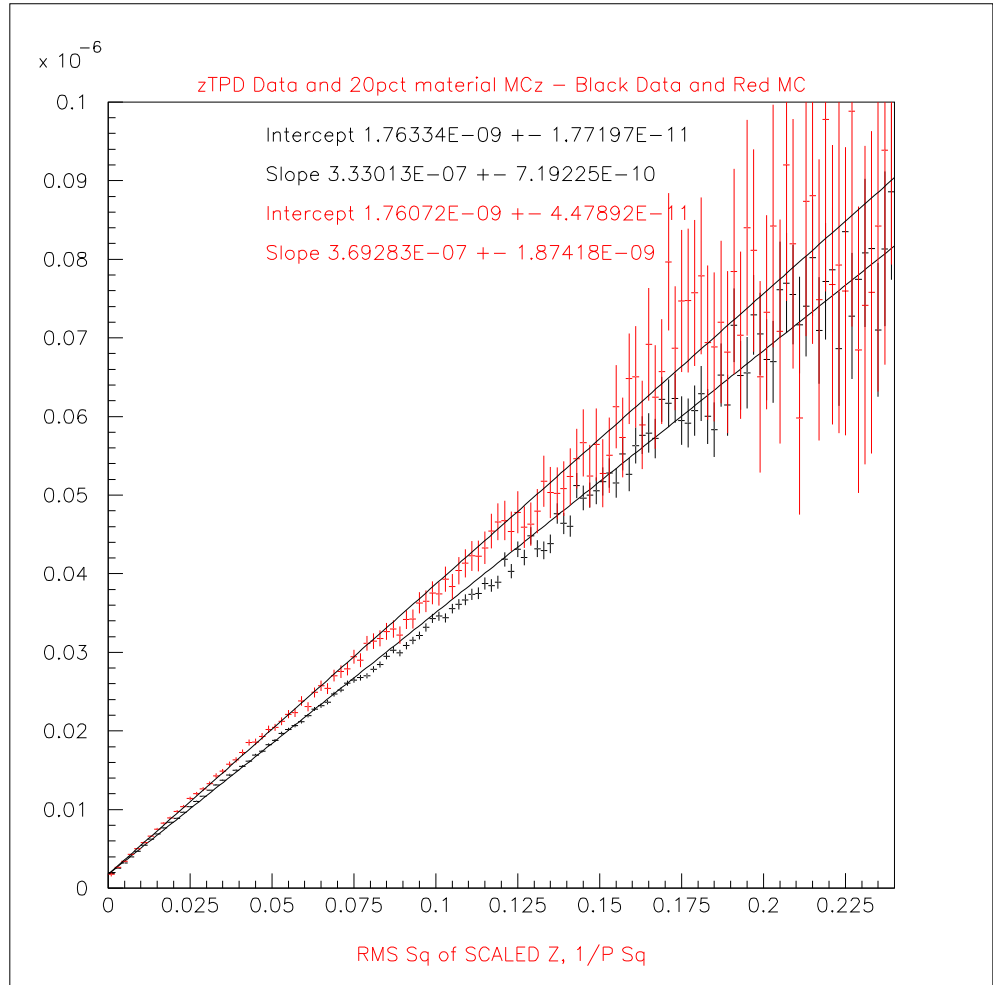


Figure B.6: RMS of Scaled Z in bins of $1/P^2$ for the normalization data and Monte Carlo with 20% material.

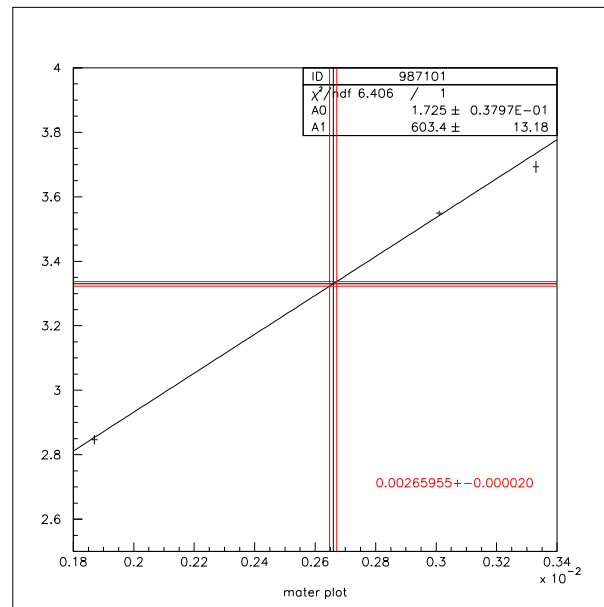


Figure B.7: The slope of RMS of Scaled Z from 3 different Monte Carlos versus the material they were generated at. The horizontal line is the equivalent slope from the data. The vertical line is the intersection of the data with a fit to the 3 Monte Carlos.

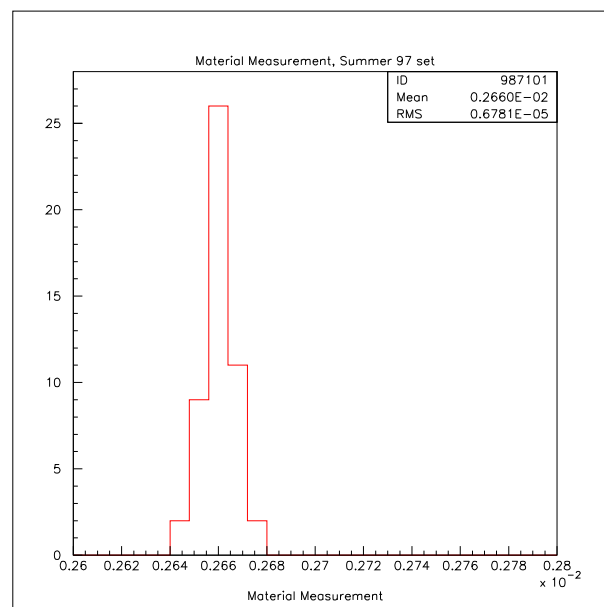


Figure B.8: The amount of material from 50 different methods of fitting the RMS of Scaled Z to a line.

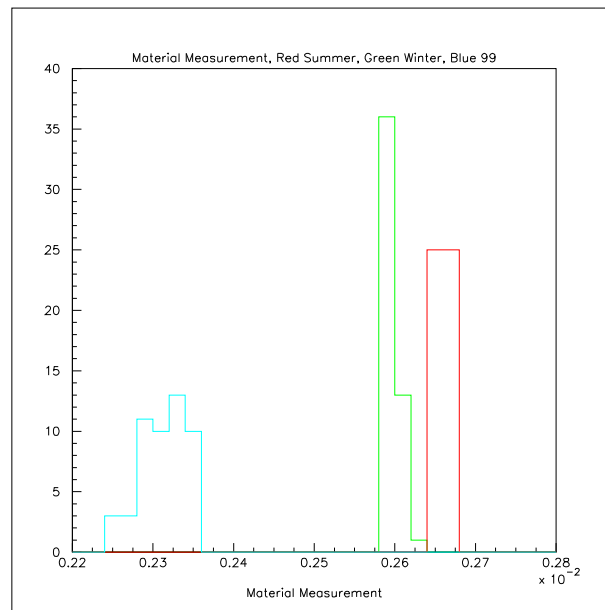


Figure B.9: The amount of material for Summer 97(red), Winter 97(green), and 1999(blue).